FREQUENCY HOPPING WIRELESS POWER TRANSFER WITHIN THE SAE J2954 OPERATING FREQUENCY BANDWIDTH FOR CHARGING ELECTRIC VEHICLES

Thesis submitted for the degree of Doctor of Philosophy (PhD)

Graham Afonyaa Blankson

Department of Electrical and Electronics Engineering,

Brunel University London

2025

Abstract

Wireless Power Transfer (WPT) is a means of transferring electric power through a magnetic or electric field via an airgap. This technology has resulted to the recent independence of plug in systems to charge equipment. The propagation of electric vehicles (EV) necessitates advancements in WPT technologies to enhance security, efficiency and reduced EV dwell time for charging. It is expected that wireless EV chargers will be installed in hospitals, railway and other non-domestic car parks which has equipment that emits electromagnetic waves thus, the potential to interfere with the wireless charging sessions. Conversely, the operation of the wireless EV chargers, if not shielded, has similar potential in its electromagnetic field strength to negatively impact the operation of near field equipment. Consequently, this research has been undertaken to develop an engineering solution to address these issues.

Sparse research has been undertaken in the field of immunization of WPT power signals. Most studies focused on the vulnerability of WPT as it operates at 85kHz which apparently can be a single point of failure as interference, spoofing, power theft, and jamming can severely impact its charging session. The few solutions propounded by the researchers have not been generally developed and implemented this may be due to the lack of urgency of this technology.

In this research the Frequency Hopping (FH) technique was incorporated in the WPT power and control circuitry as a solution to the risks associated with a single operating frequency. This novel design intervention founded the FH Wireless Power Transfer (FHWPT). FHWPT was developed as a system to introduce resilience and redundant operating frequencies in the WPT. FH is an existing technology used in communications to send and receive messages securely. This scheme was adopted to enable the WPT to operate in environments where conditions e.g. radio frequency interferences, power theft and jamming are hostile towards the predominant operating frequency.

This thesis demonstrates the feasibility of enabling FHWPT with key circuit modifications to existing WPT systems. It highlights the potential of FH to enhance security and operational

resilience in EV charging and covers system design, implementation, and prototype development.

Table of Contents

Abstract		2
Table of Cont	ents	4
Table of Figur	es	9
Table of Table	es	12
Abbreviations	5	13
Chapter 1 Int	roduction	15
1.1 Novelt	у	15
1.2 Techni	cal overview	15
1.3 Resear	ch Questions	19
1.4 Aim ar	nd Objectives	20
1.5 Metho	dology	21
1.5.1	Overview	22
1.5.2	Research Focus	22
1.5.3	Frequency bandwidth compliance	23
1.5.4	Software Used	23
1.5.5	Ethical Considerations	23
1.6 Summ	ary	23
Chapter 2 Lite	erature Review	25
2.1 Introd	uction to the Literature Review	25
2.1.1	History of the electric vehicle	25
2.1.2	Electric vehicle and conductive chargers	25
2.1.2.	1. Opportunity chargers for electric bus	27
2.1.2.	2. Opportunity chargers for trains	28
2.1.2.	3. Ultrafast chargers and CHAdeMO Standard	28
2.1.2.	4. Rapid and Slow chargers and CHAdeMO Standard	29
2.1.3	Wireless Power Transfer	29
2.1.4	Analogy of Wireless Power Transfer	30
2.1.5	History of Wireless Power Transfer	31
2.2 Classif	ication of Wireless Power Transfer Technologies	33
2.2.1	Inductive Power Transfer	35
2.2.2	Capacitive Power Transfer	35
2.2.3	Magnetic resonant WPT	37

2.2.4	Magnetic Gear WPT Technology	38
2.2.5	Microwave WPT	39
2.2.6	Optical WPT technology	41
2.3 Coil a	nd pad configuration	41
2.3.1	Planar Coils	42
2.3.2	Isometric Coils	43
2.3.3	Magnetic cores	43
2.3.4	Metallic Shield	44
2.3.5	Components of WPT transmitter and receiver pads	45
2.4 Interd	pperability of WPT	46
2.5 Retro	fitted Wireless Power Receiver Pads in EVs	47
2.5.1	Opportunity to integrate Wireless Receiver Pads in plug in EVs	47
2.5.2	Coil selection for interoperability	48
2.5.3	Insertion of Wireless Receiver Pads in EVs	49
2.5.4	Wireless Charging of Electric Taxis	50
2.5.5	Opportunity for retrofitting FHWPT in EVs	50
2.6 Imple	mentation of Zigbee protocol for WPT communication	50
2.7 DC-D	C converter	52
2.7.1	Gallium Nitride Field Effect Transistor	53
2.7.2	Controlled Switching Network	54
2.7.3	FHWPT Resonant Tank Network and Controlled Switching Network	55
2.7.4	Effective resistance of the Rectifier	56
2.8 Impe	dance matching in wireless power transfer technology	57
2.8.1	PTE improvement of wireless power transfer by impedance matching	57
2.8.2	Multiple receiver IMC	58
2.8.3	IMC in Transmitter and Receiver Modules	58
2.8.4	Assessing SoC Influence on WPT Loading via IMC	59
2.8.5	IMC circuitry concerns	59
2.9 Circui	t analysis of WPT Mono resonant Circuits	60
2.9.1	Analogy and Analysis of the ideal transformer	60
2.9.2	Compensation circuitry	65
2.9.3	Input impedance and the compensation capacitor	65
294	Series - Series Compensation Circuit	65

2.9.4.1.	Determining the PTE	67
2.9.4.2.	Determine Compensation Capacitor	68
2.9.5 Ser	ries Parallel Circuit	69
2.9.5.1.	Determine Compensation Capacitor	71
2.9.6 Par	rallel series compensation circuit	72
2.9.6.1.	Determine Compensation Capacitor	73
2.9.7 Par	rallel - Parallel compensation circuit	74
2.9.7.1.	Determine Compensation Capacitor	75
2.9.8 Sur	mmary of WPT Mono resonant topologies	76
2.10Bifurcation	l	77
2.11Frequency	Hopping	80
2.12Summary		82
Chapter 3 Mather	matical Model of the WPT	83
3.1 Introduction	on	83
3.1.1 Me	ethodology for WPT modelling	83
3.2 WPT theore	etical model undertaken in MS Excel	85
	equency response characteristics of $ H(\omega) $ under different k, co	
3.2.2 PTI	E – Frequency characteristics under varying load resistances	86
3.3 WPT theore	etical model undertaken in LT SPICE and MATLAB Simulink	87
3.3.1 Sim	nulation results of a SS WPT circuit	87
3.4 Finite Elem	ent Methods and Maxwell equations	90
3.5 Design of V	NPT Coil on Ansys software	92
3.5.1 Coi	il configuration	92
3.5.2 Res	sults	98
3.6 Summary		99
Chapter 4 Design	of Frequency Hopping Wireless Power Transfer System	101
4.1 Introduction	on	101
4.1.1 Me	ethodology of FHWPT Design	101
4.2 Adaptive F	requency-Hopping Control for EV Wireless Charging	103
4.3 Overview o	of FHWPT circuit	105
4.4 Transmitte	r circuit	107
// / 1 Inv	verter	108

4.5	Coil Cor	nfiguration	110
4	.5.1	Determine specifications for coil's Litz Wire	110
4	.5.2	Discrepancies of coil inductance formula	111
	4.5.2.1	. Evaluation of Spiral Planar Coil inductance using Online calcula	ators 111
	4.5.2.2	. Evaluation of Spiral coil inductance using Wheelers Formula	112
	4.5.2.3	. Evaluation of Spiral Coil using Ansys	113
4	.5.3	Nominated Spiral Planar Coil configuration for research	115
4.6	Feedba	ck coil and Sensors	115
4	.6.1	Voltage Sensor	118
4	.6.2	Current Sensor	120
4	.6.3	Frequency Sensor	121
4.7	Microco	ontroller	121
4	.7.1	PWM and inverter operation	124
4	.7.2	Impedance tracking using mutual inductance	125
4.8	Freque	ncy Hopping	128
4.9	Receive	r Circuit	132
4.10)Transm	itter and Receiver Communication	134
4.11	LPrinted	Circuit Board	135
4	.11.1	Transmitter PCB	136
4	.11.2	Transmitter coil FCC PCB	137
4	.11.3	Receiver feedback coil FCC PCB	138
4	.11.4	Transmitter or receiver feedback coil FCC PCB	139
4	.11.5	Receiver PCB	140
4.12	2Coil pla	cements and optimal load	141
4.13	3Summa	ry	142
Chapt	er 5 Syst	em analysis and Business Case	143
5.1	Introdu	ction	143
5.2	Method	dology of Frequency Hopping Wireless Power Transfer Analysis	143
5.3	Perform	nance metrics and Figure Of Merit	144
5	.3.1	The effect of k for Feedback Coil	144
5	.3.2	Optimizing system – Feedback coil	145
5.4	Power I	Losses	146
5	.4.1	Types of losses in WPT	146

5.5 Electro	onic Losses	147	
5.5.1	Transmitter GaNFET Conduction P _{Loss}	147	
5.5.2	Transmitter subcircuit Capacitive P _{Losses}	148	
5.5.3	Transmitter subcircuit P _{off}	148	
5.5.4	Transmitter subcircuit Switch On P _{Losses}	148	
5.5.5	Transmitter subcircuit Switch Off P _{Loss}	148	
5.5.6	Receiver's subcircuit buck controller's GaNFET Conduction P _{Loss}	149	
5.5.7	Receiver's subcircuit Capacitive P _{Loss}	149	
5.5.8	Receiver's subcircuit Poff Losses of Buck converter	150	
5.5.9	Receiver's subcircuit Switch on P _{Loss}	150	
5.5.10	Receiver's subcircuit Switch off P _{Loss}	150	
5.5.11	Receiver's subcircuit Total buck converter P _{Loss}	150	
5.5.12	Receiver's subcircuit Rectifier diode Conduction P _{Loss}	150	
5.5.13	FCC's subcircuit GaNFET conduction P _{Loss}	151	
5.5.14	FCC's subcircuit Poff losses	151	
5.5.15	FCC's subcircuit total P _{Loss}	151	
5.6 Coil an	d magnetic losses	153	
5.6.1	Copper losses	153	
5.6.2	Skin effect losses	153	
5.6.3	Eddy Current Losses	154	
5.6.4	Comparison of 90kHz and 85kHz system losses	156	
5.7 Plosses of	contributed by the FCC subcircuits	157	
5.8 Busine	ss Case	157	
5.8.1	Energy savings payback	158	
5.8.2	Production Cost Analysis	158	
5.8.3	Downtime and Power Theft Risk Analysis	159	
5.8.4	Return on Investment	160	
5.9 Optim	ization and limitations	161	
5.9.1	Improvements	161	
5.9.2	Limitations	162	
5.10Summ	ary	163	
Chapter 6 Co	nclusion	164	
Appendix 1 P	ppendix 1 Publications arising from research167		

Apı	pendix 2 Transmitter subcircuit PCB	168
Арі	pendix 3 Receiver subcircuit Bill of Materials	172
Apı	pendix 4 FCC subcircuit Bill Of Materials	177
	erences	
Ta	ible of Figures	
Fig.	1.1 FHWPT transmitter module schematic	16
Fig.	1.2 FHWPT receiver module schematic	16
Fig.	1.3 FBCs, L ₁ C ₁ and L ₂ C ₂ inductively coupled to transmitter and receiver coils L _p and L _s and their mutual inductances	17
Fig.	1.4 Simple WPT Equivalent circuit	19
_	2.1 Components of an electric car [12]	
Fig.	2.2 EV under charging session. [13]	27
Fig.	2.3 Opportunity Charger where a pantograph delivers power to a bus [15]	27
Fig.	2.4 Opportunity Charger where a conductor rail delivers power to a train [17]	28
Fig.	2.5 Simple step-down transformer showing the primary windings, secondary windings and soft iron core [23]	
Fig.	2.6 Stator and rotor in a 3-phase induction motor: (left) winding layout; (right) motor cross-sect	
•	[24]	
Fig.	2.7 Magnetic WPT showing Ampers law and Faradays law [3]	31
Fig.	2.8 Polyphase 270kW wireless charger [36]	33
Fig.	2.9 IPT circuit diagram [12]	35
Fig.	2.10 CPT circuit diagram [12]	36
Fig.	2.11 Magnetic Resonant WPT circuit diagram [1]	37
Fig.	2.12 Magnetic Resonant WPT circuit diagram [39]	38
_	2.13 Microwave WPT block diagram [1].	
	2.14 Vehicle mounted microwave WPT system [39]	
_	2.15 Optical WPT diagram [1]	
	2.16 Typical transmitter and receiver coil configurations [40]	
_	2.17 Air core wound helix coil [42]	
_	2.18 Solenoid a copper coil wound round an iron/magnetic core [43]	
_	2.19 Magnetic flux lines generated by an energised solenoid [44]	
_	2.20 WPT with a flux pipe spiral would coil [45]	
	2.21 WPT coil structure [48]	
_	2.22 WPT circuitry schematic. [53]	
_	2.23 Structure of proposed quadruple coil on mounted on a ferrite plate and aluminium shield.[54]	
_	2.24 (a) Toyota RAV4 EV (b) Scion IQ EV (c) Toyota Prius Plug-in (d) Chevy Volt [53]	
	2.26 Conductive EV charging system [57]	
_	2.27 Wireless EV charging system [57]	
_	2.28 DC-DC converter with loosely coupled transformer coils [60].	
_	2.29 (a) Equivalent circuit of CSN and (b) its respective fundamental harmonic sine wave and nth harmonic sine wave and nthe harmonic sine wave and nth	
٠ '5'	square wave forms [67]	
Fiσ	2.30 Series Resonant Loaded Converter [64]	

Fig.	2.31 Impedance matching circuit overview [69]	57
Fig.	2.32 Electromagnetic circuit	60
Fig.	2.33 Magnetic circuit	61
Fig.	2.34 Symbol of ideal transformer	62
Fig.	2.35 Ideal transformer model	62
Fig.	2.36 Magnetic circuit of a non-ideal transformer	63
Fig.	2.37 Model of non-ideal transformer	64
Fig.	2.38 T circuit of non-ideal transformer.	64
Fig.	2.39 WPT circuit showing dependent voltages.	65
Fig.	2.40 SS secondary impedance Zs referred to the primary side	66
Fig.	2.41 SP topology	69
Fig.	2.42 Secondary side SP topology reconfigured to a current source I _{ss}	70
Fig.	2.43 SP secondary impedance Z₅ referred to the primary side	71
Fig.	2.44 PS topology	72
_	2.45 PP topology	
Fig 2	2.46 Frequency domain RLC circuit	78
Fig.	2.47 Patent diagram for first FH communication system [86]	81
Fig.	3.1 Flow chart ilustrating methodology of WPT modelling	84
Fig 3	3.2 Frequency response of WPT with a k = 0.2	85
Fig 3	3.3 Frequency response of WPT with a k = 0.4	86
Fig.	3.4 PTE of various EV battery internal resistances between 0 and 400kHz	87
Fig.	3.5 simulation of SS WPT input left hand side (LHS) and output right hand side (RHS) voltage and current	88
Fig.	3.6 simulation of SS WPT input LHS and output RHS voltage and current using optimum $R_{\text{\tiny L}}$	89
Fig.	3.7 simulation of SS WPT input LHS and output RHS voltage and current of computed maximum Cmaxn,	
	Lmaxη and optimum R∟	89
Fig.	3.8 WPT transmitter coil	92
_	3.9 Ansys result Table showing excitation current of 1A, self inductance of 137.4 μH	
Fig.	3.10 WPT transmitter and receiver coils with air gap of 180mm	93
Fig.	3.11 Ansys result Table showing excitation current of 1A, coupling coefficient of 0.019 at 180mm air gap	
	between transmitter and receiver coils.	94
	3.12 simulated 137.4µH 180mm air gap WPT circuit on Simplorer	
Fig.	3.13 PTE of 44.3% at 83.2kHz	95
Fig.	3.14 PTE of 34.32% at 97.68kHz	95
_	3.15 PTE of 33.2% at 147.76	
Fig.	3.16 PTE of 34.07% at 194.95kHz	96
_	3.17 PTE of 70.19% at 245.45kHz	
_	3.18 PTE of 50.83% at 295.12kHz	
_	3.19 PTE of 33.56% at 346.85kHz	
_	3.20 PTE of 33.4% at 397.76kHz	
_	3.21 Trend of Ansys and mathematical model's PTE - Operating frequency sweep for a 10Ω impedance \mbox{lc}	
		99

Fig.	4.1 Development Methodology of the FHWPT	102
Fig.	4.2 FHWPT control flow chart	104
Fig.	4.3 Overview of FHWPT Transmitter circuit	106
Fig.	4.4 Overview of FHWPT Receiver circuit	106
	4.5 12V power supply schematic	
_	4.6 5V power supply schematic.	
	4.7 3.3V power supply schematic	
_	4.8 Full bridge inverter schematic.	
	4.9 Kaizer's online spiral inductor calculator [100]	
_	4.10 All about electronic circuit's online spiral inductor calculator [101]	
	4.11 Parameters of coil	
_	4.12 Ansys Model of 40 turns coil	
_	4.13 Ansys Self inductance result	
_	4.14 High-impedance interface for feedback voltage sensing.	
	4.15 Shut resistor for feedback current sensing	
_	4.16 Optocoupler in the voltage sensor subcircuit.	
_	4.17 Differential amplifier for voltage signal circuit	
_	4.18 Frequency sensor	
_	4.19 Microcontroller schematic	
Fig.	4.20 PWM pin assignment	124
Fig.	4.21 PWM frequency assignment	124
_	4.22 PWM frequency and duty cycle assignment	
Fig.	4.23 Significant Mutual inductance between coils.	125
Fig.	4.24 ADC pin assignment.	127
Fig.	4.25 Calibration code of voltage and current.	127
Fig.	4.26 microcontroller code to determine impedance.	128
Fig.	4.27 Illustration of Frequency channel selection using a variable capacitor	128
Fig.	4.28 IO expander and schedule for all coils	129
	4.29 Multiplexer and VGS booster circuit for GANFETs	
_	4.30 FCC for all coils	
_	4.31 FH instruction set	
_	4.32 Rectifier circuit	
_	4.33 switched regulator circuit	
	4.34 buck controller pin assignment	
_	4.35 buck controller PWM and duty cycle allocation	
_	4.36 buck controller schematic	
_	4.37 defining basic data exchange between the transmitter and receiver microcontroller	
_	4.38 Transmitter PCB layout	
_	4.39 PCB for Transmitter coil FCC layout	
_	·	
	4.40 PCB for receiver coil FCC layout	
_	4.41 PCB for Transmitter or receiver FBC FCC layout.	
_	4.42 Receiver PCB layout	
_	4.43 FHWPT coil displacements enclosed in air	
	5.1 Methodology of FHWPT analysis	
_	5.2 V _{feedback} and I _{feedback} over different L _{feedback} coils (5μH to 47μH)	
_	5.3 Cross section of the coil indicating diameter of Litz wire. [98]	
_	5.4 Distribution of Ploss in FHWPT	
Fig.	5.5 Cost allocation for FHWPT	158

Table of Tables

Table 2.1 WPT technology and their respective power throughput range. [12]	34
Table 2.2 Summary of Mono resonant WPT topologies	76
Table 4.1 Microcontroller determinants for adaptive operation	105
Table 4.2 Assessment of various microcontrollers for FHWPT application	123
Table 4.3 Schedule of FH channel tuning capacitance for 47µH inductor	132
Table 4.4 transmitter and receiver data type exchange schedule	135
Table 4.5 Schedule of FHWPT PCBs	136
Table 5.1 parameters to determine k for FBC	145
Table 5.2 Schedule of FHWPT subcircuits and Associated GaNFETs	147
Table 5.3 Total GaNFET losses in FHWPT	152
Table 5.4 Summary of Plosses on the coils at 85kHz and 90kHz	156
Table 5.5 85kHz and 90kHz Plosses	156
Table 5.6 Cost Structure of Prototype (excluding coils) and scale of economy	159
Table 5.7 Salient features of FHWPT versus WPT	160
Table 5.8 Downtime and Power theft risk analysis	160

Abbreviations

Α **Amps** В Magnetic flux C Capacitor CHAdeMO Charge de Move DC **Direct Current** dt small change in time dΦ small change in magnetic flux Ε Electric Field intensity (V/m) **EMC Electromagnetic Compatibility EMF** Electromotive force Electro Magnetic Interference EMI ΕV Electric Vehicle permittivity or dielectric strength ε F Farads FBC Feedback coil FCC Frequency Channel Controller FSC Frequency Selector Circuit FΗ Frequency Hopping FHWPT Frequency Hopping Wireless Power Transfer GaNFET Gallium Nitride Field Effect Transistor Н Magnetic Field intensity (A/m) HF **High Frequency** Hz Frequency unit 1 Current Internal combustion engine ICE ICNIRP International Commission on Non-Ionizing Radiation Protection Impedance matching circuit IMC J **Joules**

Coupling coefficient

Kilo Herts

k

kHz

kW Kilo Watt

kWh Kilo watt hour

L inductor

LASER Light Amplified and Stimulated Emission Radiation

LF Low Frequency

m meter

M Mega

M Mutual inductance

mm milli meter

N Number of Turns

OEM Original Equipment Manufacturer

OFCOM Office of Communications

PCB Printed circuit board

PWM Pulse Width Modulation

PTE Power Transfer Efficiency

PS Parallel Series

PP Parallel Parallel

Q Quality factor of coil

R resistor

RoC Rate of Charge

ROI Return on Investment

SAE Society of Automotive Engineers

SoC State of Charge

SS Series Series

SP Series Parallel

T Tesla

THz Tera Hertz

 μ permeability

 μH micro Henry (unit of inductance)

V Volts

WPT Wireless Power Transfer

Z impedance

Chapter 1 Introduction

The increased acceptance of EV in society has driven the demand for EV charging infrastructures. The EV original equipment manufacturers (OEM) and EV charge station OEMs have engaged in a seismic race towards fast, efficient and smart power trains, batteries cells, on board battery management systems and charging EV stations. Among these innovative breakthroughs is the WPT which has gained traction due to its potential to deliver power in a futuristic, contactless, automated and stylish mode. Despite these benefits the WPT is vulnerable to and can be responsible for electromagnetic interference, frequency jamming and power theft. Normally all WPTs work at a fixed operating frequency of 85kHz making it easy for malefactors to interrupt the charging sessions. This research introduces a novel enhanced adaptive FHWPT designed to overcome limitations of a fixed operating frequency system.

1.1 Novelty

The novelty of this work lies in the following contributions to the existing WPT systems:

- Integration of feedback coils (FBC) with the main transmitter and receiver coils, enabling continuous monitoring of inductive power parameters and providing real time information for adaptive control.
- Development of impedance detection circuits (IDC) updated dynamically through the FBCs, allowing the system to detect load or alignment variations.
- Implementation of a capacitor bank rastered across discrete frequency channels to provide alternative resonant frequencies, thereby supporting FH.
- Adoption of a microcontroller based communication protocol to transmit receiver parameters to the transmitter and vis versa, ensuring coordinated operation and secure data exchange between both modules.
- Deployment of microcontroller instructions to monitor anomalies and initiate FH when disturbances occur, enhancing system resilience against operational anomalies.

1.2 Technical overview

The research topic is to design and build a FHWPT system to operate at any 1kHz channels between 79kHz and 90kHz discreetly, providing resilience to the wireless charging operation.

The block diagram in Fig. 1.1 and Fig. 1.2 below presents the schematics of the FHWPT transmitter and receiver modules respectively.

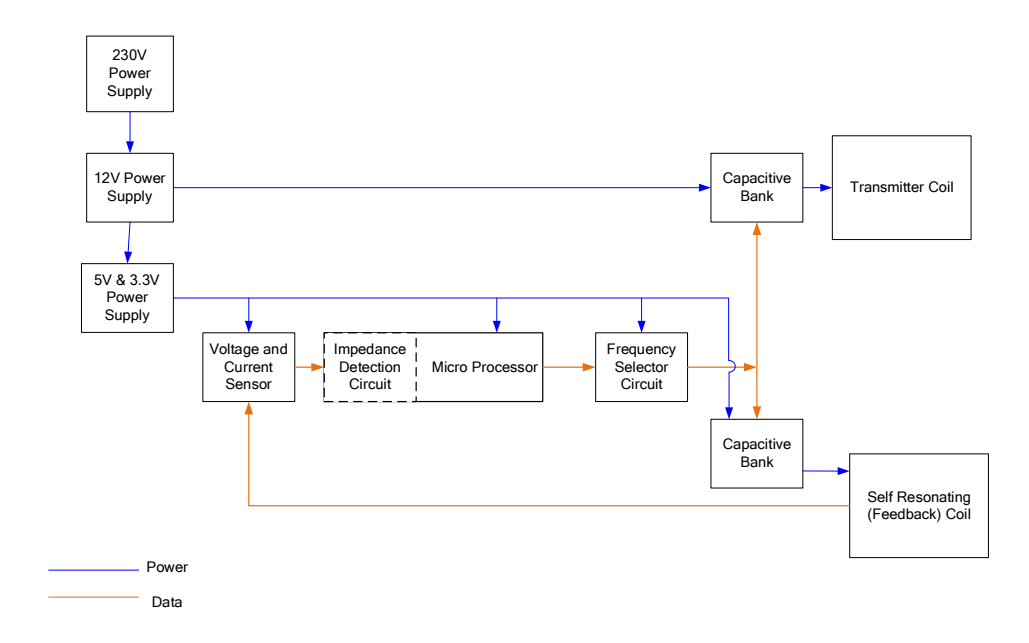


Fig. 1.1 FHWPT transmitter module schematic

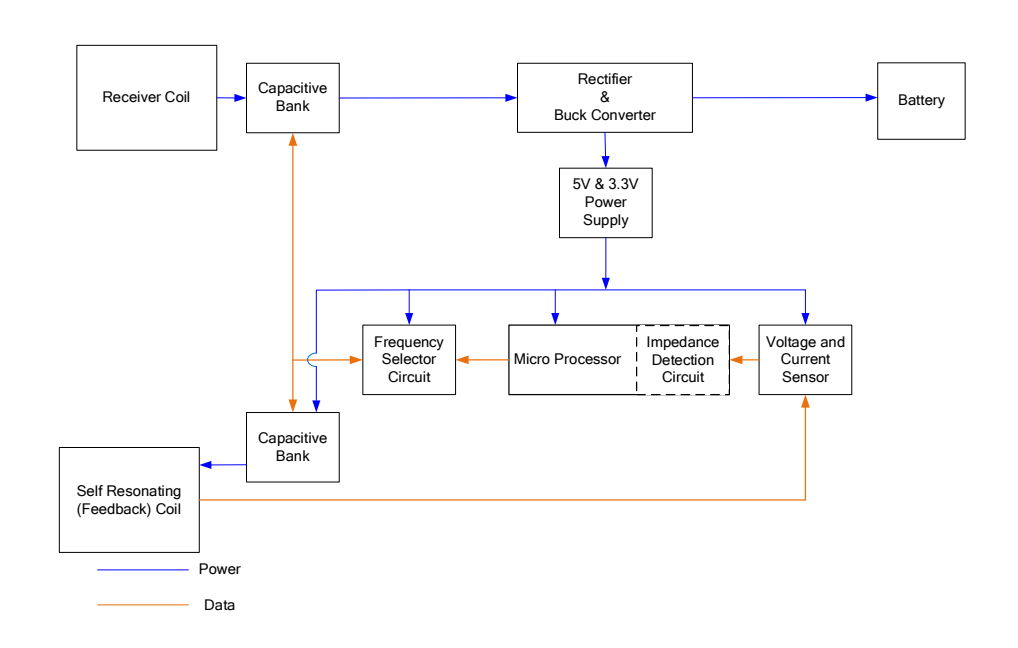


Fig. 1.2 FHWPT receiver module schematic

Power from the mains, 230V single phase at 50Hz is supplies the Rectifier. The Rectifier will convert the alternating current (AC) signal to direct current (DC), the inverter in series will convert the DC signal back to AC at a high frequency, 85kHz. Power transferred from the

transmitter coils is fundamentally dictated by Amperes circuital law, which induces the receiver's coil to generate a voltage at the receiver coil's terminals as governed by Faradays law. The AC induced voltage is delivered to the rectifier which converts it to DC to charge the car battery.

If the Frequency Selector Circuit (FSC) selects a particular frequency channel, the inverter will produce the high frequency AC signal at that given operating frequency. The resonant circuit composing of transmitter coil, and variable capacitor shall oscillate at the same frequency as the inverter. The transmitter's FBC constitutes of the coil and the variable capacitor in series. The variable capacitor shall be switched in tandem with the main transmitter coil by the FSC.

This same operation holds on the receiver circuit side. The receiver coil is connected to the compensating capacitor and the load R_{battery}. The receiver side's FBC is controlled by the receiver side's FSC by switching the variable capacitor.

The FBCs inductively coupled to the transmitter and receiver coils are only powered via mutual inductance by the transmitter and receiver coils see Fig. 1.3 below.

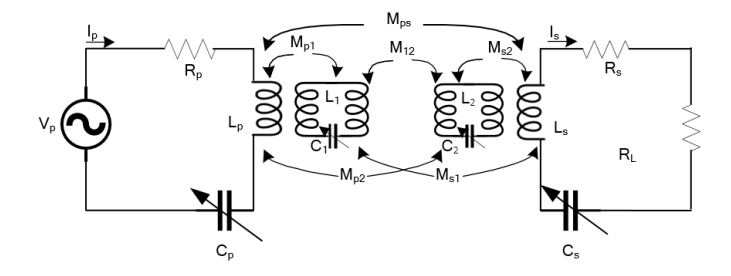


Fig. 1.3 FBCs, L_1C_1 and L_2C_2 inductively coupled to transmitter and receiver coils L_p and L_s and their mutual inductances

The mutual inductances between all four coils are listed below.

- primary and secondary coils M_{ps},
- primary coil and primary FBC Mp1,
- primary and secondary FBC M_{p2},
- primary FBC and secondary FBC M₁₂,
- secondary coil and secondary FBC M_{s2}

secondary coil and primary FBC M_{s1}

The FBCs provides the measurands for the IDC which monitors the mutual inductances of all coils of the FHWPT. Furthermore, the microcontroller which has preset thresholds, detects changes in impedance via the IDC.

In the event when the threshold is breached, the transmitter's microcontroller instructs the FSC to switch the variable capacitors C_p , C_1 , in the transmitter circuit thus, completing a hop of operating frequency. Consequently, the transmitter's microcontroller communication protocol will instruct the receivers' microcontroller to switch C_s and C_2 via its FSC so both receiver and transmitter operate at new resonant frequency.

The receiver's IDC will continuously provide, the impedance, battery state of charge (SoC), battery rate of charge (RoC) and battery internal impedance values to the transmitter via microcontroller communication protocol as a backup feedback reference.

To initiate an EV charging session all operating status of the transmitter i.e. battery SoC and impedance, and operating resonance frequency will be exchanged with the receiver through the microcontroller's communication protocol. Charging will commence once the transmitter's frequency mode is activated.

This research is necessary due to the obvious lack of resilience in dynamic and static WPT designs. While the risk of jamming the operating frequency in a WPT system is low, the potential impact can be significant, potentially rendering the WPT system inoperative. Also, minor disruptions to the resonant frequency due to frequency jamming and interference can severely degrade power transfer efficiency compromising the WPT system's functionality.

This research proposes a security measure designed to mitigate inadvertent risks and offer assurance to Office of Communications, OFCOM and other regulatory agencies. The assurance is that the FHWPT system's magnetic field strength and its associated harmonic orders, measured in Amps per meter A/m, will not pose a permanent interference or operational issues to other near field electromagnetic equipment operating within the bandwidth. Additionally, the cost of the supplementary components required to upgrade a standard WPT system to a FHWPT is marginal relative to the substantial gains in system resilience and reliability which this enhancement provides.

In this research two studies were undertaken the first study was the relationship between the power transfer efficiency (PTE) and operating frequency under different loads. A 137.4µH WPT transmitter and receiver coil has been modelled. The PTE, mutual inductance, and coupling coefficient of the transmitter and receiver coils have been simulated at 85kHz. A frequency sweep from 85kHz to 400kHz has been conducted for this WPT to determine the optimum PTE. From the results, at the statutory operating frequency of 85kHz, which Society of Automotive Engineers (SAE) Standard, J2954 stipulated, the PTE was circa 40% but at 250kHz the PTE was circa 70%. It is important to note that 250kHz is not recommended by SAE but if proven that electromagnetic emissions (EMI), losses, and other safety issues can be controlled it stands a good chance to be adopted.

The second study was the development of the FHWPT which has been introduced in great depth.

1.3 Research Questions

WPT is the technology of transferring electric energy wirelessly from a source to its load using resonant magnetic flux see Fig 1.4 below.

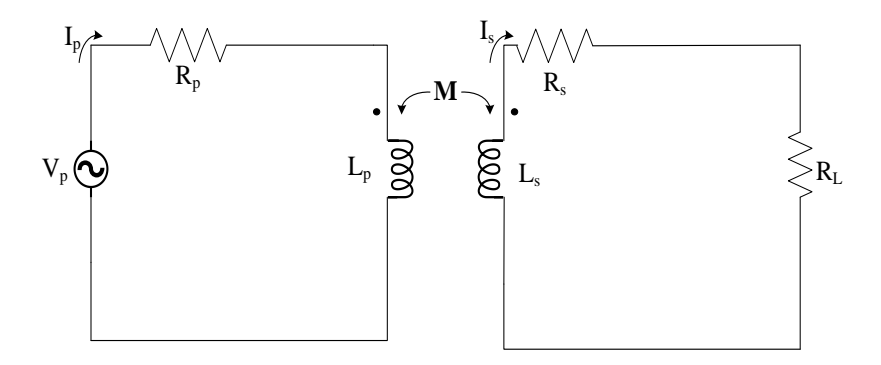


Fig. 1.4 Simple WPT Equivalent circuit

WPT technology has been commonly used in electronic devices such as mobile phones, electric toothbrushes, inductive cookers and biomedical equipment, and now being used for EV charging [1],[2]. The demand curve for EV WPT becomes steeper every year due to the elegance, hands free, clean, futuristic, autonomous, speed, safe, cost effective and reliable aspects it provides the user [3]. In the UK the government announced the end of sales of new petrol and diesel cars by 2030 which leads the way to the manufacturing of new EVs and their essential electric chargers. In addition to that, one of the three main objectives of

the new Green Agenda held at Glasgow Scotland in 2022 was to reduce carbon emissions which is directly linked to the use of fossil fuels [4]. Petrol and diesel vehicles come in different sizes and so will the WPT enabled EVs, which poses a challenge as each EV's WPT receiver module will have a unique impedance, coil design, distance from the WPT transmitter, power capacity just to mention a few. Thus, my research aims to answer these salient questions.

- 1. Does the existing WPT EV and WPT chargers have the capability to interoperate?
- 2. Can the WPT operations ride through adverse conditions?
- 3. Can existing WPT EV and charger's circuitry be easily modified or tuned to adapt to different operating frequencies?
- 4. Is the existing WPT designs future proof?
- 5. Can a WPT operation be immunized from interferences or secured?

1.4 Aim and Objectives

The aim of this research is to develop and experimentally validate a novel prototype for a FHWPT system. This system is specifically designed to detect inductive coupling variations and provide alternative resonant frequency channels to enhance operational resilience of a WPT. Unlike conventional fixed frequency WPT systems, this research introduces an intelligent FH mechanism that responds to anomalies during a WPT charging session. The research includes prototype development, experimental testing, and comparing the outcomes with theoretical predictions and simulation results. The objectives to achieve this goal are listed below.

- Literature Review and Theoretical Foundation: To critically review the evolution, classifications, and associated systems of existing WPT technologies. With a focus on the need for adaptive frequency solutions such as FH.
- Circuit Theory and Design Optimization: To derive and validate empirical design
 equations within the circuit theory framework of WPT. Thus, enabling the
 optimization of key parameters such as PTE, load impedance, resonant frequency,
 and coil quality factor of the WPT system. With the focus on implementing FH.

- 3. Multiphysics Simulation and Electromagnetic Characterisation: To create a Multiphysics model of a series-series WPT system and simulate it to determine the self inductance, mutual inductance, magnetic field distribution, and coupling coefficient under varying operating frequencies.
- 4. Adaptive Frequency-Hopping Control Integration: To implement FH control strategies in the WPT system by integrating a FBC to detect coupling variations. Installing voltage and current sensors to extract real time measurands for monitoring and control from FBC. Also incorporating a variable capacitive bank to enable dynamic tuning of the system to various resonant frequencies. These subsystems will be installed in both transmitter and receiver units to enable adaptive, closed loop operation.
- 5. Prototype Development and Experimental Validation: To design and fabricate the FHWPT prototype, including schematic development, PCB layout, hardware implementation, and experimental validation of system performance.
- Business Case and Performance Evaluation: To develop a business case for the
 proposed FHWPT system by analysing power losses, the cost of additional
 components, and the operational resilience benefits compared to conventional WPT
 systems.

1.5 Methodology

This research adopts a quantitative methodology based on design, simulation and implementation as illustrated in Fig. 1.4.

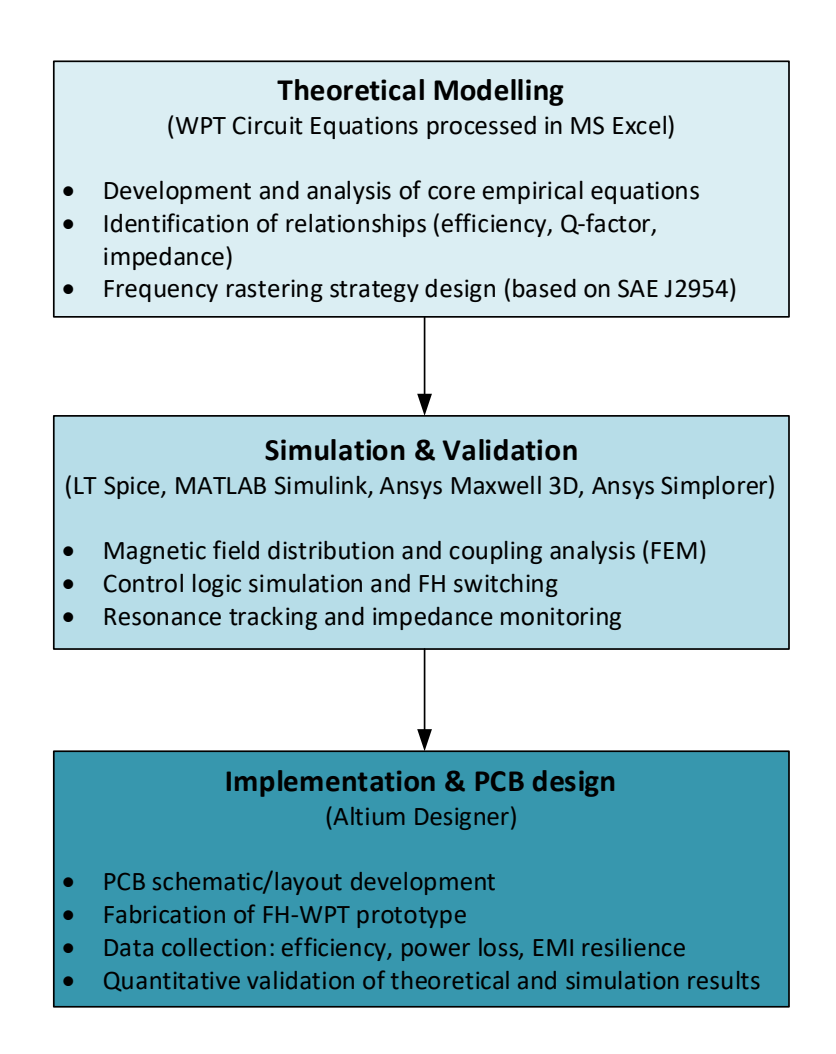


Fig. 1.4 Flowchart illustrating methodology of research

1.5.1 Overview

The framework steering this research is based on two main pillars which are (1) the empirical formulas of WPT circuit theory, and (2) the practical application of FH technology. By integrating both, the research addresses key concerns around security, PTE degradation, and electromagnetic interference susceptibility in WPT systems, particularly for EV charging.

1.5.2 Research Focus

The research framework aligns closely with the study's aims and objectives of immunizing or enhancing the operational resilience and reliability of the WPT under abnormal conditions. It does so by utilizing FH to mitigate interference issues and potential jamming, which are critical concerns in environments with high electromagnetic noise.

1.5.3 Frequency bandwidth compliance

The SAE J2954 recommendations, which specifies an operating frequency bandwidth between 79kHz and 90kHz, is central to this framework. It provided the basis for designing the system to dynamically switch across twelve 1kHz frequency channels (using a frequency raster), ensuring continuous operation even in hostile environments.

1.5.4 Software Used

Data was gathered by modelling and stimulations carried out on the following software

- Electronic circuit design, (MATLAB Simulink and LTspice).
- Finite Element Method (Ansys Maxwell 3D and Ansys Simplorer),
- Printed Circuit Board design (Altium Designer)

1.5.5 Ethical Considerations

There were no ethical concerns in my research work.

1.6 Summary

The introduction of the FHWPT system presents a significant step forward in enhancing the operational resilience and security of EV wireless charging systems. By leveraging existing communication technology such as FH, this system introduces alternative operating frequencies to mitigate the impact of interference, misalignment, and power theft, thus improving the overall PTE of WPT. The design integrates multiple components, including FBC, IDCs, and the FSC, all working in tandem to ensure that the WPT operates reliably across various conditions.

This research leverages the SAE J2954 bandwidth, enabling the system to dynamically switch between twelve 1kHz channels arranged in a frequency raster, ensuring optimal performance and security even in environments susceptible to EMI. This research also provides a blueprint for future WPT designs, addressing the need for adaptive frequency mechanisms and proving that the supplementary components required for such enhancements are both feasible and cost-effective.

This chapter has outlined the critical need for a robust and adaptable WPT system, framed within the context of the growing EV market and the demand for more resilient charging solutions. The subsequent chapters will delve deeper into the development, testing, and real world implications of the FHWPT system, building on the foundations established here. The literature review of the WPT shall be detailed in the next chapter.

Chapter 2 Literature Review

2.1 Introduction to the Literature Review

In chapter one the concept of the FHWPT was explained. This chapter explores the evolution and operation of WPT with a particular focus on its relevance to EVs and the emerging need for FH techniques. While WPT has received extensive study, limited work addresses adaptive resilience, interference mitigation, and standardised interoperability, which this review aims to highlight.

Information on the operation of a WPT is copious, authors of [5] expounded the operation of a basic WPT. This review will highlight most of their salient points and other important notes on the EV, WPT history, types, and classes of WPT. Emphasis will be placed on the most relevant modules of the WPT to this research which are the impedance matching circuits, coil configurations, retrofitting of wireless pads in EVs, retrofitting WPT system in existing EVs, DC-DC converters, derivation of various mono resonant WPT topologies, bifurcation, and FH.

2.1.1 History of the electric vehicle

The annals tell that around 1832 Robert Anderson a British inventor developed the first crude EV about the time when innovators in Hungary, Netherlands, and United States where working on the same craft [6]. This incredibly, was over 50 years before Carl Benz submitted his patent for the first internal combustion engine (ICE) vehicle in 1885 [7]. It was later in 1890 that William Morison an American developed a six-carriage electric car which ran at a top speed of 14 miles per hour. Ever since these inventions, the electric car's commercial development generally hibernated until 2006 when Ford developed the EV1 which has a range of 80 miles and an acceleration of 0 to 50 miles per hour in 1 second [6].

2.1.2 Electric vehicle and conductive chargers

As the popularity of the electric car increases so does the need for the battery charging facilities. There are about 31.9 million ICE vehicles and 8, 378 petrol stations in the UK [8],[9]. Based on the 2022 EV market statistics there are 530,000 battery electric cars and

405,000 plug-in hybrids [10] this number of EVs are bound to increase meaning that charging facilities are to be equally or more available in comparison with the ICE vehicles and petrol stations.

About 33.4kWh of energy is stored in a gallon of gasoline and a compact ICE vehicle has about 15 gallons or 60 litres which is about 500kWh, a similar size of electric car will have just 75kWh stored in its batteries[11]. The battery having a lower power density than petrol will need more frequent recharges to achieve a comparable range to that of the conventional ICE vehicle. To combat his challenge there has been a suggestion to swap depleted EV batteries with fully charged ones at "swapping stations" [3], to save time but this is yet to be investigated as there are many more issues that could go wrong with the car during the session at the "swapping stations". This shows the pressing need to extend the range of the EV safely thus, the development of more sophisticated EV charge points which includes WPT. The components of an EV are illustrated below in Fig 2.1.

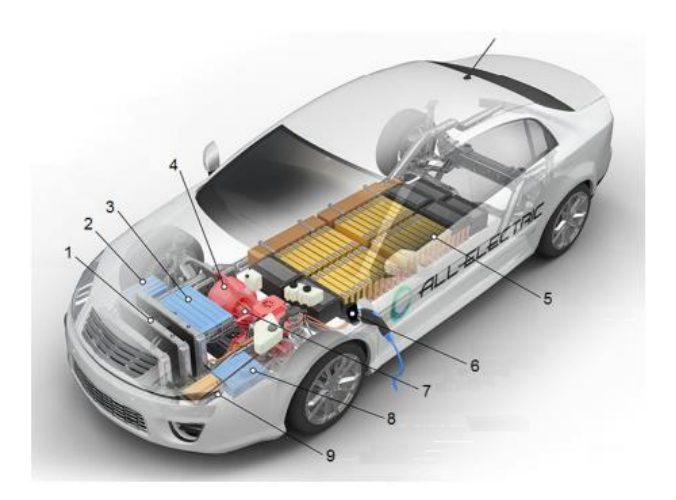


Fig. 2.1 Components of an electric car [12]

The parts of the EV as presented in Fig. 2.1 are 1. cooling system; 2. DC-DC convertor; 3. power electronics board; 4. electric motor; 5. traction battery; 6. charging contact; 7. transmission; 8. charging device; 9. operational battery [12].

The major way EV's are charged are by conductive charging this is where an electric cable is connected to the vehicle to charge its batteries as shown in Fig 2.2



Fig. 2.2 EV under charging session. [13]

There are mainly four classes of charging which are based on the speed and power delivered during the charging session these are the Opportunity Chargers, Ultrafast chargers, Rapid chargers and Slow chargers.

2.1.2.1. Opportunity chargers for electric bus

Most Opportunity Chargers rated from 350kW to 600kW use DC to charge electric buses see Fig 2.3. An EV bus having about 90kWh battery can be charged from a 20% SoC to about 90% SoC within 5 minutes [14].



Fig. 2.3 Opportunity Charger where a pantograph delivers power to a bus [15]

The exposed metal components in opportunity chargers pose inherent safety risks, mitigated only when the bus is correctly positioned. In contrast, WPT eliminates these risks entirely by removing physical connectors and reducing the need for mechanical engagement [1].

2.1.2.2. Opportunity chargers for trains

The Opportunity Charger for a battery powered train can deliver up to 1MW conductor rails at the docking station. Vivatrain, Class 230 battery train is a repurposed London Underground D stock train, that runs on batteries on an existing diesel track. This train has six onboard 84kWh battery rafts, located at the two ends of the train which are fast charged for about 3.5 minutes. The onboard batteries are charged when the train shoe makes contact with the short conductor rails. The short conductor rail has a 750VDC potential difference and can deliver up to 1kA [17]–[19] see Fig 2.4.



Fig. 2.4 Opportunity Charger where a conductor rail delivers power to a train [17]

While Vivatrain's use of high-current conductor rails enables rapid charging, it relies on mechanical contact and exposed high-voltage interfaces, which introduce safety and maintenance concerns. In contrast, WPT eliminates physical connectors, enhancing system robustness, reducing wear, and offering safer, contactless energy transfer—particularly suitable for dynamic or autonomous rail applications.

2.1.2.3. Ultrafast chargers and CHAdeMO Standard

CHAdeMO is a DC charging standard for EVs and in 2020 the CHAdeMO association initiated development for a protocol and hardware for up to 900kW charging [16]. Ultrafast chargers rated to 150kW to 175kW can charge an EV battery of 40kWh to 50kWh for a 100-mile range for about 10 minutes [20] using the CHAdeMO protocol and hardware.

2.1.2.4. Rapid and Slow chargers and CHAdeMO Standard

The rapid chargers rated at 50kW can charge an EV with a 50kWh battery in 30 minutes [11] using the CHAdeMO protocol and hardware. The slow chargers are mostly AC chargers, 7kW to 22kW can charge an EV with a 50kWh battery for up to 4 hours.

In all, most of these chargers are vulnerable to vandalism and theft and obviously poses a potential hazard thus exposing the user to a degree of discomfort [12].

Despite the growing power capabilities of CHAdeMO and other conductive standards, these systems remain physically exposed and reliant on manual engagement. This leaves them susceptible to vandalism, weathering, safety hazards, and user inconvenience. In contrast, WPT offers a sealed, contactless, and fully automated alternative reducing maintenance, enhancing safety, and enabling seamless integration into autonomous or public EV infrastructure.

WPT technology provides a solution not only to charge the vehicles but to provide security comfort and style to the customer during charging sessions. WPT provides an avenue for charging driverless EVs as it has the basic properties of being fully automated [12]. And FHWPT provides a more robust and resilient system for wireless charging.

2.1.3 Wireless Power Transfer

Wireless power transfer has been in existence, from my positionality as a man of Christian faith, since creation. The sun wirelessly powers the earth and its atmosphere to sustain and promote life [21]. The sun's wireless gravitational pull maintains all the planets to revolve round it in their orbits and the electromagnetic waves from the sun forms the basis of a majority of the science, technology and engineering breakthroughs we enjoy in the civilised world. A common example is the solar panels energy is given off from three main electromagnetic waves, ultraviolet, visible light and infrared light [22]. The electricity received from solar photovoltaic panels was delivered from the sun about 150 million km away from the earth. Hence, the full harness of WPT alongside the feasibility and commercial availability for various applications is worth exploring.

2.1.4 Analogy of Wireless Power Transfer

As mentioned earlier WPT has been used in various applications the typical ones are the power transformers and inductive motors. The power transformers transform power from one voltage energy level to another voltage energy level, from Fig. 2.5 below it is evident that the coils on the primary winding are not galvanically connected to the coils on the secondary however, power from the primary winding is transferred to the secondary winding via induction or magnetic fluxes though the iron core.

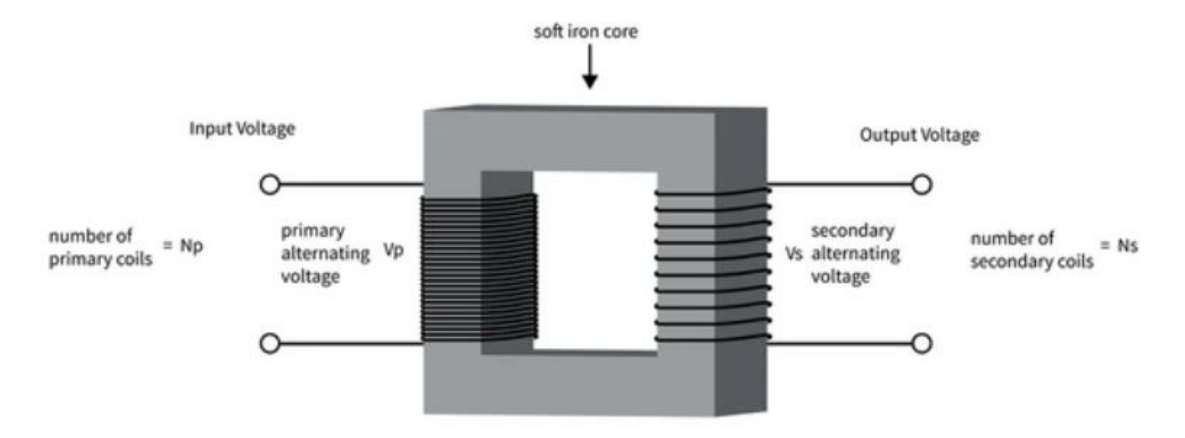


Fig. 2.5 Simple step-down transformer showing the primary windings, secondary windings and soft iron core [23]

For a clearer illustration looking at Fig. 2.6, the induction motor has windings on the stator, which is the permanent section of the motor and windings on the rotor which is the movable part locked coaxially to the stator.

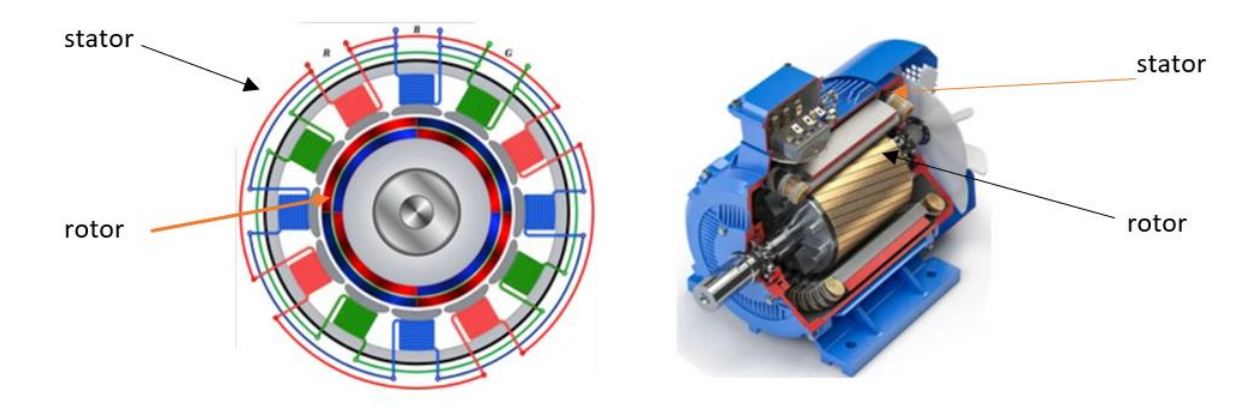


Fig. 2.6 Stator and rotor in a 3-phase induction motor: (left) winding layout; (right) motor cross-section. [24]

When current passes through the coils of the windings in the stator it induces a voltage in the rotor, produces a torque and causes the rotor to rotate. From the diagram it is also evident that there is no connection between the windings in the stator and in that in the rotor and unlike the transformer were the magnetic flux is strongly linked between the primary and secondary windings via the soft iron core, the flux linkage between the stator and rotor windings in the induction motor is through an air gap, a typical example of WPT.

2.1.5 History of Wireless Power Transfer

WPT operating principle is firstly based on Amperes Law and Faradays Law. In the early 1820's André-Marie Ampère a French physicist combined the theory of electricity and magnetism [25]. Amperes law states that the product of the magnetic field (or area of influence) and sum of the length element in the circuit is proportional to the product of the electric current passing through the circuit and the permeability of its circuit's conductor.

$$\int B_t * dl = \mu_0 * IN_n$$
 (2.1)

Where B_t , dl, μ_0 , I, N_p are varying magnetic flux with time, length of conductor, permeability of free space, current and number of turns in primary winding respectively see Fig. 2.7.

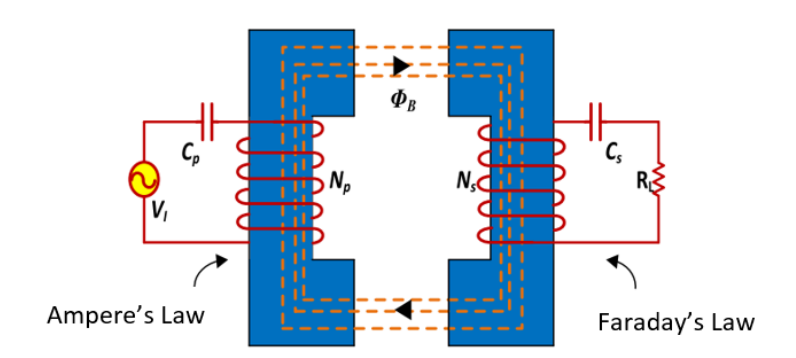


Fig. 2.7 Magnetic WPT showing Ampers law and Faradays law [3].

In 1831 Michael Faraday a British physicist and chemist discovered electromagnetic induction [26]. Faraday's law also states that the electromagnetic flux is proportional to the negative rate of change of flux with time

$$E = -N_S \frac{d\Phi_B}{dt} (2.2)$$

Where E, N_s , $d\Phi_B/dt$ are the Electromotive force or voltage, number of turns on secondary winding, rate of change of magnetic flux with respect to time respectively.

Years later in 1873 James Clerk Maxwell a Scottish mathematician presented equations based on Amperes and Faradays laws for electromagnetic energy transmission through space. He developed the partial differential equations which relate the electric and magnetic fields as well as the electric charges and currents [27]. And between 1885 -1889 Heinrich Hertz a German physicist verified Maxwells equations, the behaviour of electromagnetic waves [12].

In 1897 Nicola Tesla, who developed commercial AC current transmitted microwave signals over 48km he also lighted about 200 bulbs from a power source 25 miles away [1]. He demonstrated that electromagnetic power can be transferred between two circuits across a given air gap using magnetic field coupling at resonance [12], [28]. In 1964 a helicopter was also powered via microwave [12],[29] - [31]. In 1968, Peter Glaser introduced the concept of a satellite power system that could take solar power from the sun transform it to microwaves then transmit microwaves from the lower space to earth through beams [1]. In 1976 dynamic WPT was invented at Lawrence Berkely National Laboratory, California, united states [12]. In 1993 the Qualcomm's Halo in collaboration with University of Auckland invented the Double D transmitter and receiver coils which has a higher PTE and tolerance to misalignments compared to the circular planar coils [12].

In 1996 GM developed the inductive charger called Magne charge which was used to charge their first EV EV1 [12],[32]. In 2002 the first wireless induction power transfer (IPT) charger charged an Electric bus which are in operation at Rotorua, New Zealand. The IPT operated at 60kW rating with an air gap of 40mm and achieved 90% PTE. Oakridge National Laboratory (ORNL) developed a single phase 100kW wireless IPT that could operate at a PTE of circa 97% [28],[33] In 2007 Massachusetts Institute of Technology (MIT) physicists lit a 60W bulb 2 meters away [34]. Since then, various companies like Integrated Infrastructure Solutions (INTIS), WaveIPT, Bombardier-PRIMOV, Korea Advanced Research Institute (KAIST), Momentum Dynamics, Electreon and others have developed WPT from low power in milli Watts to up to 300kW [12]. ORNL and Volkswagen collaborated to develop a 270 kW wireless charger see Fig 2.8. The system was tested with an air gap of approximately 120 mm demonstrating high-power wireless charging potential [35].



Fig. 2.8 Polyphase 270kW wireless charger [36]

While the evolution of WPT from Faraday's induction to Tesla's resonance and modern highpower IPT systems demonstrates remarkable progress, most developments have focused on fixed-frequency operation. Few have addressed adaptive tuning, or resilience under interferences, gaps which this research tackles through FHWPT.

2.2 Classification of Wireless Power Transfer Technologies

The historical development of WPT clearly demonstrates that multiple methods exist for transmitting power wirelessly. In this section, we will provide an in-depth analysis of the various classifications of WPT technologies.

WPT technology can be classified into two types, near field and far field. The near field WPT technology are mainly inductive, capacitive, and resonant inductive. In the IPT system, power is normally transferred by magnetic field at a close range, 50Hz to 1MHz using inductors. The capacitive power transfer (CPT) technology power is transferred via electric field and a wide range of frequencies from 10Hz to 70MHz using capacitors. Resonant inductive power transfer normally referred to as WPT in this discourse operates at a range from 50kHz to 1GHz.

Far field WPT consists mainly of the microwave technology and the optical technology. The microwave technology is designed to transfer and receive power at high frequencies using magnetron and a rectenna respectively they operate in frequencies between 1GHz to 100THz [1],[12]. An example of the optical technology is the solar energy, light is beamed from its source and it is received by photovoltaic panels.

Table 2.1 WPT technology and their respective power throughput range. [12]

Types of W	/PT technology	Ranges	Operating	Nominal coil
Types of w	rr tecimology	Kanges	Frequency	/antenna size
	Inductive	up to 50mm	100Hz to 1MHZ	10 to 50cm
				diameter
Near field	Capacitive	up to 100mm	10Hz to 50MHz	Plate area: 10
				× 10 cm to 50
coupling				× 50 cm
	Resonant	up to 300mm	50Hz to 1GHz	30 to 100cm
	inductive			diameter
	Microwave	up to several	1GHz to 1THz	Patch
		km		antenna: 5 –
				30 cm
				Parabolic
				antenna: 0.5
Far Field				– 3 m
coupling	Optical	up to several	1THz to 200THz	Lasar
		km		aperture 5 –
				200mm
				Photovoltaic
				cell: 5×5 cm
				to 30×30 cm

Conventional WPT classifications focus on field type and range but overlook frequency-agile systems. FHWPT introduces temporal adaptability, challenging the existing static taxonomies and prompting the need for expanded classification models that reflect dynamic spectral behaviour.

2.2.1 Inductive Power Transfer

Wireless IPT is a simplistic form of WPT. Fig 2.9 shows how the transmitter and receiver coils (shown in the dotted area) are mutually coupled by their respective inductances. Here Amperes law and Faradays Law are at play. The transmitter circuit generates a varying magnetic flux, B_t by the current passing through it see equation (2.1). The receiver circuit generates an electromotive force E, or voltage by the time varying magnetic flux that cuts through its coils see equation (2.2). The combination of these occurrences forms the bases of WPT.

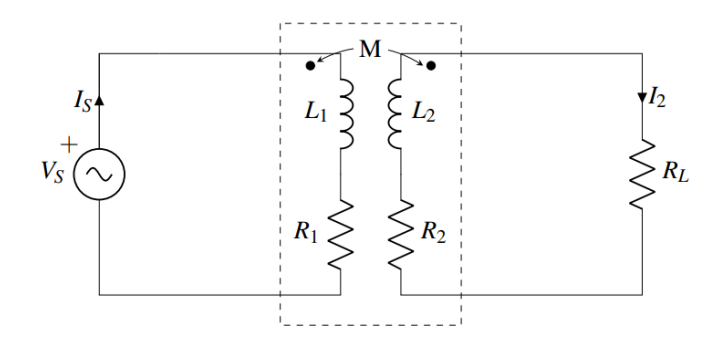


Fig. 2.9 IPT circuit diagram [12]

While IPT is foundational, its PTE rapidly declines with misalignment and increased coil separation. It lacks the adaptive tuning required for dynamic environments, limitations which FHWPT is designed to overcome.

2.2.2 Capacitive Power Transfer

Capacitive driven WPT technology transferers power from the transmitter to the receiver via an electric field as illustrated in Fig. 2.10.

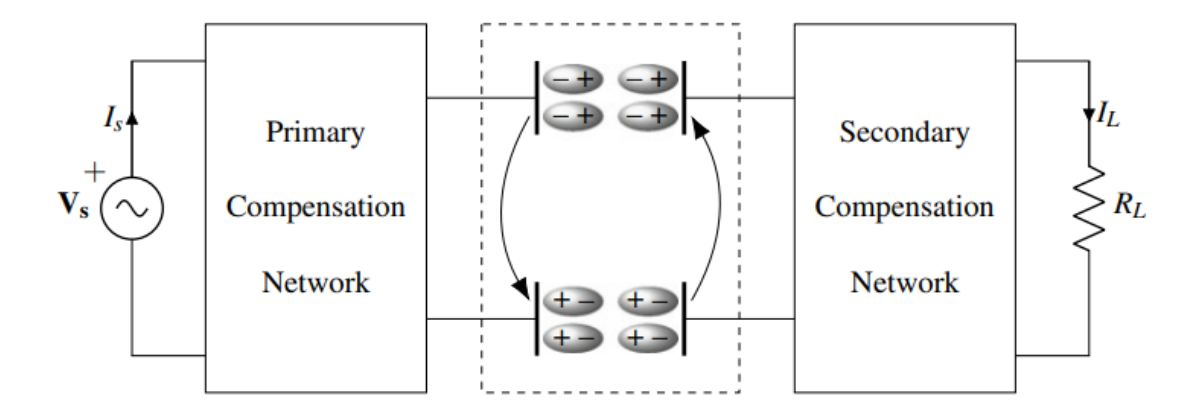


Fig. 2.10 CPT circuit diagram [12]

Capacitive driven WPT technology transferers power from the transmitter to the receiver via an electric field. The equation of a capacitor, C as shown in equation 2.3 shows that the given capacitance C is the ratio of the product of the dielectric strength, ε of the material and the area, A between the two conductors and its distance, d apart. Hence the further the distance between the plates the smaller the capacitance between the plates.

$$\mathbf{C} = \frac{\varepsilon * A}{d} (2.3)$$

Furthermore, we can see that the time varying voltage, $\frac{dV}{dt}$ on the transmitter and receiver plates creates an electric field, ε between the plate and causes current to flow in the receiver circuit see equation 2.4.

$$I = C \frac{dV}{dt}$$
 (2.4)

Capacitive WPT are attractive due to the cost per weight of the materials required to configure them. They apparently require less parts compared to resonant magnetic WPT systems. They can operate at high frequencies to produce more capacitive current for WPT operation and still radiate less EMI compared to inductive WPTs because the power transfer medium used is an electric field [37]. Nevertheless, at high frequencies stray capacitive current is dissipated as heat due to the capacitance between the plates and ground, shielding the plates reduce the plate to ground capacitance but there is also a plate to shield capacitance which can be mitigated as well [38].

While FHWPT is theoretically compatible with CPT, especially due to CPT's wideband nature, practical implementation faces significant EMI, shielding, and impedance tuning challenges.

In contrast to magnetic systems, CPT lacks a robust frequency-selective tuning mechanism for dynamic conditions.

FHWPT may augment CPT at low power or short range, but is less viable for high-power, misalignment-prone applications like EV charging. The magnetic-resonant domain remains the optimal class for FHWPT due to its inherent selectivity and tuneable reactance.

2.2.3 Magnetic resonant WPT

As earlier mentioned, Nicola Tesla was able to send power wirelessly at long distances using magnetic resonance. When a system is at resonance it uses its natural self-oscillation to operate almost perpetually, consider a pendulum in a vacuum. This notion can be best used to describe the magnetic resonance WPT. A circuit with an inductor, L and capacitor, C is said to be at resonance when the reactance or opposition to the flow of AC current of the inductor $X_L = jwL = 2\pi f L$ is equal to the reactance of the capacitance $X_C = \frac{1}{jwC} = \frac{1}{2\pi f C}$. When reactance $X_C = \frac{1}{jwC} = \frac{1}{2\pi f C}$. When reactance is represented as the compensation networks as shown in Fig. 2.11.

$$F_r = \frac{1}{2\pi\sqrt{LC}}$$
 (2.5)

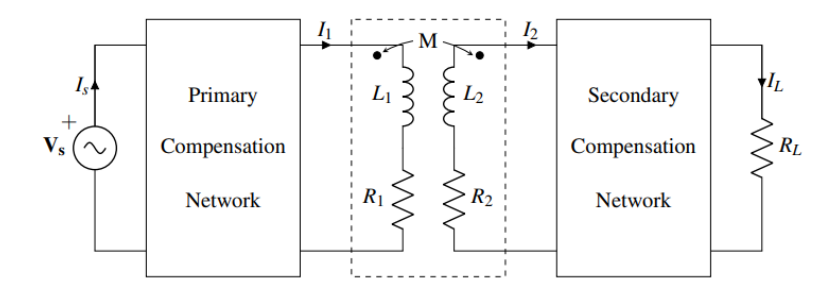


Fig. 2.11 Magnetic Resonant WPT circuit diagram [1]

At resonant frequency, the only opposition to the flow of current will be the parasitic resistance of the coils and other circuitry modules in the WPT system hence, the losses are reduced. The magnetic resonant WPT is an improvement to the IPT system [1]. It is interesting to note that this thesis is based on magnetic resonant WPT technology.

Although magnetic resonance enables high PTE through natural oscillation, it is inherently frequency locked, assuming static coil conditions. This rigidity limits adaptability in real-world environments where coupling and load impedance vary dynamically. FHWPT redefines resonance not as a fixed point, but as a searchable, shiftable operational zone, enabling continuous optimisation without reliance on a single tuned frequency.

2.2.4 Magnetic Gear WPT Technology

Operation of the magnetic WPT technology goes thus, mechanical energy, torque and magnetic flux generated in the transmitter's rotating winding is transferred the receiver's winding see Fig. 2.12 below.

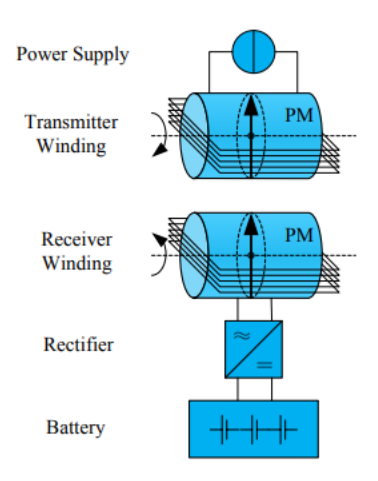


Fig. 2.12 Magnetic Resonant WPT circuit diagram [39]

The transmitter and receiver windings are made up of permanent magnets and windings. The magnet in the Transmitter rotates with respect to the driving AC operating frequency. The magnet in the receiver rotates in synchronism with the transmitter's frequency. The rotating magnetic flux in the receiver cuts through the winding generating an EMF in the windings which is then rectified by power electronic devices to feed specific loads. [1],[39]. This system is used in medical implants, EV motors and wind turbines [40], [41].

Despite that rotary magnetic WPT systems offer compact, contactless torque and power transfer, they rely on precise mechanical alignment and synchronised rotation, which increases complexity, wear risk, and control burden. Their dependence on moving parts

makes them less suitable for stationary or wide-gap EV charging scenarios where FHWPT offers a solid-state, low-maintenance alternative with greater spatial tolerance.

2.2.5 Microwave WPT

The microwave WPT technology uses a microwave device to transform electrical energy into electromagnetic energy then transmits it through space or earth's atmosphere to the receiving microwave device, rectenna which then converts the electromagnetic energy back to electrical energy. This is illustrated in the block diagram in Fig. 2.13.

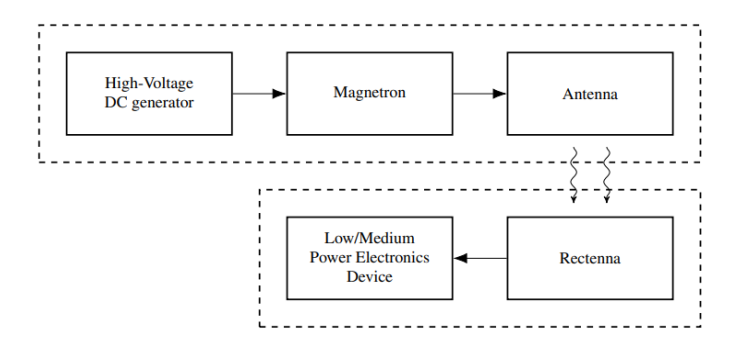


Fig. 2.13 Microwave WPT block diagram [1].

A DC generator produces a high voltage DC which heats up a magnetron [1]. The magnetron is an oscillator which generates a microwave signal. It consists of a cathode, a coaxial anode designed as a resonant circuit, and a pair of permanent magnets. When the cathode is heated up it emits electrons, the electrons pass through permanent magnets either side of the anode towards the antenna at a resonant frequency of about 2.4GHz based on the size of the magnetron. The antenna transmits the microwaves which is then received by the rectenna as shown in Fig. 2.14. The rectenna is an antenna and rectifier configured in a common unit. Power electronic devices then transform the electromagnetic energy from the rectenna back to electrical energy.



Fig. 2.14 Vehicle mounted microwave WPT system [39]

The first microwave WPT was designed by William C. Brown in 1964 this was used to power a helicopter. In 1968 Peter Glaser introduced the concept of Space Solar Power Satellite (SSPS) in this concept the satellite bearing solar panels, magnetrons and antennas in space converts the solar energy to microwave electromagnetic energy then transfers it to the rectennas on earth [1], [29], [30]. Further studies in Japan have postulated that the SSPS will orbit the earth in the Geostationary Earth Orbit. Additionally, the electromagnetic energy transmitted from the SSPS to ground via microwave has a greater PTE compared with a similar power rated solar photovoltaic system [12]. On the ground microwave WPT can be used in small offices to power Internet of Things (IoT) driven devices [39]. Microwaves can be beamed directionally or in an isotropic transmission [1]. When beamed directly at high frequencies up to 900MHz it can transfer power up to 3W whereas in an isotropic transmission where the beams are less concentrated the power transfer is up to 1W. Companies like Powercast, WattUp and Ossia's Cota can transmit microwave beams up to 5 metres but at a low power rating.

Though microwave WPT enables long-distance power transfer, its application is limited by low power density, strict beam alignment, and radiation safety constraints. Nevertheless, FHWPT can be applied within regulated frequency bands to deliver secure, adaptable wireless power in nearfield environments avoiding the exposure risks and alignment demands inherent in microwave systems.

2.2.6 Optical WPT technology

Optical WPT uses visible light, Light Amplified and Stimulated Emission Radiation (LASER), or infrared to transmit energy wirelessly. From the diagram in Fig. 2.15 the Laser diode delivers the laser beams to the beam director which transmits the laser in the frequency bandwidth of 1THz. The photovoltaic cells receive this light beam which is then transformed to electrical energy via the power and control electronic devices [1],[12].

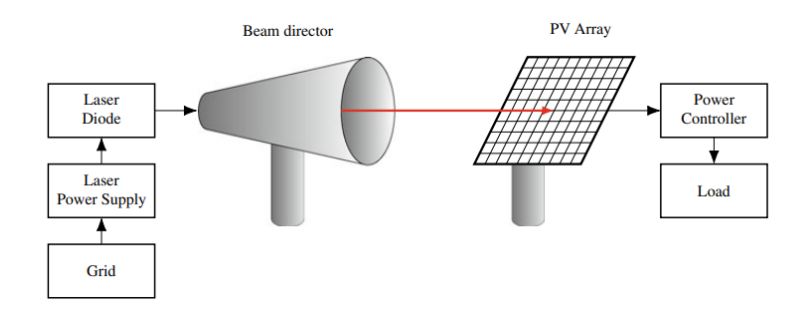


Fig. 2.15 Optical WPT diagram [1]

Low power applications using infrared waves are used in offices and homes Wi-Charge have developed this Optical WPT system using infrared waves. Wi-Charge configured this system such that the beam director or antenna is on the ceiling and the devices are all online of sight from the antenna [1].

Although optical WPT achieves high directional PTE, it is limited by line-of-sight constraints, tracking complexity, and ocular safety regulations. While FHWPT operates in a distinct near-field regime, its frequency agility and contactless nature make it better suited for mobile or misaligned power transfer scenarios where optical systems are impractical.

2.3 Coil and pad configuration

The coil plays a very vital role in the WPT system as the sole output and input power port of the system. The transmitter and receiver coils of a WPT system are designed to maximize the propagation and reception of magnetic fluxes over an air gap. The coils are designed such that for a given length of wire when wound in a particular pattern, the self-inductance,

mutual inductance, and quality factor are achieved [1]. In this section existing coil configurations shall be explored.

2.3.1 Planar Coils

The self inductance of a particular length of wire depends on the final geometry of how it is wound. Since the inception of WPT, transmitter and receiver coil designs have been developed to optimize maximum PTE for wider air gaps. These coils configured are the following Rectangular, Circular, Double D, Double DQ and Bipolar as shown in Fig. 2.16 [1], [12], [16].

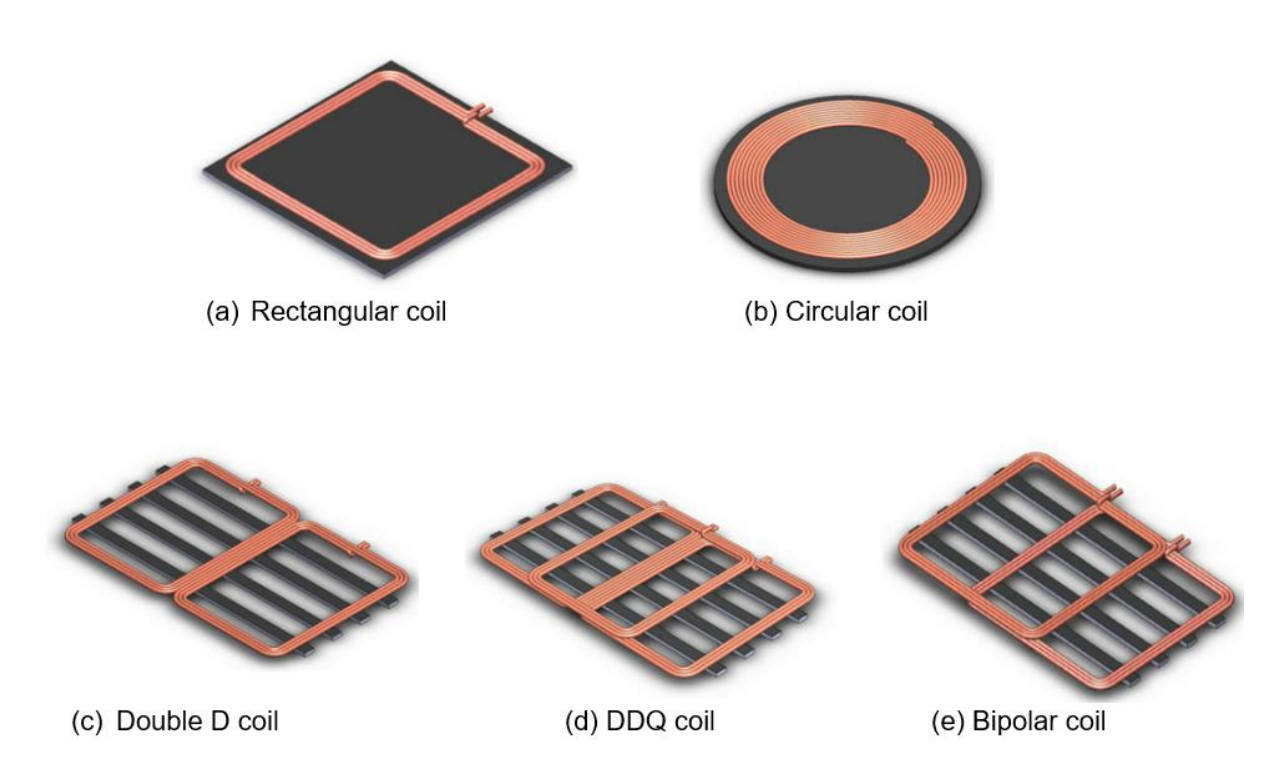


Fig. 2.16 Typical transmitter and receiver coil configurations [40]

In FHWPT systems, the choice of coil geometry is especially critical. Since the system operates over a band of frequencies rather than a fixed point, coil designs must sustain high mutual inductance and quality factor across that range. Configurations such as the Double D and Double DQ coils are particularly advantageous in FHWPT due to their improved tolerance to misalignment and broader bandwidth characteristics, which help maintain efficient coupling as the system hops between frequencies.

2.3.2 Isometric Coils

Most WPT coil designs have a planar orientation as found in Fig 2.16, there is a winding with an isometric orientation gaining a reputation of high self-inductance but has a trade-off of the space and weight. Coils wound in an isometric orientation forms higher concentration of magnetic flux lines within its core a good example is the spiral wound air core coil see Fig 2.17.



Fig. 2.17 Air core wound helix coil [42]

2.3.3 Magnetic cores

To amplify the magnetic flux generated by the AC current flowing though the coils a magnetic core is installed in the WPT coil's configuration. For planar coils the magnetic core is normally installed beneath the coils. For helix coils the magnetic core is installed in the axis of the winding, forming a solenoid see Fig. 2.18. The magnetic flux path for the solenoid is presented in Fig. 2.19.



Fig. 2.18 Solenoid a copper coil wound round an iron/magnetic core [43]

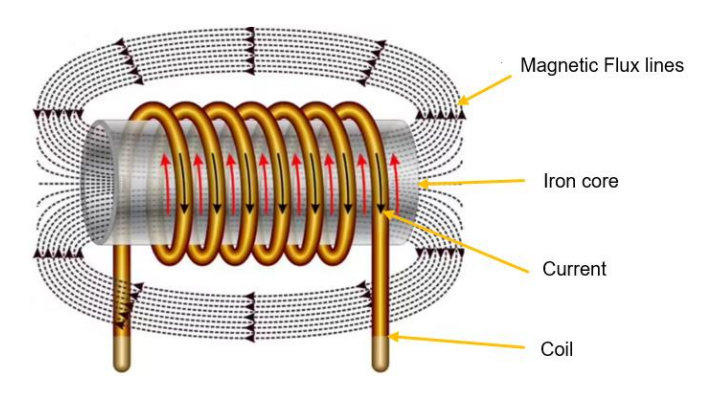


Fig. 2.19 Magnetic flux lines generated by an energised solenoid [44]

The magnetic flux generated by a solenoid as shown in Fig. 2.19 is used as the basis of the flux pipe WPT as shown in Fig. 2.20 below. The flux pipe configuration has more tolerance to misalignments compared to the planar coils [45], [46].



Fig. 2.20 WPT with a flux pipe spiral would coil [45]

In FHWPT the system, a FBC inductively coupled to a solenoidal transmitter can effectively monitor coupling or detuning without interfering with power transfer. The axial flux of the solenoid enables strong mutual inductance, but care must be taken to manage parasitic coupling, signal distortion, and space constraints, particularly in compact or thermally loaded designs. When properly placed, this setup supports reliable closed-loop frequency control. However, the FHWPT design is based on planar coil and not solenoid coil topologies.

2.3.4 Metallic Shield

Due to the HF of the magnetic fluxes and the inevitable inductance leakages in a WPT system, the EMI could breach the stipulated limits specified in the International Commission on Non-Ionizing Radiation Protection (ICNIRP) Standard and electromagnetic compatibility

(EMC) directive 2014/30/EU. Hence, a metallic shield normally made of Aluminium is placed on the base of the magnetic core (for planar coils configurations) and enclosed around the windings (for spiral coil configurations).

Shielding remains essential in WPT systems particularly under high-frequency operation to comply with ICNIRP and EMC standards and to suppress leakage fields during FH. However, in FHWPT, the shield shall be carefully engineered to ensure it remains effective across the full hopping bandwidths without introducing excess losses or detuning effects.

2.3.5 Components of WPT transmitter and receiver pads

The WPT coil consists of the copper coil which is made up of a Litz wire. A Litz wire is a bunch of insulated copper strands having diameters in micrometres. A Litz wire has laminations in each strand to reduce eddy current and still maintain the magnetic flux like the laminations of a transformer core.

The configuration of a coil pad is illustrated in Fig. 2.21. Here the coil former is a frame to keep the coils in position. The ferrite or iron bars are permanent magnets that amplify the magnetic fluxes generated by the high frequency AC in the coils. The aluminium shield contains all flux leakages within the pad the back cover and plastic cover protects all devices.

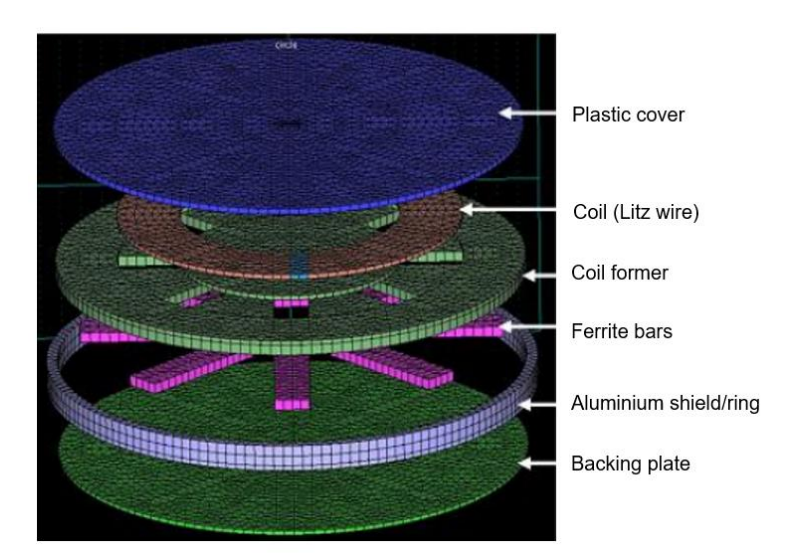


Fig. 2.21 WPT coil structure [48]

In the FHWPT system, the FBC shall be installed between the ferrite bars and the aluminium shield. This location ensures effective magnetic coupling while minimising interference. A non-conductive spacer may be used to reduce eddy currents from the shield.

2.4 Interoperability of WPT

As EVs are penetrating the commercial market, the need of readily available wireless EV chargers for public use is persistent. To prevail over EV and its associated EV chargers incompatibility issues instigated by various OEM design, national and international industry standards have stipulated parameters to enhance interoperability [49]. The key parameters to be considered are the operating frequency, agreed power levels, coil to coil air gap operation and coil alignment tolerances [49]. This section will discuss the studies caried out on various proposals to enhance interoperable WPT.

Interoperable WPT can be achieved in various ways, the most intuitive approach is setting an industrial recommendation as stipulated by SAE. Amongst the parameters guiding WPT operations SAE classified air gaps into three zones, Z_1 is 100mm to 160mm, Z_2 is 160mm to 220mm, and Z_3 is 220mm to 280mm [49]. Power levels were set to 3.3kW and 6.6kW.

Authors of [49] proposed using a universal base pad configured with a Double D (DD) coil. Qualcom carried out an interoperable design using a transmitter DD wound coil matched with three types receiver coils, Circular, Double D and Solenoid coil. The DD coil being a polarised coil is known to interoperate with the other 3 coils [49],[50]. The researchers of [49] modelled the various pads on FEM Maxwell 3D software the key characteristics modelled where the coils, ferrite layer rated at a permeability of 2000 and an aluminium shield. From the results it showed 95% to 99% PTE for all 3 coils even with up to 150mm offset with air gaps set to Z_1 and Z_2 . This proposes that a configured transmitter DD coil can provide power to various configured receiver coils. It is worth noting that the coil-to-coil PTE plays a critical role in the WPT PTE [51].

The interoperability of WPT systems, as seen with the SAE standards and the use of universal base pads like the DD coil, shows that achieving seamless power transfer across different EV designs is feasible. Incorporating such adaptability into the FHWPT system enhances this capability by allowing the system to shift across various frequency channels and align with diverse receiver coil designs. This ensures that the FHWPT can accommodate a range of EV

charger configurations, improving system resilience and ensuring consistent, secure charging performance. This presents one of the answers of the first research question in Section 1.3.

2.5 Retrofitted Wireless Power Receiver Pads in EVs

As discussed in the previous Section, the foreseen drawback in WPT are the non-standardised designs of the EV components. The EVs charging protocols, voltages, currents, power levels, ramp rates, chassis height and response times vary in magnitude and complexity [52],[53]. The OEM maintain their right to the competitive market to continue to produce their unique patent designs. This calls for an adaptable engineering design to install add-on wireless power receiver (WPR) modules for installation in EVs.

The major advantages of WPT interoperability are the following

- Future Proofing. EV software, hardware and firmware and be easily upgraded in the EV's without the need of recalling products back to the workshops. This presents one of the answers to the fourth research question in Section 1.3.
- Availability of points for charging on a national scale. EVs can use any charger anywhere in the country.
- Standardization of WPT power parameters. OEM will design to specifications to comply with international standards to reduce greenhouse gas emissions.
- Readily available OEM approved compatible parts.
- Affordable and available non OEM spare parts.

2.5.1 Opportunity to integrate Wireless Receiver Pads in plug in EVs

A perceived quick win to achieve WPT interoperability for plug in EVs is to design portable receiver modules that can be retrofitted in any EV. This way, an EV can be simply modified to accommodate wireless charging. In this section, research into the coil design of the WPR pad and integration of the WPR pads to EVs shall be discussed. The schematic in Fig. 2.22 below shows a standard WPT circuit.

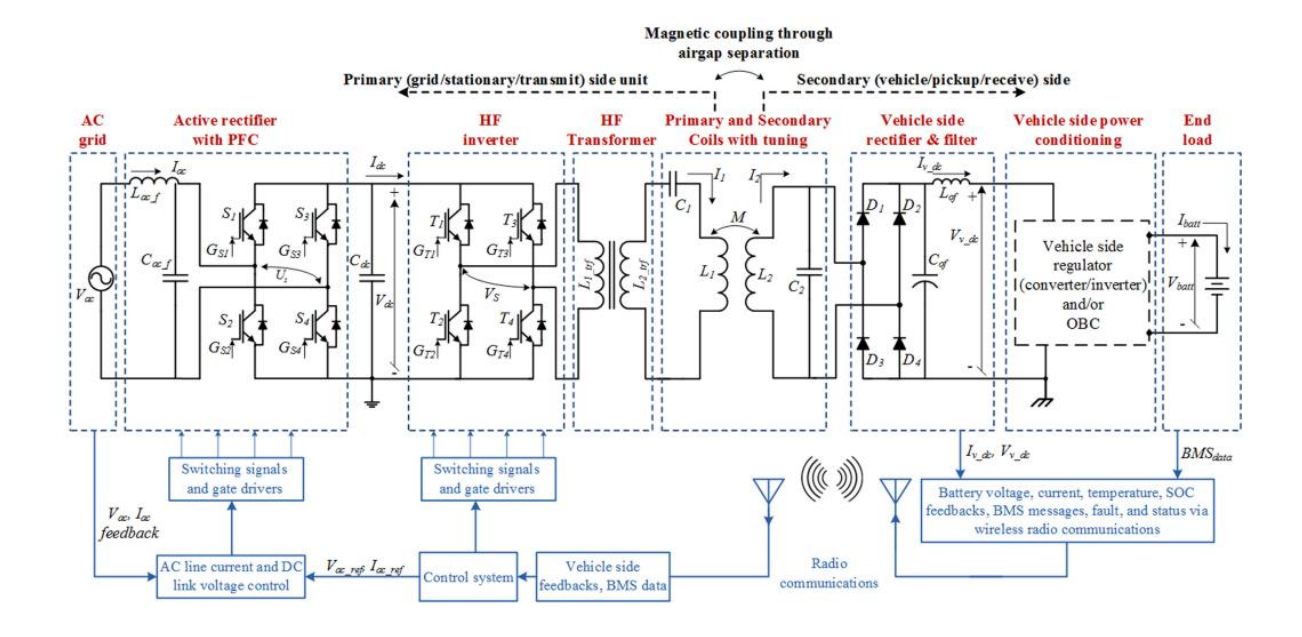


Fig. 2.22 WPT circuitry schematic. [53]

From this circuit in Fig. 2.22 we can see that the components of the WPT on the vehicle are the Secondary coils, Vehicle side rectifier and filer, vehicle side power conditioning and load. The WPR consists of the wireless receiver coil module and rectifier and its associated filter. The WPR shall operate at the transmitter's operating magnetic resonance frequency. The rectifier will rectify the AC signal to a DC signal then deliver the power to the EV charging system. The primary aim of the WPT is to charge the EV battery and as such, integrating the WPR to the EV's online battery charging system.

2.5.2 Coil selection for interoperability

Research has been carried out on the coil design to optimize the power transfer. The fundamental challenge with the design of the power pad is to maximize the quality factor and the geometrical arrangement [54]. An interoperable WPT study was carried out using a quadruple coil structure on a Circular, Double D (DD) and Double D and Quadrant (DDQ) coil topology. The study showed that Quadruple coil to DDQ coil has the maximum PTE at misalignments up to 15mm compared to the others [54]. The proposed quadrupole coil pad arrangement is presented in Fig. 2.23.

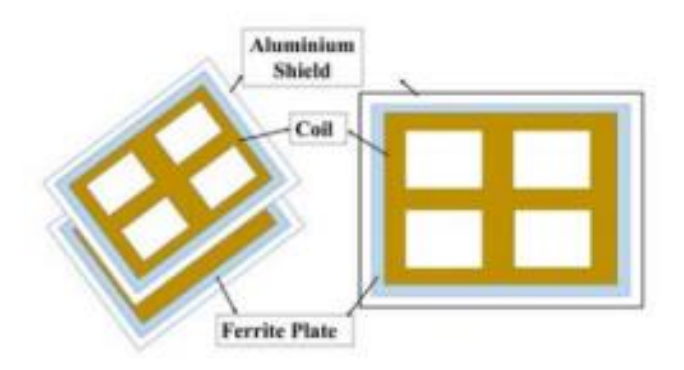


Fig. 2.23 Structure of proposed quadruple coil on mounted on a ferrite plate and aluminium shield.[54]

2.5.3 Insertion of Wireless Receiver Pads in EVs

The diagrams in Fig. 2.24 below show the circuitry of the WPR integrated in four different EV power systems. From the diagram presented in Fig 2.24(a) it shows the WPR connected directly to the EV battery. Fig 2.24(b) shows WPR connection to the CHAdeMO system in the Scion IQ EV. Fig 2.24(c) and Fig 2.24(d) shows WPR connection to the Online Battery Charger (OBC) of the Toyota Prius Plug-in and Chevy Volt EV respectively.

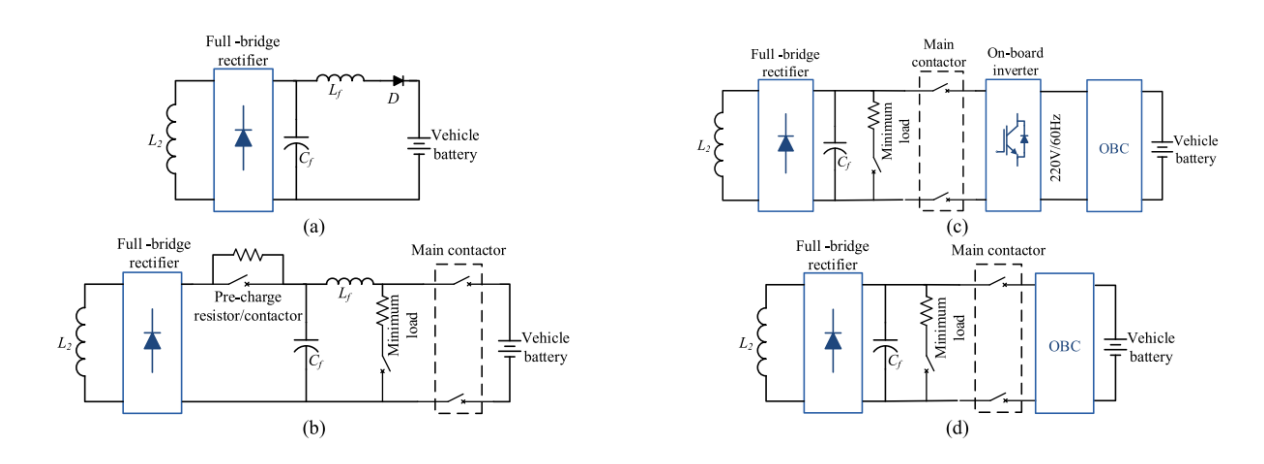


Fig. 2.24 (a) Toyota RAV4 EV (b) Scion IQ EV (c) Toyota Prius Plug-in (d) Chevy Volt [53]

2.5.4 Wireless Charging of Electric Taxis

Centre of Excellence for Low Carbon and Fuel Cell Technologies (CENEX) [55] in collaboration with Wireless Charging of Electric Taxis (WiCET) [56] retrofitted 9 LEVC and Nissan Dynamo ENV200 EV taxis for a demonstration of wireless charging on a Taxi Rank at Nottingham [55]. Two of these vehicles were demonstrated for the Transport for London in that event close up pictures of the EVs were taken. It is important to note that the integration of the WPR and the existing EV charging system were made at the terminals of the on-board inverter see Fig. 2.25.

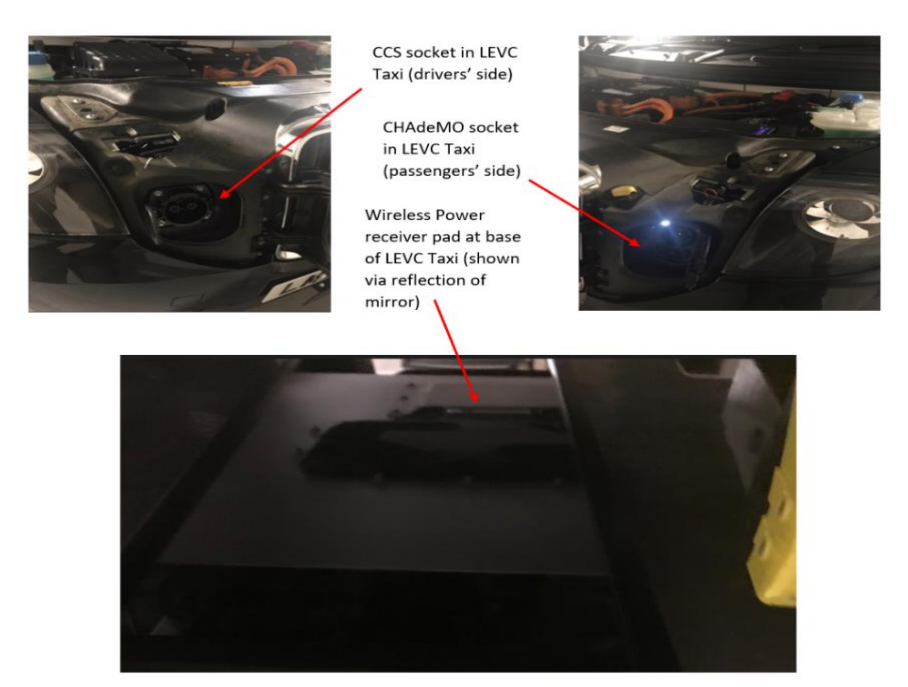


Fig. 2.25 Pictures showing various hardware interfaces for EV charging on LEVC Taxi.

2.5.5 Opportunity for retrofitting FHWPT in EVs

Retrofitting an existing WPT system to a FHWPT configuration involves incorporating specific hardware modifications which can be implemented. Given the ongoing research into retrofitting wireless systems for plug-in EVs, there is also potential for FHWPT technology to be integrated into existing plug-in EVs, provided OEMs collaborate on the design adaptations. This presents another answer of the first research question in Section 1.3.

2.6 Implementation of Zigbee protocol for WPT communication

As part of welcoming interoperability of WPT for EVs, it is important to consider the communication between the EV and the chargers. The writers of [57] shed light on the communication and signalling standard proposed in IEC 61980 part 2 (CD). They noted that a

"wireless pilot pin" with a Wi-Fi wireless local area network as implemented in the conductive charger system will overcome the interference occurring with close by wireless chargers see Fig. 2.26.

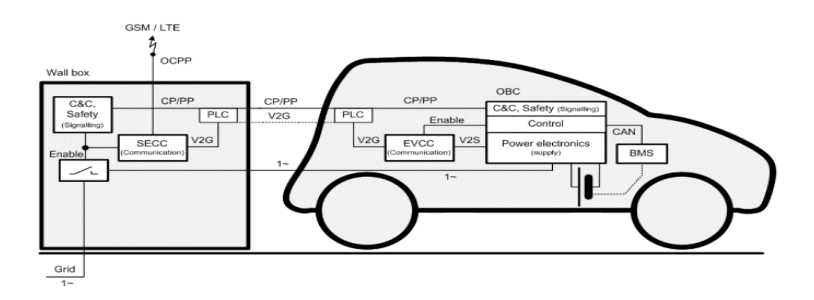


Fig. 2.26 Conductive EV charging system [57]

It is imperative that the data exchange between the EV and Charge Point (CP) for a WPT system should be immune to the near field magnetic resonance power transfer frequencies propagated by the local and adjacent WPT stations. In that light, it is expected that similar security measures which uphold the integrity of the conductive EV charging system is adopted. Hence, ISO 15118 protocol stack was implemented to develop the wireless communication and signal protocol for WPT[57].

The traditional EV CP cable has three main interface links thus, the power line, control pilot lines and communication lines. For every safe and successful charging session the control and communication cables provide interface between the charge point and the EV. One of the main safety features which the control and communication cables provide is the stop of bidirectional power flow in the event of an electric fault in the charger or damaged cable.

For the wireless charging, the power cables or links and socket are replaced by magnetic field and transmitter. The safety functionality provided by the control pilot cable is replaced by the near field communication. The ethernet cable line for communication can be replaced with a Wi-Fi certified wireless local area network (WLAN according to IEEE 802.11) [57] see Fig 2.27.

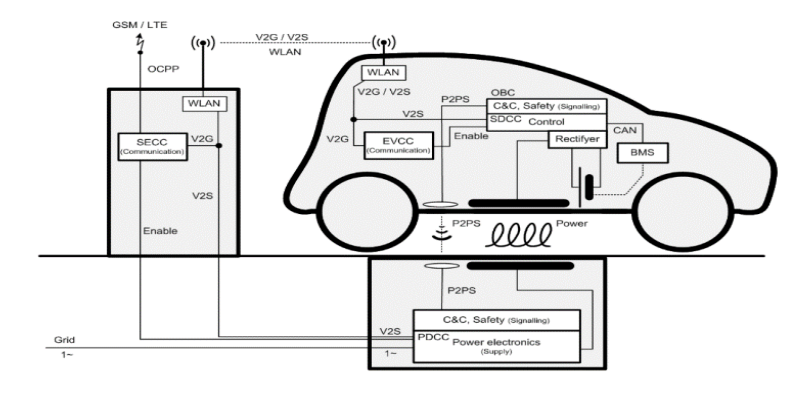


Fig. 2.27 Wireless EV charging system [57].

In this research the Zigbee protocol was reviewed, Zigbee wireless technology falls within the IoT's IEEE 802.15.4 protocol which has a low power and low-data rate wireless personal area network within a 10-meter communications range and transfer rate of 250 kbit/s. Zigbee communication protocol can be used for multiple WPT hubs [58].

Zigbee can operate at 868MHz, 915MHz or 2.45GHz whereas the WPT operating frequency bandwidth as stipulated by the SAE J2954 is between 79kHz and 90kHz. For the design of the FHWPT, the central operation frequency of 85kHZ will be implemented for the power transfer thus the operating frequency of the ZigBee will not interfere with the power transfer frequencies[59]. In the FHWPT design Zigbee will only be used for administrative purposes i.e. FHWPT performance monitoring, power profile, security etc. And not for the main operation of the FHWPT.

However, for the FHWPT all operational communications shall be undertaken by the Microcontroller, EPS32 WROOM 32's embedded communication protocol, ESP-NOW which shall be discussed in Chapter 4.

2.7 DC-DC converter

The mechanisms of the WPT systems can be split into two parts the DC-DC converters or power modules and the loosely coupled coils. In fact, as the loosely coupled coils can be analyzed as a transformer, so the entire WPT system can be analyzed as an isolated DC-DC converter [60]. The common differences between the WPT system and the transformer or DC-DC converter are its detachment of the transmitter side and receiver side and the

equivalent series resistance ESR or parasitic resistance of the coils at the transmitter and receiver modules of the WPT [60] see Fig. 2.28 As a result, it is prudent to consider the operation of a DC-DC converter.

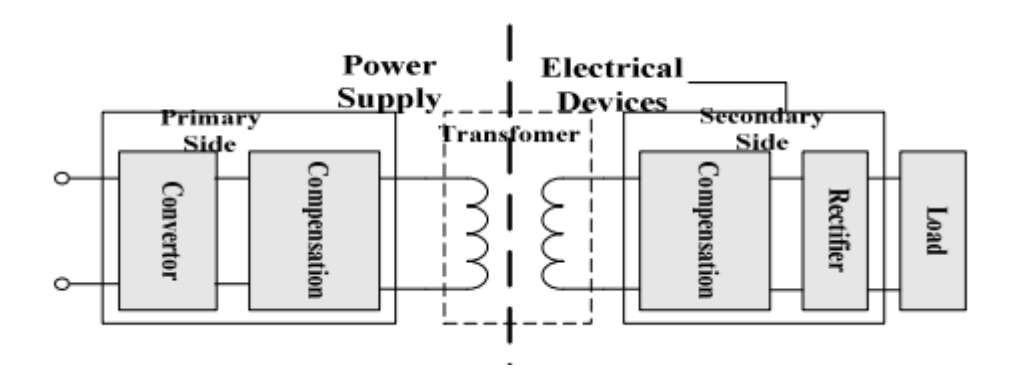


Fig. 2.28 DC-DC converter with loosely coupled transformer coils [60].

2.7.1 Gallium Nitride Field Effect Transistor

Silicon (Si) has been used as a semiconductor, but it has its limitations like the low electron mobility, low thermal conductivity, low magnetic field, and energy gap [61]. Gallium Nitride (GaN) is a wide band gap semiconductor which has high electron mobility, very low onresistance in comparison to Si for a given breakdown voltage [62]. GaN field effect transistor (FET) has a smaller output charge than Si MOSFET or Si Carbide (SiC). Also there are no significant reverse recovery losses in GaNFETs due to the absence of minority carriers, it requires low drive voltage and does not require a reverse voltage to turn off. Due to the high PTE, power density and positive temperature coefficient for the on-resistance the GaNFET heat sink, overall size and weight of the DC-DC converter is reduced [62]. Furthermore, studies carried out on a GaNFET DC-DC isolated converter shows the full load switching efficiency is 99.4% at 85kHz [62]. This clearly indicates a 0.4% drop in efficiency which is relatively insignificant.

For all these attributes of the GaNFET this semiconductor shall be used in the FHWPT DC-DC converter. A Class E² [60] soft switching zero voltage switch ZVS DC-DC resonant power converter (RPC) shall be employed as it has a reduced EMI due to zero derivative switching (ZDS), reduced device stress, and reduced switching losses as the switch is turned off when the voltage across it is zero compared to other DC-DC converters [63]-[66].

2.7.2 Controlled Switching Network

The RPC's half bridge or full bridge inverter has a controlled switching network (CSN) which generates a square wave $V_s(t)$ whose fundamental frequency's wave form $V_{s1}(t)$ is a sine wave. The Fundamental wave form is dominant with about 85% to 90% of the entire square wave form as presented in Fig. 2.29.

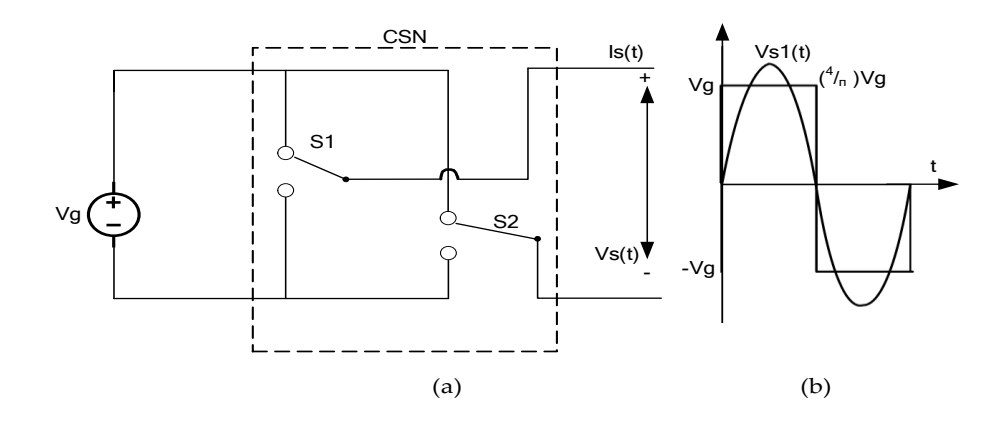


Fig. 2.29 (a) Equivalent circuit of CSN and (b) its respective fundamental harmonic sine wave and nth harmonic square wave forms [67]

The equation of the Fourier series of a square wave generated from the CSN is

$$V_s(t) = \frac{4V_g}{\pi} \sum_{n=1,3,5,\dots} \frac{1}{n} \sin(n\omega_s t)$$
 (2.6)

And the Fundamental sine wave

$$V_{s1}(t) = \frac{4V_g}{\pi} \sin(n\omega_s t) \tag{2.7}$$

Current delivered

$$i_s(t) = I_{s1} \sin(\omega_s - \varphi_s)$$
 (2.8)

And the average DC current

$$I_{in} = \frac{2}{T_s} \int_0^{\frac{T_s}{2}} i_s(t) d_t = \frac{2}{\pi} I_{s1} \cos(\varphi_s)$$
 (2.9)

Where V_s V_g , π , \sum , n, $\omega_s t$, V_{s1} , i_s , I_{s1} , φ_s , I_{in} , T_s , are the AC output voltage, DC input voltage, constant radian measure, summation, harmonic order number, switching angular frequency with respect to time, fundamental harmonic voltage, switching current, fundamental

harmonic current, phase shift with respect to switching, and DC input current, switching period.

2.7.3 FHWPT Resonant Tank Network and Controlled Switching Network

The CSN and resonant tank network (RTN) in the case of this FHWPT will operate between 79kHz and 90kHz from equations (2.6-2.9) it is evident that the amplitude of the current and voltage delivered to the inverter is frequency dependent. Careful considerations shall be made to ensure that CSN and RTNs VA is properly rated. The RTN shall be configured as a two element circuit, one inductor and one capacitors, LC [67]. The capacitors shall be a variable capacitor to switch the resonant frequency band from 79kHz to 90kHz in 1kHz frequency raster. And the inductor shall be the coils self inductance. Also the variable capacitor and FBC forming part of the feedback RTN shall also be used for the IDC. This topology applies to both transmitter and receiver modules.

The RTN has a trio capability which are to attenuate harmonics thus reduce EMI's and extend battery life, produce a minimized frequency based impedance, and provide quality factor, Q. AC output from the RTN shall supply the transmitter coils. Fig. 2.30 shows the Series Resonant Loaded Converter where the RTN A is connected to Transformer A which acts as the transmitter and receiver coils of a WPT.

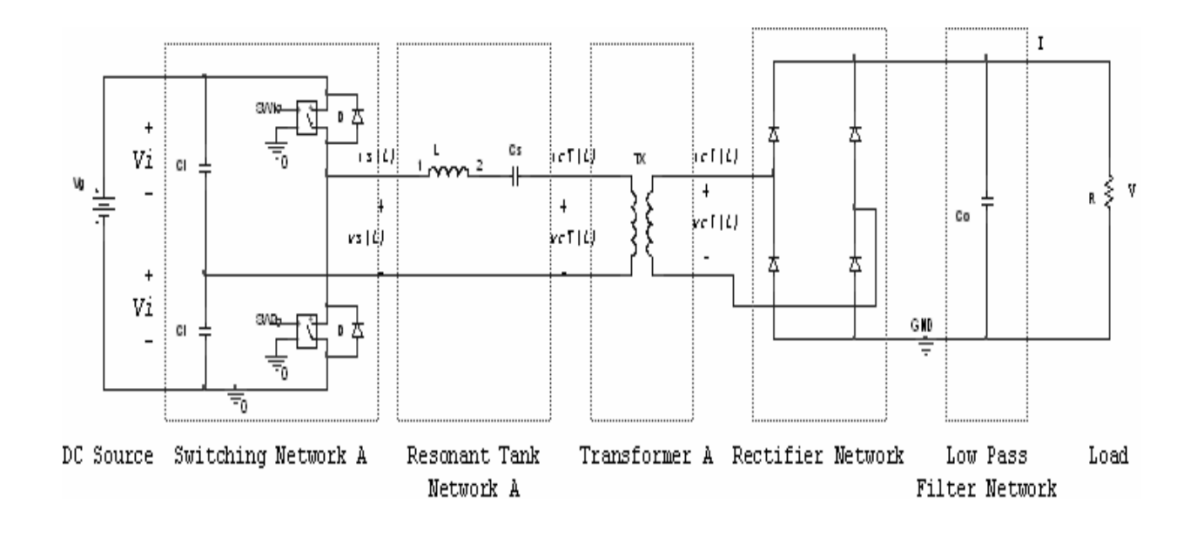


Fig. 2.30 Series Resonant Loaded Converter [64].

2.7.4 Effective resistance of the Rectifier

The effective resistance of the rectifier $R_{\text{effective}}$ is the static conduction resistance. This is important for managing power losses and designing heat sinks the $R_{\text{effective}}$ shall be derived in this section.

Current delivered to the rectifier from the receiver coil is

$$i_R(t) = I_P \sin(\omega_s t - \varphi_s) \tag{2.10}$$

EMF generated by the receiver coil

$$V_R(t) = \frac{4V_0}{\pi} \sum_{n=1,3,5,\dots} \frac{1}{n} \sin(n\omega_s t - \varphi_s)$$
 (2.11)

Voltage across the battery

$$V_{R1}(t) = \frac{4V_0}{\pi} \sin(\omega_s t - \varphi_s)$$
 (2.12)

Current delivered to charge battery

$$I_0 = \frac{2}{T_s} \int_0^{\frac{T_s}{2}} i_R(t) d_t = \frac{2}{\pi} I_R$$
 (2.13)

The effective resistance of the rectifier [12] value shall be computed in the FHWPT receiver's microcontroller to determine SoC and RoC.

$$R_{effective} = \frac{V_{R1(t)}}{I_{r(t)}} = \frac{\left(\frac{2\sqrt{2}}{\pi}\right)V_0}{\left(\frac{\pi}{\pi 2\sqrt{2}}\right)I_0} = \frac{8}{\pi^2} R_{Load}$$
 (2.14)

Where i_R , I_{P_1} , V_R , V_0 , V_{R1} , I_0 , I_R , R_{ac} , R_{Load} are the AC input current, DC output current, AC input voltage, DC output voltage, fundamental harmonic voltage, RMS DC output current, RMS DC input current, AC equivalent resistance of battery, DC resistance of the battery.

The rectifier shall be configured as a full bridge rectifier in series with a low pass filter to reduce harmonic distortions and EMI in the vehicle. In all, the response of the DC-DC converters ensures optimal PTE when delivering power at different frequencies during FH. Also, measurands from the rectifier output, that support the battery SoC and RoC plays a crucial role in detecting power theft, which is one of the features in the FHWPT.

2.8 Impedance matching in wireless power transfer technology

The impedance matching circuit (IMC) ensures an optimal PTE for the WPT by matching the impedance between the transmitter and receiver coils. Changes in the alignment between the transmitter and receiver coils and loss of line of sight between both coils can change the impedance of the WPT[68][69]. In this section a critical review of the research undertaken in WPT IMC is documented.

Its worth noting that in the FHWPT an IDC is implemented rather than an IMC although the operate on the same principles, providing intelligence to the FHWPT system. However, the distinction between the IMC and the IDC will be explained in section 2.8.4.

2.8.1 PTE improvement of wireless power transfer by impedance matching

The authors of [69] suggested using an additional coil with capacitors to correct the impedance mismatch. They stated that for maximum PTE two conditions shall be met thus, the impedance of the power transmission circuit is the same as the input impedance of the transmission coil and the impedance of the power reception circuit is the same as the input impedance of the reception coil. The additional coil is referred to as a loop, this loop of wire is magnetically coupled to the transmitter coils on the transmitter module and magnetically coupled to the receiver coils on the receiver module see Fig. 2.31. This assembly is similar to the FBC in the FHWPT system being researched.

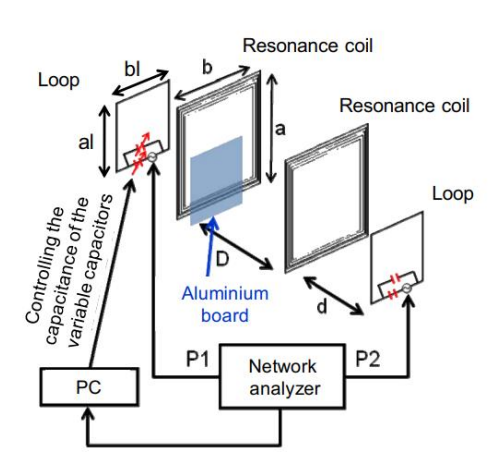


Fig. 2.31 Impedance matching circuit overview [69]

On the transmitter side the loop is made of a coil of wire and two variable capacitors and on the receiver sided the loop is made of a coil of wire and two lumped capacitors. An additional network analyser circuit monitors the coils on the transmitter and receiver circuit simultaneously for imbalance and when an imbalance is detected the transmitter IMC adjusts the variable capacitors to match the new impedance. Experiments to recover PTE in the event of a loss of line of sight was undertaken their results showed that the IMC facilitated the restoration of the PTE.

In this system an additional network analyser circuit with its associated communication circuit are required this incurs weight cost and complexity to the WPT system. In the FHWPT this network analyser circuit is akin to the microcontroller. The equilibrium state for their system was not shown for lower operating frequencies (SAE bandwidth). However, the FHWPT research is based on SAE bandwidth.

2.8.2 Multiple receiver IMC

The IMC is also useful for transmitting power to multiple receivers. The authors in [70] presents the case that the inclusion of mutual inductance of non-adjacent coils in the IMC can improve the system's PTE. This scheme also enhances PTE under spatial misalignments.

While such methods improve coupling uniformity across distributed receivers, FHWPT systems do not require multiple receiver coils or complex multi-node coupling topologies. Instead, they rely on a single FBC per transmitter and receiver pair to monitor coupling variations and adaptively retune the system via FH. This significantly simplifies the hardware architecture while retaining adaptability and maintaining high PTE under dynamic conditions.

2.8.3 IMC in Transmitter and Receiver Modules

Furthermore, the authors of [68] proposed to include IMC in both the transmitter and receiver modules of the WPT. The receiver IMC enhances the PTE between the transmitter and receiver by converting the input resistance of the receiver's rectifier to the optimum impedance.

From their experiments the WPT system with the IMC provides a better PTE compared to a WPT system without an IMC. Their experiments shows that the IMC provides intelligence to halt the transmitter from delivering power when the receiver module is not in the system.

In the researched FHWPT system, IDCs will be integrated into both the transmitter and receiver circuits, not only to optimise impedance matching across frequency hops but also to enhance operational resilience under varying load and coupling conditions.

2.8.4 Assessing SoC Influence on WPT Loading via IMC

Lithium Nickel Manganese Cobalt Oxide (NMC) cells are a popular lithium-ion battery chemistry in EVs due to their high energy density and thermal stability. Their internal impedance is influenced by both SoC and aging. As reported by the authors of [71], the ohmic resistance Ro, in fresh NMC cells ranges between $1.27m\Omega$ and $1.46m\Omega$, while aged cells exhibit significantly higher Ro resistance, from $3.0m\Omega$ to $3.9m\Omega$.

Although this variation appears significant in absolute terms, the corresponding impact on the PTE is minimal. This is because the WPT system operates with load impedances typically in the $0.1~\Omega$ to multi-ohm range, making milliohm level shifts relatively negligible from the power electronics' perspective. Thus, the IDC in the proposed FHWPT architecture is not primarily for correcting large impedance mismatches, but rather to facilitate adaptive frequency control, ensuring resonance is maintained under dynamic misalignment conditions.

2.8.5 IMC circuitry concerns

In mass production of electrical components there is a deviation of the component's rated values [72]. That means the capacitance of a 470uF capacitor can have a tolerance of +/-10% which could affect the performance of the WPT. The authors of [72] carried out studies on various IMC capacitor configurations in various WPT topologies [72]. The study was to determine the deviation of their respective PTE based on their intrinsic capacitive tolerance. From the study some WPT topologies IMCs achieved larger PTEs than others. The Series - Series (SS) WPT topology had a lower PTE variation thus, one of the reasons why the SS WPT topology is used in this research for FH.

In all, the role of the impedance detection in the FHWPT is inevitable. The detection principles of the IMC shall be implemented to inform the microcontroller to activate FH. The

proposed topology for the FHWPT is SS this is due to its simplicity and voltage source arrangement. The research in IMC helps to answer the second research question in Section 1.3.

2.9 Circuit analysis of WPT Mono resonant Circuits

The derivation of analytical expressions for both PTE and optimal load conditions in the WPT system shall be derived from first principles in this Section. Thereafter, the resonant compensation capacitor formula for the mono resonant or primary WPT compensation circuit topologies will be derived. As part of the derivation, the mono resonant WPT topologies shall examined to characterize their unique functional profiles. This assessment will highlight the advantages of each topology in terms of source-type behaviour (voltage or current source), and their ability to generate zero phase angle (ZPA) or real power transfer and PTE. These derivations inform the theoretical foundation for selecting a topology that best supports performance, control, and stability requirements of the FHWPT system.

2.9.1 Analogy and Analysis of the ideal transformer

The WPT, can be termed as a loosely coupled transformer. And as such some parameters and formulas of the ideal transformer theory shall be utilized to determine the characteristics of the WPT. A simple electromagnetic circuit shall be developed to establish metrics in the electrical and magnetic circuit. Fig 2.32 below shows a simple electromagnetic circuit.

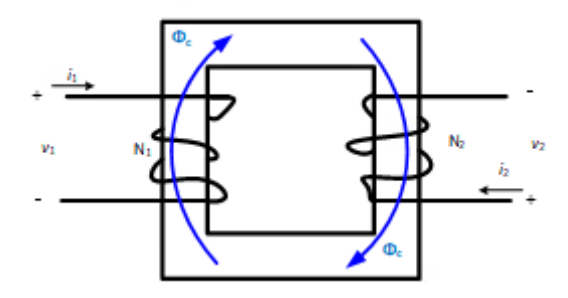


Fig. 2.32 Electromagnetic circuit

Where v_1 , i_1 , N_1 and v_2 , i_2 , N_2 are the primary and secondary voltage, current, and number of turns respectively, φ_c is the flux in the core. A magnetic circuit can be derived from this circuit as shown in Fig 2.33 below.

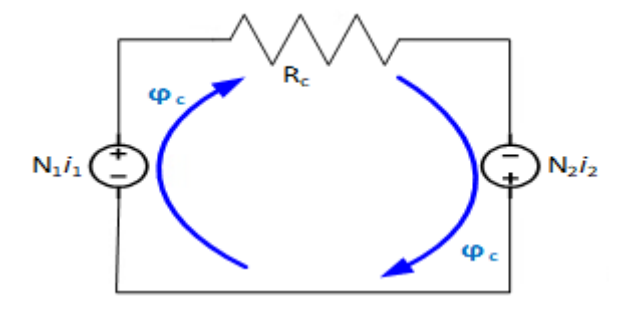


Fig. 2.33 Magnetic circuit

Where i_1 , N_1 and i_2 , N_2 are the primary and secondary current, and number of turns respectively. Note that the product N_1i_1 is the magnetomotive force, MMF. φ_c and R_c is the flux and reluctance in the core.

From Fig 2.32 and 2.33 we can express the voltage and MMF thus

$$v_1 = N_1 \frac{\delta \varphi_c}{\delta t}$$
 (2.15)

$$v_2 = N_2 \frac{\delta \varphi_c}{\delta t}$$
 (2.16)

Note that (2.15) and (2.16) are equivalent expressions of the voltage across the inductor which is

$$v = L \frac{\delta i}{\delta t}$$
 (2.17)

where L is the inductance and I is the current. If we differentiate (2.15) and (2.16) with respect to φ_c we have

$$v_1 = N_1$$
 (2.18)

$$v_2 = N_2$$
 (2.19)

And determining the voltage gain or transfer ratio of the transformer we have

$$\frac{v_2}{v_1} = \frac{N_2}{N_1}$$
 (2.20)

Using Kirchoff's Voltage Law in Fig. 2.34 we have

$$N_1 i_1 + N_2 i_2 = R_c \varphi_c$$
 (2.21)

If the permeability of the core μ_c is large such that $R_c=0$ then

$$N_1 i_1 = -N_2 i_2$$
 (2.22)

And the currents can be expressed as

$$\frac{i_2}{i_1} = -\frac{N_1}{N_2} \ (2.23)$$

From (2.22) and (2.23) we can determine the voltage terminals, flux, current flow and other parameters of the Ideal transformer as shown in Fig. 2.34 and Fig. 2.35

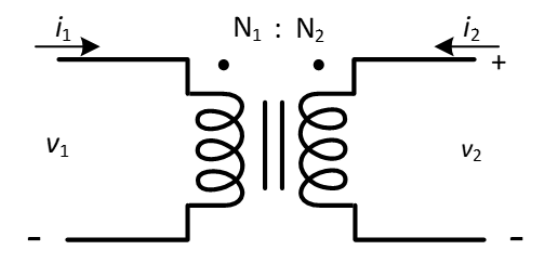


Fig. 2.34 Symbol of ideal transformer

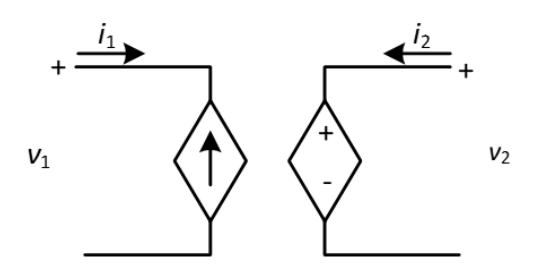


Fig. 2.35 Ideal transformer model

The direction of i_2 is explained in (2.22)

From the equations of the ideal transformer it indicates that if $i_2 = 0$, the terminals of v_2 are open circuited then $i_1 = 0$ but that is not true. When a transformer is not loaded the open circuit voltage is at its maximum and there is an imaginary current which is termed as the magnetising current thus $i_1 \neq 0$.

This calls for the model of the non-ideal transformer as presented in Fig. 2.36 to enable us understand that if $i_2 = 0$ and the secondary terminals are open circuited then $i1 \neq 0$. Thus, the imaginary magnetizing circuit I_m is now accounted for.

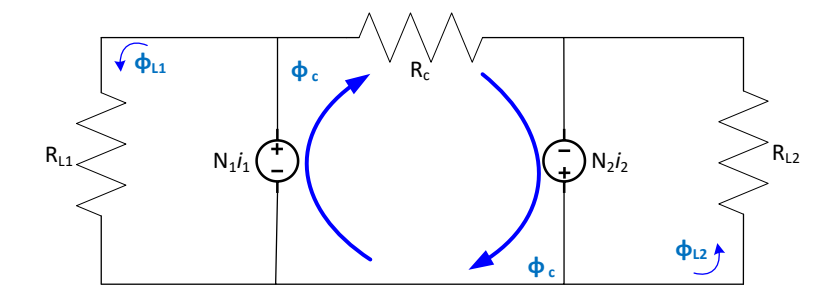


Fig. 2.36 Magnetic circuit of a non-ideal transformer

From the circuit we have

$$\varphi_c = \frac{N_1 i_1 + N_2 i_2}{R_c} \ (2.24)$$

$$\varphi_{l1} = \frac{N_1 i_1}{R_{l1}}$$
 (2.25)

$$\varphi_{l2} = \frac{N_1 i_2}{R_{l2}}$$
 (2.26)

It is also worth noting that the flux linkage, λ relating the fluxes can be expressed as

$$\lambda = N\varphi = \int v \, dt$$
 (2.27)

Thus, from Fig 2.37 we have

$$\lambda_1 = N_1(\varphi_{l1} + \varphi_c) = \frac{N_1^2 i_1}{R_{l1}} + \frac{N_1^2 i_1}{R_c} + \frac{N_1 * N_2 i_2}{R_c}$$
 (2.28)

$$\lambda_2 = N_2(\varphi_{l2} + \varphi_c) = \frac{N_2^2 i_2}{R_{l2}} + \frac{N_2^2 i_2}{R_c} + \frac{N_1 i_1 * N_2}{R_c}$$
 (2.29)

In Matrix form this can expressed as

$$\begin{bmatrix} \int v_1 \, dt \\ \int v_2 \, dt \end{bmatrix} = \begin{bmatrix} \lambda_1 \\ \lambda_2 \end{bmatrix} = \begin{bmatrix} \frac{N_1^2}{R_{l_1}} + \frac{N_1^2}{R_c} & \frac{N_1 * N_2}{R_c} \\ \frac{N_2 * N_1}{R_C} & \frac{N_2^2}{R_{l_2}} + \frac{N_2^2}{R_C} \end{bmatrix} \begin{bmatrix} i_1 \\ i_2 \end{bmatrix} (2.30)$$

Noting that $L = \frac{N^2 i}{R}$ and if the equation is differentiated, we then have

$$\begin{bmatrix} v_1 \\ v_2 \end{bmatrix} = \begin{bmatrix} L_{11} & L_{12} \\ L_{21} & L_{22} \end{bmatrix} \begin{bmatrix} \frac{\delta i_1}{\delta t} \\ \frac{\delta i_2}{\delta t} \end{bmatrix}$$
(2.31)

Where L_{11} , L_{22} , L_{21} are the primary and secondary self inductances and Mutual inductance respectively.

The determinant of the inductance matrix in (2.31) Where $L_{11} = L_{22}$ we have

$$L_{11} * L_{22} - M^2 \approx 0$$
 (2.32)

$$M = k \sqrt{L_{11} L_{22}}$$
 (2.33)

Where k is the coupling factor. For the ideal transformer k=1 for a non ideal power transformer $k \approx 1$ for a WPT typically, 0.1 < k < 0.4. This presents major drawback on WPT technology, however introducing a compensation circuit in the WPT the Q factor of the WPT coils PTE can reach up to 93%.

This non ideal transformer can be presented in the schematic in Fig 2.37 below

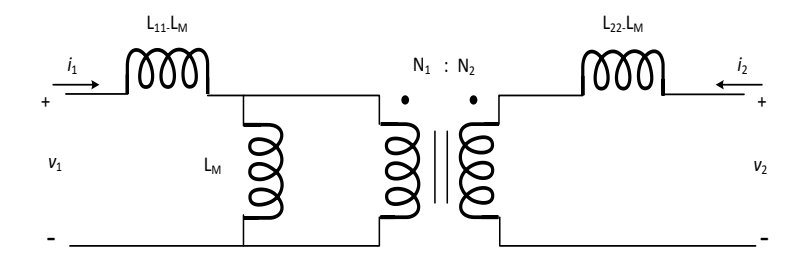


Fig. 2.37 Model of non-ideal transformer

And also simplified in the schematic in Fig 2.38 below.

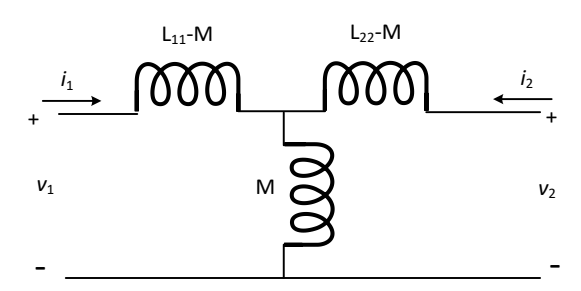


Fig. 2.38 T circuit of non-ideal transformer.

The terms $L_{11}-M$ and $L_{22}-M$ indicate the leakage inductance in the primary and secondary windings.

2.9.2 Compensation circuitry

As earlier mentioned, the coupling factor, k is proportional to the mutual inductance, M thus if k tends to 0 the PTE reduces even if there is a high VA input in the primary winding. As such for a WPT whose 0.1 < k < 0.4 a compensation circuit shall be embedded in the WPT to improve the PTE. The compensation circuit is designed to produce a resonant circuit such that the product of the k and Q factor at a resonant frequency generates a high PTE. In this section, the basic mono resonant circuits shall be studied.

2.9.3 Input impedance and the compensation capacitor

Input impedance of the WPT system is directly linked to the resonant frequency of the coils in the circuit. The compensation is required to eliminate or reduce the VA thus, understanding the frequency dependant compensating capacitor, C_p required to resonate with the coil at the frequency is important. From the studies it shall be revealed how complicated the derivation and the value of C_p can get. The compensating circuit for all topologies is dependent on the primary circuit capacitor C_p .

2.9.4 Series - Series Compensation Circuit.

The SS mono resonant circuit is the most basic WPT configuration and has its advantage of no reactive energy dissipation. It is also a preferred option for bi-directional wireless charges [1]. Fig 2.39 below shows a SS mono resonant circuit.

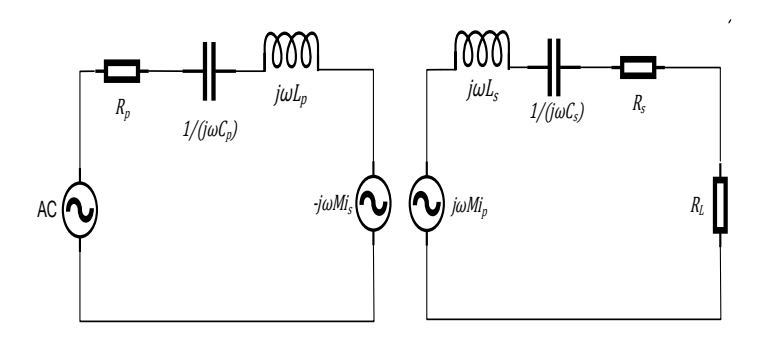


Fig. 2.39 WPT circuit showing dependent voltages.

To determine the PTE the WPT circuit is modelled using voltage dependent sources as shown in Fig 2.40 where, in the transmitter circuit, V_p is voltage, i_p is current, R_p is the parasitic resistance, $1/(j\omega C_p)$ is the frequency dependent capacitive impedance, $j\omega L_p$ is the frequency dependent inductive impedance. Also in the receiver circuit, i_s is current, R_s is the

parasitic resistance, $1/(j\omega C_s)$ is the frequency dependent capacitive impedance, $j\omega L_s$ is the frequency dependent inductive impedance, R_L is the battery load resistance and ω is the angular operating frequency $2\pi f$. M is the mutual inductance, $j\omega M$ is the frequency dependent mutual inductive impedance.

Analysing the receiver circuit we have

$$i_S = \frac{j\omega M i_p}{R_S + R_L + j\omega \left(L_S - \frac{1}{C_S}\right)}$$
 (2.34)

Let
$$Z_s = R_s + R_L + j\left(\omega L_s - \frac{1}{\omega Cs}\right)$$

$$i_s = \frac{j\omega M i_p}{Z_s} \tag{2.35}$$

 Z_s is the total impedance in receiver side circuit. Hence, reflected impedance in transmitter side winding.

$$\frac{j\omega M i_s}{ip} = \frac{\omega^2 M^2}{Z_s} i_p \tag{2.36}$$

Thus, Z_s referred as shown in Fig. 2.40 is

$$Z_{\rm r} = \frac{\omega^2 M^2}{Z_{\rm c}} \tag{2.37}$$

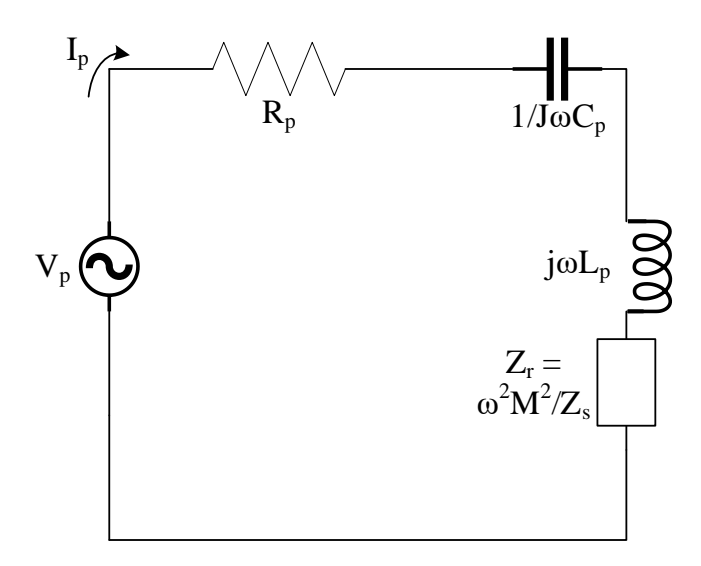


Fig. 2.40 SS secondary impedance Zs referred to the primary side.

Analysing the transmitter circuit

$$i_p = \frac{V_{in}}{R_p + j(\omega L_s - \frac{1}{\omega C_s}) + \frac{\omega^2 M^2}{Z_s}}$$
 (2.38)

Let
$$Z_p = R_p + j \left(\omega L_p - \frac{1}{\omega C_p}\right)$$
 (2.39)

2.9.4.1. Determining the PTE

$$i_p = \frac{V_{in} * Z_S}{Z_p Z_S + \omega^2 M^2}$$
 (2.40)

$$i_S = \frac{j\omega MV_{in}}{Z_n Z_s + \omega^2 M^2} \tag{2.41}$$

At resonance $Z_p = R_p$ and $Z_s = R_s + R_L$ thus, Power in, P_{in} at resonance

$$P_{in} = \frac{V_{in}^2 * (R_S + R_L)}{R_n R_S + R_n R_L + \omega^2 M^2}$$
 (2.42)

Power out, P_{out}

$$P_{out} = \frac{\omega^2 M^2 V_{in}^2 * R_L}{\left(R_p R_s + R_p R_L + \omega^2 M^2\right)^2}$$
 (2.43)

And PTE, η

$$\eta = \frac{P_{out}}{P_{in}} = \frac{\omega^2 M^2 * R_L}{(R_S + R_L) * (R_R R_S + R_R R_L + \omega^2 M^2)}$$
(2.44)

From this equation it is evident that the frequency ω , can have a possible effect on the PTE, η . Due to the changing internal impedance of the EV batteries during a charging session, the equivalent load resistance will impact the fixed optimal PTE [73]. The maximum PTE is derived by taking the derivative of η with respect to R_L and set it to zero such that

$$\frac{d\eta}{dR_{I}} = 0$$
 (2.45)

$$\frac{d}{dR_L} \left(\frac{\omega^2 M^2 * R_L}{(R_S + R_L) * (R_p R_S + R_p R_L + \omega^2 M^2)} \right) = 0$$
 (2.46)

We have R_L is given below [74]

$$R_L = R_S \sqrt{1 + \frac{\omega^2 M^2}{(R_p R_S)}}$$
 (2.47)

$$R_L = R_s \sqrt{1 + k^2 Q_p Q_s}$$
 (2.48)

Where Q_pQ_s are the quality factors, $\frac{wL}{R}$ of the respective coils. Also, the maximum PTE can be derived [75] as

$$\eta_{max} = \frac{k^2 Q_p Q_s}{\left(1 + \sqrt{1 + k^2 Q_p Q_s}\right)^2} \approx \frac{kQ}{2 + kQ} (2.49)$$

The maximum PTE is dependent on the air gap distance, d between the transmitter and the receiver coils. The society for automotive engineers recommends in SAE J2954 air gaps up to 300mm [76] for EV wireless charging. Further to that a relationship between k, M and d for a circular spiral coil was developed by [76] and expressed below.

$$k \approx \frac{1}{2\left(\frac{d}{\sqrt{radius_p radius_s}}\right)^3}$$
 (2.50)

Where $radius_p$ and $radius_s$ are the radii of the primary and secondary coils.

2.9.4.2. Determine Compensation Capacitor

 Z_p is the total impedance in the transmitter circuit Z_{in} is the total impedance in the circuit thus $Z_{in}=Z_p+Z_s$ (2.51)

$$Z_{in} = R_p + j\left(\omega L_p - \frac{1}{\omega C_p}\right) + R_s + R_L + j\left(\omega L_s - \frac{1}{\omega C_s}\right)$$
(2.52)

To determine the imaginary we have

$$Imag Z_{in} = \left(\omega L_p - \frac{1}{\omega C_n}\right) + \left(\omega L_s - \frac{1}{\omega C_s}\right) (2.53)$$

$$Imag Z_{in} \left(\omega L_p - \frac{1}{\omega C_p} \right) = \left(\omega L_s - \frac{1}{\omega C_s} \right) = 0$$
 (2.54)

$$C_p = \frac{1}{(\omega^2 L_p)}$$
 (2.55)

Also
$$\omega^2 = \frac{1}{L_S C_S}$$
 (2.56)

Thus,
$$C_p = \frac{L_s C_s}{L_p}$$
 (2.57)

From the studies on the SS WPT both the primary and secondary circuits compensation capacitors are in series. This topology is preferred due to its simpler design also it is easier to regulate the voltage since it is inherently a voltage-sourced circuit. It is suitable for mid to long range power transfer applications due to its ability to maintain a high level of PTE over varying distances.

2.9.5 Series Parallel Circuit

The series parallel (SP) compensation circuit is presented in Fig 2.41 below the advantages of this circuit is the current source it provides in the secondary circuit and the constant voltage output [77]. The authors of [78] – [81] in their study shows

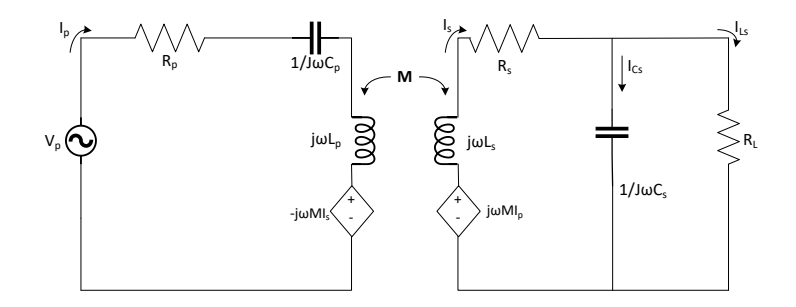


Fig. 2.41 SP topology

$$V_{in} = \left(j\omega L_p - \frac{1}{j\omega C_p}\right)I_p + R_pI_p - j\omega MI_s \quad (2.58)$$

$$j\omega MI_p = -(R_s + j\omega L_s)I_s = \frac{I_{Cs}}{j\omega C_s} = R_L I_L$$
 (2.59)

For simplicity the secondary winding shall be reconfigured to a current source as shown in Fig. 2.42

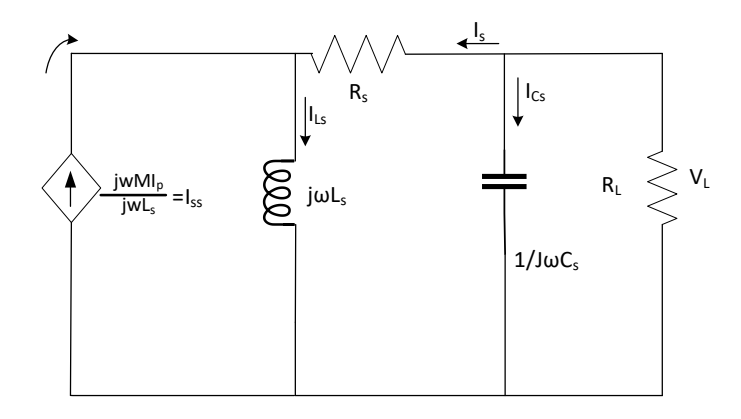


Fig. 2.42 Secondary side SP topology reconfigured to a current source Iss

$$KCL = I_{SS} = I_{LS} - I_{S}$$
 (2.60)

$$I_S = I_{LS} - I_{SS}$$
 (2.61)

Note that
$$I_s = \left(\frac{V_L}{j\omega Ls} - \frac{j\omega M I_p}{j\omega Ls}\right)$$
 and $V_L = \frac{M I_p}{Ls} * R_L$ (2.62)

thus
$$I_S = \left(\frac{MI_p}{Ls} * \frac{R_L}{j\omega Ls} - \frac{j\omega MI_p}{j\omega Ls}\right)$$
 (2.63)

$$I_{S} = I_{p} \left(\frac{MR_{L}}{j\omega L_{s}^{2}} - \frac{j\omega M}{j\omega L_{s}} \right) (2.64)$$

$$Z_{r} = j\omega M \frac{I_{S}}{I_{p}} = \frac{j\omega M I_{p} \left(\frac{MR_{L}}{j\omega L_{S}^{2}} - \frac{j\omega M}{j\omega L_{S}}\right)}{I_{p}} = \left(\frac{M^{2}R_{L}}{L_{S}^{2}} - j\omega \frac{M^{2}}{L_{S}}\right) (2.65)$$

Note that $M^2 = k^2 L_p L_s$ thus,

$$Z_{r} = k^{2} \left(\frac{Lp}{L_{s}} R_{L} - j\omega Lp \right)$$
 (2.66)

The simplified SP circuit is shown in Fig 2.43

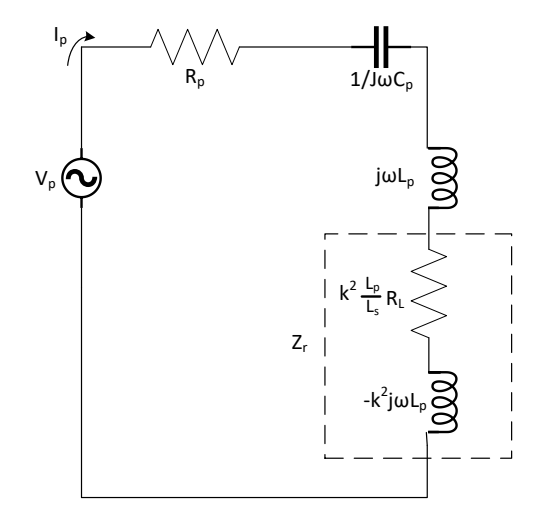


Fig. 2.43 SP secondary impedance $Z_{\scriptscriptstyle S}$ referred to the primary side.

The negative inductor is indicative of the reactive behaviour of the effectively reversed inductor. This phenomenon can be utilized to design or tune the compensating capacitor to enhance ZPA conditions or adjust the resonant frequency of the system, thereby enhancing the PTE. In SP topology, negative inductance can fine-tune the resonant frequency of the system under different loading or coupling coefficients.

2.9.5.1. Determine Compensation Capacitor

$$Z_{in} = j\omega L_p + \frac{1}{j\omega C_p} - k^2 j\omega Lp + k^2 \frac{Lp}{L_s} R_L$$
 (2.67)

Imaginary we have

$$Im(Z_{in}) = \omega L_p - \frac{1}{\omega C_p} - k^2 \omega Lp$$
 (2.68)

And the primary compensation Capacitor can be determined as

$$C_p = \frac{1}{\omega^2 L p (1 - k^2)} \tag{2.69}$$

This expression shows that there shall be a reactive energy at resonance frequency in the secondary circuit.

Studies of the SP circuit shows that there is a combination of the voltage and current regulation. The secondary side is a current-sourced circuit thus easier to regulate the current and overcurrent conditions under fluctuating loads. SP provides better PTE on low loads i.e.

impedances of about 50Ω to 100Ω . This is ideal for charging where constant current is required. Further to this since the secondary side is a current source the secondary coil windings are reduced compared to the primary side saving weigh and costs.

2.9.6 Parallel series compensation circuit

The Parallel Series (PS) compensation circuit diagram is presented in Fig. 2.44 below.

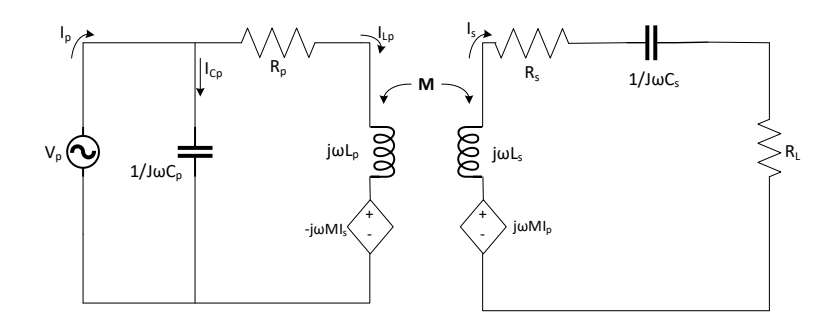


Fig. 2.44 PS topology

$$V_p = (R_p + j\omega L_p) I_{Lp} - j\omega M I_s \qquad (2.70)$$

Note that current flowing in the capacitor branch is $I_{\mathcal{C}p}=j\omega\mathcal{C}_pV_p$

$$j\omega M I_{Lp} = (R_L + R_s) I_s + \left(j\omega L_s - \frac{1}{j\omega C_p}\right) I_s$$
 (2.71)

$$I_{s} = \frac{j\omega M}{(R_{s} + R_{L}) + j\left(\omega L_{s} - \frac{1}{\omega C_{s}}\right)} I_{Lp} \qquad (2.72)$$

$$V_p = \left(R_p + j\omega L_p\right) I_{Lp} - j\omega M \frac{j\omega M}{(R_S + R_L) + j\left(\omega L_S - \frac{1}{\omega C_S}\right)} I_{Lp}$$
 (2.73)

$$V_{in} = \left[\left(R_p + j\omega L_p \right) + \frac{\omega^2 M^2}{(R_s + R_L) + j\left(\omega L_s - \frac{1}{\omega C_s}\right)} \right] I_{Lp} (2.74)$$

In the primary circuit we also have from KCL that

$$I_p = I_{Cp} + I_{Lp}$$
 (2.75)

And Voltage and current in the Capacitor branch is

$$V_p = I_{Cp} * \frac{1}{i\omega C_n} (2.76)$$

And substituting I_{Lp} for $I_p-V_pj\omega C_p$ (2.75) we have

$$V_p = \left[\left(R_p + j\omega L_p \right) + \frac{\omega^2 M^2}{\left(R_s + R_L \right) + \left(j\omega L_s - \frac{1}{j\omega C_s} \right)} \right] \left(I_p - V_p j\omega C_p \right) \tag{2.77}$$

$$Z_{in} = \frac{V_p}{I_p} = \frac{\frac{(R_p + j\omega L_p) + \frac{\omega^2 M^2}{(R_s + R_L) + (j\omega L_s - \frac{1}{j\omega C_s})}}{(1 + j\omega C_p)(R_p + j\omega L_p) + \frac{\omega^2 M^2}{(R_s + R_L) + (j\omega L_s - \frac{1}{j\omega C_s})}}$$
(2.78)

At resonance the secondary compensation circuit resonates at ω_0

$$Z_{in} = \frac{V_{in}}{I_p} = \frac{(R_p + j\omega_0 L_p) + \frac{\omega_0^2 M^2}{(R_S + R_L)}}{1 + j\omega_0 C_p (R_p + j\omega_0 L_p) + \frac{\omega_0^2 M^2}{(R_S + R_L)}}$$
(2.79)

2.9.6.1. Determine Compensation Capacitor

To determine the compensating capacitor's value we separate the imaginary components of Z_{in} , Imag Z_{in} . In this case the terms in the numerator and denominator shall be rearranged to separate out the real and imaginary parts and present a complex number. After the complex conjugate is computed Imag Z_{in} is presented below.

$$Imag Z_{in} = \frac{\omega_0 L_p (1 - \omega_0^2 L_p C_p) - \omega_0 C_p \left(R_p + \frac{\omega_0^2 M^2}{(R_S + R_L)} \right)^2}{\left(1 - \omega_0^2 L_p C_p \right)^2 + \omega_0^2 C_p^2 \left(R_p + \frac{\omega_0^2 M^2}{(R_S + R_L)} \right)^2}$$
(2.80)

Solving for the compensating compensator value we set the numerator to 0 thus

$$\omega_0 L_p (1 - \omega^2 L_p C_p) - \omega_0 C_p \left(R_p + \frac{\omega_0^2 M^2}{(R_c + R_L)} \right)^2 = 0$$
 (2.81)

$$\omega_0 L_p = \omega_0^3 L_p^2 C_p + \omega_0 C_p \left(R_p + \frac{\omega_0^2 M^2}{(R_s + R_I)} \right)^2 (2.82)$$

$$L_p = C_p \left(\omega_0^2 L_p^2 + \left(R_p + \frac{\omega_0^2 M^2}{(R_S + R_L)} \right)^2 \right)$$
 (2.83)

$$C_p = \frac{L_p}{\omega_0^2 L_p^2 + \left(R_p + \frac{\omega_0^2 M^2}{(R_S + R_L)}\right)^2}$$
 (2.84)

 R_p and R_s are $<< R_s$ thus, $\left(R_p + \frac{\omega_0^2 M^2}{(R_S + R_L)}\right)$ can be approximated to $\left(\frac{\omega_0^2 M^2}{R_L}\right)$ also substituting ω_0^2 for $L_s \mathcal{C}_s$ we have

$$C_p = \frac{L_p}{\frac{L_p^2}{L_s C_s} + \left(\frac{M^2}{L_s C_s R_L}\right)^2} = \frac{L_s C_s}{L_p + \frac{M^4}{L_p L_s C_s R_L}} (2.85)$$

The Capacitors \mathcal{C}_p and \mathcal{C}_s are interdependent indicating that both capacitors may have different values but has a constant factor relating them to achieve a particular resonant frequency. We can see that the load resistor, R_L and mutual inductance M which can change during a charging session can impact the resonant frequency matching causing bifurcation and low PTE.

From studies undertaken on the PS topology, the voltage source fluctuations have minimum impact on the operation of the WPT since the primary side is a current source. PS also requires less input current. PS provides a stable voltage supply to the load and a good PTE for short range due to its high current delivered via the coils.

2.9.7 Parallel - Parallel compensation circuit

The Parallel - parallel (PP) WPT topology shall be studied in this section Fig. 2.45 shows the circuit.

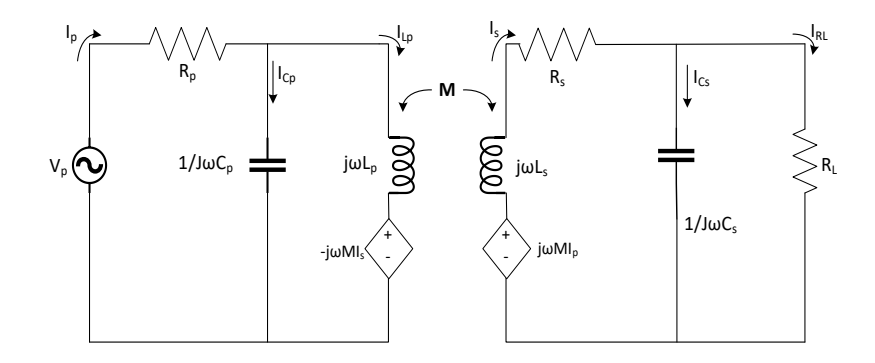


Fig. 2.45 PP topology

$$V_p = \left(R_p + j\omega L_p\right) I_{Lp} - j\omega M I_s = I_{cp} \frac{1}{j\omega C_p}$$
 (2.86)

$$-j\omega MI_{Lp} = -(R_s + j\omega L_s) I_s = R_L I_L \qquad (2.87)$$

From KCL

$$I_p = I_{cp} + I_{Lp}$$
 and $I_s = I_{cs} + I_L$ (2.88)

Also we can state that

$$I_{cp} = V_{in} j\omega C_p$$
 and $\frac{I_{cs}}{j\omega C_s} = R_L I_L$ (2.89)

$$I_S = \omega C_S R_L I_L + I_L = (j\omega C_S R_L + 1)I_L$$
 (2.90)

Substituting I_s in (2.89) we have

$$R_L I_L = -(R_s + j\omega L_s) (j\omega C_s R_L + 1) I_L + j\omega M I_{Lp}$$
 (2.91)

$$I_{L} = \frac{j\omega M}{(R_{s} + j\omega L_{s})(j\omega C_{s}R_{L} + 1) + R_{L}}I_{Lp}$$
 (2.92)

And

$$I_{S} = \frac{(j\omega C_{S}R_{L} + 1)j\omega M}{(R_{S} + j\omega L_{S})(j\omega C_{S}R_{L} + 1) + R_{L}}I_{Lp}$$
(2.93)

$$Z_{in} = \frac{V_p}{I_p} = \frac{R_p + j\omega L_p + \frac{(j\omega C_S R_L + 1)j\omega M}{(R_S + j\omega L_S)(j\omega C_S R_L + 1) + R_L}}{j\omega C_S R_L + 1\left(R_p + j\omega L_p + \frac{(j\omega C_S R_L + 1)j\omega M}{(R_S + j\omega L_S)(j\omega C_S R_L + 1) + R_L}\right)} (2.94)$$

2.9.7.1. Determine Compensation Capacitor

Imag Z_{in} =
$$\frac{\left(\omega L_p - \frac{\omega M^2}{L_2}\right) \left(1 - \omega C_p \left(\omega L_p - \frac{\omega M^2}{L_S}\right)\right) - \omega C_p \left(\frac{M^2 R_L}{L_S^2}\right)^2}{\left(1 - \omega C_p \left(\omega L_p - \frac{\omega M^2}{L_S}\right)\right)^2 - \left(\omega C_p\right)^2 \left(\frac{M^2 R_L}{L_S^2}\right)^2}$$
(2.95)

And setting Imag Zin to Zero we can determine the compensating capacitor Cp thus

$$C_p = \frac{C_S L_S^2 (L_p L_S - M^2)}{(L_p L_S - M^2)^2 + \frac{M^4 R_L^2 C_S}{L_S^2}} (2.96)$$

Studies on PP circuit revealed its high PTE for low impedance loads due to its current regulation characteristics. PP topology is appropriate for high-power applications due to its low significant losses. PP is also good for short range applications.

2.9.8 Summary of WPT Mono resonant topologies

In this section qualities of each WPT topology shall be highlighted. Table 2.2 provides a summary of the various topologies based on their input source ZPA and PTE.

Table 2.2 Summary of Mono resonant WPT topologies.

Topology	Source type	ZPA	PTE	Key Remarks
SS	Behaves as voltage source	ZPA Simplistically achieved independent of R _{Load} . At resonance input looks more resistive.	Highest PTE, especially under coupling variation	Best candidate for FHWPT
SP	Voltage source input	ZPA only occurs at fixed R _{Load} and deviations impact the PTE	PTE drops with load variations	Not stable under variable coupling conditions which FHWPT is designed for
PS	Current source input	Like SP the unity power factor is achieved at fixed R _{Load} .	PTE lower than SS, sensitive to detuning	Not ideal for multichannel Capacitors as required for FHWPT
PP	Current source input	Prone to leave ZPA in changes to k, w or R _{Load} .	Lowest PTE, poor robustness to coupling variation	Poor ZPA robustness under dynamic switching high circulating VA. Not appropriate for FHWPT

Series Compensation circuits provides a steady ZPA condition, high PTE, facilitates a high impedance matching and avoids current spikes due to load or supply changes in the system.

This topology keeps the system stable over a range of frequencies near the resonance and bifurcation. Thus, nominated for the FHWPT. On the other hand, in SP, PS and PP compensation topologies, perturbations can lead to current spikes when the operating frequency deviates from resonance. They are less stable when detuned from the resonant frequency. And susceptible to reactive current fluctuations, which could negatively impact system PTE especially when frequency will be changing. The only topology which guarantees a ZPA under ideal tuning is the SS topology which shall be implemented in the FHWPT system. The SS circuital simplicity also enables incorporation of the additional circuitry for FHWPT.

2.10 Bifurcation

Bifurcation is a nonlinear phenomenon observed in resonantly coupled systems, wherein a perturbation, such as a variation in load, coupling coefficient, or frequency, causes the system's steady-state response to deviate significantly from its original operating point, often resulting in multiple possible solutions or abrupt shifts in behaviour [1],[82],[83].

The perturbation, as statistically recorded in power transmission, is mostly related to load changes in the power distribution system. In WPT systems, perturbations leading to bifurcation often arise from impedance mismatches between the transmitter and receiver circuits, mutual coupling, abrupt switching of load. In all, any of these factors affect can the PTE at the system's original operating frequency and alter its steady-state frequency response.

A common trait of bifurcation in resonant coupled systems is frequency splitting. This can mathematically be expressed as

$$\omega \pm = \omega_0 \sqrt{1 \pm k}$$
 (2.97)

Where ω_0 denotes the nominal operating frequency, and $\omega\pm$ represent the bifurcation induced boundary frequencies. This expression effectively predicts the system's potential to operate at two distinct, symmetrically offset frequencies, determined by the coupling coefficient k.

To evaluate the system's dynamic stability across a range of angular frequencies ω , and determine if the system is operating under bifurcation, a more comprehensive expression namely, Normalised Frequency Response of a Second-Order Resonant System, is typically employed. The magnitude of the frequency response, $|H(\omega)|$ reveals key system behaviours such as mode splitting, energy cancellation or detuning, reduced damping, nonlinear dynamics, and asymmetry in the boundary operating points. These are features that the initial expression alone cannot reveal.

Thus, the formula for the frequency response H(w), of a second order bandpass filter based on a simple RLC series circuit shall be derived from first principles.

For a simple series RLC circuit with a sinusoidal input voltage $V_{\text{in}}(t)$, the differential equation is

$$L\frac{d^{2}i(t)}{dx^{2}} + R\frac{di(t)}{dt} + \frac{1}{c}i(t) = \frac{dV_{in}(t)}{dt}$$
(2.98)

If we excite the circuit with an sinusoidal input voltage of the complex form, $V_{in}(t)=V_0e^{j\omega t} \text{ and the steady-state current response is } I(t)=I_0e^{j\omega t} \text{ we have the circuit's frequency-domain as shown in Fig 2.46 below to be}$

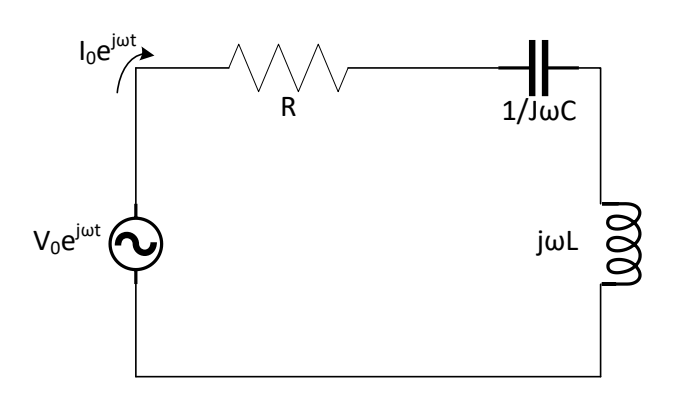


Fig 2.46 Frequency domain RLC circuit

$$I_0 = \frac{V_0}{R + J(\omega L - \frac{1}{\omega C})}$$
 (2.99)

let
$$Z_{RLC} = R + J(\omega L - \frac{1}{\omega C})$$
 (2.100)

$$|Z_{RLC}| = \sqrt{R^2 + \left(\omega L - \frac{1}{\omega c}\right)^2} (2.101)$$

Thus, frequency response is

$$|H(w)| = \frac{I_0}{V_0} = \frac{1}{|Z_{RIC}|} (2.102)$$

To analyse the relative frequency response behaviour of the FHWPT system across a range of operating frequencies (e.g., 79 kHz to 90 kHz), the frequency response $H(\omega)$ is normalised by expressing the impedance terms Z_{RLC} in terms of the damping ratio ζ and the natural frequency ω_0 . This yields a dimensionless form of $H(\omega)$, facilitating comparisons across varying frequencies.

The damping ratio, ζ can be expressed

$$\zeta = \frac{R}{2} \sqrt{\frac{c}{L}} = \frac{R}{2L\omega_0} (2.103)$$

So the real part of $Z_{\it RLC}$, R can be expressed as

$$R = 2\zeta L\omega_0 (2.104)$$

The natural frequency ω_0 is expressed as

$$\omega_0 = \frac{1}{\sqrt{LC}}$$
; $\omega_0^2 = \frac{1}{LC}$ (2.105)

So the imaginary part of Z_{RLC} , $J(\omega L - \frac{1}{\omega C})$ now can be expressed as

$$J\left(\omega L - \frac{1}{\omega C}\right) = jL\left(\omega - \frac{\omega_0^2}{\omega}\right)$$
 (2.106)

To simplify the terms in the bracket we have

$$\omega - \frac{\omega_0^2}{\omega} = \omega_0 \left[\frac{\omega}{\omega_0} - \frac{\omega_0}{\omega} \right] = \omega_0 * \frac{\left(\frac{\omega}{\omega_0} \right)^2 - 1}{\left(\frac{\omega}{\omega_0} \right)}$$
 (2.107)

Thus,

$$|Z_{RLC}| = \sqrt{(2\zeta)^2 L^2 \omega_0^2 + L^2 \omega_0^2 \left[\frac{\left(\frac{\omega}{\omega_0}\right)^2 - 1}{\left(\frac{\omega}{\omega_0}\right)} \right]^2}$$
 (2.108)

Factoring out $L^2\omega_0^{\ 2}$ we have

$$|Z_{RLC}| = L\omega_0 \sqrt{(2\zeta)^2 + \left[\frac{\left(\frac{\omega}{\omega_0}\right)^2 - 1}{\left(\frac{\omega}{\omega_0}\right)}\right]^2}$$
 (2.109)

thus, multiplying through by $\left(\frac{\omega}{\omega_0}\right)^2$ and letting A, the nominalized amplitude equal the constant term $1/L\omega_0$ we have

$$|H(\omega)| = \frac{A}{\sqrt{\left[2\zeta\left(\frac{\omega}{\omega_0}\right)\right]^2 + \left[1 - \left(\frac{\omega}{\omega_0}\right)^2\right]^2}}$$
(2.110)

For a WPT system comprising two magnetically coupled resonant tanks, one at the transmitter and one at the receiver, $|H(\omega)|$ of the system can be expressed as follows

$$|H(\omega)| = \frac{A_1}{\sqrt{\left[1 - \left(\frac{\omega}{\omega_1}\right)^2\right]^2 + \left[2\zeta_1\left(\frac{\omega}{\omega_1}\right)\right]^2}} + \frac{A_2}{\sqrt{\left[1 - \left(\frac{\omega}{\omega_2}\right)^2\right]^2 + \left[2\zeta_2\left(\frac{\omega}{\omega_2}\right)\right]^2}}$$
(2.111)

Where A1, A2, ω_1 , ω_2 , ζ_1 , ζ_2 are the amplitudes, response frequencies and damping factors for the transmitter and receiver modules respectively.

The authors of [82] presented a graph illustrating frequency splitting; however, this was based on the WPT output power expression, also represented in Equation (2.43), which does not inherently exhibit frequency splitting behaviour. In contrast, $H(\omega)$ not only reveals frequency splitting more explicitly but also captures additional traits indicative of bifurcation.

The FHWPT system mitigates bifurcation by dynamically adjusting the operating frequency, thereby avoiding split mode conditions during system perturbations. The impedance detection system in the FHWPT monitors the system impedance. The frequency sensors in the FHWPT can also identify perturbations that may lead to bifurcation. Both sensors provide information for the microcontroller to hop to more stable frequencies at the event of a perturbation. This adaptability helps maintain PTE and resonance alignment even under varying coupling or load conditions. As a result, FHWPT enhances system robustness against nonlinearity induced instabilities. This indicates another solution for the second research question in Section 1.3. In Chapter 3 a worked example of bifurcation based on the developed FHWPT model is presented.

2.11 Frequency Hopping

Frequency Hopping FH, also known as Frequency Hopping Spread Spectrum (FHSS) is a method of transmitting radio signals by rapidly switching among different frequency channels within a broad frequency bandwidth [84]. This is commonly used in secure

communications and various wireless technologies see Fig. 2.47. The development of FHSS rises from the need for reliable, secure, and interference-free communication systems invented by Guglielmo Marconi and Karl Ferdinand Braun in late 19th and early 20th century. In the 1940's during World war II actress Hedy Lamarr and composer George Antheil: invented a FH system for torpedo control signals. Their 1941 patent (U.S. Patent 2,292,387) proposed a piano based system to switch frequencies between transmitter and receiver [85].

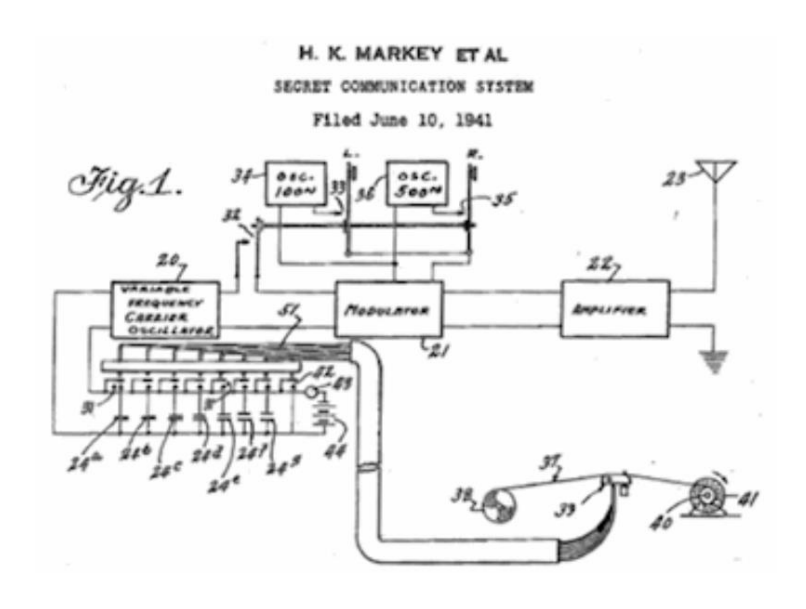


Fig. 2.47 Patent diagram for first FH communication system [86]

In the 1950s and 1960s, FH were utilised in military devices and operations. The Cold War ramped the demand for secure and anti-jamming communication systems, The U.S. military, via agencies like the Defense Advanced Research Projects Agency (DARPA), funded majority of the research in FHSS [87].

In the 70s and 80s FHSS was used for satellite communications and cellular systems. In the 90 and 2000s FHSS was the basic technology in Bluetooth and early Wi-Fi (IEEE 802.11) standards. Bluetooth also uses a form of FH to avoid interference with other wireless devices operating in the 2.4 GHz industrial, scientific, and medical (ISM) band [88]. Although later Wi-Fi standards (e.g., IEEE 802.11b) moved to direct-sequence spread spectrum (DSSS), early implementations relied on FHSS [88]. 5G Networks use FHSS in dense environments [89]

In FHSS, the transmitter and receiver share a hopping pattern that dictates the sequence of channels the signal will hop to during transmission. The data is divided into small packets, each transmitted over different frequencies in rapid succession [90]. A pseudo-random code

or algorithm controls the frequency changes at regular intervals [91]. Other key features of the FHSS are the hop rate and the frequency band width.

In all, the FHSS technique used to enhance communication security by rapidly switching between different frequency channels, as part of this research, is implemented in FHWPT. Also to ensure that the field strength of a WPT at 85kHz does not interfere with adjacent near field wireless devices and communications FHWPT can be implemented as a solution. This also answers the third and fifth research questions in Section 1.3.

2.12 Summary

This literature review covers major aspects of EV charging touching on the history and evolution of the EV and their associated conductive EV chargers. The classification, coil and pad configuration, interoperability, DC - DC converters, IMC, GaNFETs, various mono resonant topologies, bifurcation and FH are all chronicled within this chapter. The literature review shows that many researchers have undertaken extended studies in this field. The research also identifies the gaps in WPT technology that has led to the innovation of FHWPT. Also from this literature review, the research questions have been answered, although more developments on these research questions shall be undertaken in the next Chapters.

The FHWPT technology though is new in the WPT space, is a feasible feature that enhances the WPT operation. In the next Chapter the modelling of the WPT shall be undertaken.

Chapter 3 Mathematical Model of the WPT

3.1 Introduction

The literature review in Chapter 2 covered a broad range of WPT development, circuit theory, bifurcation and the origins of FH. Which strengthened the case for the requirement of a FHWPT.

To systematically investigate and optimise the performance of the FHWPT system, a phased modelling approach is adopted. This commenced in the previous Chapter with the analytical formulation of PTE using the derived equation (2.44). Further investigations into dynamic stability, including the onset of bifurcation under perturbation, was carried out by incorporating the second-order band-pass frequency response, as expressed in equation (2.111). In this Chapter the WPT shall be modelled.

3.1.1 Methodology for WPT modelling

The methodology employed for the modelling of the WPT is based on a progressive framework comprising theoretical, circuit-based, and finite element approaches, as illustrated in Fig. 3.1.

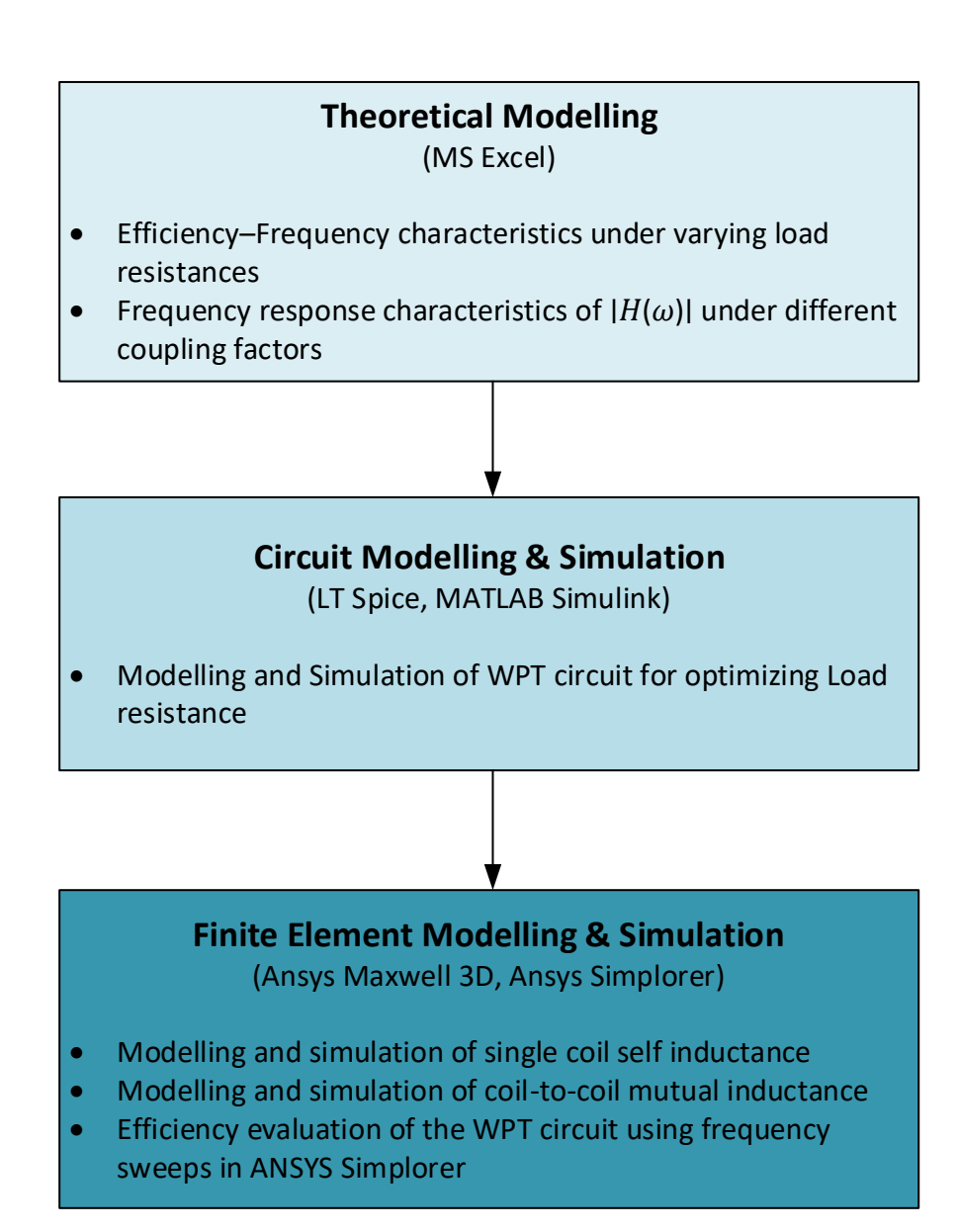


Fig. 3.1 Flow chart ilustrating methodology of WPT modelling

The FHWPT theoretical model is developed in Microsoft Excel to determine the variations in operating frequency, coupling coefficient, and load resistance, with respect to PTE and transfer function. The results from the Microsoft Excel's circuit study is then validated using LT SPICE IV and MATLAB Simulink. The modelled WPT circuit is implemented in Ansys for finite element analysis. This multi-stage methodology ensures analytical rigour, empirical validation, and readiness for hardware implementation.

3.2 WPT theoretical model undertaken in MS Excel

This section presents the theoretical model developed in Microsoft Excel, two main analyses were undertaken. The first examines the frequency response characteristics of $|H(\omega)|$ under varying coupling coefficients (k), while the second evaluates the PTE - frequency characteristics across different load resistances.

3.2.1 Frequency response characteristics of $|H(\omega)|$ under different k, coupling coefficients.

The derivations of the frequency response $|H(\omega)|$ presented in Chapter 2 provide the foundation for a study of the FHWPT, which is conducted using the circuit parameters introduced in the subsequent chapters i.e. , $L_p=L_s=47uH$, $C_p=C_s=94.6nF$, $R_p=R_s=0.6\Omega$, $R_L=2.47\Omega$, $\omega=2\pi f$, f=85kHz, k=0.2. We can compute the forecasted ω_1 and ω_2 splitting frequency at 85kHz using the formula.

The expression in equation (2.97) yields the bifurcation bandwidth boundary frequencies, where ω — or ω_1 is approximately 76 kHz and ω + or ω_2 is approximately 93 kHz. These frequency values are then substituted into the frequency response function $|H(\omega)|$, in equation (2.111) which is used to generate the plot shown in Fig. 3.2. In Fig. 3.2 the two peaks correspond to the split resonances ω_1 and ω_2 due to strong coupling. The valley between them corresponds to the destabilised original resonant frequency ω_0 .

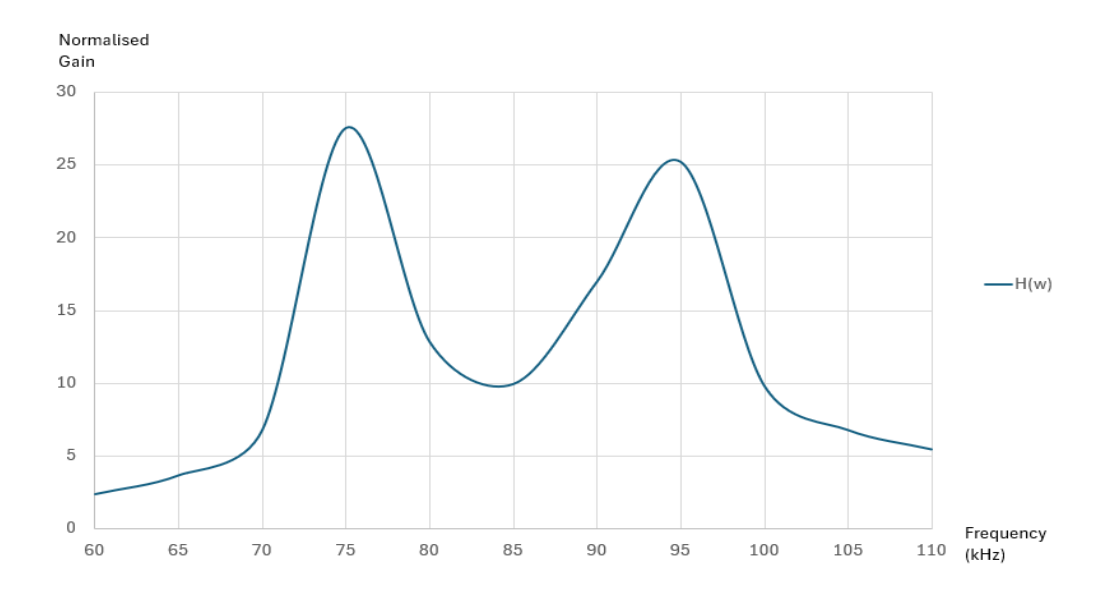


Fig 3.2 Frequency response of WPT with a k = 0.2

A similar plot for the frequency response is undertaken for the FHWPT for k = 0.4. The graph in Fig. 3.3 shows obvious traits of bifurcation, two well-separated resonance peaks around 65kHz and 100kHz with a significant dip between. This is an indicator of mode splitting due to strong coupling. Also, the asymmetry of the peaks suggests Load or Coupling Imbalance which could be due to a non-ideal load, unequal damping, or asymmetric coupling between the transmitter and receiver.

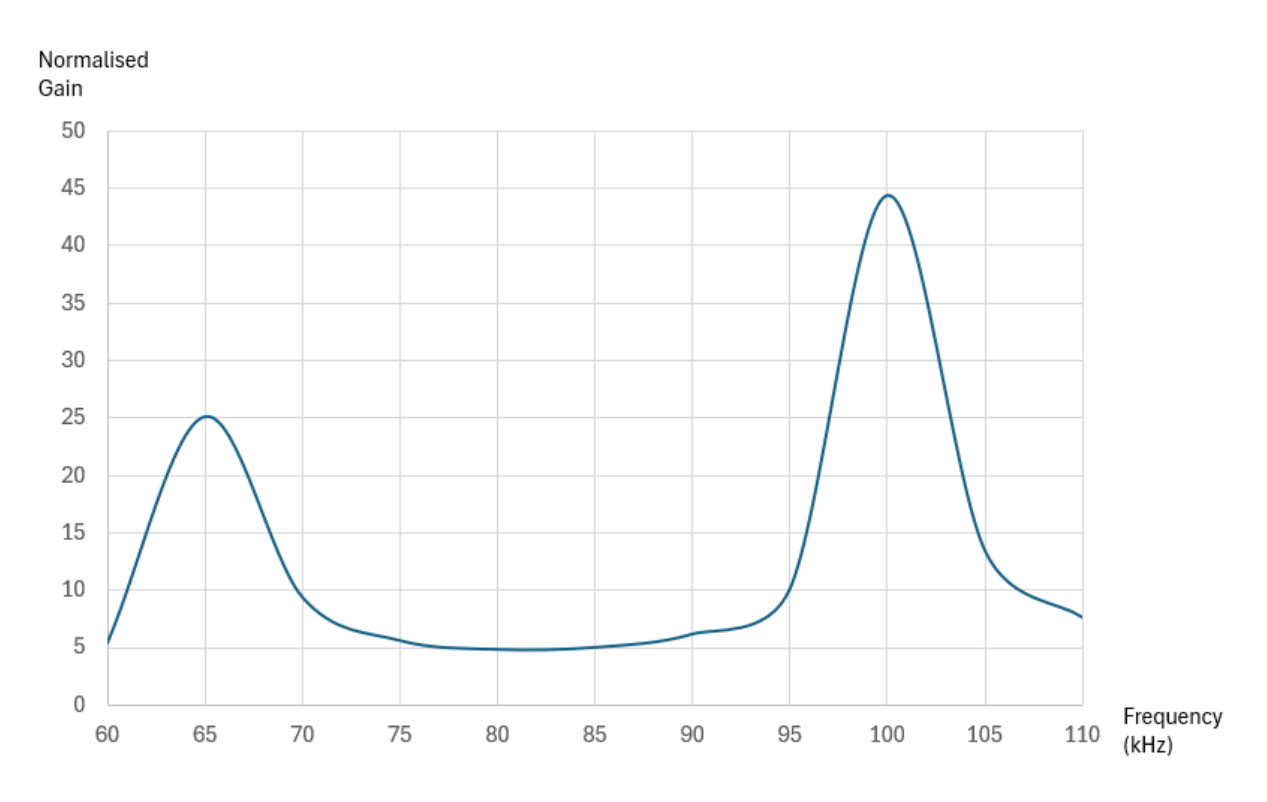


Fig 3.3 Frequency response of WPT with a k = 0.4

The findings of this study guided the selection of a coupling coefficient k = 0.2 for the design of the FHWPT. In addition, the FHWPT is designed to track both impedance and frequency, thereby mitigating bifurcation in the presence of system perturbations.

3.2.2 PTE – Frequency characteristics under varying load resistances

A frequency sweep to determine the efficiencies of different load impedances based on the mathematical model was undertaken. From the results it was evident that on the mathematical model at 250kHz, the PTE for a 5Ω and 10Ω impedance was above 90%. Also, the PTE for a $40m\Omega$ impedance which is almost the same impedance of an EV battery, at 85kHz was about 28% see Fig 3.4 below.

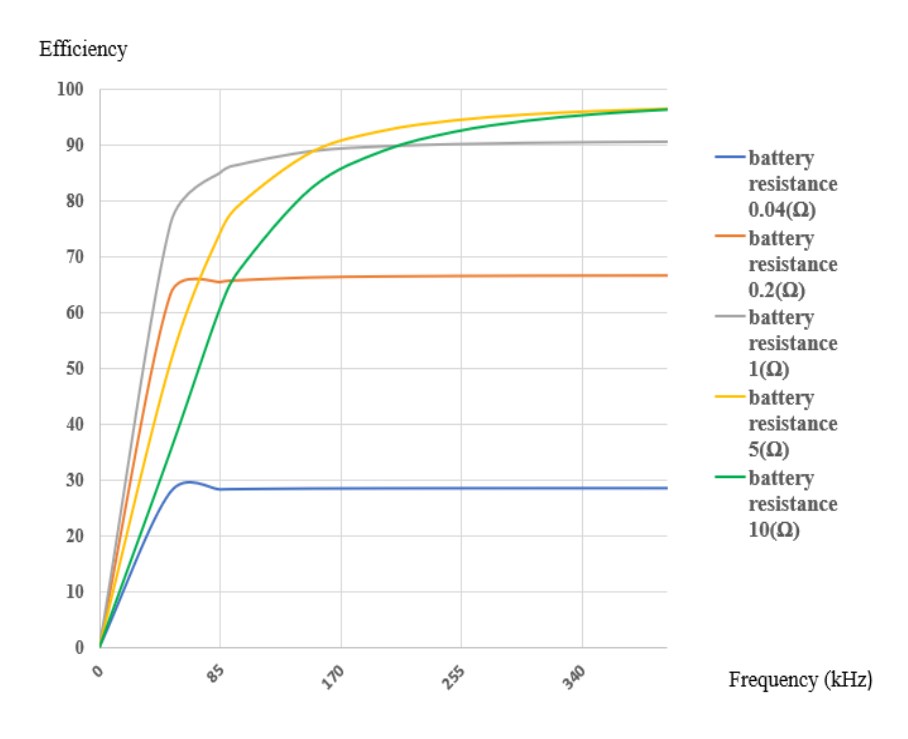


Fig. 3.4 PTE of various EV battery internal resistances between 0 and 400kHz

This result gave rise to the concept for an initial FHWPT design to operate at two frequencies (85kHz and 250kHz) [84]. The upper frequency 250kHz, which is outside the SAE standard, was chosen because of the PTE at 93%. However, the FHWPT the operating frequencies are within the SAE recommended bandwidth.

While the load resistance of 10Ω exceeds the EV battery's internal resistance of $40m\Omega$, the buck converter in the receiver can emulate this impedance. Also, the authors in [92] used a 20Ω load in their research.

3.3 WPT theoretical model undertaken in LT SPICE and MATLAB Simulink

In this section the theoretical models are developed in a computer software dedicated to circuit simulation to validate the theoretical results. Here the SS WPT was developed with the aim to identify the optimal load resistance.

3.3.1 Simulation results of a SS WPT circuit

A simulation of the SS WPT was undertaken to validate the PTE's formula. The parameters of the circuit thus, $V_p=14.14V_{pk}$ $L_p=L_s=1.136uH$, $C_p=C_s=3.086uF$, $R_p=R_s=0.1\Omega$, $R_L=1.5\Omega$, $\omega=2\pi f$, f=85kHz, k=0.2, M=0.2272uH the simulation was undertaken

on MATLAB's Simulink R2023a with a time step of 1μ s and a stop time of 10s. The results of the simulation are presented in Fig. 3.5 below.

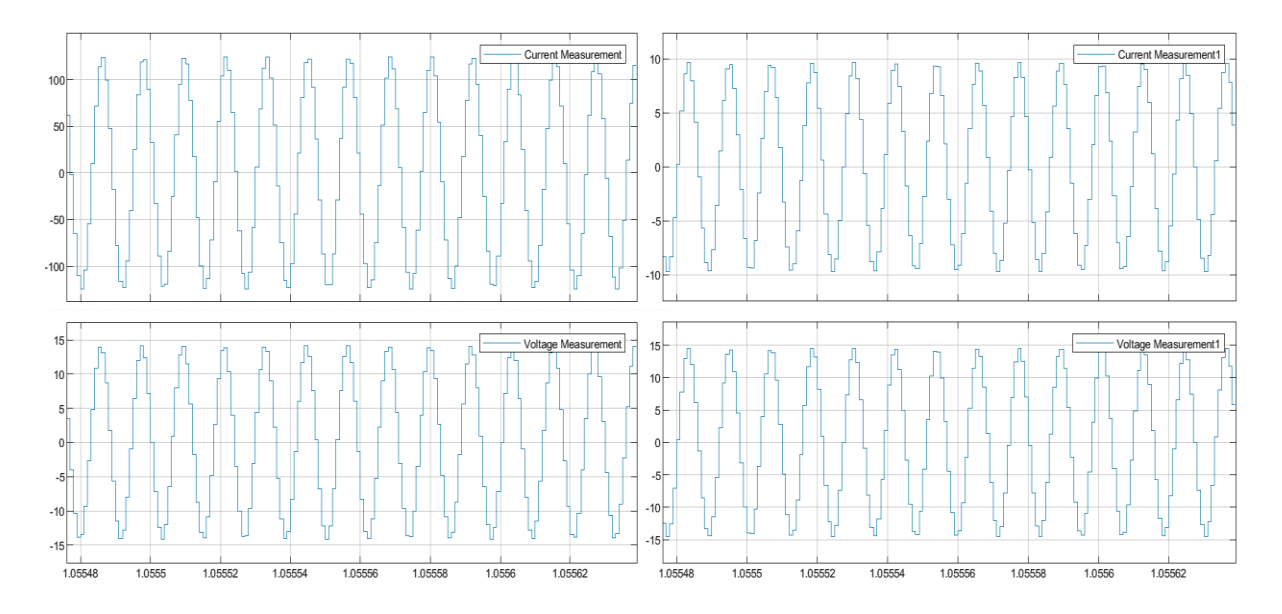


Fig. 3.5 simulation of SS WPT input left hand side (LHS) and output right hand side (RHS) voltage and current

The traces on the LHS and RHS indicate the input current and voltage i_p and V_p and the output current and voltage i_s and V_s respectively. From the graph we can calculate PTE, η as shown below

$$\eta = \frac{P_{out}}{P_{in}} = \frac{140W}{1759W} = 0.0759 (3.1)$$

From the results the PTE is approximately 8%. The PTE can be optimised by proper impedance matching intervention as shown in equations (2.48) and (2.49). Implanting this we can determine that the new $R_L = 0.504\Omega$. Inserting this value in the simulation we have the results presented in Fig. 3.6 below.

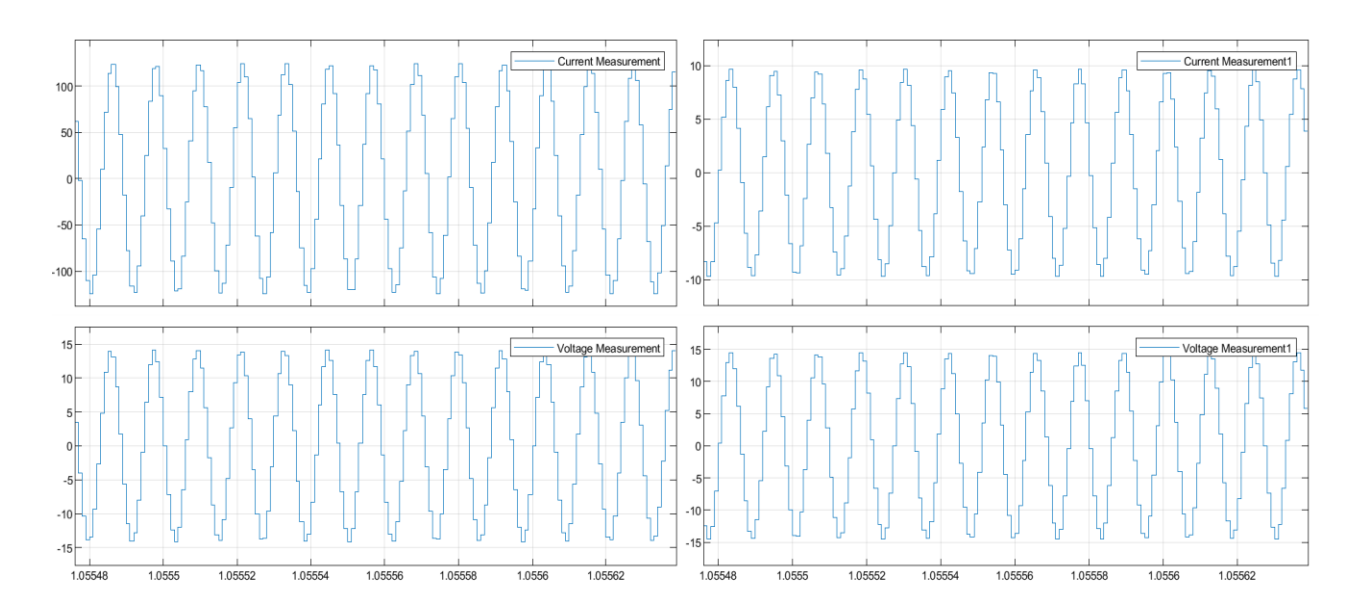


Fig. 3.6 simulation of SS WPT input LHS and output RHS voltage and current using optimum $$R_{\mbox{\scriptsize L}}$$

$$\eta = \frac{P_{out}}{P_{in}} = \frac{256.7W}{1552.6W} = 0.1653$$
 (3.2)

The new PTE is approximately 17%. It is evident that the initial inductance of 1.136uH is too low thus we can compute an optimal inductance by forecasting $\eta=0.9$. Where k=0.2, Q can be computed as 94.87. Using $R_p=R_s=0.1\Omega$, $\omega=2\pi f$, f=85kHz, $C_p=C_s=C_{max\eta}=197.4nF$. The new $L_p=L_s=L_{max\eta}$ can be computed as 17.76uH from (2.44). From these values the original WPT circuit was remodelled and simulated the results are shown in Fig 3.7 below.

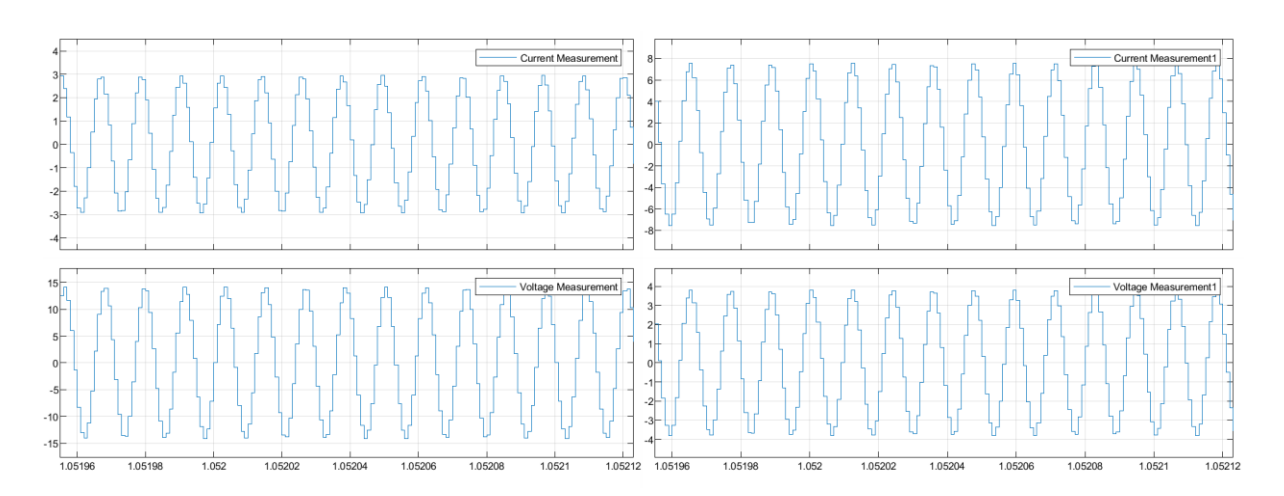


Fig. 3.7 simulation of SS WPT input LHS and output RHS voltage and current of computed $maximum\ Cmax\eta,\ Lmax\eta\quad and\ optimum\ R_L$

$$\eta = \frac{P_{out}}{P_{in}} = \frac{32W}{42W} = 0.762 \quad (3.3)$$

The new PTE is approximately 76%, whereas EV WPT systems typically achieve efficiencies above 90% [93]. Further modifications required to optimise PTE will be discussed in Section 5.9.1. Nonetheless, implementing the optimal resistance formula has significantly improved the WPT circuit design parameters, raising the PTE from 8% to 76%. Initial circuit simulations were performed in LT SPICE IV however, due to limitations in producing readable graphical outputs, the subsequent studies were carried out in MATLAB Simulink.

3.4 Finite Element Methods and Maxwell equations

The WPT design was now finally modelled in the Finite Element Analysis software. Finite Element Method (FEM) like Digital Signal Processing (DSP) is an engineering tool used for modelling a physical body to determine approximate solutions when the body is subjected to various conditions.

Partial Differential Equations or System of Linear equations are carried out on an iterative process on the subdivided parts (mesh) of the particular modelled physical body.

The converged results of each mesh's iteration are then processed in a matrix and the final solution provides the model of the approximate representation of the given condition. FEM modelling is important in WPT design for the following major reasons

- Model Coils and determine the self inductance, magnetic flux paths and magnetic strength region
- 2. Provide simulated results of the Coupling Coefficient and Mutual inductance between transmitter and receiver coils at given distance(s)
- 3. Provide simulated results of the PTE between transmitter and receiver coils
- 4. Model the losses or Eddy current of coils at various frequencies to determine heat losses

It is also a numerical technique used to solve the Maxwell differential equations. Maxwell equations are continuous partial differential equations. The FEM discretises or approximates the model to small elements called meshes converting the PDE to linear algebraic equations [94]. Each mesh can be solved individually approximating the field characteristics in that

region. Following that, Boundary Conditions are applied to ensure the element's solution adheres to the physical constrains e.g. if plant is in a confined space like transformer windings or in open space e.g. antenna [95]. Then the field variables e.g B, E, H, A, V are approximated at discrete points e.g. small volumetric regions in space, wires nodes or terminals of a winding. For instance, the infinitesimal segment of the Ampere loop dl of Ampers law closed loop, is converted to a discrete numerical value Δl such that the differential equation is converted to a numeric, discrete value as shown in equation (3.4) below

$$\oint H \cdot dI = I_{enclosed} \approx \sum H \cdot \Delta I \approx I_{enclosed}$$
 (3.4)

Finally, the solution is represented in a matrix equation where each row represents a relationship at a node in terms of the electromagnetic field and element properties e.g permittivity, ϵ and permeability, μ .

For example, discretising Faradays Law

$$\nabla \times E = -\frac{\partial B}{\partial t}$$
 (3.5)

assuming working in 1 dimensional form **E** is define as E(x,t) and B as B(x,t) the equation now becomes

$$\frac{\partial E}{\partial x} = -\frac{\partial B}{\partial t}$$
 (3.6)

We can let $x=x_i=i\Delta x$ where i is the spatial index and Δx is the space between spatial points. And $t=t_n=n\Delta t$ where n is the time index and Δt is the time step. Thus, discretising both spatial and time derivatives $\frac{\partial E}{\partial x}$ and $\frac{\partial B}{\partial t}$ we use finite differences at point (i,n) as

$$\frac{\partial E}{\partial x} \approx \frac{E_{i+1}^n - E_i^n}{\Delta x}$$
 and $\frac{\partial B}{\partial t} \approx \frac{B_i^{n+1} - B_i^n}{\Delta t}$ (3.7)

So rearranging we have

$$\frac{E_{i+1}^n - E_i^n}{\Delta x} = \frac{B_i^{n+1} - B_i^n}{\Delta t}$$

To solve for **B** we can rearrange the formula

Thus,
$$B_i^{n+1} = B_i^n \frac{\Delta x}{\Delta t} (E_{i+1}^n - E_1^n)$$
 (3.8)

These meshes are computerised for every spatial and time indices to provide the matrix PDE matrix equation. The solutions from FEM are generally reliable based on the rigorous iterations of PDEs undertaken for every model. This model usually takes a lot of time up to 18 hours based on the model and does take up a lot of computing memory and storage. For the studies undertaken it took over 20 hours to complete the simulation and up to 10GB memory capacity.

3.5 Design of WPT Coil on Ansys software

The transmitter and receiver coils were modelled in Ansys Maxwell 3D to translate the theoretical and circuit-level parameters into physical geometries. This enabled evaluation of inductance, coupling, and flux distribution, forming the basis for optimising coil performance under spatial and PTE constraints

3.5.1 Coil configuration

A spiral coil of 2mm diameter, 40 turns, 20mm inner diameter 0.1mm turn spacing outer diameter of 188mm and total length wire of 13.07m was modelled on Ansys as shown in Fig. 3.8.

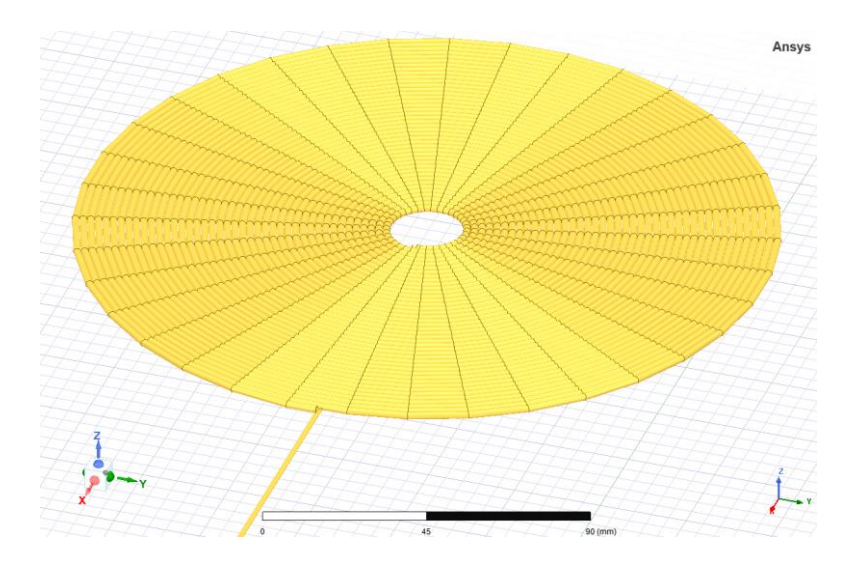


Fig. 3.8 WPT transmitter coil

For the simulation, the coil was excited with a current of 1A the simulation results showed a self-inductance of $137.4\mu H$ as presented in Fig. 3.9 below.

L Table 1 Maxwell3DDesign1 Ansys

i [A]	Matrix1.L(Rx_in,Rx_in) [uH]	Matrix1.L(Rx_in,Rx_in) [uH]	Matrix1.L(Tx_in,Rx_in) [uH]	Matrix1.L(Tx_in,Rx_in) [uH]
	Setup1 : LastAdaptive	Setup1 : LastAdaptive	Setup1 : LastAdaptive	Setup1 : LastAdaptive
	dist='-120mm'	dist='180mm'	dist='-120mm'	dist='180mm'
1 1.00000	0 137.406513	137.406513	2.757486	2.757486

Fig. 3.9 Ansys result Table showing excitation current of 1A, self inductance of 137.4μH

A pair of coils were modelled to represent the transmitter and receiver coils with the same parameters, as shown in Fig. 3.10. The coils are arranged coaxially with an air gap of 180mm along the Z-axis, highlighting their geometry and spatial orientation. This configuration enables the evaluation of mutual inductance and coupling coefficients, which are critical parameters for characterising WPT system performance.

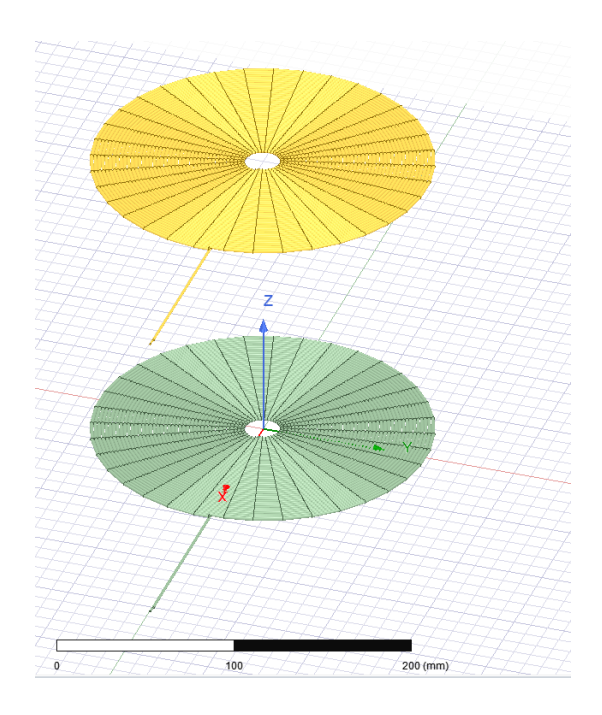


Fig. 3.10 WPT transmitter and receiver coils with air gap of 180mm

The results from this simulation shows a mutual inductance of $2.75\mu H$ at 180mm air gap between transmitter and receiver coils as presented in Fig. 3.11.

Coupling Coeff Table 1

	i [A]	Matrix1.CplCoef(Rx_in,Rx_in) Setup1:LastAdaptive dist='-120mm'	Matrix1.CplCoef(Rx_in,Rx_in) Setup1 : LastAdaptive dist='180mm'	Matrix1.CplCoef(Tx_in,Rx_in) Setup1 : LastAdaptive dist='-120mm'	Matrix1.CplCoef(Tx_in,Rx_in) Setup1: LastAdaptive dist='180mm'
1	1.000000	1.000000	1.000000	0.019691	0.019691

Fig. 3.11 Ansys result Table showing excitation current of 1A, coupling coefficient of 0.019 at 180mm air gap between transmitter and receiver coils.

Utilizing transmitter and receiver coils of 137.4µH at 180mm air gap a frequency sweep from 85kHz to 400kHz was simulated on Ansys Simplorer, a multi domain software where electronics and multi physics circuits can be modelled and simulated see Fig 3.12. The Ansys Simplorer software tool was implemented to determine if operating frequencies higher than 85kHz will show an improved PTE and presented in the mathematical model.

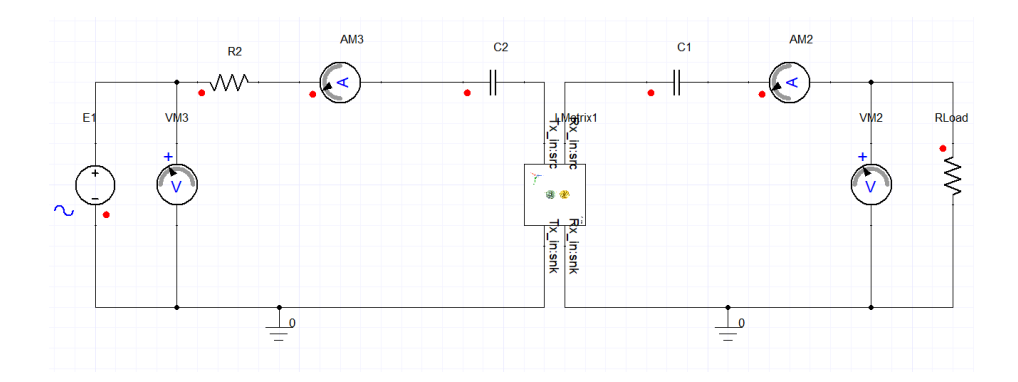


Fig. 3.12 simulated 137.4µH 180mm air gap WPT circuit on Simplorer

A circuit was built in Simplorer with an original operating frequency (OpF) of 85 kHz, which was parameterised to vary (e.g., 100 kHz, 150 kHz, etc.) for conducting frequency sweeps to evaluate PTE. The parasitic resistance, R2 was 0.1Ω , R_{Load} was 10Ω , the self inductances, for the transmitter and receiver coils were 137.4 μ H, mutual inductance M and coupling coefficient k, from Fig 3.11, 2.76 μ H, 0.019 respectively. The capacitance values C2 and C3, expressed as functions of frequency, were calculated in Ansys using the governing formula in equation (3.9) An operating voltage of 1V was used. VM1, AM1, VM2, AM2 were the voltmeters and ammeters in the transmitter and receiver sides.

$$C = \frac{1}{4*\pi^2*OvF^2*Ltx}$$
 (3.9)

The graphs in Fig. 3.13 to Fig. 3.20 present the results of the frequency sweep, where Fig. 3.13 indicates a PTE of 44.3% at the 85kHz operating frequency, while Fig. 3.17 shows an improved PTE of 70.19% at about 250kHz.

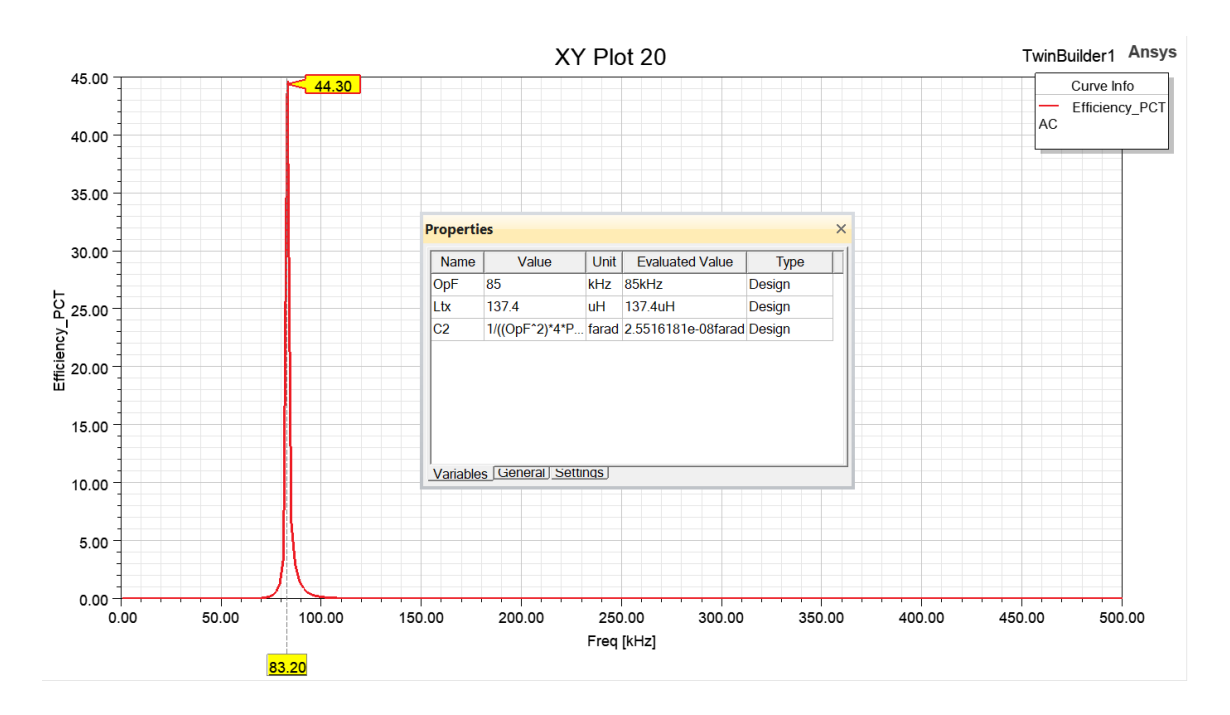


Fig. 3.13 PTE of 44.3% at 83.2kHz

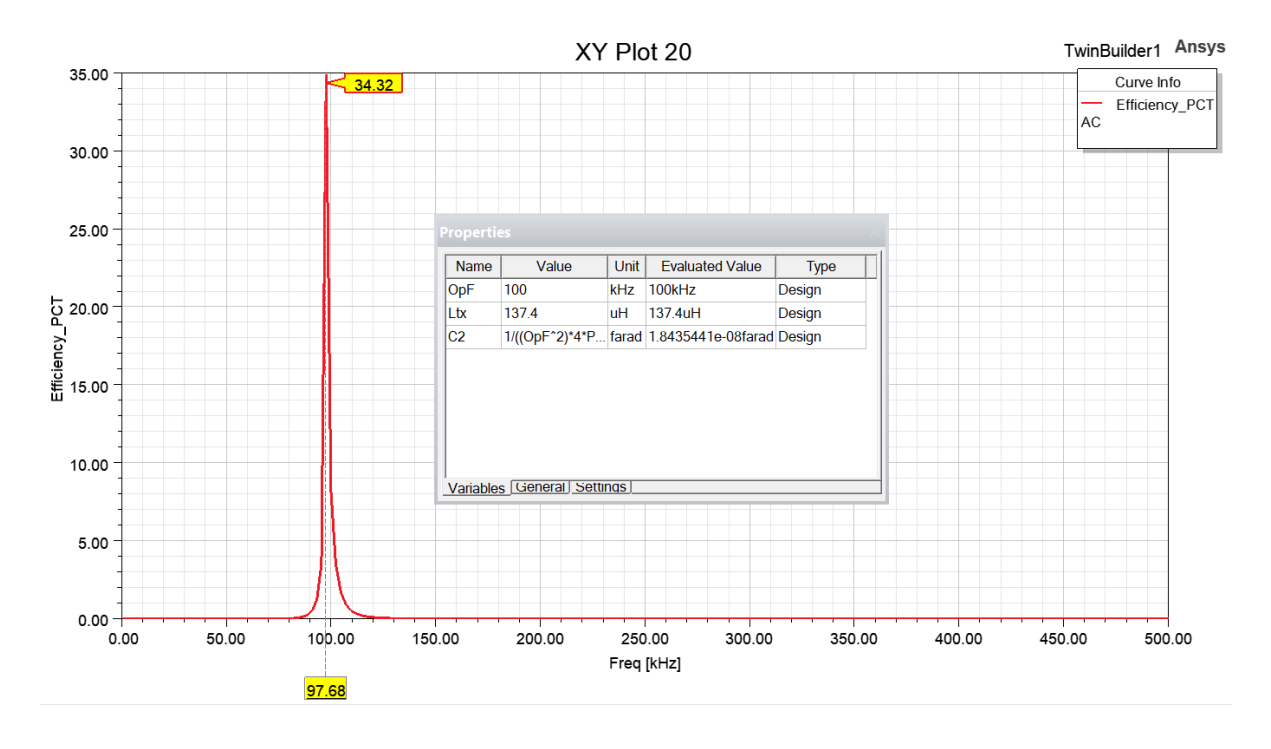


Fig. 3.14 PTE of 34.32% at 97.68kHz

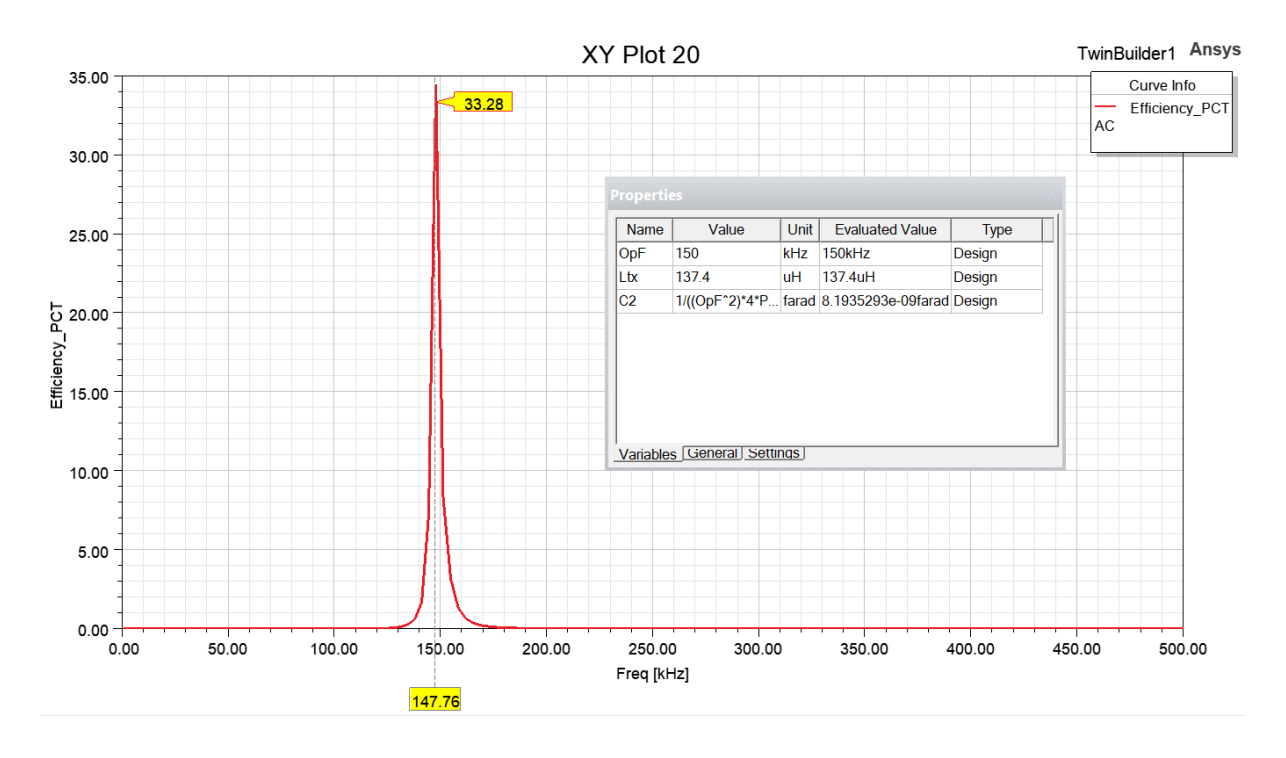


Fig. 3.15 PTE of 33.2% at 147.76

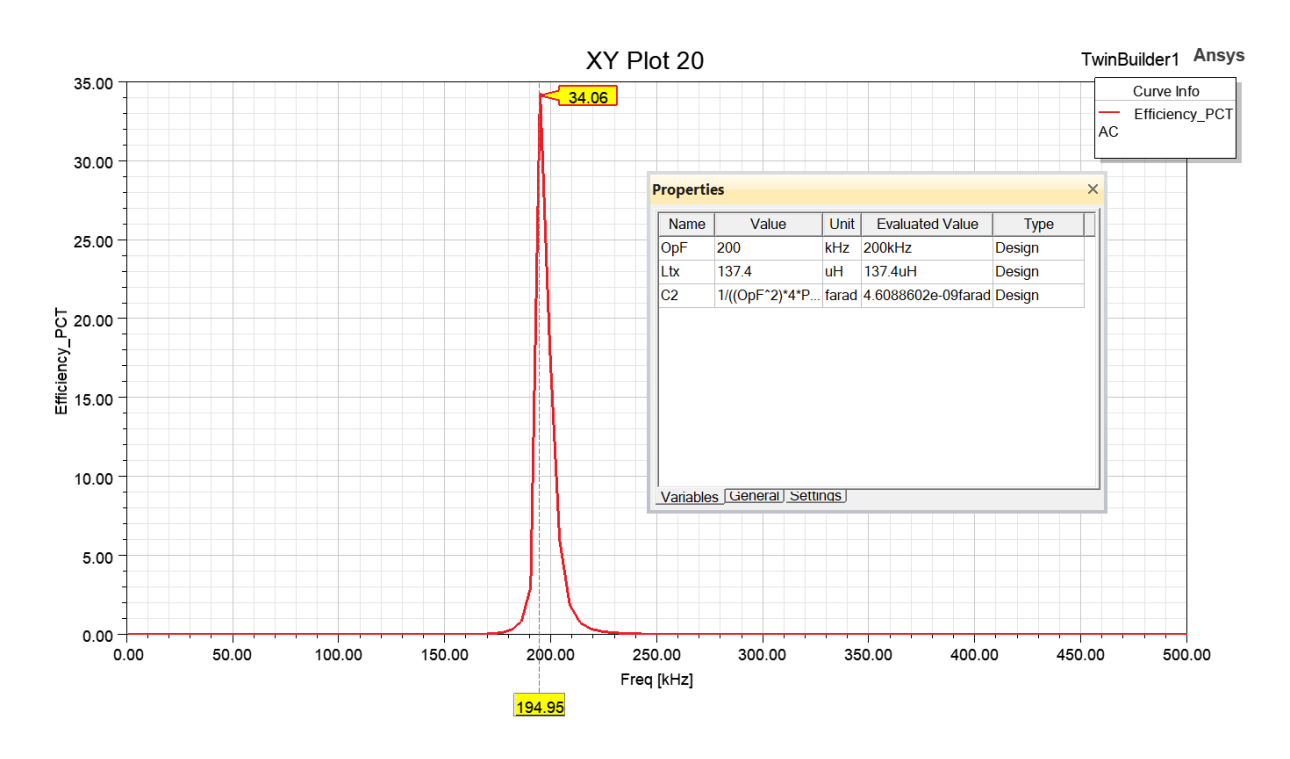


Fig. 3.16 PTE of 34.07% at 194.95kHz

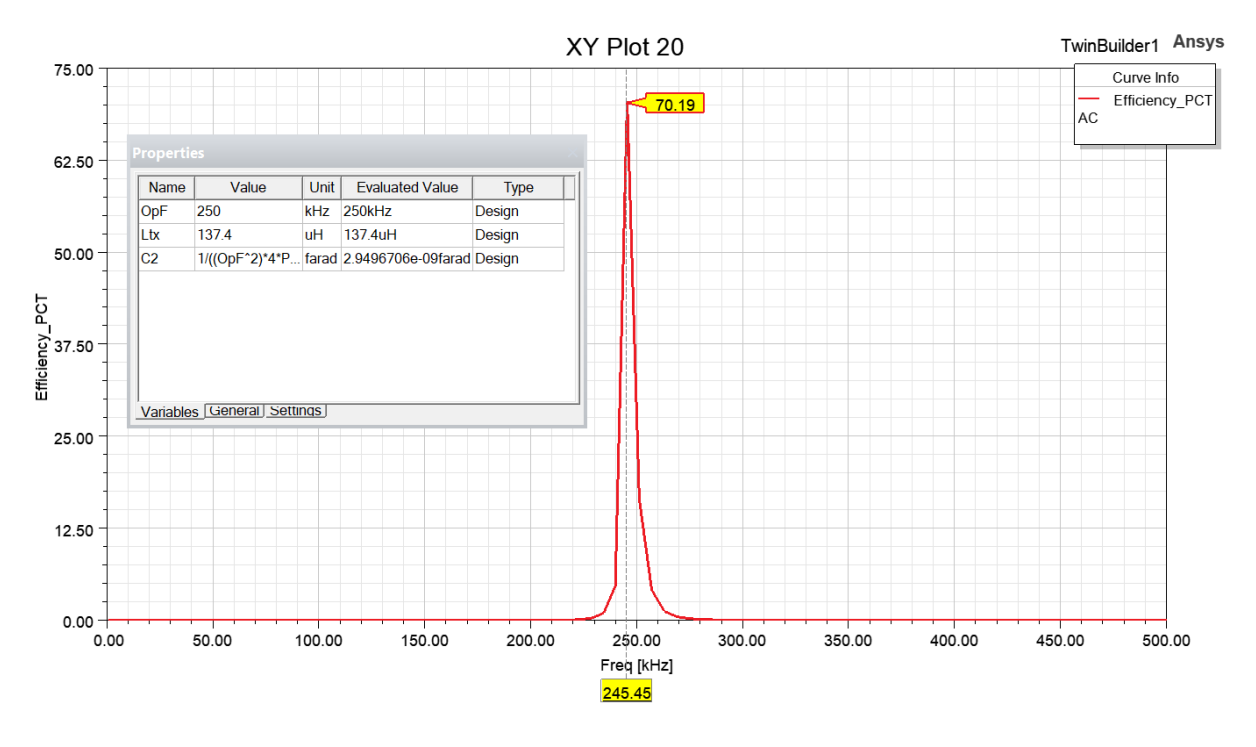


Fig. 3.17 PTE of 70.19% at 245.45kHz

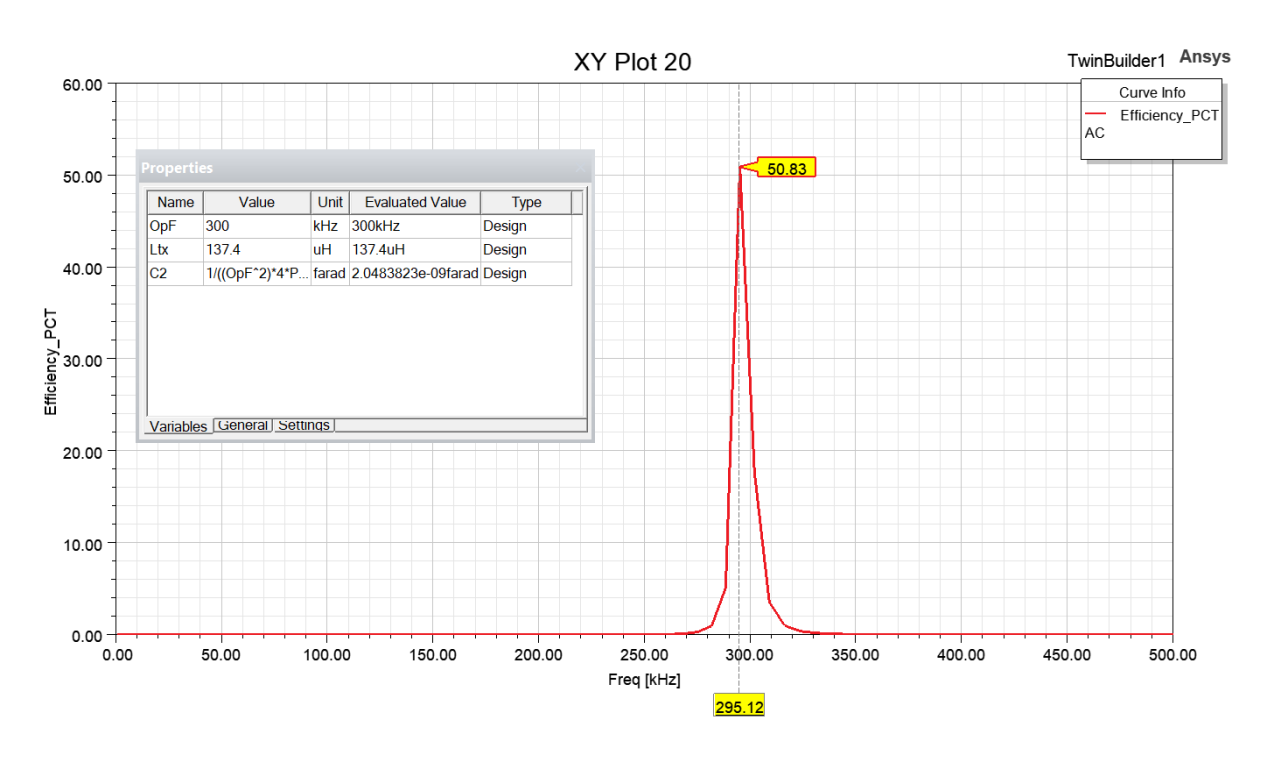


Fig. 3.18 PTE of 50.83% at 295.12kHz

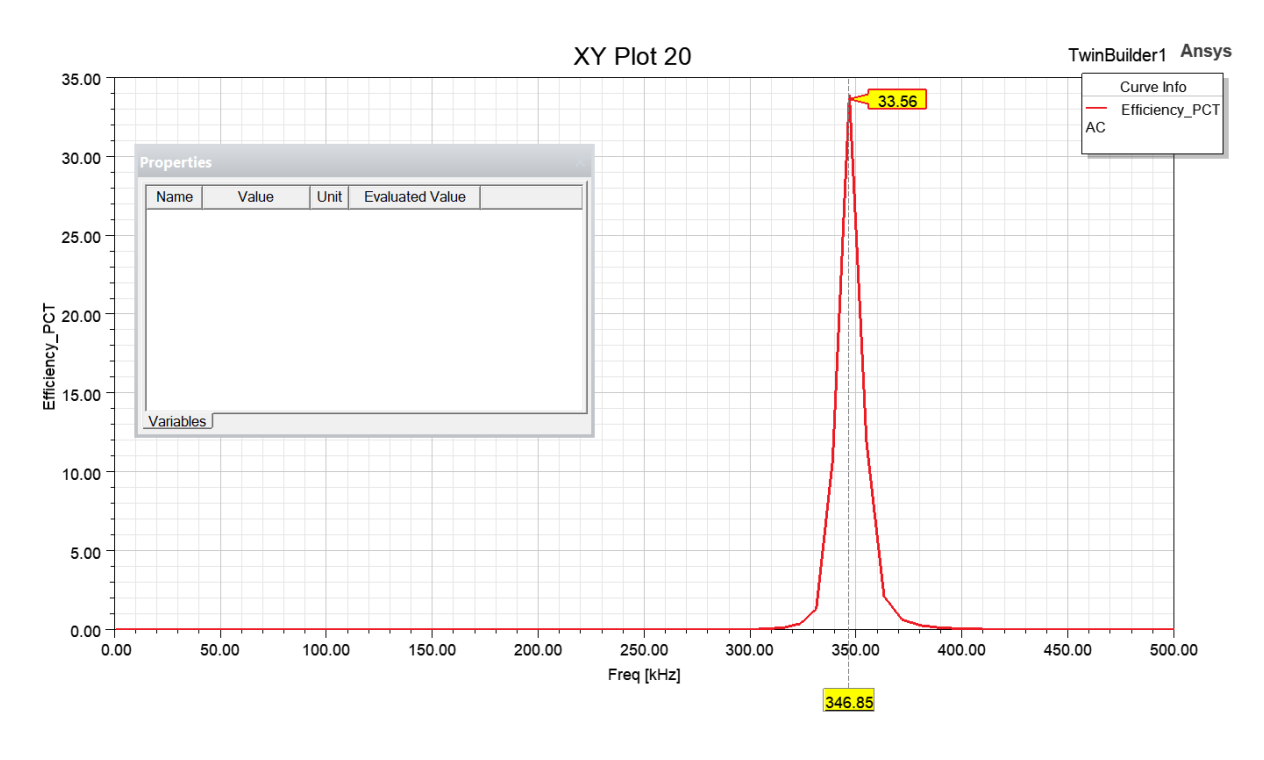


Fig. 3.19 PTE of 33.56% at 346.85kHz

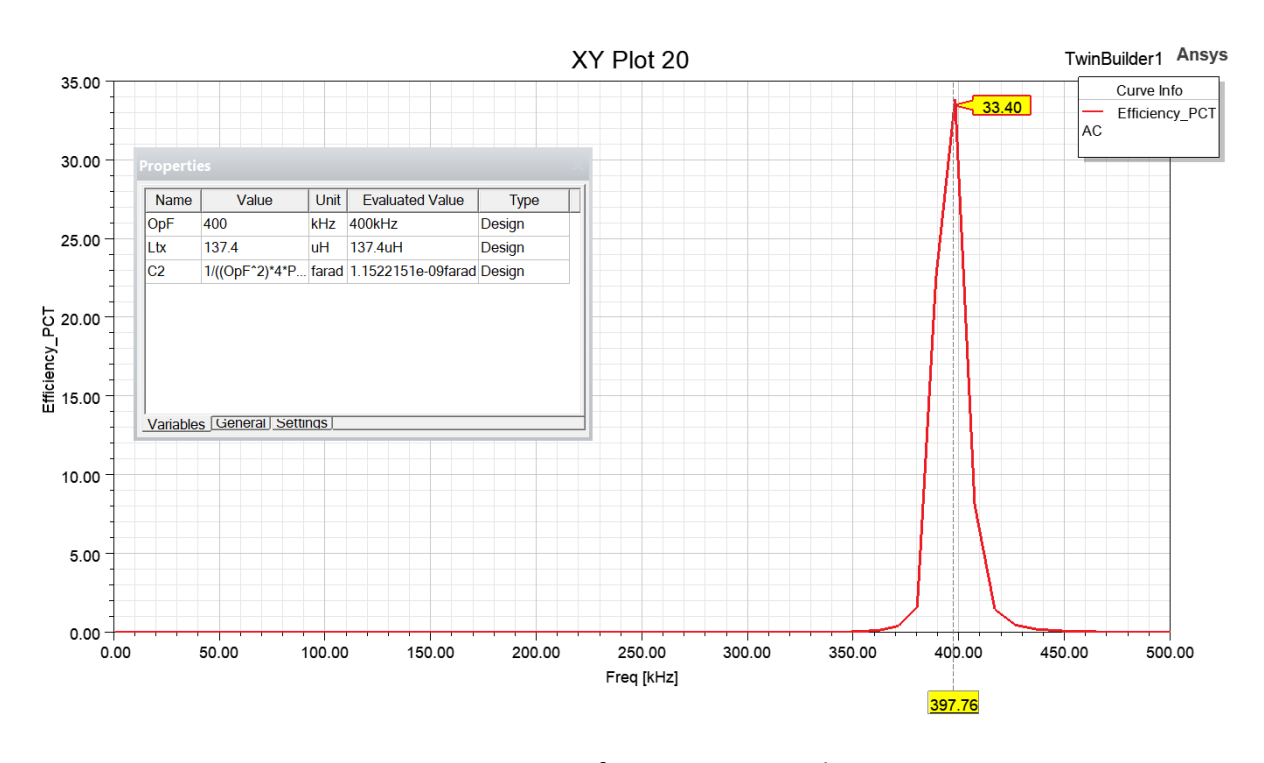


Fig. 3.20 PTE of 33.4% at 397.76kHz

3.5.2 Results

Fig. 3.21 compares the PTE from the mathematical model and Ansys simulations. The mathematical model shows a smooth monotonic rise towards saturation, whereas the Ansys results remain relatively flat up to 200 kHz, peak at 250 kHz, and then decline. This illustrates

the complementary role of mathematical modelling for theoretical prediction and FEM simulations for capturing practical non-idealities in WPT design.

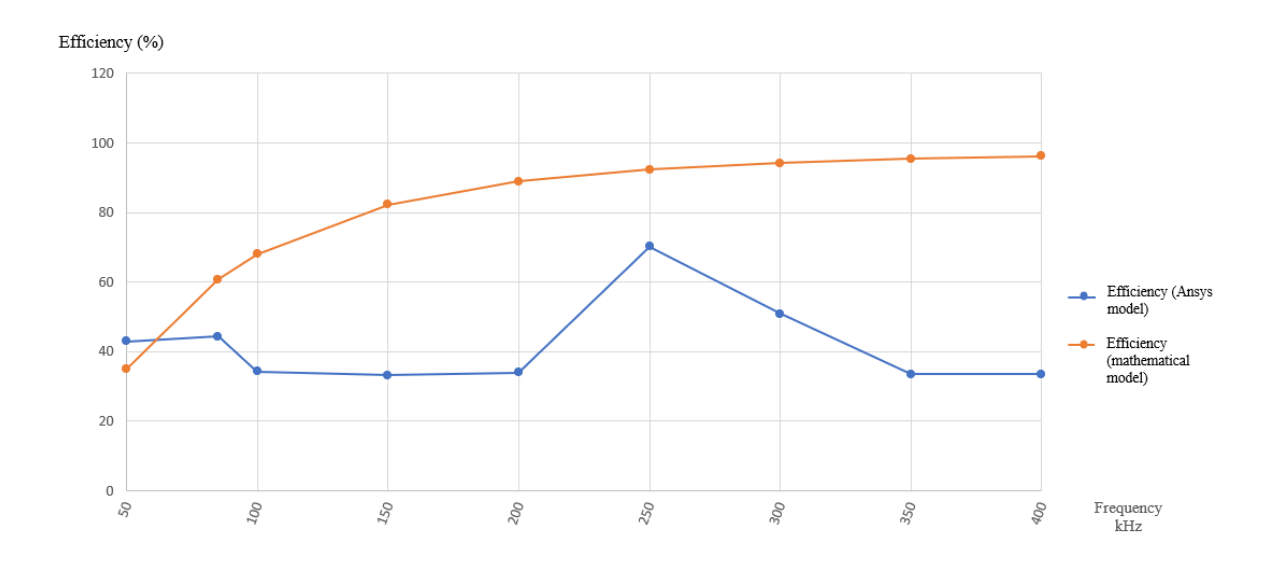


Fig. 3.21 Trend of Ansys and mathematical model's PTE - Operating frequency sweep for a 10Ω impedance load

3.6 Summary

In this section the WPT model was developed through a phased approach, progressively refining simulations using MS Excel, LT Spice, MATLAB Simulink, and Ansys Maxwell 3D. The SS WPT circuit simulations, progressively optimised through impedance matching and adjustment of inductance and load resistance values, demonstrated an PTE improvement from 8% to 76%, with further enhancements to be discussed in Chapter 5. The fundamentals of the FEM were analysed as a numerical technique for solving Maxwell's equations, providing the basis for modelling coil inductance, coupling, PTE, and losses in the WPT design.

The Ansys frequency sweeps reveal a near linear increase in PTE between 85kHz and 250kHz for a 10Ω load, which motivated the adoption of a dual-frequency design. Although not within the scope of this study, it is noted that the FHWPT could present a virtual load

impedance through the receiver buck converter to align the load resistance with its optimal value, as discussed in Section 3.2.2 and in the concluding chapter.

Maxwell's equations framed the electromagnetic behaviour, and finite element modelling in Ansys enabled precise calculations of coil self-inductance, coil to coil mutual inductance, and its associated coupling coefficient. The final model, using a spiral coil configuration, achieved a self-inductance of 137.4µH. This incremental process highlighted the importance of multi-frequency operation and modelling accuracy in optimizing WPT for high PTE applications.

The subsequent Chapter presents the detailed design of the FHWPT system.

Chapter 4 Design of Frequency Hopping Wireless Power Transfer System

4.1 Introduction

In the previous chapter, the mathematical and computer aided models of the WPT system were developed and simulated. Building on these foundations, this chapter details the design of the FHWPT, with the main software packages used being Altium Designer for schematic and PCB development, and Arduino software for microcontroller programming.

4.1.1 Methodology of FHWPT Design

The methodology for the FHWPT design follows a structured sequence beginning with the description of the adaptive frequency hopping control algorithm. After which the configuration of the transmitter module, followed by the selection of coils suitable for high frequency power delivery. Then the development of the FBC's voltage and current sensors are developed in line with the microcontroller specifications to ensure compatibility.

The microcontroller coding for mainly the PWM control and impedance tracking are developed alongside the formulation of each module's sub circuit. FH circuitry and the associated microcontroller's instruction set are subsequently implemented. Following that, the design of the receiver module and its sub circuits, together with transmitter receiver communication microcontroller instruction set are developed.

The workflow continues with the PCB design for each module. Concluding with the evaluation of transmitter, receiver and their associated FBC's positioning follows after that.

The flow diagram in Fig. 4.1 below shows the steps on how the design work was undertaken.

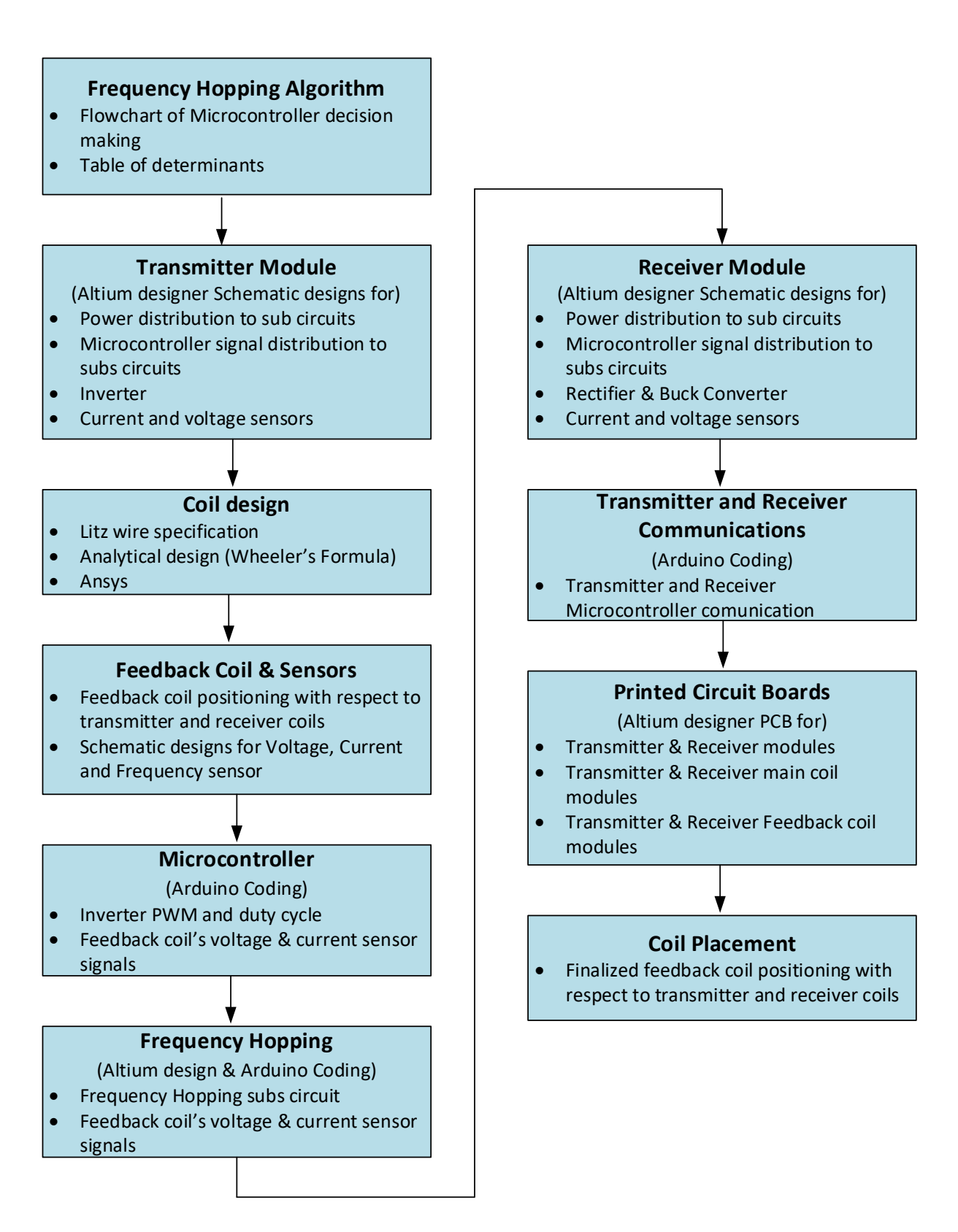


Fig. 4.1 Development Methodology of the FHWPT

4.2 Adaptive Frequency-Hopping Control for EV Wireless Charging

The operation of the FHWPT goes thus, the transmitter initializes the session at the default operating frequency of 85kHz if no EV is detected or the receiver's operating frequency is not within the authorised set, microcontroller notifies the user and returns the system to standby else, the session proceeds to charge.

As charging commences the system is checked for misalignment on the event of a misalignment the session is terminated, returns to standby and the user is notified.

Concurrently, the radio frequency (RF) within the charging envelope is monitored for interference. When interference is identified, the microcontroller characterizes the RF profile and executes a FH routine within the authorised 79 to 90kHz band. Charging resumes on the next unaffected channel, if all twelve channels are affected, both the user and local security are notified of a broad band interference event and the system returns to standby.

Output power is also monitored continuously against the preset threshold. If demand exceeds this limit, and the EV's battery RoC is low, then there is a possible power theft. Thus, the microcontroller stops the session, notifies the user, and returns to standby else, the session continues.

Finally, once the battery $SoC \ge 97\%$ the session is completed and goes to Standby. The flow chart in Fig 4.2 illustrates how the microcontroller sequences instructions during a charging session.

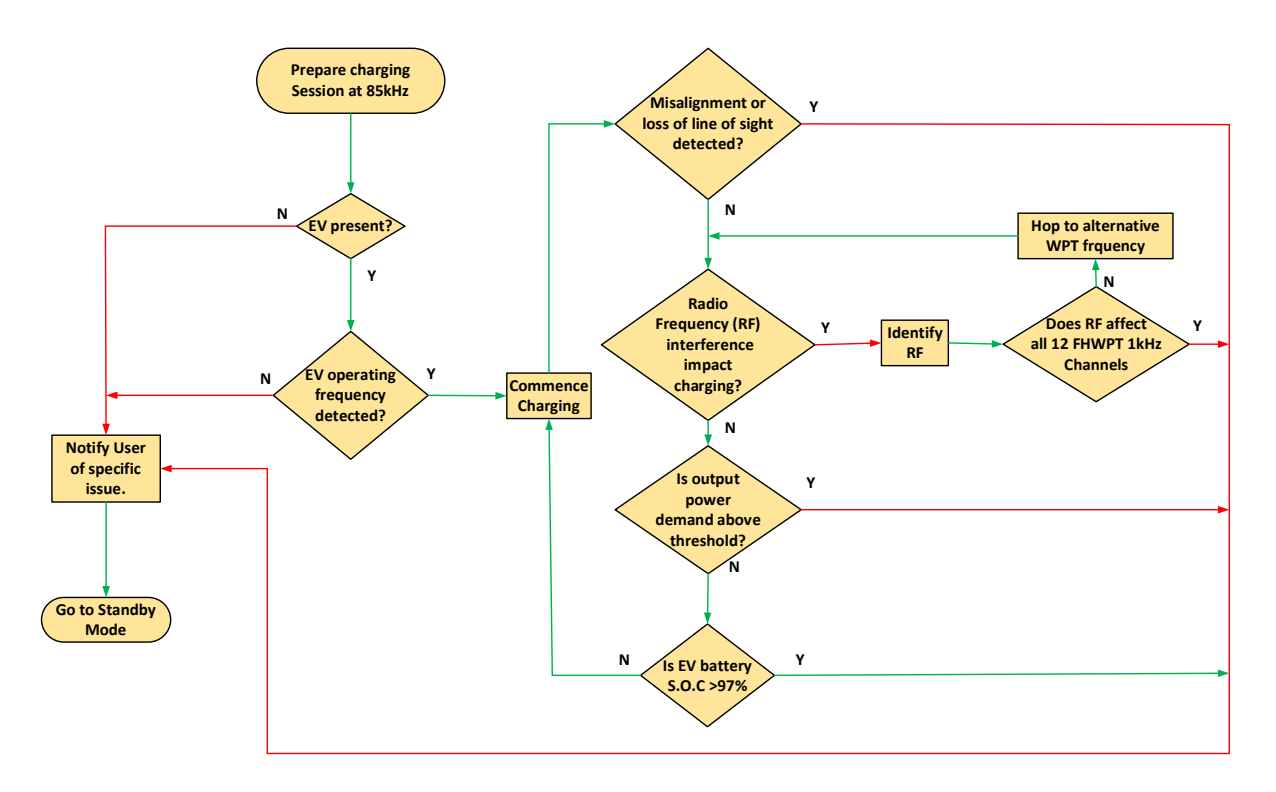


Fig. 4.2 FHWPT control flow chart

The flowchart describes the adaptive measures undertaken by the FHWPT. Table 4.1 below shows the interventions undertaken by the microcontroller to maintain the charging session or notify the user.

Table 4.1 Microcontroller determinants for adaptive operation

Conditions	Determinants		
EV present	If Z _{feedback, new} is < Z _{feedback} AND transmitter's		
	microcontroller pairs with receiver's		
	microcontroller.		
EV operating frequency detected	When transmitter's microcontroller confirms		
	operating frequency from receiver's		
	microcontroller.		
Misalignment or loss of line of sight	Receiver present AND Z _{feedback} low AND battery		
detected	charge rate is low		
Radio Frequency (RF) interference	Receiver present AND Z _{feedback} fluctuating		
impact charging?			
Does RF affect all 12 FHWPT 1kHz	All channels low		
Channels:			
Is output power demand above	Receiver present AND Z _{feedback} for all channels		
threshold?	low AND battery charge rate is low		
Is EV battery S.O.C >97%:	Receiver present AND battery SoC >97%		

The detail design for the FHWPT commences in the next Section.

4.3 Overview of FHWPT circuit

The objective is to design and build a 18W adaptive FHWPT to demonstrate the FH operation. A block diagram of the FHWPT is presented in Fig 4.3 and Fig 4.4.

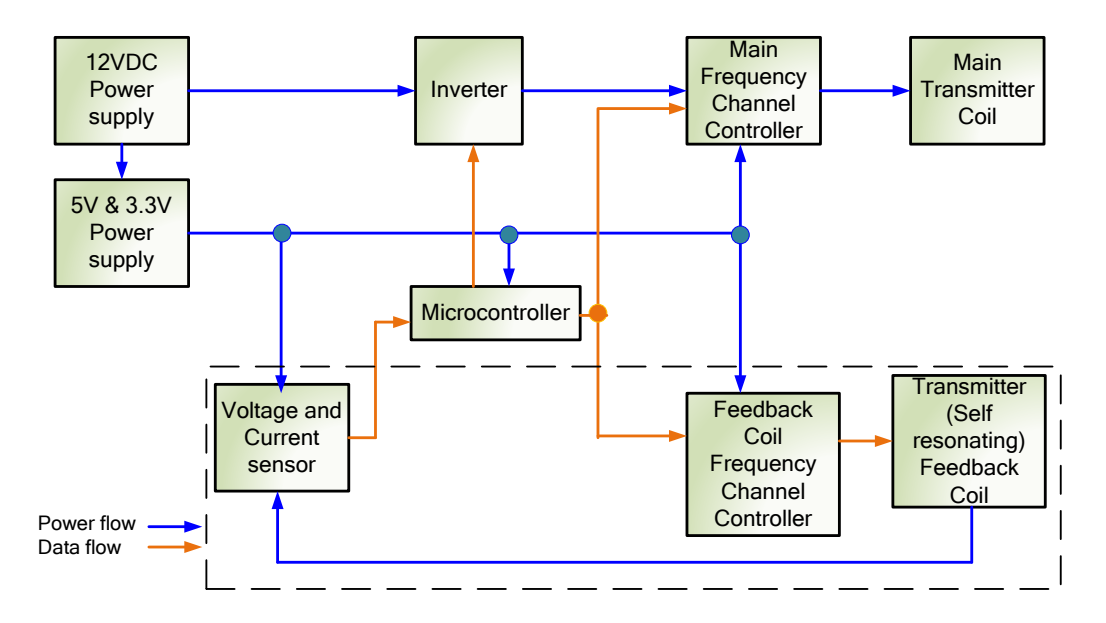


Fig. 4.3 Overview of FHWPT Transmitter circuit

The block diagram in Fig 5.1 presents the overview of the FHWPT transmitter circuit. 12VDC supply is delivered to the 5V and 3.3V voltage regulators and inverter. The inverter generates a high frequency AC signal to the transmitter coil via a Frequency Channel Controller (FCC) circuit that manages the channel selection for FH. The FBC inductively coupled to and energised by the transmitter coils provides a voltage and current signal for the microprocessor. The microprocessor instructs both the main and FBC controllers to hop to the next frequency simultaneously. This allows the transmitter and FBC to resonate at the same operating frequency.

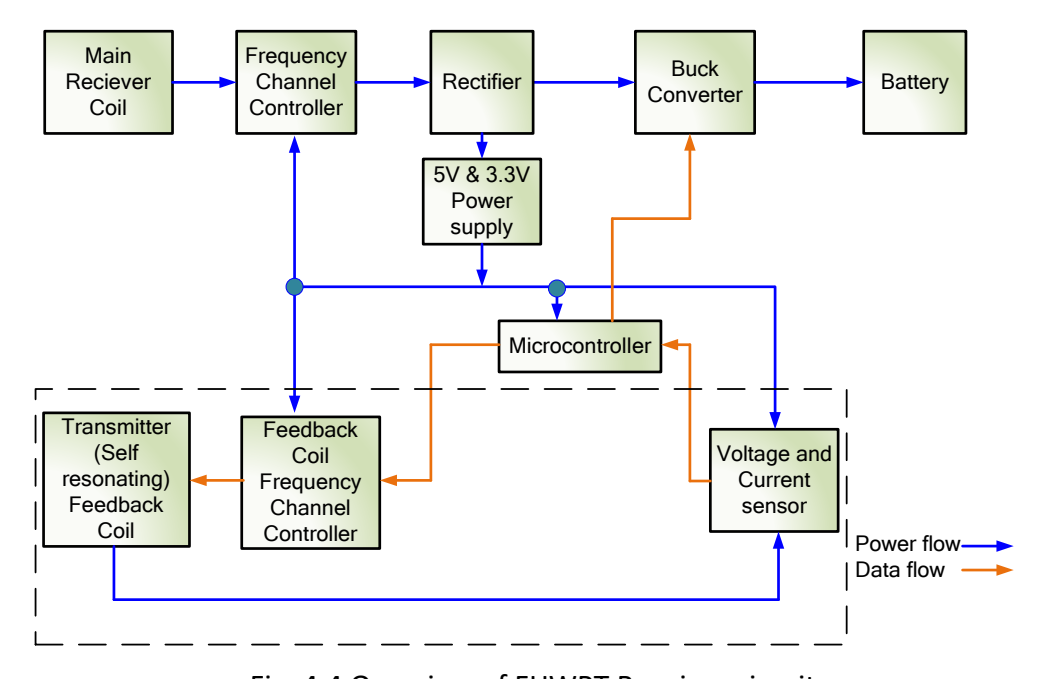


Fig. 4.4 Overview of FHWPT Receiver circuit

The receiver circuit mirrors the transmitter circuit. Main receiver coil delivers power induced from the transmitter's generated magnetic flux to the rectifier which then supplies power to the buck converter to charge the battery. Power from the rectifier is delivered to the 5V and 3.3V voltage regulators which in turn powers the control circuits. The receiver's microcontroller via its embedded communication protocol receives information from its peer transmitter's microcontroller to synchronize with the transmitter's operating frequency. The battery management system reads the battery SoC and RoC and shares it with the microcontroller. The receiver's microcontroller is programmed to execute FH in tandem with the transmitter.

4.4 Transmitter circuit

In the design a MULTICOMP PRO 18W, 12VDC, 1.5A, AC/DC Plug-In, adapter's, output power supply is connected to the circuit via 324.8 μ F capacitance. The capacitors C34, 100 μ F and C17, 220 μ F are installed to reduce low frequency ripple, C19, 4.7 μ F stabilizes the mid frequency fluctuations and C18, 0.1 μ F reduces high frequency noise filtration. Thus, providing the circuit a reliable power quality supply with low electromagnetic interferences from the power unit to the DC-DC converter and a 5V volt regulator. See Fig 4.5

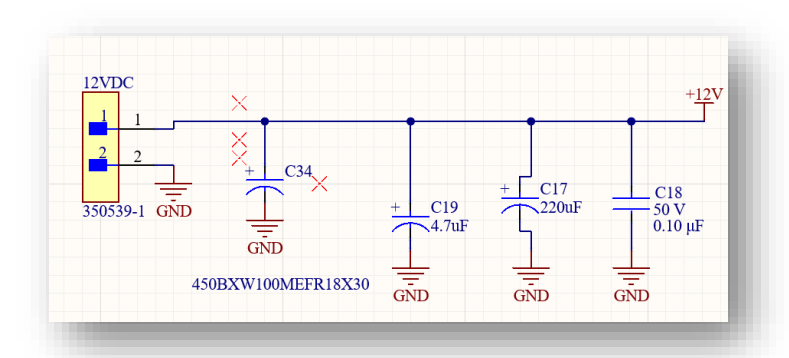


Fig. 4.5 12V power supply schematic.

The 12V output is then delivered to the 5V linear voltage regulator chip, AMS1117-5 which converts it to a 5V supply to the current and voltage sensor circuitry and other components in the circuit see Fig 4.6.

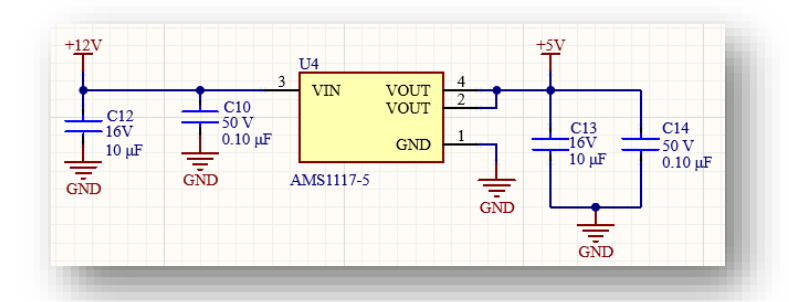


Fig. 4.6 5V power supply schematic.

The 5V supply is connected to the 3.3V linear voltage regulator chip AMS1117-3.3 which converts the 5V to 3.3V to power the Microcontroller, frequency sensor and other components in the circuit see Fig 4.7.

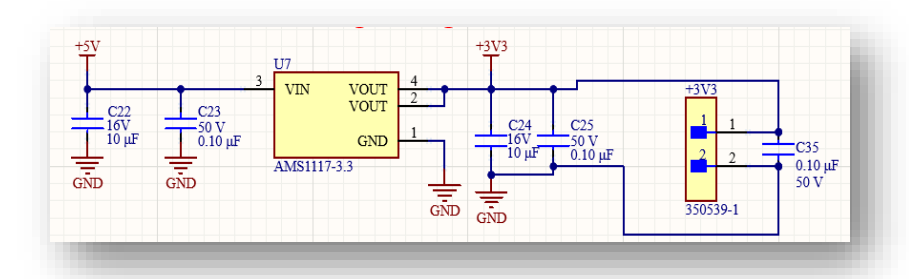


Fig. 4.7 3.3V power supply schematic.

4.4.1 Inverter

The inverter is the muscle of the system, here the 12VDC supply is converted to a 12V 85kHz AC supply. The inverter is configured as a full bridge and the transistors selected for the commutation are GaNFETs see Fig 4.8.

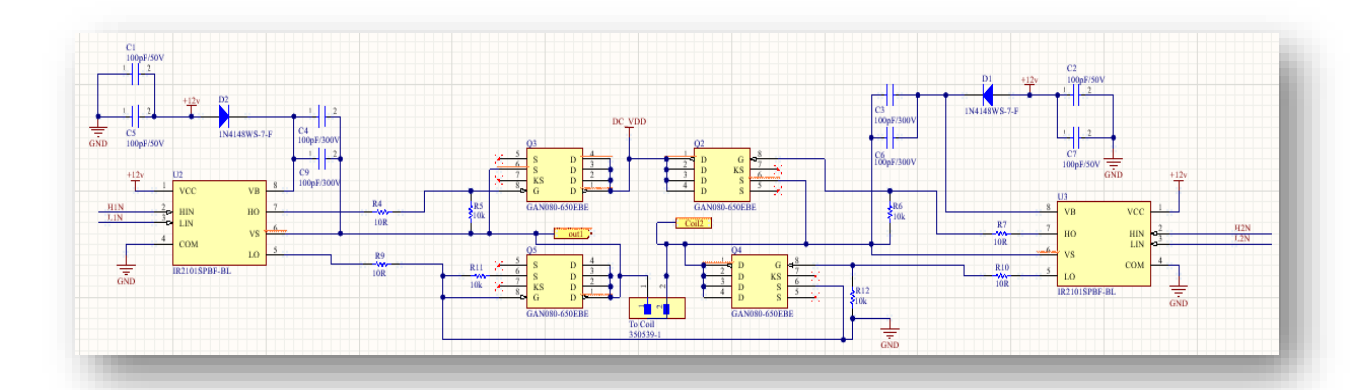


Fig. 4.8 Full bridge inverter schematic.

Nexperia's GaNFET, GAN080-650EBE, (Q2, Q3,Q4 and Q5) is implemented in this circuit because of its low drain source resistance $R_{DS(on)}$, 0.8Ω , high switching speed in the order of MHz, low gate charge of 6nC, low gate drive voltage 6V and low power losses [96].

The Q2, Q3,Q4 and Q5 are driven by the gate driver chip IR2101SPBF-BL which composes of a bootstrap circuit to drive the high side GaNFETs are Q3 and Q2. The bootstrap voltage V_{BOOT} , operates with the principle where the Gate to Source voltage V_{GS} should be greater than the Drain to Source voltage V_{DS} thus, $V_{GS} > V_{DS}$ for the high side GaNFET [97]

$$V_{GS} = V_{BOOT} - V_S (4.1)$$

$$V_{BOOT} \approx V_{DD} + V_{DS}$$
 (4.2)

Where V_S is GaNFET source voltage and V_{DD} is the driver supply voltage. The bootstrap circuitry which is part of the gate driver circuit is composed of a 100pF capacitors C3, C4, and a fast recovery silicon diode 1N4148WS-7-F, D2, D1 to switch Q3 and Q2 respectively, the low side GaNFETs are Q5 and Q4. The gate drivers are triggered by a range of pulse width modulation (PWM) signal frequencies (79kHz to 90kHz at 1kHz step) from the microcontroller to fulfil the FH.

4.5 Coil Configuration

The transmitter and receiver coils and their associated FBCs play a vital role in the FHWPT. From the PTE formula presented in (2.44) it is evident that the PTE, η is proportional to the mutual inductance, M. And M is dependant on the coupling coefficient k and the self-inductance L thus, having a coil with a large L increases the PTE of the WPT.

The aspiration was to design a self-made bespoke planar spiral coil with a self-inductance of $380\mu H$. To achieve the $380\mu H$ coil careful consideration of the coil's wire diameter, turns, space between turns and inner diameter were made. These parameters shall be disclosed here.

4.5.1 Determine specifications for coil's Litz Wire

The coils are constructed from conductive wires therefore, to address the various factors influencing FHWPT coil efficiency at high frequencies, a study was conducted to determine the optimal wire geometry. The first consideration was to determine the skin depth at 85kHz to size the wires diameter. The skin depth was determined using the equation (4.3)

$$\delta = \sqrt{\frac{1}{\mu_0 \sigma f \pi}} (4.3)$$

Where f, δ , $\mu_{0,\sigma}$ are the skin depth, permeability $4\pi \times 10^{-7}$ H/m and conductivity 5.8×10⁷ S/m and frequency 85kHz.

$$\delta = \sqrt{\frac{1}{4\pi \times 10^{-7} * 5.8 \times 1^{7} * 85 * 10^{3} * \pi}} = 0.227 \text{mm (4.4)}$$

Thus, a wire with a diameter less than 0.22mm is required. Another check made was to determine the AC resistance at 85kHz. This is important as the improving the quality factor Q, of the coil. From the formula the R_{ac} impacts the Q

$$Q = \frac{\omega L}{R_{ac}} (4.5)$$

The DC resistance, R_{dc} of a 32AWG or 0.202mm diameter magnet wire is 538.3m Ω /m [98]. The AC resistance at 85kHz is calculated by the formular below.

$$R_{ac} \approx R_{dc} * \frac{r}{\delta}$$
 (4.6)

Where r is the radius of the wire and thus,

$$R_{ac} \approx 538.3 * 10^{-3} * \frac{0.101*10^{-3}}{0.227*10^{-3}} \approx 240 \text{m}\Omega/\text{m} (4.7)$$

A further iteration was undertaken with a popular 38AWG or 0.1mm diameter wire to determine the R_{ac} . The R_{dc} of the 38 AWG is 659.6m Ω/m [98].

$$R_{ac} \approx 659.6 * 10^{-3} * \frac{0.0505 * 10^{-3}}{0.227 * 10^{-3}} \approx 160 \text{m}\Omega/\text{m} (4.8)$$

Assuming an inductance is $47\mu H$ the Q for 32 AWG is 104.6 and the 38 AWG is 156.8. As such, a 38 AWG or 0.1mm was selected because of its high Q and affordability compared to the 32 AWG. The current carrying capacity of 38AWG wire is 22.8mA. Thus, for a 1.5A system, a minimum 65 strands of magnet wire is required.

4.5.2 Discrepancies of coil inductance formula

The FHWPT coil was modelled by inputting the number of turns, pitch, wire diameter, and other parameters into online inductance calculators to obtain the target inductance. Then the Wheeler's formula was then applied using the same parameters, but it produced a different result. To further validate these findings, the coil was simulated in Ansys under identical conditions, which again yielded a different inductance value. These discrepancies illustrate the limitations of both analytical and calculator based approaches, thereby justifying the use of finite element modelling for a more accurate estimation.

4.5.2.1. Evaluation of Spiral Planar Coil inductance using Online calculators

The coil has been designed in a spiral planar configuration which was selected due to its simple structure, symmetry and low production cost [99]. The parameter of the coils goes thus, $No.of\ turns = 40$, $inner\ diameter = 45mm$, $wire\ diameter = 2mm$, $pitch\ or\ turns\ spacing = 5mm$. However, from online calculators the inductance given for these parameters was about 380µH. See Fig 4.9 and Fig 4.10



Fig. 4.9 Kaizer's online spiral inductor calculator [100]

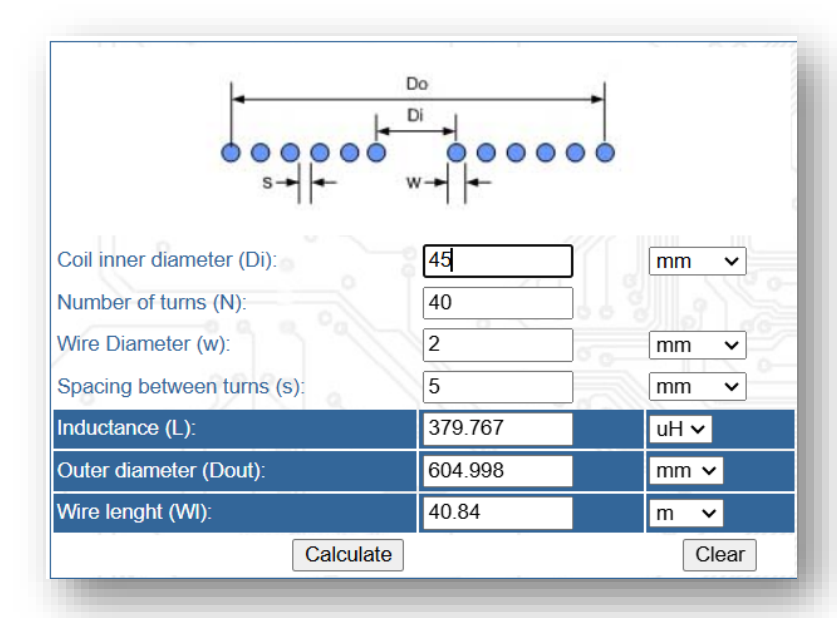


Fig. 4.10 All about electronic circuit's online spiral inductor calculator [101]

4.5.2.2. Evaluation of Spiral coil inductance using Wheelers Formula

The developers of the Online calculators state that Wheeler's formula underpins their computations [100],[101]. However, the results obtained differed from those calculated directly using Wheeler's formula [102]. The parameters for the coil is computed using Wheeler's formula as presented below.

$$L = \frac{r^2 * N^2}{(8r+11w)}$$
 (4.9)

Where L, r, N and w are the self-inductance, average radius of coil, number to turns and width or diameter of the wire. To determine the average coil the formula goes thus,

$$r = \frac{r_{outer} + r_{inner}}{2} (4.10)$$

And router is calculated by the formular given below

$$r_{outer} = r_{inner} + N(w + s) (4.11)$$

Where s is the pitch or spacing between turns. Thus, for a coil wire 2mm diameter, 40 tuns, 5mm pitch, 45mm inner diameter the outer radius can be calculated in inches as

$$r_{outer} = 0.8858 + 40(0.0787 + 0.1969) = 11.909$$
inches (4.12)

From (5.10) r = 5.955inches so to solve for the inductance L we have

$$L = \frac{5.955^2 * 40^2}{(8*5.955+11*0.0787)} \approx 1.17 mH$$
 (4.13)

Thus, the self inductance of the coil is now 1.17mH.

4.5.2.3. Evaluation of Spiral Coil using Ansys

Due to inconsistencies between the results obtained from online inductance calculators and Wheeler's formulas, a finite element study was conducted in Ansys using the same parameters. The information in Fig 4.11 shows the coil parameters specified in the Ansys properties modeller dialogue box.

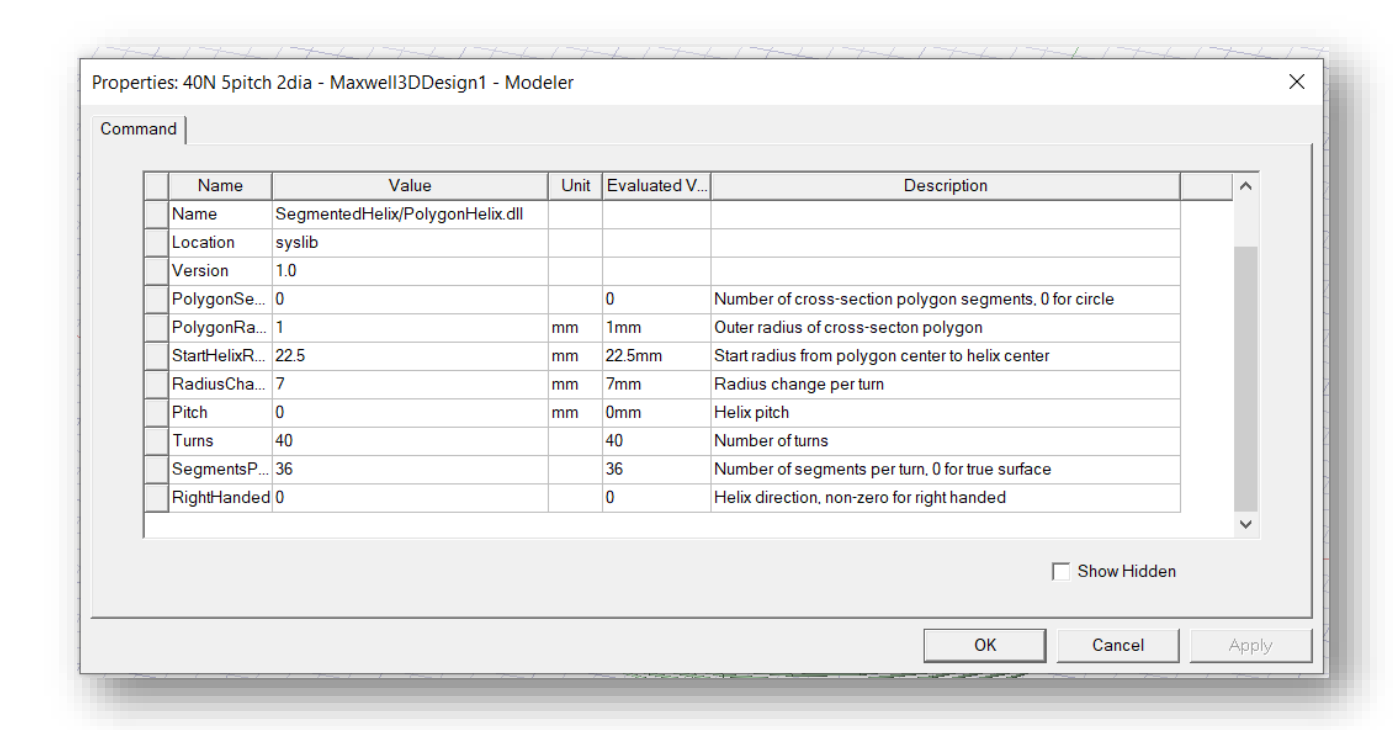


Fig. 4.11 Parameters of coil

The parameters entered in the Ansys properties modeller dialogue box generated the threedimensional coil geometry, as illustrated in Fig. 4.12.

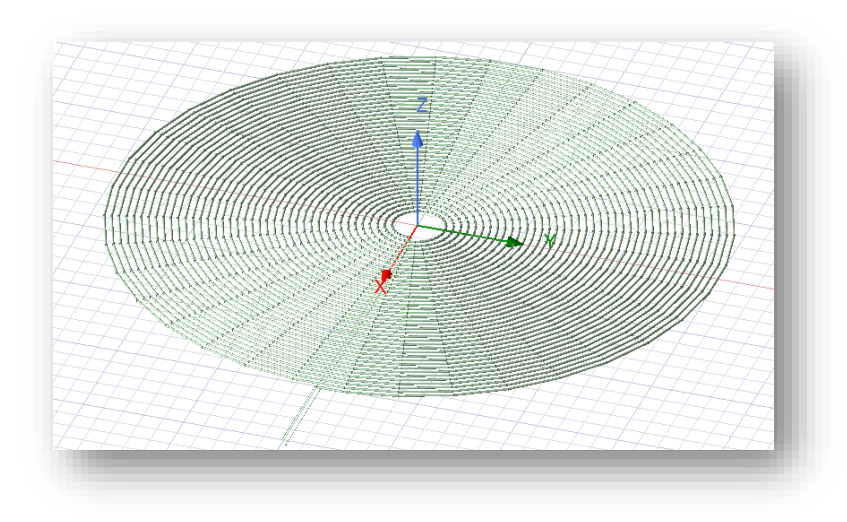


Fig. 4.12 Ansys Model of 40 turns coil

From this study, the coil was found to yield an inductance of approximately 40 μH as shown in Fig 4.13 below.



Fig. 4.13 Ansys Self inductance result

4.5.3 Nominated Spiral Planar Coil configuration for research

As a result of these three different divergent values it was pertinent to use an off the shelf $47\mu H$, 1.5A, 0.5Ω Wurth $47\mu H$ WE-WPCC Receiver Qi spiral coil for the FHWPT [103]. 8 of these coils arranged in series will provide $376\mu H$ which is close to the $380\mu H$ target. However, from these studies it was clear that procuring an off the shelf $47\mu H$ coil for the demonstration of the FHWPT will be sufficient.

4.6 Feedback coil and Sensors

To ensure the FHWPT works effectively, the voltage, current and frequency feedback signals from the transmitter and receiver FBCs are required to provide real time data for the microcontroller.

The incorporation of a FBC is a significant distinguishing feature that differentiates the FHWPT from conventional WPT systems. The FBC is designed to resonate at the same frequency with their associated transmitter and receiver coils. Resultantly, the transmitter, receiver and FBC properties are similar. Nonetheless, to ensure the FBCs enhance the FHWPT and provide accurate voltage and current data consideration of the FBCs load and coupling coefficient were undertaken.

The load connected to the FBC and the FBC has an impedance $Z_{feedback}$. The magnitude of FBC's reflected impedance $Z_{reflected}$ on the main transmitter and receiver coils are calculated to determine the burden of the feedback circuitry on the main transmitter or receiver coils. The Russian scientist Heinrich Friedrich Emil Lenz who propounded the term "back EMF" says in his law, Lenz law, that the induced current in a secondary coil opposes the primary coil's current. And using Lenz Law we can derive a relationship between $Z_{reflected}$ and $Z_{feedback}$

$$\varepsilon = -\frac{d\Phi_B}{dt}(4.14)$$

Where ε , B are the induced emf and flux. And

$$\Phi_B = LI$$
 (4.15)

Where L is inductance of the transmitter coil and I is the primary current Itx thus

$$\varepsilon = -L \frac{dI_{tx}}{dt} (4.16)$$

For mutual inductance, M the induced voltage in FBC V_{feedback} due to I_{tx} ,

$$V_{feedback} = -M \frac{d}{dt} I_{tx} (4.17)$$

For a given system where I_{tx} oscillates with frequency ω we have

$$I_{tx} = Ie^{j\omega t} (4.18)$$

Thus

$$\frac{d}{dt}I_{tx} = j\omega I_{tx}$$
 (4.19)

So

$$V_{feedback} = -j\omega M I_{tx}$$
 (4.20)

Also Z_{reflected} is the ratio of the V_{feedback} and I_{feedback} thus

$$I_{feedback} = \frac{-j\omega M I_{tx}}{Z_{feedback}}$$
 (4.21)

And

$$I_{tx} = \frac{Z_{feedback}}{-j\omega M} * I_{feedback} (4.22)$$

Z_{reflected} provides the determinant of the burden or impedance to be applied to the FBC as this is inverse to the reflected impedance. We need the FBC not to draw significant power from the transmitter coil but still have sufficient power to enable switching of the GaNFETs in the FBC's FCC circuit.

Substituting $V_{feedback}$ for $= -j\omega M I_{tx}$ we have and from (5.20) we have

$$Z_{reflected} = \frac{(wM)^2}{Z_{feedback}} (4.23)$$

This derivation aligns with the transformer theory shown in (3.21) to (3.23). This principle was used to determine the loading of the FBC and optimal coupling coefficient between their associated transmitter and receiver coils. Figures 4.14 and 4.15 illustrate the high impedance voltage sensor and the current sensor circuitry, respectively, both of which are connected to the FBC.

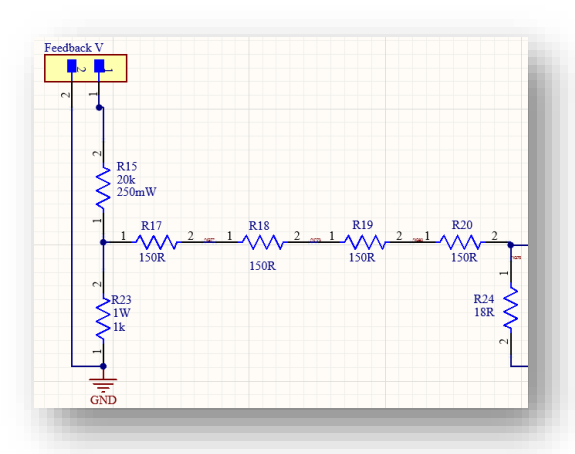


Fig. 4.14 High-impedance interface for feedback voltage sensing.

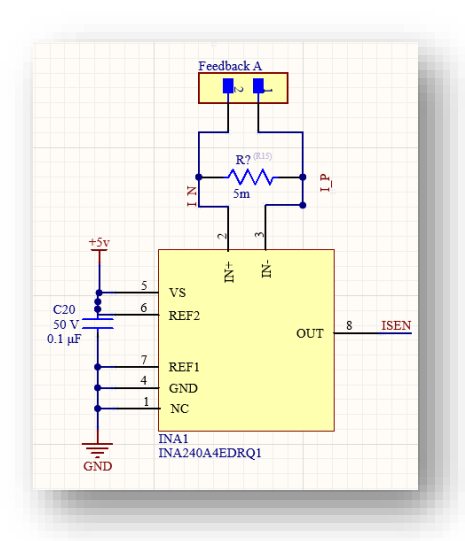


Fig. 4.15 Shut resistor for feedback current sensing

From Fig 4.14 and Fig 4.15 the total impedance seen by the FBC can be calculated. Note that R_{coil} is 0.5Ω [103].

$$Z_{feedback} = R_{shunt} + R_{Voltage\ Sensor} + R_{coil}$$
 (4.24)

$$Z_{feedback} = 0.5m\Omega + 1570\Omega = 1570.505\Omega$$
 (4.25)

Since $0.505\Omega \ll 1570\Omega$

$$Z_{feedback} = 1570\Omega (4.26)$$

The self inductance of both the transmitter and receiver coils and their associated FBC is $47\mu H$. The focus will be made on the transmitter side of the FHWPT. The voltage across the transmitter coil is 12V and the max current of the inductor is 1.5A. from these parameters we can determine voltage in the FBC.

4.6.1 Voltage Sensor

Lenz law or back emf manifests as the reflected impedance z_{reflected} in the transmitter coil and this is dependant of the coupling coefficient k. The k of 0.5 between transmitter and FBC was determined in an analysis shown in Section 5.3.1. Thus, for a k of 0.5 such that the FBC away from the coil the transmitter coil,

$$M = 0.5 * 47 \mu H = 23.5 \mu H$$
 (4.27)

$$Z_{reflected} = \frac{(2\pi*85*10^3*23.5*10^{-6})^2}{1570} = 0.1\Omega (4.28)$$

And the losses in the transmitter coil due to Lenz law at k 0.5 is

$$P_{Lenz} = I_{Primary}^2 * Z_{reflected}$$
 (4.29)

$$P_{Lenz} = 1.5^2 * 0.1 = 0.226$$
W. (4.30)

This indicates that 1.3% of the power in the transmitter coil in dissipated due to the impedance of the FBC. Another consideration is the Voltage across, and the current delivered by the FBC at k = 0.5.

$$V_{feedback} = j\omega M * I_{tx}$$
 (4.31)

$$V_{feedback} = 2\pi * 85 * 10^3 * 23.5 * 10^{-6} * 1.5 = 18.83V$$
 (4.32)

This value is sufficient to provide voltage reference data to the microcontroller. From Fig 4.14 there is a voltage divider and in Fig. 4.15 there is an additional amplification of the voltage in the voltage sensor circuit this value shall be reflected in the scaling factor in the microcontroller.

For the voltage divider V1 which shall be named V measured feedback, V_{m feedback}, we have

$$V_{m \, feedback} = V_{feedback} * \frac{R_{23}/R_{15}*R_{24}}{(R_{23}/R_{15}+R_{17}+R_{18}+R_{19}+R_{20}+R_{24})*(R_{17}+R_{18}+R_{19}+R_{20}+R_{24})}$$
(4.33)
$$V_{m \, feedback} = V_{feedback} * \frac{952\Omega*18\Omega}{(952\Omega+618\Omega)*(618\Omega)} = V_{feedback} * 0.0177$$
(4.34)

Where $V_{feedback}$ = 18.83V then

$$V_{m feedback} = 18.83V * 0.0177 = 0.333V (4.35)$$

 $V_{m \, feedback}$ is connected to the VIN+ VIN- terminals of the Toshiba isolation amplifier TLP7920 or optocoupler which is employed to provide the microcontroller with a stable voltage signal. This chip is powered with 5V at the primary side and 3.3V at the secondary side [104] as presented in Fig 4.16. This has an input voltage range of $\pm .5V$ thus, $V_{m \, feedback}$ of 0.33V is fit for purpose.

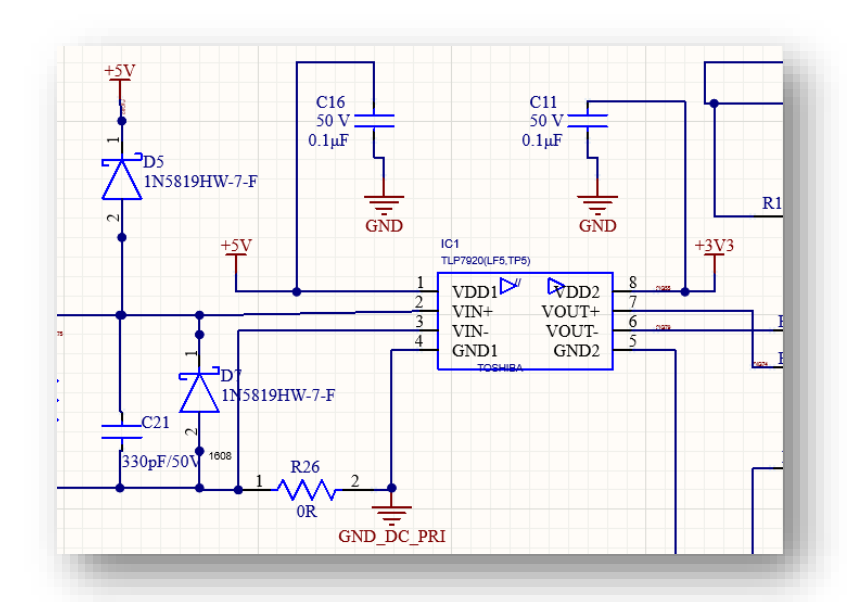


Fig. 4.16 Optocoupler in the voltage sensor subcircuit

The output of the optocoupler is connected to the differential see operational amplifier Fig. 4.17, whose gain is 3 based on the expression

$$Gain = \frac{R_f}{R_g} \text{ (4.36)}$$

Where R_f is $36k\Omega$ and R_g is $12k\Omega$ the gain is 3 thus the $V_{measured\ feedback}$ will be amplified by 3 and read by the microcontroller via the pin ADCO.

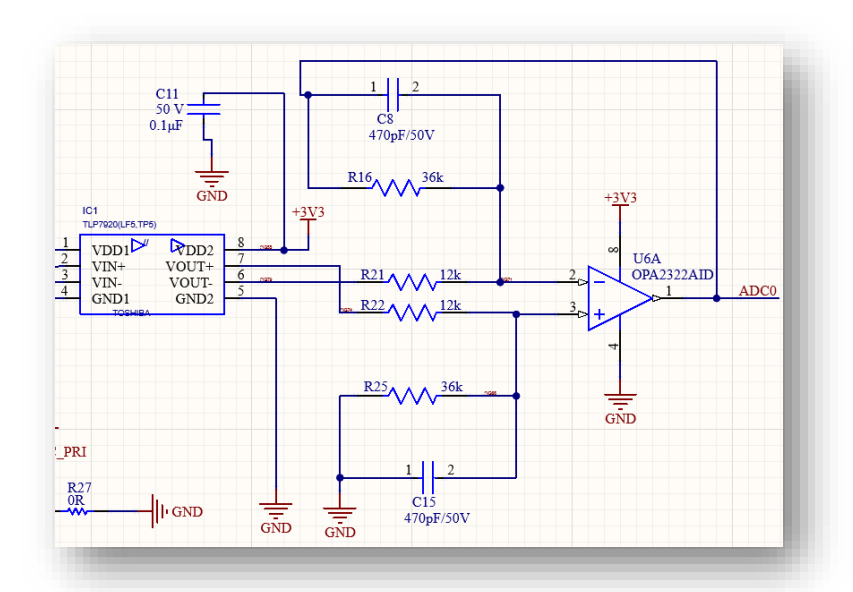


Fig. 4.17 Differential amplifier for voltage signal circuit.

$$V_{ADC0} = V_{m feedback} * 3 (4.37)$$

$$V_{ADC0} = 0.999V \approx 1V (4.38)$$

To properly scale the microcontroller so it processes data based on the original voltage signals, V_{feedback} . We have

$$scaling\ factor = \frac{Actual\ Voltage\ (V_{feedback})}{Measured\ Voltage\ (V\ m\ feedback)} = 18.83\ (4.39)$$

4.6.2 Current Sensor

In the same vein I_{feedback} can be calculated as follows

$$I_{feedback} = \frac{V_{feedback}}{Z_{feedback}} (4.40)$$

$$I_{feedback} = \frac{18.83V}{1570\Omega} = 12mA$$
 (4.41)

The current sensor presented in Fig 4.15 shows a shunt resistance of $5m\Omega$ thus the equivalent voltage drop across R_{shunt} that shall be detected by the current sensor can be calculated as

$$V_{drop} = R_{shunt} * I_{feedback}$$
 (4.42)

$$V_{drop} = 5m\Omega * 12mA = 0.06mV$$
 (4.43)

The voltage range of Texas Instruments' current sensor INA240A4EDRQ1 is -4V to 80V with a fixed gain of 200V/V [105]. The minimum voltage before noise interference or V_{min} is 25uV. For accurate detection

$$V_{drop} > V_{min}$$
 (4.44)

$$0.06mV > 25.5\mu V$$
 (4.45)

The output signal for the feedback current from the current sensor chip connected to the microcontroller via the connector ISEN is shown below.

Current sense Output Voltage = $Gain * V_{drop}$ (4.46)

Current sense Output Voltage =
$$\frac{200V}{V} * 0.06mV = 12mV$$
 (4.47)

4.6.3 Frequency Sensor

Vishay's 6N137 high speed optocoupler is employed as a frequency sensor. This chip is connected to the transmitter coil to provide a backup check on the coils frequency as shown in Fig 4.18. [106]

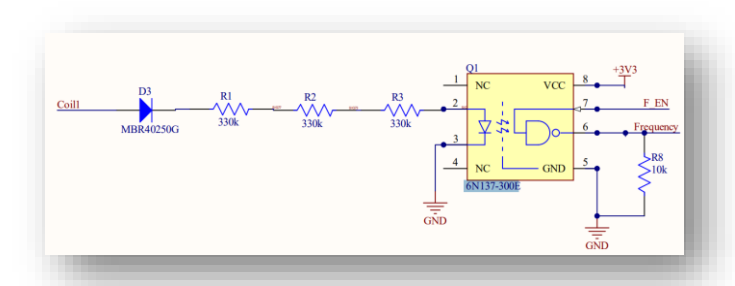


Fig. 4.18 Frequency sensor

4.7 Microcontroller

The microcontroller governs the operations of the transmitter circuit and receiver circuit. However, the receiver circuit has a similar microcontroller installed. The microcontroller employed is Espressif's ESP32-WROOM-32, chosen for its integrated Wi-Fi, which enables native IP networking; the transmitter and receiver modules each obtain their own IP address via a Dynamic Host Configuration Protocol (DHCP). Also, for its ample processing headroom (dual-core), motor-control pulse width modulation (PWM) for precise gate-drive timing,

processing speed, up to 24MHz. Also to add, it has an on-chip 12-bit analogue to digital converter (ADC) sufficient to process the FBC sensory data which is central to the proposed FHWPT control and monitoring architecture. Since the ESP32-WROOM-32 lacks an embedded IEEE 802.15.4, local pairing for administrative management and performance reporting can be enabled by adding a Zigbee via an external IEEE 802.15.4 transceiver. It also has Bluetooth (BT) and Bluetooth Low Energy (BLE) communication module. Table 4.2 presents a comparative assessment of eight candidate microcontrollers and the rationale for selecting the ESP32-WROOM-32.

Table 4.2 Assessment of various microcontrollers for FHWPT application

Microcontroller make and model	Core	Clock Speed	Integrated communication module	Exclusive Features
Espressif ESP32-WROOM-32	Dual-core Xtensa LX6	240 MHz	Wi-Fi 2.4 GHz + BT/BLE	Dual cores separate the control and communication modules. Zigbee can be added if required. [107]-[111]
STMicroelectronics STM32G474 (G4 series)	ARM Cortex- M4F	170 MHz	_	Precise PWM, fast ADC, on-chip analogue (opamps/comparators). Zigbee can be added if required. [112],[113]
Raspberry Pi RP2040	Dual-core Cortex- M0+	133 MHz	_	Strong deterministic Input Output signal (no jitter). Zigbee can be added if required.[114]
Texas Instruments TI C2000 TMS320F280049C	C28x	100 MHz	_	Good for traction control; deterministic control loops. Zigbee can be added if required. [115]
Espressif ESP32-H2-MINI-1	Single-core RISC-V	96 MHz	802.15.4 (Zigbee/Thread) + BLE	Native Zigbee. [116],[117]
Microchip dsPIC33EP256MC5 06	dsPIC33,	70 MHz	_	Cost-effective, Zigbee can be added if required. [118],[119]
Nordic nRF52840	Cortex- M4F,	64 MHz	BLE + 802.15.4 (Zigbee/Thread)	Excellent Zigbee control- loop capability [120],[121]
Texas Instruments TI CC2652R	Cortex- M4F,	48 MHz	BLE + 802.15.4 (Zigbee/Thread)	Low-power Zigbee. [122]- [124]

A program for the operation of the microcontroller was written in Arduino IDE version 2.3.4 software package. Excerpts of the program shall be taken to demonstrate the instruction set developed for the executions of the microcontroller. The operation of the microcontroller shall be divided into four main parts. The PWM generation, feedback and impedance acquisition, data exchange between transmitter and receiver microcontrollers and FH operations. Fig 4.19 shows the schematic and pin schedules of the microcontroller.

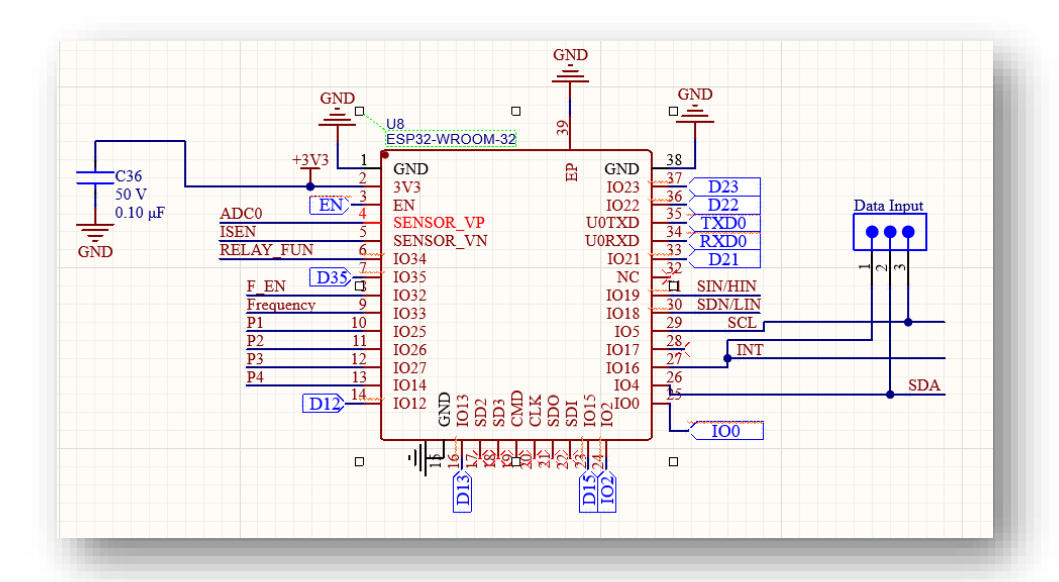


Fig. 4.19 Microcontroller schematic

4.7.1 PWM and inverter operation

The PWM generated by the microcontroller is supplied to the gate driver chip IR2101SPBF-BL, Hi and Lo pins. The instruction sets in Fig 4.20 shows how the PWM pins are assigned

```
5 // Pin Definitions
6 #define PWM_P1 25 // PWM Output for gate driver (Channel 1)
7 #define PWM_P2 26 // PWM Output for gate driver (Channel 2)
8 #define PWM_P3 27 // PWM Output for gate driver (Channel 3)
9 #define PWM_P4 14 // PWM Output for gate driver (Channel 4)
```

Fig. 4.20 PWM pin assignment

Fig 4.21 declares the frequency allocation for the FHWPT where 85kHz is the base or default frequency. Also, the frequency range of 79kHz to 90kHz and the rastered 1kHz frequency step for the hopping is detailed.

```
31 // Frequency Control
32 #define BASE_FREQUENCY 85000 // 85kHz
33 #define MIN_FREQUENCY 79000 // 79kHz
34 #define MAX_FREQUENCY 90000 // 90kHz
35 #define FREQ_STEP 1000 // 1kHz step
```

Fig. 4.21 PWM frequency assignment

The code in Fig. 4.22 assigns the declared PWM to the four pins and establishes a 50% duty cycle for the PWM.

```
// Configure PWM for multiple channels
          ledcSetup(0, BASE_FREQUENCY, pwmResolution);
56
57
          ledcSetup(1, BASE_FREQUENCY, pwmResolution);
          ledcSetup(2, BASE_FREQUENCY, pwmResolution);
58
59
          ledcSetup(3, BASE_FREQUENCY, pwmResolution);
60
61
          ledcAttachPin(PWM_P1, 0);
         ledcAttachPin(PWM P2, 1);
62
          ledcAttachPin(PWM_P3, 2);
63
          ledcAttachPin(PWM_P4, 3);
64
65
66
          ledcWrite(0, 128); // 50% Duty Cycle
          ledcWrite(1, 128);
68
          ledcWrite(2, 128);
          ledcWrite(3, 128);
```

Fig. 4.22 PWM frequency and duty cycle assignment

These are the salient instruction set that governs the PWM for the inverter however, it is expected that the transmitter coil will oscillate at the same frequency with the PWM by switching the capacitor tuned to the specific frequency this shall be discussed in the FH section.

4.7.2 Impedance tracking using mutual inductance

From Fig. 4.23 we can see the transmitter FBCs L_1 , and receiver FBC L_2 inductively coupled to the transmitter and receiver coils L_t and L_r , and their mutual inductances.

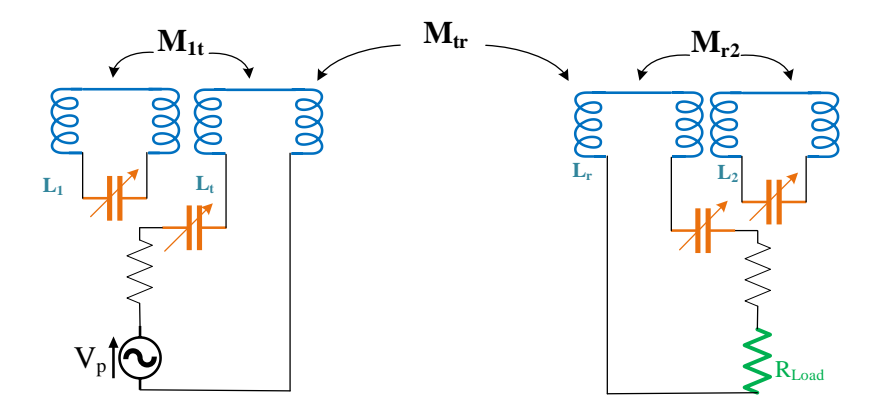


Fig. 4.23 Significant Mutual inductance between coils.

Data from the mutual inductance measured between the transmitter and receiver coils M_{tr} , and transmitter coil and transmitter FBCs M_{1t} , are required to determine FH.

At standby when M_{1t} = 23.5 μ H as shown in (4.21) a $Z_{feedback}$ value is registered in the microcontroller and a threshold is set as we expect the FBC to be in a fixed position.

When the receiver coil L_r is in proximity to L_t and taking load M_{tr} influences M_{1t} . To determine M_{tr} we shall derive the Mutual inductance and self inductance relationship equation commencing with Kirchhoff's voltage law of the circuit. Thus, Kirchoff's voltage law for the voltage in the transmitter and receiver coils V_t and V_r we have

$$V_t = j\omega L_t I_t - j\omega M_{tr} I_r$$
 (4.48)

$$V_r = j\omega L_r I_r - j\omega M_{tr} I_t$$
 (4.49)

Where I_t and I_r are the currents in the transmitter and receiver coils respectively Solving for I_r we have

$$I_r = \frac{j\omega M_{tr}I_t}{j\omega L_r} = \frac{M_{tr}I_t}{L_r} (4.50)$$

By substituting I_r in (V_t eqn) we have

$$V_t = j\omega \left(L_t - \frac{M_{tr}^2}{L_r}\right) I_t$$
 (4.51)

Thus, effective inductance on transmitter coil caused by the receiver coil is Lt,eff

$$L_{t,eff} = L_t - \frac{M_{tr}^2}{L_r}$$
 (4.52)

From this equation $L_{t,eff} < L_t$ affecting $Z_{feedback}$, the new $Z_{feedback}$, $Z_{feedback}$, $Z_{feedback}$, is registered in the microcontroller as a vehicle in position to commence charging.

If the receiver coil in proximity to charge has $L_r = 47\mu H$, and k = 0.2. $Z_{feedback, new}$ can be calculated as

$$M_{tr} = k\sqrt{L_t L_r} = 0.2 * 47 \mu H = 9.4 \mu H$$
 (4.53)

$$L_{t,eff} = 47\mu H - \frac{9.4\mu H^2}{47\mu H} = 47\mu H - 1.88\mu H = 45.12\mu H$$
 (4.54)

$$M_{1t,new} = k_{1t} \sqrt{L_{t,eff} L_{feedback}}$$
 (4.55)

Where k_{1t} = 0.5, justification of this k is in Section 5.3.1 between transmitter and receiver coil we have

```
M_{1t,new} = 0.5\sqrt{45.12\mu H * 47\mu H} = 23.03\mu H  (4.56) V_{feedback,new} = j\omega M_{1t,new} * I_{tx}  (4.57)
```

Note that transmitter coil is limited to Itx of 1.5A thus

```
V_{feedback,new} = 2\pi * 85 * 10^3 * 23.03 * 10^{-6} * 1.5 = 18.45V (4.58)
```

The analogue to digital converter (ADC) of the microcontroller supports a 12-bit Successive Approximation Register ADC [107]. The voltage and current sensor's terminals ISEN and ADCO are connected to the microcontrollers input output (IO) ports as shown in Fig 4.19. The instruction set to read data from the current sensors are in Fig 4.24 below.

```
#define ADC_VOLTAGE_PIN 36 // Voltage measurement (ADC0)
#define ADC_CURRENT_PIN 39 // Current sensor (ISEN)
```

Fig. 4.24 ADC pin assignment.

The scaling factor for the input voltage and current is determined by the impedance network of the respective sensors. The voltage scale factor of 18.83 is derived from the output voltage sensor as shown in (4.39). Current scale is based on the shunt resistor rating of $5m\Omega$ as shown in Fig. 4.15. The microcontroller code is presented below in Fig. 4.25

```
42. // ADC Calibration Constants
43. #define VOLTAGE_DIVIDER_RATIO 18.83
44. #define CURRENT_SENSE_GAIN 0.005
```

Fig. 4.25 Calibration code of voltage and current.

The changes observed in the FBC's impedance is proportional to the mutual inductance between the transmitter and FBC, transmitter coils voltage and current hence, any changes affecting the transmitter or receiver coil will impact the associated FBC impedance. As such the measured impedance in the microcontroller Z_{feedback} can be described as

```
Z_{feedback} = \frac{V_{measured via ADC0}}{I_{measured via ISEN}} (4.59)
```

Thus, the Z_{feedback} is generated in the code found in Fig. 4.26.

Fig. 4.26 microcontroller code to determine impedance.

4.8 Frequency Hopping

The FH is initiated when the impedance Z_{feedback}'s set threshold is breached. Once breached, two activities occur first, the PWM is incremented from the default frequency 85kHz, or the existing frequency to the next 1kHz frequency step. Second, the LC resonant tank in the transmitter, receiver and associated FBCs are switched to the associated resonant frequency by switching the related capacitor to that resonant frequency see Fig 4.27

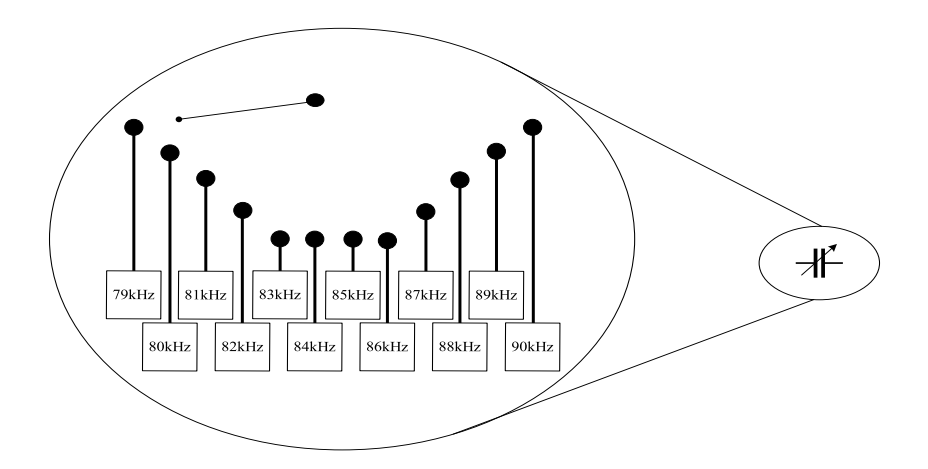


Fig. 4.27 Illustration of Frequency channel selection using a variable capacitor.

All coil's FCC manages the switching of the channels as presented in Fig 4.27. There are 12 frequency channels and as such the IO pins to switch these channels is not available on the ESP32 WROOM 32 chip. So, the I2C or Inter-Integrated Circuit communication device within the microcontroller is employed to communicate with the general purpose IO expander chip,

PCA9555118. This is achieved via the serial data line (SDA) and Serial Clock Line (SCL) pins and Interrupt (INT). The data input 3 pin socket connects the SDA, SCL and INT pins from the microcontroller to the IO expander as shown in Fig 4.28 and Fig 4.29 because both chips are on separate printed circuit boards.

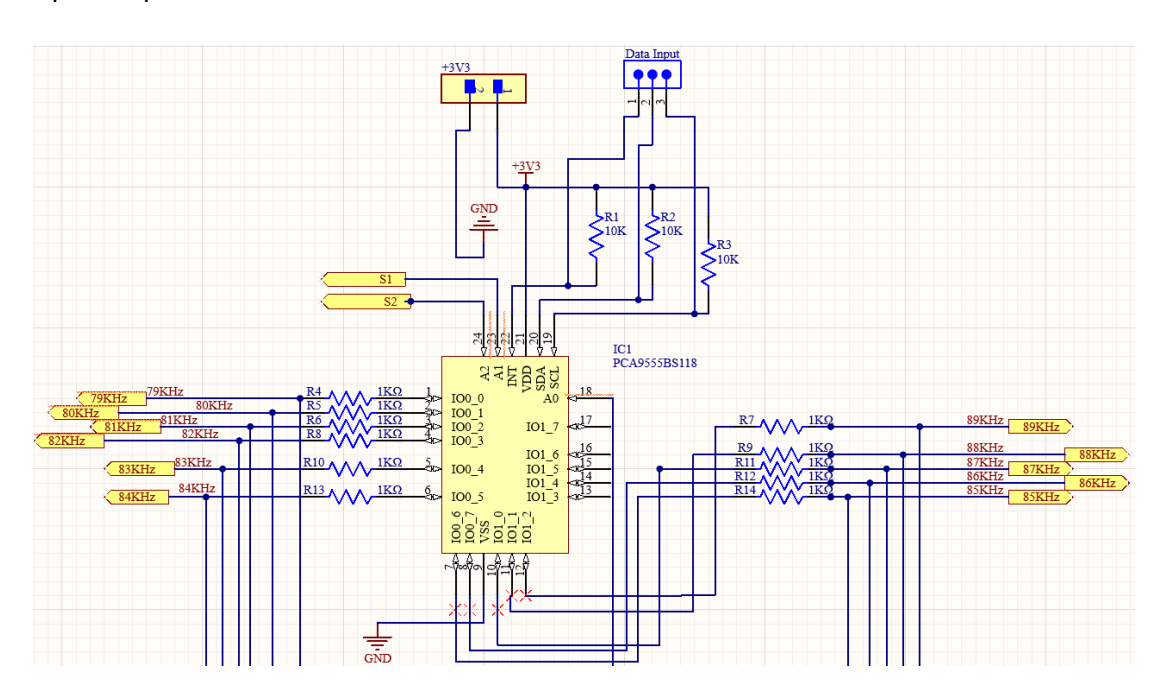


Fig. 4.28 IO expander and schedule for all coils.

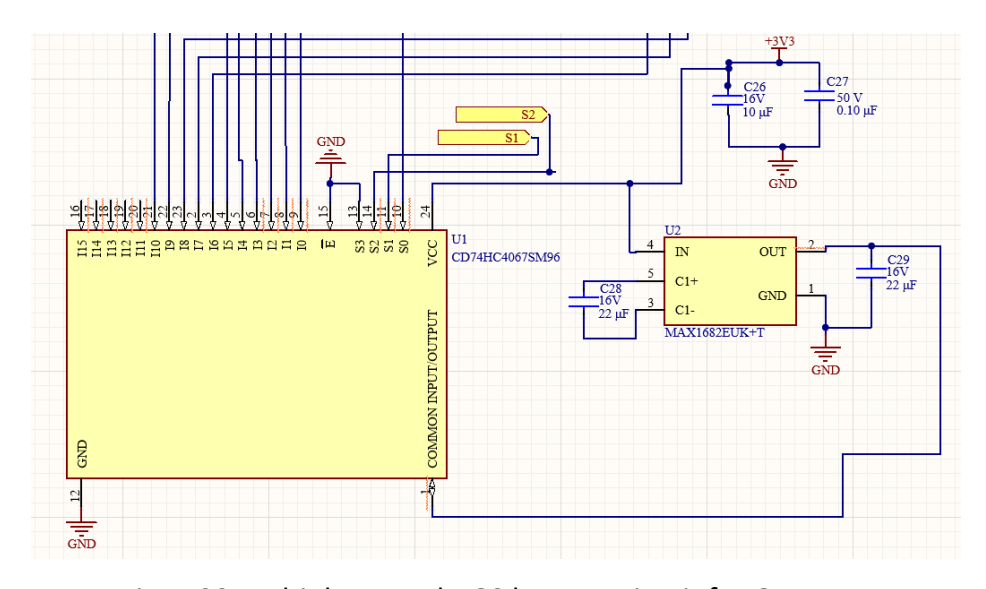


Fig. 4.29 Multiplexer and VGS booster circuit for GANFETs

The IO expander chip, "IC1" output pins are connected to the gates of each GANFET via a multiplexer and pump charge voltage doubler. The IO voltage of 3.3V from the IO expander

chip is insufficient to switch on the GaNFET whose V_{GS} is 6V. Thus, the 16 bit multiplexer chip CD74HC4067SM96, enables a connection to the voltage doubler charge pump IC MAX1682 that increases the signal V_{GS} from 3.3V to 6.6V. This is for two reasons first to eliminate the need for a gate driver for each GaNFET and secondly to eliminate the need for an extra 6V supply to the circuit to achieve V_{GS} of 6V for the gate drivers to switch on the GaNFETs. Also, each GaNFET is dedicated to a specific frequency channel to enable them to perform the FH. The GaNFETs in this circuit acts as a static switch and not a high frequency switch.

The microcontrollers instruction to hop to a frequency channel, will contain the IO address in the IO expander chip and the corresponding IO address on the multiplexer chip. The charge pump via the selected channels on both circuits will deliver $6.6V\ V_{GS}$ to the specific GaNFET's gate.

The GaNFETs Q1 to Q11 are dedicated to switching the capacitors such that only one is on at a time see Fig. 4.30. Note that the capacitor C25, called the base capacitor is dedicated to the maximum frequency, 90kHz is not commutated by a GaNFET.

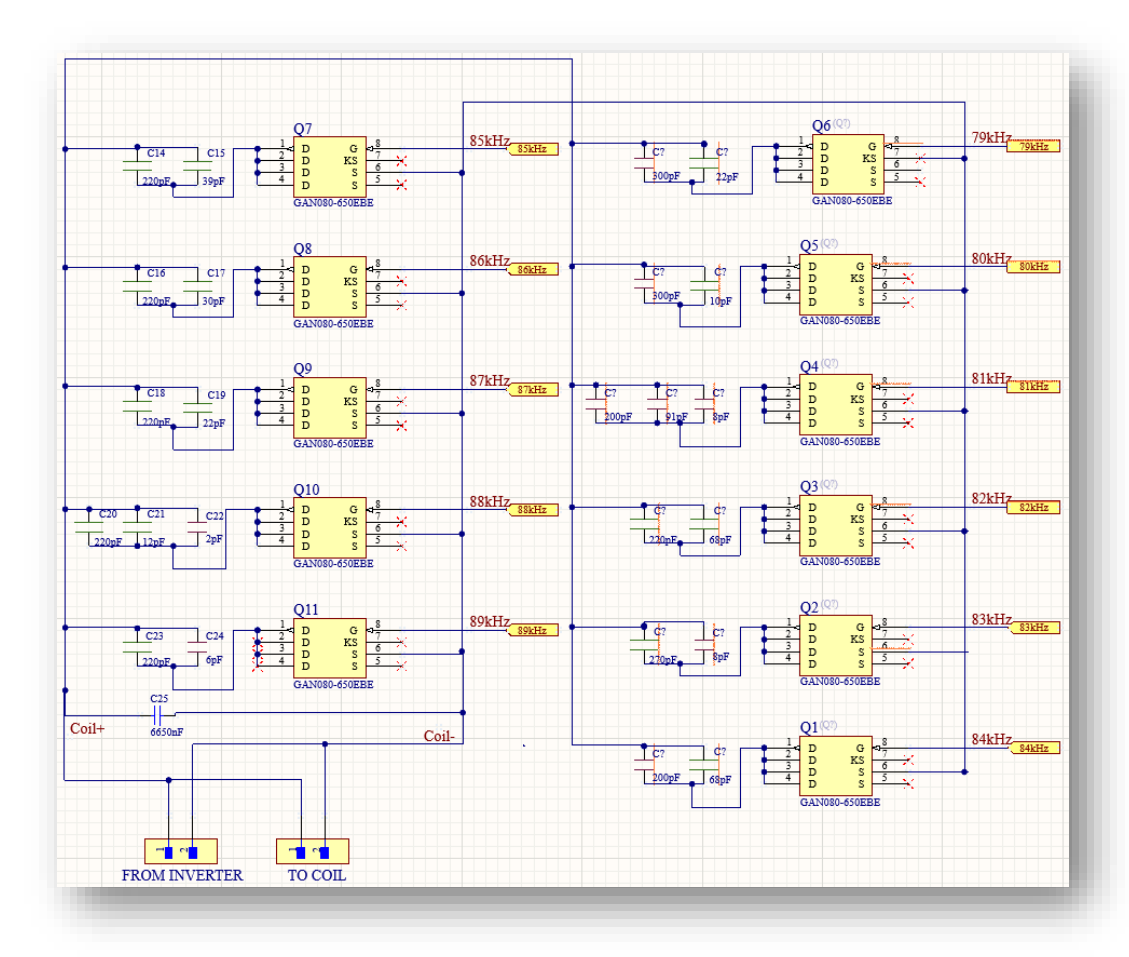


Fig. 4.30 FCC for all coils

Capacitors associated to channels Q1 to Q11 are to be connected to the base capacitor to ascertain their respective frequency. For a coil with inductance $47\mu H$ the base capacitor at 90kHz is calculated below.

$$C_{90kHz} = \frac{1}{\omega_{90kHz}^2} (4.60)$$

$$C_{90kHz} = \frac{1}{(2*\pi*90*10^3)^2*47*10^{-6}} = 6.65uF (4.61)$$

From this value to achieve the resonant frequencies 79kHz to 89kHz Table 4.3 provides the capacitance that shall be connected to the base capacitor.

Table 4.3 Schedule of FH channel tuning capacitance for 47µH inductor

Frequency	Channel tuning capacitor
79kHz	1.98nF
80kHz	1.77nF
81kHz	1.56nF
82kHz	1.36nF
83kHz	1.17nF
84kHz	968pF
85kHz	806pF
86kHz	633pF
87kHz	460pF
88kHz	306pF
89kHz	150pF

The instruction set assigning the resonant compensating capacitors to switch ON and OFF and the increment of PWM frequency as part of the FH process is in Fig 4.31 below.

```
157
           if (impedance < 5.0 && currentFrequency < MAX_FREQUENCY) {</pre>
158
              currentFrequency += FREQ_STEP;
              updatePCA9555Channel(1);
159
          } else if (impedance > 10.0 && currentFrequency > MIN_FREQUENCY) {
160
              currentFrequency -= FREQ_STEP;
161
162
              updatePCA9555Channel(2);
163
164
165
          updatePWMFrequency(currentFrequency);
```

Fig. 4.31 FH instruction set

4.9 Receiver Circuit

The receiver circuit arrangement is similar to the transmitter circuit save the rectifier, buck converter and switching regulator controller BM2P129TF-E2 circuit. The receiver coil delivers high frequency AC power to the rectifier. The rectifier is configured with a full bridge

MBR40250G rectifier diode. The rectifier distributes DC voltage, VSEN to the buck converter's GaNFET and switching regulator controller as shown in Fig. 4.32, and Fig. 4.33.

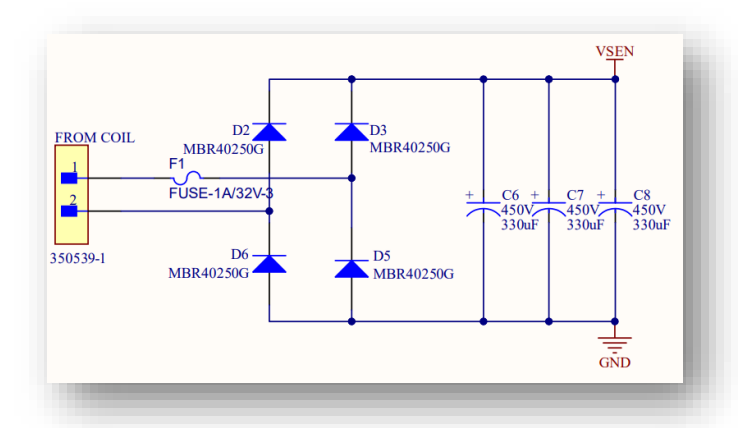


Fig. 4.32 Rectifier circuit

The switching regulator circuit presented in Fig 4.33 converts the DC voltage VSEN to a steady 12VDC to support the operation of the gate driver chip IR2101SPBF-BL which forms part of the control circuit for the buck converter. The 12VDC supply is also delivered to the 12V to 5V linear regulator chip AMS1117-5 which delivers 5VDC supply to the control circuit including the 5V to 3.3V linear regulator chip AMS1117-3.3. The 5V to 3.3V linear regulator chip AMS1117-3.3 in turn delivers 3.3VDC supply to the microcontroller and other control chips in the receiver circuit as previously described.

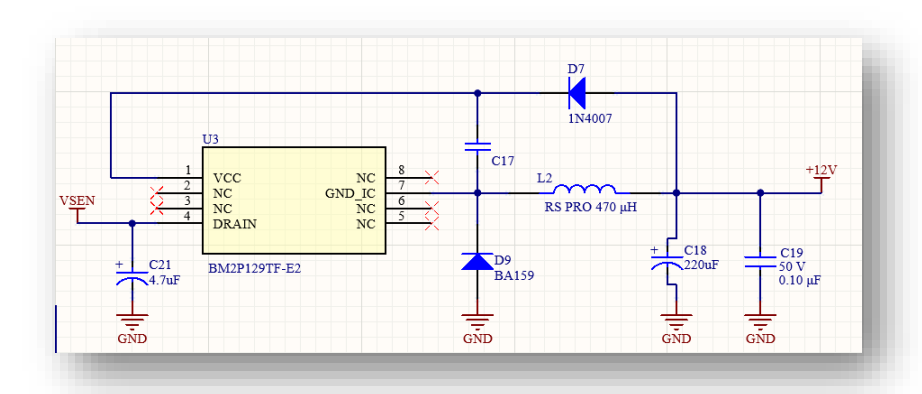


Fig. 4.33 switched regulator circuit

The buck converter converts the rectified voltage VSEN to the desired voltage to drive the battery charger in this case the battery will be charged at 9V. The microcontroller provides the PWM to the gate driver at a 75% duty cycle see Fig 4.34 and Fig. 4.35

```
#define HIN_PIN 25 // HIN for Gate Driver // High-side gate driver input (IR2101SPBF-BL)
#define LIN_PIN 26 // LIN for Gate Driver // LIN for Gate Driver // Low-side gate driver input (IR2101SPBF-BL)
```

Fig. 4.34 buck controller pin assignment

```
29 #define BUCK_PWM_FREQ 85000 // 85kHz PWM frequency
30 #define BUCK_PWM_RESOLUTION 8 // 8-bit resolution
31 #define BUCK_DUTY_CYCLE 191 // 75% duty cycle (191/255)
```

Fig. 4.35 buck controller PWM and duty cycle allocation

The bootstrap circuit constituting diode D1 and capacitor C2 drives the high side GaNFET as shown in Fig 4.36.

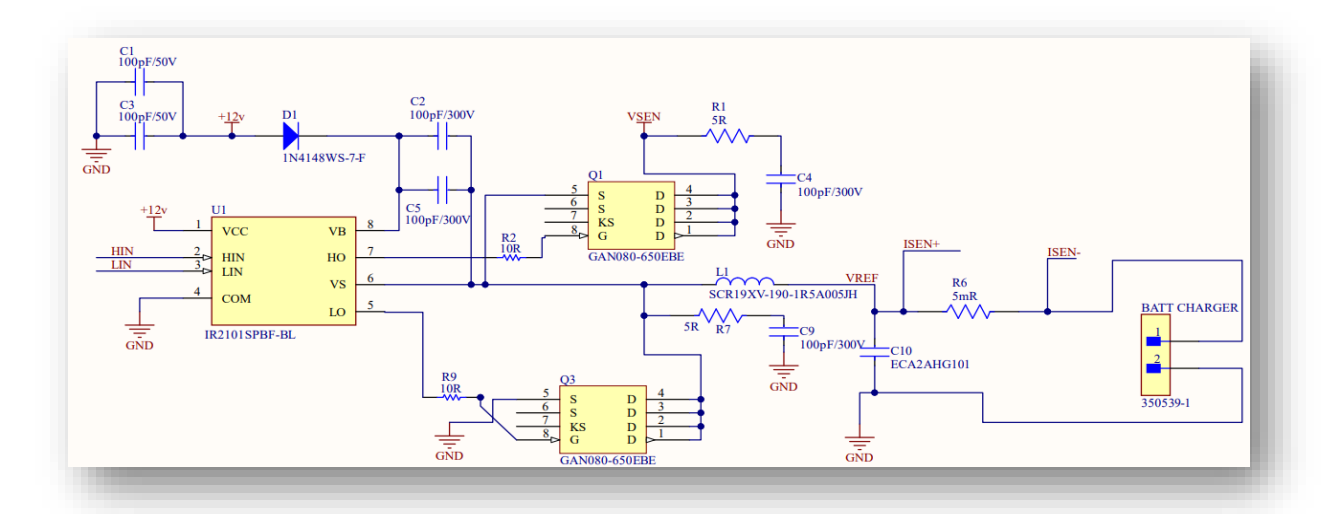


Fig. 4.36 buck controller schematic

4.10 Transmitter and Receiver Communication.

The receiver is designed to have a similar FHWPT hardware and circuit and as such the operating frequencies and FH sequences of the transmitter shall be synchronized with the receiver. It is key to note that the $Z_{feedback}$ of the receiver coil provides information to the transmitter's microcontroller to help detect operational breaches. The microcontroller's wireless communication protocol, ESP-NOW in the transmitter and receiver circuit is used to transfer information. The ESP-NOW communication system has a range up to 200m [125].

The set of instructions in Fig. 4.37 details the structure of the information to be exchanged between the transmitter's and receiver's microcontroller.

```
65. // Structure to send data to Receiver MCU via ESP-NOW
66. typedef struct {
       float frequency;
69.
       int capacitorChannel;
71. } DataPacket;
72. DataPacket data;
74. // Structure to receive data from Receiver MCU via ESP-NOW
75. typedef struct {
       float batterySOC;
77.
       float receivedImpedance;
78.
       float receivedFrequency;
       float batteryChargeRate;
79.
82. } ReceivedData;
83. ReceivedData receivedData;
```

Fig. 4.37 defining basic data exchange between the transmitter and receiver microcontroller. The Table 4.4 below provides the transmitter receiver data type exchange schedule.

Table 4.4 transmitter and receiver data type exchange schedule

Data type	From	То
	microcontroller	microcontroller
Transmitter Operating	Transmitter	Receiver
frequency		
Transmitter Frequency	Transmitter	Receiver
channel		
Battery SoC	Receiver	Transmitter
Receiver impedance	Receiver	Transmitter
Receiver frequency	Receiver	Transmitter
Battery charge rate	Receiver	Transmitter

4.11 Printed Circuit Board

The printed circuit board (PCB) was designed using the Altium Designer Professional version 25.2.1 software. Most of the chips were surface mounted and their respective footprints were designed from scratch. The chip sizes were also determined for space management

and safe placement on the PCB. To enhance the design, there were six separate PCBs, three each for the transmitter and receiver as listed in the Table 4.5 below.

Table 4.5 Schedule of FHWPT PCBs

Serial	РСВ	Function
No.		
1	Transmitter	Generate PWM and wireless power
2	Transmitter Coil	Manage frequency channel switching for main
	controller	coil
3	Transmitter FBC	Manage frequency channel switching for FBC
	controller	
4	Receiver	Receive wireless power and charge battery
5	Receiver Coil controller	Manage frequency channel switching for main
		coil
6	Receiver FBC controller	Manage frequency channel switching for FBC

4.11.1 Transmitter PCB

The transmitter circuit receives 12VDC from an external source via the "12VDC" socket at the top right of the PCB as presented in Fig 4.38. The socket "+3V3", is the 3.3VDC delivery point on the PCB designated to export power to the IO expander chips on the transmitter and transmitter's FBC's FCC PCBs. The socket, "To Coil" is the 12V high frequency AC delivery point to the transmitter and transmitter's FBC's FCC PCB. The sockets "Feedback V" and "Feedback A" are the incoming terminals for sensing the voltage and current signals from the transmitter FBC. The "Data Input" socket is the communication portal for the IO expander. And the "USB1" socket to allows programming and reading outputs from the microcontroller.

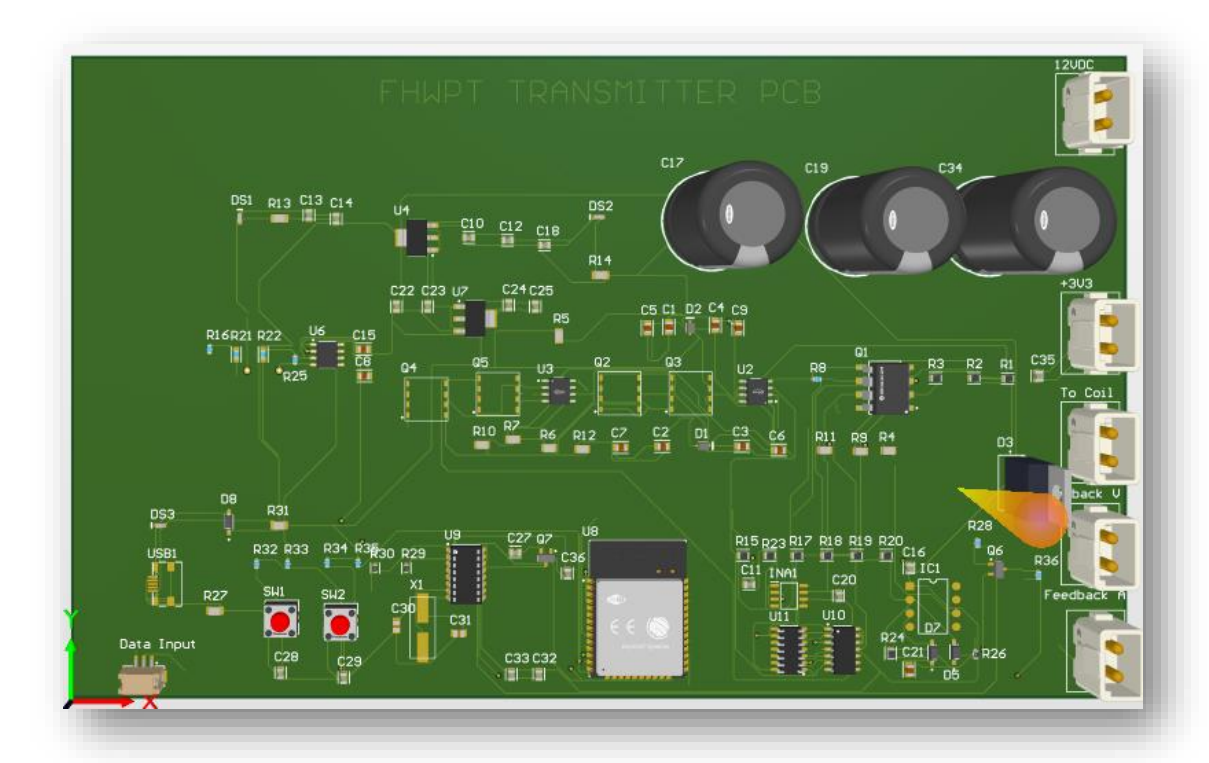


Fig. 4.38 Transmitter PCB layout

4.11.2 Transmitter coil FCC PCB

The transmitter's main coil's FCC PCB is shown in Fig 4.39. Here the socket "TO COIL" is the point of connection for the high frequency AC supply to the Coil. The socket "FROM INVERTER" is the connection point for the inverter's high frequency AC supply from the transmitter's PCB. The socket "Data Input" is the data connection point to IC1 chip from the microcontroller in the transmitter PCB. The socket, "3V3" is the connection point for power supply to the IC1 chip from the transmitter PCB.

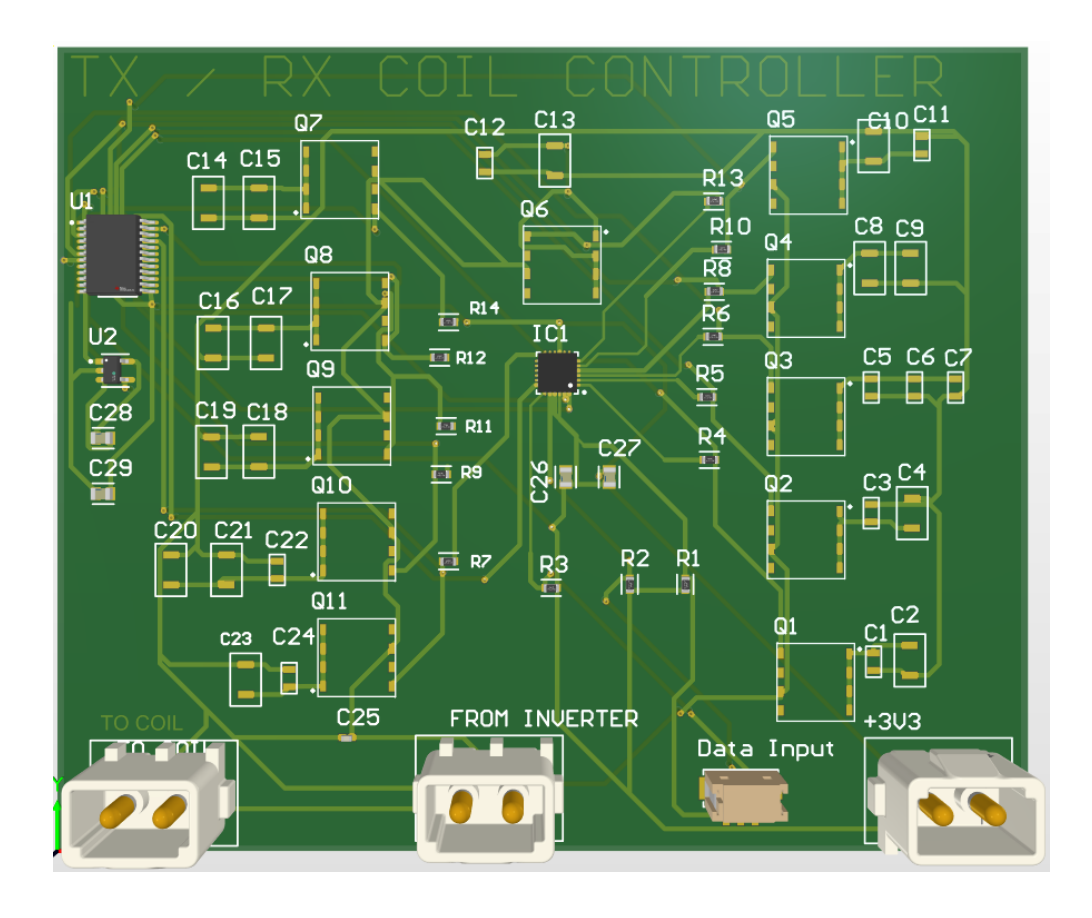


Fig. 4.39 PCB for Transmitter coil FCC layout

4.11.3 Receiver feedback coil FCC PCB

The receiver's main coil FCC PCB is displayed in Fig 4.40. The socket "FROM COIL", is the connection point for the high frequency AC supply from the receiver's coil. The socket "TO RECTIFIER" is the point of connection for the high frequency AC supply to the rectifier. The "Data Input" and "3V3" socket designations are similar to the transmitter's main coil FCC PCB.

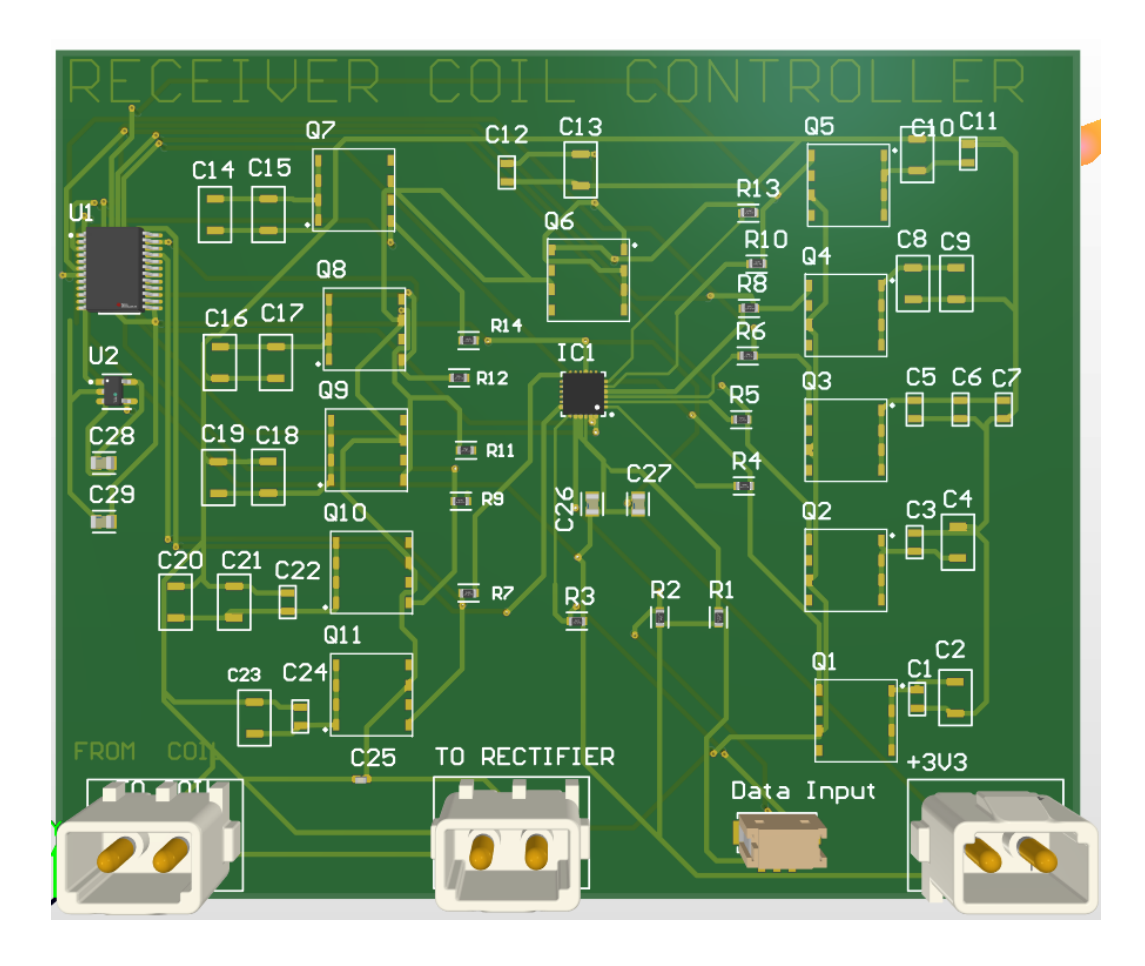


Fig. 4.40 PCB for receiver coil FCC layout

4.11.4 Transmitter or receiver feedback coil FCC PCB

The FCB FCC PCB see Fig 4.41, is dedicated to the FBCs, however for the FBC to resonate in tandem with the transmitter and receiver main coils, the FBCs need to be controlled in parallel. The terminal "FROM COIL" is the connection point for either transmitter or receiver the FBC. Also a, "FEEDBACK" is available to connect the V_{feedback} and I_{feedback} to the voltage and current sensor terminals in the transmitter or receiver PCB. The "3V3" and "Data Input" have the same functionalities as detailed for the main coil FCC PCBs.

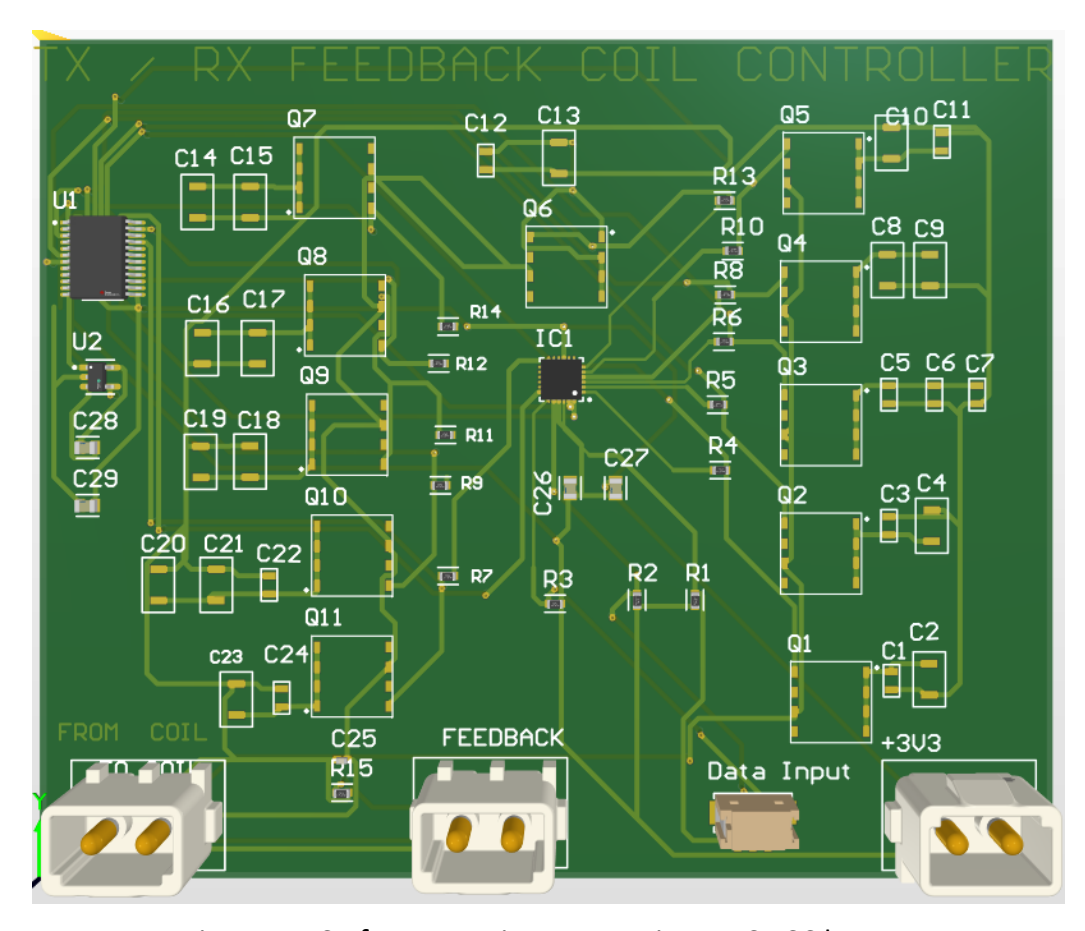


Fig. 4.41 PCB for Transmitter or receiver FBC FCC layout.

4.11.5 Receiver PCB

The receiver circuit, see Fig 4.42 receives a high frequency AC from the receiver coil via the "FROM COIL" terminals at the top right of the PCB. This supply is actually from the receiver FCC PCB. The "+3V3", is the 3.3VDC delivery point on the PCB to supply the IO expander chips on the receiver and receiver FBC FCC PCB. The socket, "BATT CHARGER" is the 9VDC delivery point to the battery charger. The sockets "Feedback V" and "Feedback A" are the incoming terminals for sensing the voltage and current signals from the receiver FBC. This feed actually derived from the FBC's FCC PCB. The "Data Input" 3 pin is the communication portal for the IO expander. And the "USB1" is the socket to allow programming and acquiring data from the microcontroller.



Fig. 4.42 Receiver PCB layout

4.12 Coil placements and optimal load

In this section the positioning of the transmitter and receiver coil and their associated FBCs shall be discussed. In Fig 4.43, the blue and green coils are the receiver main and receiver FBC. The gold and red are the transmitter main and transmitter FBC.

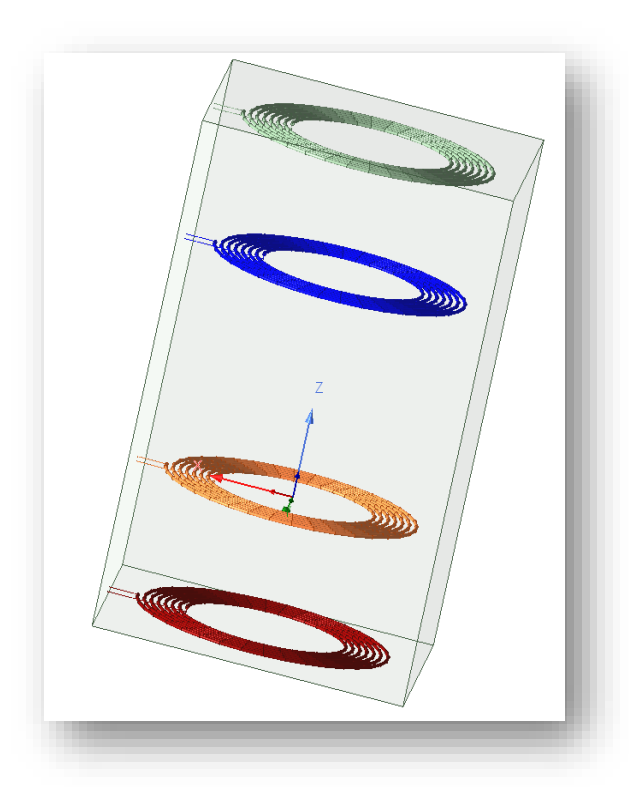


Fig. 4.43 FHWPT coil displacements enclosed in air

The initial step is to determine the PTE that leverages the air gap displacement between the transmitter and receiver coils. To determine the PTE of the transmitter and receiver coils for a $47\mu H$ coil with a radius 13.15 mm, k = 0.2, $R_{load} 2.47\Omega$, $R_s = R_p = 0.6\Omega$, the formula in (2.44) is implemented. Thus,

$$\eta = \frac{25.2*2.47}{(3.07)*(1.842+25.2)} * 100 = 74.5\%$$
 (4.62)

The distance between the main transmitter and receiver coils can be calculated using the formula in (2.50) which gives approximately 18mm.

From determining the power losses in the main transmitter and receiver coils due to the back EMF from their respective FBC, k = 0.5 was used which gives the equivalent displacement 13.15mm. Thus, the blue and green and the gold and red coils in Fig 4.43 are separated by 13.5mm. Whilst the blue and gold coils are separated by 18mm.

4.13 Summary

This chapter details the design work undertaken to develop a FHWPT most of the operation hinges on the resilience of the microcontroller. The PTE was used to determine the k between the main transmitter and receiver coils whilst Lenz law was used to determine the k between the FBCs and their respective transmitter and receiver coils.

The microcontroller depends on the data received from FBC for FH operation. The FBC is held in a fixed position to ensure that the measurands provided to the microcontroller are reliable.

The microcontroller's embedded communication protocol increases the measurands required for decision making, as it allows data to be exchanged from the paired transmitter and receiver circuits. The components for building the prototype are off the shelf and the budget price is relatively moderate for device of such complexity and value in the WPT market. Most of the footprints were not available on Altium Designer Professional software rendering the PCB design journey more educational than time consuming.

The subsequent chapter presents an analysis of the FHWPT and a comparison with a conventional WPT system.

Chapter 5 System analysis and Business Case

5.1 Introduction

In the previous chapter the design of the FHWPT was detailed. In this chapter a wider analysis of the PTE, power losses (P_{loss}), and costs of the FHWPT shall be undertaken.

5.2 Methodology of Frequency Hopping Wireless Power Transfer Analysis

The methodology adopted in this chapter proceeds as follows. First, the figure of merit (FoM) and efficiencies of WPT and FHWPT are compared to highlight performance differences. The determination of the coupling coefficient k, for the FBC is then justified, as it influences system stability. Next, power loss analysis is undertaken, including GaNFET switching losses and coil-related magnetic losses, to identify PTE constraints. A business case is subsequently developed, addressing energy savings, payback, and return on investment (ROI) to assess practical viability. Finally, FHWPT areas of improvement and constraints are discussed. The sequence is illustrated in the flowchart of Fig. 5.1.

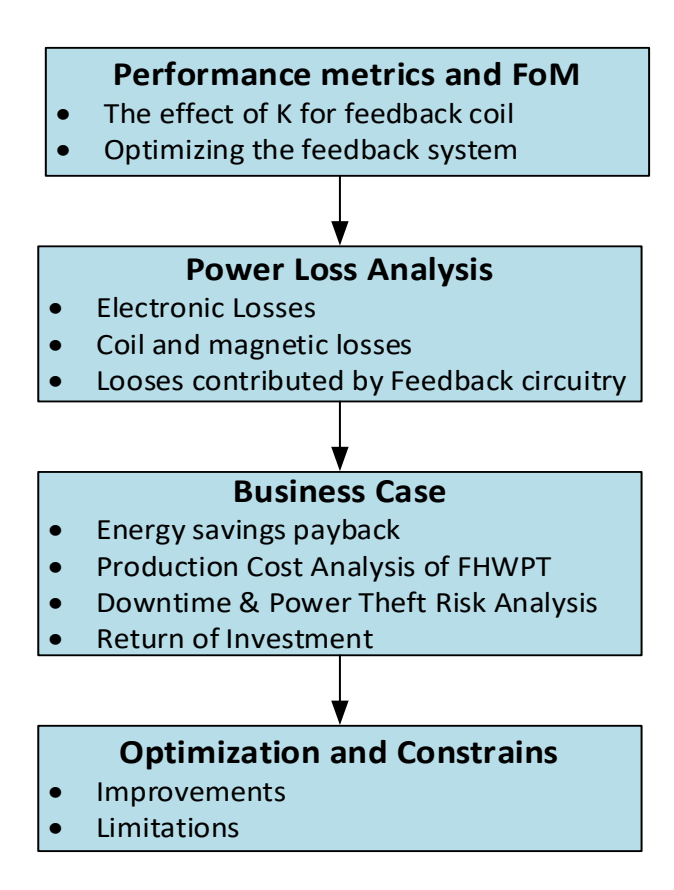


Fig. 5.1 Methodology of FHWPT analysis

5.3 Performance metrics and Figure Of Merit

The Figure of Merit (FoM) shall be used to compare the baseline WPT with FHWPT. Let the WPT use case parameters be L_{WPT} = 47 μ H, r_p = r_s = 0.6 Ω , R_L = 2.47 Ω , f = 85kHz, k = 0.2.

The calculated PTE of a normal WPT based on (2.44) is 74.9%. And the designed FHWPT based on the information in Section 4.13 and (4.62) we have an PTE of 74.5%. It is important to note that the FOM only looks at the unloaded system so the $r_p = r_s = 0.5\Omega$ being the parasitic resistance of the coil [126]. There would not be much difference as both WPT and FHWPT have the same loading characteristics.

Thus, the WPT FOM is

$$FOM_{WPT} = k^2 * Q_{tx} * Q_{rx} = 100.81 (5.1)$$

and the FOM_{FHWPT} is 92.89. The FOM_{FHWPT} is lower due to the introduction of the FBCs as $L_{FHWPT} = L_{effective} = 45.12 \mu H$ (4.54) and the difference is less than 10 concluding that difference in PTE of both systems is negligible.

5.3.1 The effect of k for Feedback Coil

As mentioned in Section 4.7.2 the analysis of Z_{feedback} will be detailed here. From the previous Section we can see a trade off that introducing resilience of the WPT mildly impacts the PTE. Here the analysis undertaken to determine the k of the FBC was undertaken. Table 5.1 below presents the major parameters that will guide the design to ensure the feedback information is reliable and the losses it introduces to the system is minimal.

Table 5.1 parameters to determine k for FBC.

			Distance	
k	$Z_{referred}(\Omega)$	$V_{feedback}(V)$	(mm)	V _{sensor} (V)
0.1	0.00	3.77	22.49	0.07
0.2	0.02	7.53	17.85	0.13
0.3	0.04	11.30	15.59	0.20
0.4	0.06	15.06	14.17	0.27
0.5	0.10	18.83	13.15	0.33
0.6	0.14	22.59	12.37	0.40
0.7	0.20	26.36	11.75	0.47
0.8	0.26	30.12	11.24	0.53
0.9	0.33	33.89	10.81	0.60

Using and impedance of 1570Ω see (4.26) and Lenz law Table 5.1 shows that k between 0.4> k < 0.6 is ideal as $Z_{referred}$ is low enough and provides a simple scaling factor for post processing and analysis. Furthermore, given the order of magnitude of the load, the system operates in an overdamped regime, where the dominant resistive load suppresses oscillatory behaviour. As a result, the bifurcation effect is rendered negligible, and its impact on system dynamics can be reasonably disregarded

5.3.2 Optimizing system – Feedback coil

The existing FBC has the same inductance as the transmitter and receiver coils. To optimize the FBC, an assessment was undertaken to determine the impact if a coil with a lower inductance was coupled to the main transmitter and receiver coils. The optimization of the FBC will reduce the space and cost of the FHWPT to a degree. From the studies undertaken as shown in Fig. 5.2 a 5μ H coil can provide sufficient current and voltage for the voltage and current sensors pick up the current on standby mode when the FBCs experience the highest induction from the main coils.

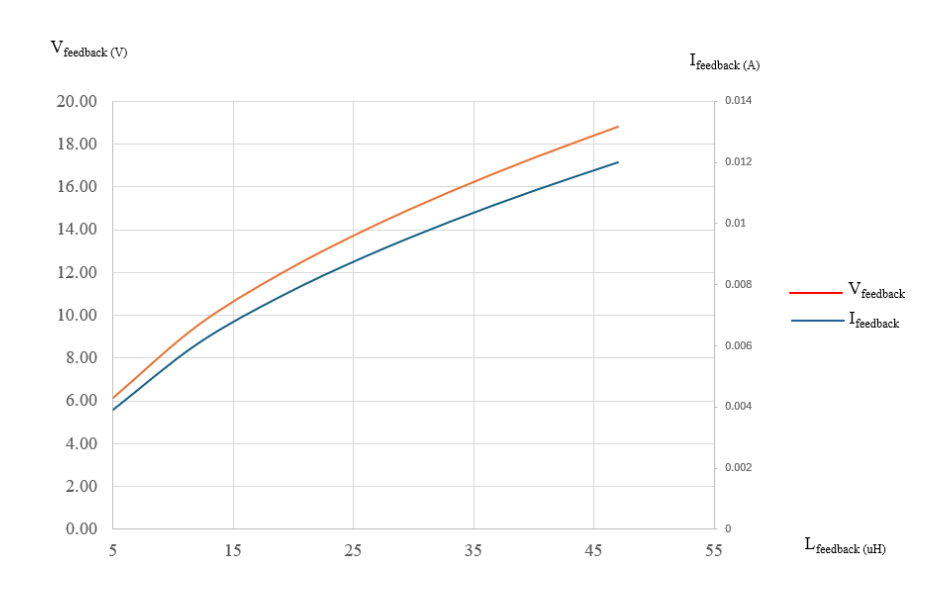


Fig. 5.2 V_{feedback} and I_{feedback} over different L_{feedback} coils (5μH to 47μH)

The chart shows the $V_{feedback}$ and $I_{feedback}$ for FBC with L < 47 μ H from the study it is evident that the FBCs must not have the same self inductance as the main transmitter and receiver coils.

5.4 Power Losses

In this section the losses of the FHWPT shall be analysed. Determining the losses of the system is an important analytical approach for optimizing the PTE of a system. This analysis helps to reduce costs, predict performance, extend system longevity and more essentially for the FHWPT, provide indicators to minimise electromagnetic interferences. The cooling system, component selection are identified from the Ploss analysis as well. From the Ploss analysis, the conduction losses of the initial 2mm diameter wire used to design the coils gave rise to the utilization of the Litz wire with multiple 38 AWG strands. Modelling the losses of a multi strand wire on Ansys was very complicated thus a mathematical model for the coil losses was developed.

5.4.1 Types of losses in WPT

The P_{loss} in the FHWPT can be subdivided into the electronic losses (DC-DC and AC to DC converters), and radiation or magnetic losses (coil losses).

5.5 Electronic Losses

The electronic devices analysed in this section are the GaNFETs and the rectifier diodes. The breakdown of the subcircuits and their associated GaNFETs are in Table 5.2. All information of the GaNFET is in the manufacturer's datasheet [96].

Table 5.2 Schedule of FHWPT subcircuits and Associated GaNFETs

Subcircuit	Number of	Designation
	GaNFETs	
Transmitter	4	Full bridge inverter
Receiver	2	Buck converter
Transmitter & Receiver	22	FH implementation
FCC		
Transmitter & Receiver	22	FH implementation
Feedback FCC		

During a charging session it is expected that only one GaNFETs in all four FCCs will be on at a given time. And all 6 GaNFETs in the transmitter and receiver circuits shall be on.

5.5.1 Transmitter GaNFET Conduction PLoss

We determine the I_{RMS} for the I_{tx} of 1.5A at a 50% duty cycle D, of the full bridge inverter described in Section 4.8.1 thus,

$$I_{RMS} = I_{tx} * \sqrt{D} (5.2)$$

$$I_{RMS} = 1.5 * \sqrt{0.5} = 1.06A (5.3)$$

So, conduction Ploss, for an inverter with an AC current can be calculated as

$$P_{conduction} = I_{RMS}^2 * R_{DS on}$$
 (5.4)

Where $R_{\text{DS on}}$ is the resistance between the drain and source

$$P_{conduction} = 1.06^2 * 190 * 10^{-3} = 0.213W$$
 (5.5)

5.5.2 Transmitter subcircuit Capacitive PLosses

For capacitive losses the formula below is used

$$P_{Coss} = \frac{1}{2}C_{oss} * V_{DS}^2 * F_{sw}$$
 (5.6)

Where C_{oss} and F_{sw} are the output capacitance and frequency switching, 85kHz shall be used in this instance Table 5.3 shows the P_{coss} for other switching frequencies.

$$P_{Coss\ inverter=} = \frac{1}{2} * 70 * 10^{-12} * 144 * 85000 = 0.43 mW$$
 (5.7)

5.5.3 Transmitter subcircuit Poff

The off losses P_{off}, is quite important in that out of the 50 GaNFETs only 10 are used at any given time and 40 are redundant.

$$V_S * I_{DSS}$$
 (5.8)

Where V_s is the Source to ground voltage of 12V and I_{DSS} is Leakage current

$$P_{off \ loss \ inverter} = 12 * 1 * 10^{-6} = 12 \mu W (5.9)$$

5.5.4 Transmitter subcircuit Switch On PLosses

The switch on losses are particular to the inverter and buck converter GaNFETs

$$E_{on} = I_{RMS(on)} * V_{DS} * \frac{t_{fv} + t_{ri}}{2}$$
 (5.10)

Where T_{fv} and T_{ri} are the voltage fall and current rise time of 4ns for the GaNFET. Using the calculated inverters I_{RMS} in equation 5.3 E_{on} is

$$E_{on\ inverter} = 1.06 * 12 * \frac{4*10^{-9} + 4*10^{-9}}{2} = 50.88nJ$$
 (5.11)

$$P_{on\ inverter} = E_{on} * F_{sw}$$
 (5.12)

$$P_{on\ inverter} = 62.4 * 10^{-9} * 85000 = 4.32 mW$$
 (5.13)

5.5.5 Transmitter subcircuit Switch Off PLoss

The P_{loss} due to switch off is similar to the switch on time as the current fall T_{fi} and voltage rise T_{rv} are similar to T_{fv} and T_{ri}

$$E_{off} = I_{RMS(on)} * V_{DS} * \frac{t_{fi} + t_{rv}}{2} = E_{on}$$
 (5.14)

Thus.

$$P_{on\ inverter} = P_{off\ inverter} = 4.32mW$$
 (5.15)

The total Ploss for the inverter is

$$P_{total\ inverter} = (P_{conduction} + P_{switch\ on} + P_{switch\ off} + P_{off} + P_{coss}) * 4 (5.16)$$

$$P_{total\ inverter} = (0.213W + 4.32mW + 4.32mW + 12\mu W + 0.43mW) * 4 = 0.888W$$
(5.17)

5.5.6 Receiver's subcircuit buck controller's GaNFET Conduction PLoss

The buck converter configured with 2 GaNFETs is in the receiver subcircuit hence, the drain to source current I_{DS}, can be determined by the input current I_r from the equation 5.50 and the duty cycle.

$$I_r = \frac{9.4*10^{-6}*1.5}{47*10^{-6}} = 0.3A (5.18)$$

To determine the I_{DS} for the 0.3A input to the buck converter with a 75% duty cycle D as described in Section 4.9 we have

$$I_{DS} = \frac{I_r}{D} (5.19)$$

$$I_{DS} = \frac{0.3}{0.75} = 0.4A (5.20)$$

Thus, P_{loss} due to conduction for the DC current conducted when GaNFETs are on in the buck converter is

$$P_{conduction} = I_{DS}^2 * R_{DS on}$$
 (5.21)

$$P_{condutction} = 0.4^2 * 190 * 10^{-3} = 30.4 mW (5.22)$$

5.5.7 Receiver's subcircuit Capacitive PLoss

Also, the V_{DS} for the buck converter is

$$V_{DS} = Vin * D = 12 * .75 = 9V (5.23)$$

$$P_{Coss\ buck\ conv} = \frac{1}{2} * 70 * 10^{-12} * 81 * 85000 = 0.24 mW$$
 (5.24)

5.5.8 Receiver's subcircuit Poff Losses of Buck converter

From (5.9) we can calculate the off losses thus,

$$P_{off \ loss \ buck \ conv} = 9 * 1 * 10^{-6} = 9 \mu W \ (5.25)$$

5.5.9 Receiver's subcircuit Switch on PLoss

The buck converters normally operate at different switching frequencies. For the FHWPT receiver circuit, the gate driver shall synchronize with the FHWPT system frequency to minimize EMI and inter harmonics. Using the calculated buck converter's I_{DS}, E_{on} is

$$E_{on\ buck\ conv} = 0.4 * 9 * \frac{4*10^{-9} + 4*10^{-9}}{2} = 14.4nJ$$
 (5.26)

$$P_{on\ buck\ conv} = 14.4 * 10^{-9} * 85000 = 1.22 mW$$
 (5.27)

5.5.10 Receiver's subcircuit Switch off PLoss

As expressed in equation (5.15)

$$P_{on\ buck\ conv} = P_{off\ buck\ conv} = 1.22mW$$
 (5.28)

5.5.11 Receiver's subcircuit Total buck converter PLoss

The total power loses for the buck converter is

$$P_{total\ buck\ conv} = (P_{conduction} + P_{switch\ on} + P_{switch\ off} + P_{off} + P_{coss}) * 2$$
 (5.29)

$$P_{total\ buck\ conv} = (30.4mW + 1.22mW + 1.22mW + 9\mu W + 0.24mW) * 2 = 66.18mW$$
 (5.30)

5.5.12 Receiver's subcircuit Rectifier diode Conduction PLoss

The rectifier diode MBR40250 has a forward voltage V_f, of 0.86V as noted in [127]. Thus,

$$P_{diode} = I_r * V_{fwd} = 0.258W$$
 (5.31)

Total Loss of the rectifier is

$$P_{total\ diode} = P_{diode} * 4 = 1.032W$$
 (5.32)

5.5.13 FCC's subcircuit GaNFET conduction PLoss

From Section 4.8 we learn that the GaNFETs are employed as static switches thus, the I_{feedback} = I_{feedback RMS} and from the equation 4.41 we have

$$I_{feedback} = 12mA (5.33)$$

$$P_{conduction} = I_{RMS}^2 * R_{DS on}$$
 (5.34)

$$P_{conduction} = (12 * 10^{-3})^2 * 190 * 10^{-3} = 27.3 \mu W$$
 (5.35)

For 4 GaNFETs switched on at any time the total conduction loss shall be

$$P_{total\ FCC\ conduction} = P_{FCC\ conduction} * 4 = 0.11 mW$$
 (5.36)

5.5.14 FCC's subcircuit Poff losses

The P_{off} losses can be computed from the equation 5.9 as below

$$P_{off loss FCC} = 18.83 * 1 * 10^{-6} = 18.83 \mu W (5.37)$$

For 40 GaNFETs switched off at any time the total conduction loss shall be

$$P_{total\ FC\ off\ loss}\ = P_{off\ loss\ FC}\ *40 = 0.75mW\ (5.38)$$

5.5.15 FCC's subcircuit total PLoss

The total losses of the 4 FCC circuits are

$$P_{total\ FC\ losses} = P_{total\ FC\ condutction} + P_{total\ FC\ off\ loss}$$
 (5.39)

$$P_{total\ FC\ losses} = 0.11mW + \ 0.75mW = 0.86mW \ (5.40)$$

The total losses of the GaNFETs in all subcircuits per operating frequency are presented in Table 5.3. From the results, the percentage difference between 79kHz P_{loss} and 90kHz P_{loss} is 0.321%. Also, the P_{loss} of electronics of the 18W system based on 90kHz P_{loss} is circa 2W.

Table 5.3 Total GaNFET losses in FHWPT

Frequency (kHz)	Inverter's P _{Coss} + P _{switching} (mW)	Inverter's P _{Conduction} + P _{off} (W)	Buck converter' s P _{Coss} + P _{switching} (mW)	Buck converter' s P _{Conduction} + P _{off} (mW)	FCC Pconduc tion + Poff (mW)	Rectifier losses (W) P _{diode}	Total P _{loss}
79	41.02944	0.852048	4.99833	60.8	0.86	1.032	1.991754
80	41.5488	0.852048	5.0616	60.8	0.86	1.032	1.992336
81	42.06816	0.852048	5.12487	60.8	0.86	1.032	1.992919
82	42.58752	0.852048	5.18814	60.8	0.86	1.032	1.993502
83	43.10688	0.852048	5.25141	60.8	0.86	1.032	1.994084
84	43.62624	0.852048	5.31468	60.8	0.86	1.032	1.994667
85	44.1456	0.852048	5.37795	60.8	0.86	1.032	1.99525
86	44.66496	0.852048	5.44122	60.8	0.86	1.032	1.995832
87	45.18432	0.852048	5.50449	60.8	0.86	1.032	1.996415
88	45.70368	0.852048	5.56776	60.8	0.86	1.032	1.996997
89	46.22304	0.852048	5.63103	60.8	0.86	1.032	1.99758
90	46.7424	0.852048	5.6943	60.8	0.86	1.032	1.998163

A figure of merit can be established to quantify the P_{loss} difference between a standard WPT system and a FHWPT system in terms of GaNFET P_{loss} . The FCC P_{losses} from Table 5.3 is 0.86mW thus, the percentage P_{losses} contributed by the FCC is circa 0.043%.

Standard WPT Ploss is

$$P_{WPT\ losses} = (P_{inverter} + P_{buck\ conv} + P_{rectifier} + P_{diode})$$
 (5.41)

The pessimistic case for FHWPT P_{loss} , as reported in Table 5.3, occurs at the maximum operating frequency of 90 kHz thus,

$$P_{FHWPT\ losses\ max\ frequency} = (P_{inverter} + P_{buck\ conv} + P_{rectifier} + P_{diode} + P_{FCC})$$
 (5.42)

Where P_{FCC} is the combined losses of the FCC, the FOM between the WPT at 85kHz and the FHWPT at 90kHz is

$$FOM_{GaNFET} = \frac{P_{FHWPT\ losses} - P_{WPT\ losses}}{P_{WPT\ losses}} * 100 = \frac{0.86*10^{-3}}{1.99525} = 0.043\% (5.43)$$

This value indicates an insignificant electronic Ploss of the FCC.

5.6 Coil and magnetic losses

In this section the losses in the coils shall be analysed.

5.6.1 Copper losses

The copper losses P_{cu} are due to the parasitic resistance in the coil, from Section 5.3 we gather that the resistance of the coil is 0.5Ω . The $I_{feedback}$ is 12mA, I_{tx} RMS 1.06A from equation (5.3) and I_r is 0.3A thus, the I_{RMS} for these currents are

$$I_{rx RMS} = 0.3 * \sqrt{0.5} = 0.212A (5.44)$$

$$I_{feedback RMS} = 12mA * \sqrt{0.5} = 8.49mA$$
 (5.45)

The coper losses can be computed with the formula below and the results are in Table 5.4.

$$P_{cu} = I_{RMS}^2 * R_{coil}$$
 (5.46)

5.6.2 Skin effect losses

The skin effect losses in the $47\mu H$ coils will be analysed in this section. Apparently, the manufacturers data sheet for the coil as noted in [103] does not provide the P_{loss} data and key coil information so assumptions have been made. The assumptions made are the coil number of turns N, strand diameter of 38 AWG magnet wire, 0.1016mm, and the number of strands in the Litz wire.

Given that L =47 μ H, coil radius 13.15mm, frequency 85kHz. For the copper wire resistivity ρ , =1.68×10⁻⁸ Ω .m, skin depth δ = 0.227mm. From Section 4.3 the R_{dc} of the single 38 AWG strand is 659.6m Ω /m. To determine N, we can use the coils outer diameter and Litz wire diameter. We know from the coil and magnet wire manufacturer's data sheet that the coil

 R_{dc} is 0.5Ω and the R_{dc} of 38AWG is 659.6m Ω/m respectively thus, the length of a strand of wire can be determined. See excerpt from the manufacturers data sheet in Fig. 5.3.

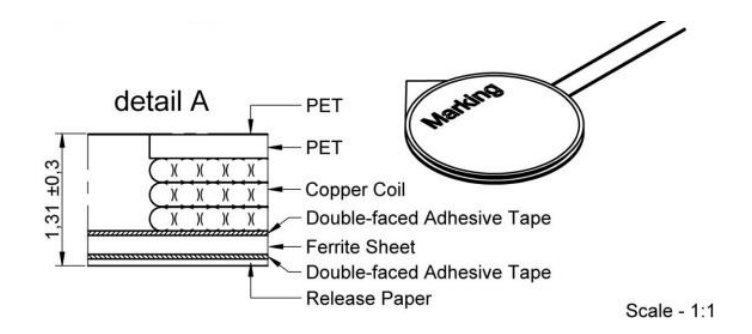


Fig. 5.3 Cross section of the coil indicating diameter of Litz wire. [98]

From Fig. 5.3 the diameter d, is estimated to be approximately 0.333mm.

We can now solve for Rac

$$R_{ac} \approx R_{dc} * \frac{r}{\delta}$$
 (5.47)
 $R_{ac} \approx 0.5 * \frac{0.1665}{0.227} = 0.366\Omega$ (5.48)

Thus Ploss due to Rac is

$$P_{ac} = I_{RMS}^2 * R_{ac}$$
 (5.49)

The results for the Pac for all coils are in Table 5.4

5.6.3 Eddy Current Losses

For us to determine the P_{loss} due to eddy currents P_{eddy} , we require the P_{eddy} per unit volume and the volume of the Litz wire used. This, in turn, depends on the magnetic flux B, in the different coils when a current I_{tx} , I_{rx} or $I_{feedback}$ flows through them.

The Eddy current losses per volume is given by the formula

$$P_{eddy} = \frac{B_{rms}^2 * d^2 * f^2 * \pi^2}{6*\rho} (5.50)$$

Where B_{RMS} is the magnetic flux density in Tesla, d is the diameter of coil 0.333mm, and ρ is the electrical resistivity of copper 1.68*10⁻⁸ Ω m. Also B_{RMS} is given by the formula

$$B_{rms} = \frac{\mu_0 * N * I}{2r}$$
 (5.51)

Where r from Section 5.10 is 13.15mm, I varies with the coil's function i.e 1.5A for I_{tx} , 0.3A for I_{rx} or 12mA for $I_{feedback}$

From the geometry of the coil having an outer diameter of 26.3mm and assuming an inner diameter of 2.3mm and 3 stacks of windings we can determine the number of turns N, algebraically. Thus,

$$N = \left(\frac{\frac{D_{outer} - D_{inner}}{2}}{d_{Litz}}\right) * 3 \approx 108 (5.52)$$

Solving for B_{rms} for I_{tx} flowing through the transmitter coil we have

$$B_{rms} = \frac{4*\pi*10^{-7}*108*1.5}{2r} = 7.74$$
mT (5.53)

For I_{rx} and I_{fb} Brms is 1.54mT and 61.9uT respectively.

Based on the assumptions the P_{eddy} is solved below.

$$P_{eddy.m^3 \ tx \ coil} = \frac{\pi^2*(7.74*10^{-3})^2*(0.333*10^{-3})^2*(85000^2)}{6*1.6810^{-8}} = 4.7 MW/m^3 \ (5.54)$$

Assuming the Litz wire is composed of a 38 AWG magnet wire (strand) and a packing factor of 1.155 as detailed in [128] we can then determine the number of strands. First, we calculate the cross section area (CSA).

Litz_{CSA} =
$$\frac{\pi}{4} * .333 * 10^{-3^2} = 0.0871 mm^2$$
 (5.55)

Solving for the CSA of a single strand of 38 AWG

Strand_{CSA} =
$$\frac{\pi}{4} * 0.1016 * 10^{-3^2} = .811 mm^2$$
 (5.56)

Thus, number of strands

Number of strands =
$$\frac{87.1*10^{-9}*1.15}{8.11*10^{-9}} = 12.5 \approx 12$$
 (5.57)

To calculate the volume we need to determine the length I, of the wire thus,

$$l_{wire} = \frac{coil R_{dc} \Omega}{12 strands in nll \Omega/m} (5.58)$$

$$l_{wire} = \frac{0.5\Omega}{55m\Omega/m} = 9.09m (5.59)$$

The length of 9.09m is purely an academic result based on the assumptions. From the Litz_{CSA} and l_{wire} the volume of the Litz wire for the coil is $0.792*10^{-6}$ m³ we can calculate P_{eddy}

 $P_{eddy} = volume \ of \ conductor * P_{eddy \ per \ unit \ volume} = 3.7W \ (5.60)$

Peddy for the other coils are in Table 5.4 below

Table 5.4 Summary of Plosses on the coils at 85kHz and 90kHz

P _{loss}	Transmitter coil	Receiver coil	FC coils (uW)	Total Pcu (W)
	(W)	(mW)		
P _{cu}	0.568	22.47	72	0.59
P _{ac(85kHz)}	0.824	33	105.4	0.857
P _{eddy(85kHz)}	3.7	147	238	3.847
P _{ac(90kHz)}	0.851	34	108.9	0.885
P _{eddy(90kHz)}	4.17	165	266	4.33

5.6.4 Comparison of 90kHz and 85kHz system losses

The difference of P_{losses} at 90kHz compared to 85kHz in the GaNFETs, coil's copper, skin depth and eddy currents losses for the FHWPT system is 0.546W. Thus, it can be concluded that the additional P_{losses} of the 18W FHWPT at 90kHz is <1W. Table 5.5 shows the coil P_{losses} at 85kHz and 90kHz. Also, the P_{losses} at 85kHz is 7.3W most of the P_{losses} is contributed by the assumed P_{eddy} . Table 5.5 presents the P_{losses} of the FHWPT when operating at 85kHz and 90kHz.

Table 5.5 85kHz and 90kHz Plosses.

P _{loss}	85kHz	90kHz	Differential P _{loss}
			(W)
P _{cu}	0.59	0.59	-
P _{ac}	0.857	0.885	0.028
P _{Lenz}	0.226	0.253	0.027
P _{eddy}	3.7	4.33	0.63
P _{GaNFET}	1.99525	1.998163	0.003
Total differential	7.3W	8.05W	0.69
P _{loss}			

5.7 P_{losses} contributed by the FCC subcircuits

The pie chart in Fig. 5.4 below shows a visualised allocation of the 7.3W P_{losses} in the FHWPT system. From the chart it is evident that over 50% of the P_{losses} are dissipated from the transmitter subcircuit. Another interesting fact is that less than 1% of P_{losses} are attributed to the FBC and FCC subcircuits. This is a basis to state the FCC subcircuit contributes negligible P_{losses} to the system. The FCC subcircuit improves the FHWPT's reliability and resilience at negligible operational costs.

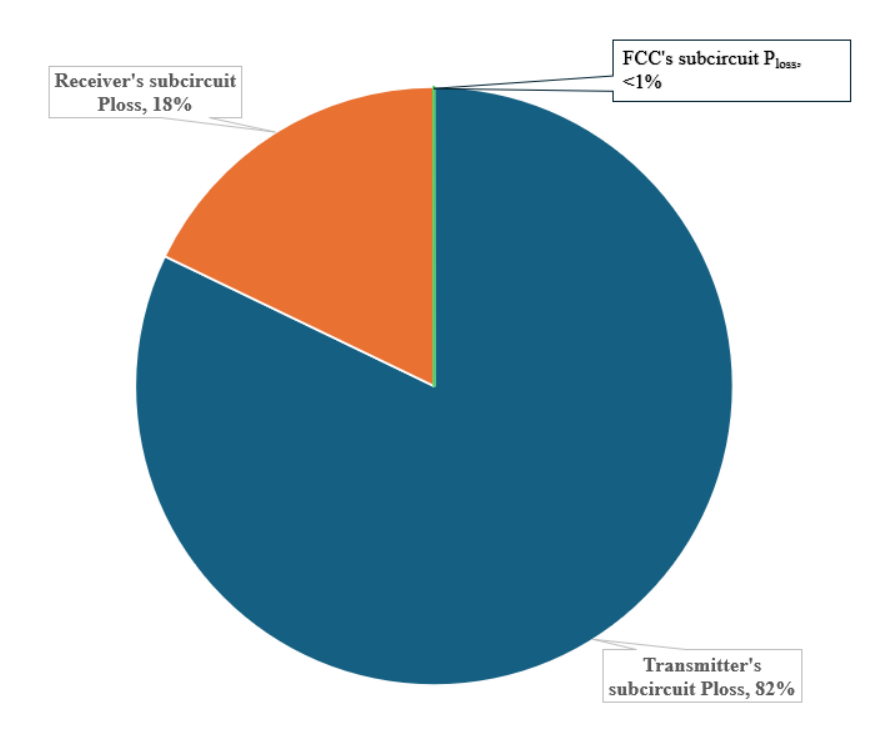


Fig. 5.4 Distribution of Ploss in FHWPT

5.8 Business Case

In this section we will briefly use the analysis generated to determine the percentage cost difference between the WPT and FHWPT. In Appendices 2 to 4 the bill of materials and PCB costs are detailed. The cost allocation for the FHWPT will be analysed by each subcircuit of the FHWPT i.e. the transmitter, receiver and FCC subcircuit Fig 5.5 below shows that 47% of the FHWPT costs is allocated to the FCC subcircuit. It can be concluded from this design, excluding mass production costs that an FHWPT is almost 50% more expensive than a WPT.

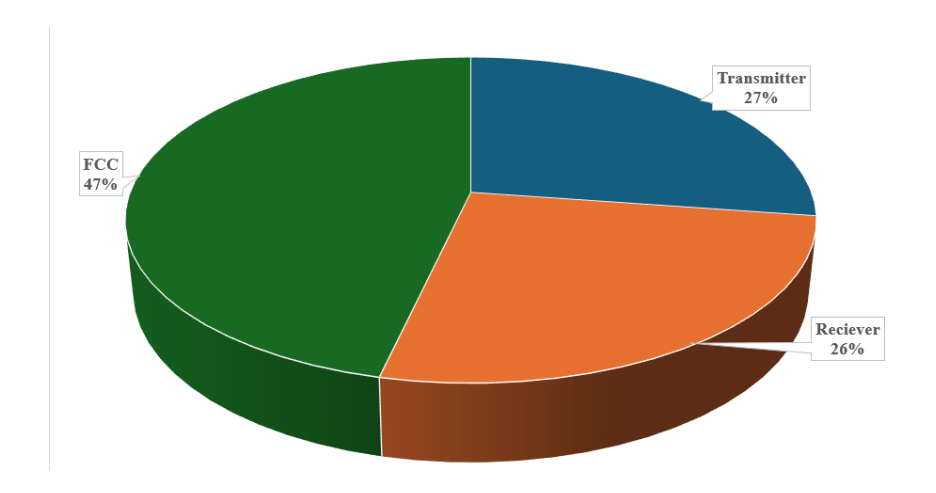


Fig. 5.5 Cost allocation for FHWPT

5.8.1 Energy savings payback

From the PTE calculations undertaken, the difference in PTE when the FHWPT increases from 85kHz to 90kHz is negligible. Thus, there is no strong business case for a FHWPT based on energy savings.

Recently there has been a rise of vandalizations of conductive electric chargers and their associated downtime, which leads to assume that the likelihood of interruptions during a charging session is moderate but severe. Hence, it is necessary to secure a charging session. To this end, the ROI can be justified by procuring a resilient and robust FHWPT.

FHWPT is a next generation WPT architecture engineered not only for higher PTE but for resilience, security, and system integrity in the face of growing electromagnetic congestion and energy theft risks. It's a solution for tomorrow's interference prone, intelligence driven energy ecosystems.

5.8.2 Production Cost Analysis

In this section the production cost of the WPT and FHWPT shall be analysed. Table 5.6 presents a cost breakdown of prototype and mass production for WPT and FHWPT systems excluding the coils. The qualitative framework is adapted from [129], while quantitative figures are referenced within Table 5.6.

Table 5.6 Cost Structure of Prototype (excluding coils) and scale of economy

System	Prototype			Mass Production (1,000+)			
	РСВ	Casing [131]	Total	PCB [130]	Casing [131]	Total	
Standard	£795	£20	£815	£318	£2	£320	
WPT							
FHWPT	£1470	£30	£1,500	£588	£3	£591	

The costs for the WPT and FHWPT systems, £795 and £1470 respectively are derived from the total Bill of Materials (BOM) for the circuitry, as detailed in Appendices 2 and 3. PCB are derived From the Table 5.6, FHWPT costs about 46% more per unit than a conventional WPT, but it's engineered for what a WPT cannot handle. With volume scaling (1,000+ units), production costs for a FHWPT unit drops by circa 60%, cutting the per-unit price from £1,500 to £591.

These costs do not include the coils. The FHWPT requires four coils, whereas the WPT requires two. At this stage, it remains undecided whether bespoke coils will be developed for the FHWPT or whether standard off-the-shelf coils will be procured to facilitate ease of replacement. While bespoke coils could be optimised for PTE, off-the-shelf coils may provide greater practicality in terms of availability, cost reduction, and maintainability

5.8.3 Downtime and Power Theft Risk Analysis

Here, the operational losses are quantified, which conventional WPT systems are unable to mitigate. In Table 5.7 the main features of the FHWPT are presented.

Table 5.7 Salient features of FHWPT versus WPT

Feature	Standard WPT	FHWPT
Frequency Jamming Resilience	None	Yes via FH
Power Theft Detection	None	Yes via impedance detection
Self-Adaptive Matching	None	Yes
Real-Time Diagnostics	None	Yes
Mission-Critical Ready	None	Yes

Based on a hypothetical forecourt comprising 20 WPT units where a WPT unit is £5K and a FHWPT is 50% more expensive thus, £7.5K. The cost and risk analysis associated with downtime is presented in Table 5.8. The costs are calculated based on a charge rate of £0.40 per kWh and a nominal charging rate of 30 kWh, resulting in an average session cost of approximately £12 per charger. A power theft incident is assumed lasts for 12 hours while a frequency Jam is assumed to disrupt for an hour.

Table 5.8 Downtime and Power theft risk analysis

Risk Type	Incidents/Year	Cost per Incident	Annual Loss (WPT)
Power Theft	4	£2880	£11,520
Frequency	3	£240	£720
Jamming			
Total			£12,240

From Table 5.8 we can see that the FHWPT neutralizes both risks and pays for itself after just a couple of major events are avoided.

5.8.4 Return on Investment

The ROI is actually the return on intelligence, i.e. the intelligence exhibited by the FHWPT. Below are factors that can quantify the return on intelligence

- Break-even in less than 4 years, even with higher unit cost.
- Payback accelerates at scale as FHWPT unit cost drops below £100.
- Offers non monetary ROI: uptime, trust, regulatory peace of mind and reputation.
- Future-proof: ready for AI-enabled diagnostics, secure edge control, and smart-grid compliance.

On can say "Conventional WPT moves power. FHWPT protects it." In an era where power theft and jamming are no longer theoretical, FHWPT turns vulnerability into visibility and cost into control.

5.9 Optimization and limitations

The findings from this research highlight areas where the FHWPT system demonstrates significant potential for optimization, particularly in enhancing PTE and system resilience. At the same time, the study reveals constraints, which delineate the practical boundaries of the technology.

5.9.1 Improvements

The coil has a parasitic resistance of 0.5Ω if future design coil has a parasitic resistance of 0.05Ω to 0.1Ω it will increase the PTE of this FHWPT to 94%.

Another area for improving PTE, in addition to reducing coil parasitic resistance, is by implementing intelligent algorithms within the microcontroller to dynamically select the optimal operating frequency. With the intelligence provided by the FBC, the microcontroller can compute the R_{load} from the reflected impedance formula (2.44). The microcontroller can forecast if R_{load} is the optimal load, if the R_{load} is not, then the microcontroller can initiate a hop to a frequency that will improve the PTE as presented in Section 3.3.1. Notably, Section 3.3.1 demonstrates a frequency sweep extending up to 400 kHz; in the proposed FHWPT system, the 400 kHz channel could be reserved as a dedicated "PTE booster" frequency. Although 400 kHz lies outside the SAE-recommended operating bands, further investigation into potential human health impacts due to exposure at this frequency could determine its viability for practical deployment.

Another potential improvement in the PTE of the FHWPT is to adjust the buck controller to emulate the optimal load resistance R_{opt} whenever the microcontroller detects a low PTE during charging. This approach mitigates PTE degradation and prevents the FHWPT from operating outside the SAE J2954 frequency bandwidth

5.9.2 Limitations

The limitations to the design of the FHWPT are dependent on the microcontroller's agility and response to anomalies during the charging session. The microcontroller's clock and central processing unit's (CPU) speed could be low. Also, the random access memory's (RAM) capacity and the analogue to digital conversion (ADC) rates could be low. All these factors could lead to a slow response to interruptions thus, delaying the FH.

An additional constraint is the impact of environmental pickup noise. The FBC is dependent on electromagnetic waves and any disruptions could influence the signal fed back to the microcontroller. For instance, if the FHWPT is installed in proximity to a 400kV phase to phase transmission line, we can determine the electric field strength E, [132]-[134].

$$E = \frac{V}{h} = V/m$$
 (5.61)

Where V is the transmission line's phase to ground voltage of 230kV and h is the height of transmission line above ground at point of sag 10m thus,

$$E = \frac{23000}{10} = 23kV/m (5.62)$$

The parasitic capacitance C_p within around the 400kV phase to phase transmission line can be calculated thus,

$$C_p = \frac{2\pi\varepsilon_0}{\ln\left(\frac{2h}{r}\right)} * l F/m$$
 (5.63)

Where C, ε_0 , r, I are the capacitance to ground, permittivity in a vacuum 8.854×10⁻¹² F/m, radius of transmission line 15mm, length between towers 400m, respectively. Thus

$$C_p = \frac{2\pi * 8.854 \times 10^{-12}}{\ln(\frac{2*10}{15*10^{-3}})} * 400 = 3.09 \, nF$$
 (5.64)

The resulting electric field E, circa 23kV/m under the 230kV phase to ground transmission line creates a capacitive ground coupling of about 3nF. This capacitive displacement currents

could inject common-mode currents that can create noise or distort feedback voltage waveforms in the FHWPT circuitry. This common mode current I_{cm} , can be calculated as shown below.

$$I_{cm \ peak} = C_p * \frac{dV}{dt} = C_p * 2\pi f V_{peak} \cos(2\pi f t)$$
 (5.65)

Where f is the power system voltage frequency of 50Hz thus

$$I_{cm \ peak} = 3 * 10^{-9} * 2\pi * 50 * 230 * 10^{-9} = 0.22A$$
 (5.66)

From the calculations 0.22A can be flowing in the electronic circuits, chassis and ground paths causing wrong calculation. This can be mitigated by shielding all the circuitry and coils.

A further constraint involves the impact of the ambient temperature. Most components are fully operation between 5°C to 35°C. Being that this equipment will be installed outdoors in a non-controlled environment it will be exposed to ambient temperature that falls outside this range. In the case of extreme cold it could take longer for the GaNFETs to conduct if left on standby mode. Also, in extreme heat the resistance of the coils could increase and affect the PTE as copper's resistivity increases about 0.4% per °C. As temperature coefficient of resistance for copper is about 0.00394 per degree Celsius [134].

Heat sinks assigned to the GaNFETs and other switching devices and forced cooling can effectively mitigate the increased thermal load. However, the temperature dependent rise in parasitic resistance of the coil remains a concern. This degrades the quality factor Q of the coil thus, thermal management strategies must ensure low resistance Litz wire are used and well-ventilated coil bobbins or support frame.

5.10 Summary

The analysis undertaken in this section indicates that although the FCC's subcircuit contributes almost 50% of the additional cost compared to a conventional WPT of similar rating, its operational costs remain negligible. Furthermore, the resilience introduced by the FCC only requires a onetime investment and does not incur extra running costs. The summary also shows the important role of managing eddy currents as the P_{eddy} contribution is significant.

Chapter 6 Conclusion

The research questions presented in Section 1.3 have been successfully addressed. Firstly, the interoperability of existing WPT EVs and chargers was demonstrated to be achievable by retrofitting Double-D Quadrature (DDQ) and Quadruple coils and by standardizing coil designs. Secondly, it was established that WPT systems can maintain functionality under adverse conditions through the deployment of FH. Thirdly, the adaptability of existing WPT circuitry to different operating frequencies was confirmed by integrating a FBC, capacitive bank, sensors, and updated microcontroller firmware. Furthermore, while current WPT designs are not inherently future proof, by enforcing interoperability schemes and the incorporation of FH offers future ready resilience. Finally, it was shown that WPT operations can be secured and made robust against interferences through the implementation of FHWPT.

The novelty of this research lies in the first time application of FH techniques, widely established in secure communication systems, to the domain of WPT within the SAE J2954 frequency band. Unlike conventional WPT systems that operate at fixed resonant frequencies and are highly susceptible to interference, misalignment, and unauthorized power diversion, the proposed FHWPT introduces a frequency channel control subcircuit that enables real-time hopping across 12 rastered 1kHz channels. The system further integrates a feedback mechanism via an inductively coupled coil with voltage and current sensing to provide dynamic adaptation, along with an impedance detection unit for security and alignment monitoring. The combined hardware design including GaNFET based inverters, rectifiers, and modular PCB architecture demonstrates a holistic, frequency-flexible WPT platform. These contributions advance the state-of-the-art by offering a secure, adaptive, and resilient WPT architecture with practical feasibility for next generation EV charging infrastructure.

This thesis adopted the FH scheme commonly used in both conventional and covert communications for application in the WPT operations. The FHWPT is designed to operate within the SAE J2954 frequency band (79kHz to 90kHz). The major contributions of this thesis include

- Identification and characterization of the distinct linear region in the PTE frequency relationship, highlighting a proportional increase in PTE with frequency prior to the asymptotic region. In addition to this, the revelation of the quantified influence of load resistance on WPT PTE-frequency relationship. The shows that increased load resistance up to 10Ω improves the PTE at higher frequencies up to 300kHz.
- Selection and justification of the SS topology for its consistent ZPA and impedance matching.
- Introduction of a frequency channel control subcircuit that enables 12 rastered 1kHz channels between 79kHz and 90kHz by configuring a capacitor bank connected to the coil's inductance to generate discrete resonant operating frequencies.
- Design of a feedback mechanism using a coil inductively coupled to the main transmitter
 and receiver coils. This FBC is connected to voltage and current sensors to provide
 dynamic operating conditions to each of the microcontrollers in both transmitter and
 receiver units.
- Integration of an impedance detection system to detect coil misalignment, power theft and frequency jamming.

To realize the proposed FHWPT system, the full hardware design of the proposed FHWPT has been completed with all components prepared for procurement, fabrication and integration. The implementation covers all subcircuits required for the full automation of the proposed FHWPT. This includes power electronics, control and PCB design. The following components have been fully prepared and will be assembled and validated in advance of the viva:

- Full-bridge GaNFET inverter designed for operation within the SAE J2954 frequency band (79 to 90 kHz), using IR2101 gate drivers.
- Full bridge rectifier and associated buck converter using IR2101 gate drivers in the receiver circuit.
- FCC subcircuits composed of GaNFETs, capacitors, IO expander a multiplexer and voltage doubler to supporting real time FH.
- IDC designed to detect misalignment and unauthorized loading.

- ESP32 microcontroller programmed to govern and execute all operations of the FHWPT.
- PCB fully developed in Altium Designer with about 70% of the schematic and PCB component footprints created.
- Modular system architecture prepared for integration and future extensibility to multi coil or dynamic charging scenarios. And to demonstrate the ability to retrofit into an existing WPT.

The result and validation from the analytical studies show that the FCC subcircuit introduces about 47% extra costs to that of a normal WPT. However, the power losses due to the FCC is minimal. This goes to say that the FHWPT presents a more robust WPT system with more upfront cost but negligible running costs.

Future work will aim to explore the following

- Multi-receiver FHWPT architectures for dynamic vehicle charging
- Machine learning based predictive FH for faster adaptation.
- Full system EMI compliance aligned with International Special Committee on Radio
 Interference (CISPR) standards for operating frequencies up to 400kHz.
- The feasibility of retrofitting FCC modules of the FHWPT in existing WPTs and EVs to enhance interoperability.

This work demonstrates the feasibility of implementing of FH in wireless power systems, combining analytical rigour, hardware implementation, and system-level integration. The proposed FHWPT system contributes a secure, efficient, and adaptive architecture ready for further development into next generation EV charging platforms.

Appendix 1 Publications arising from research

- 1. G. Blankson, M. Darwish and C. S. Lai, "Wireless Power Transfer System for Electric Vehicle Charging with Frequency Hopping A Concept and Circuit Design," *2023 58th International Universities Power Engineering Conference (UPEC)*, Dublin, Ireland, 2023, pp. 1-6, doi: 10.1109/UPEC57427.2023.10294567
- 2. G. Blankson, M. Darwish, and C. S. Lai, "Frequency Hopping Wireless Power Transfer within the SAE J2954 Operating Frequency Bandwidth—A Concept Design," in *2024 59th International Universities Power Engineering Conference (UPEC)*, Cardiff, UK, Sep. 2–6, 2024, pp. 1–5, doi: 10.1109/UPEC61344.2024.10892393.

Appendix 2 Transmitter subcircuit PCB

					Supplier Subtotal
Description	Designator	Manufacturer 1	Supplier 1	Supplier Part Number 1	1
Litz wire Coil 0.1mm 38AWG		BLOCK	RS	337-7088	25.44
CONN HEADER VERT 2POS 5.08MM	+3V3	TE Connectivity	Mouser	571-3505391	1.1
CONN HEADER VERT 2POS 5.08MM	12VDC	TE Connectivity	Mouser	571-3505391	1.1
General Purpose Ceramic Capacitor, 0805, 100pF, 1%, C0G, 30ppm/°C, 100V	C1	Kyocera AVX	Farnell	2332691	0.30779
General Purpose Ceramic Capacitor, 0805, 100pF, 1%, C0G, 30ppm/°C, 100V	C2	Kyocera AVX	Farnell	2332691	0.30779
General Purpose Ceramic Capacitor, 0805, 100pF, 1%, C0G, 30ppm/°C, 100V	C3	Kyocera AVX	Farnell	2332691	0.30779
General Purpose Ceramic Capacitor, 0805, 100pF, 1%, C0G, 30ppm/°C, 100V	C4	Kyocera AVX	Farnell	2332691	0.30779
General Purpose Ceramic Capacitor, 0805, 100pF, 1%, C0G, 30ppm/°C, 100V	C5	Kyocera AVX	Farnell	2332691	0.30779
General Purpose Ceramic Capacitor, 0805, 100pF, 1%, C0G, 30ppm/°C, 100V	C6	Kyocera AVX	Farnell	2332691	0.30779
General Purpose Ceramic Capacitor, 0805, 100pF, 1%, C0G, 30ppm/°C, 100V	C7	Kyocera AVX	Farnell	2332691	0.30779
General Purpose Ceramic Capacitor, 0805, 100pF, 1%, C0G, 30ppm/°C, 100V	C8	Kyocera AVX	Farnell	2332691	0.30779
General Purpose Ceramic Capacitor, 0805, 100pF, 1%, C0G, 30ppm/°C, 100V	C9	Kyocera AVX	Farnell	2332691	0.30779
C0805 0.10 μF X7R 30ppm/°C 10.00% 50 V	C10	KEMET	Mouser	80-C0805C104K5RACLR	0.147
C0805 0.10 μF X7R 30ppm/°C 10.00% 50 V	C11	KEMET	Mouser	80-C0805C104K5RACLR	0.147
C0805 0.10 μF X7R 30ppm/°C 10.00% 50 V	C12	KEMET	Mouser	80-C0805C104K5RACLR	0.147
C0805 0.10 μF X7R 30ppm/°C 10.00% 50 V	C13	KEMET	Mouser	80-C0805C104K5RACLR	0.147
C0805 0.10 μF X7R 30ppm/°C 10.00% 50 V	C14	KEMET	Mouser	80-C0805C104K5RACLR	0.147
General Purpose Ceramic Capacitor, 0805, 100pF, 1%, C0G, 30ppm/°C, 100V	C15	Kyocera AVX	Farnell	2332691	0.30779
C0805 0.10 μF X7R 30ppm/°C 10.00% 50 V	C16	KEMET	Mouser	80-C0805C104K5RACLR	0.147
CAP ALUM 100UF 20% 450V RADIAL	C17	Rubycon	Digikey	1189-3221-ND	4.65
C0805 0.10 μF X7R 30ppm/°C 10.00% 50 V	C18	KEMET	Mouser	80-C0805C104K5RACLR	0.147
CAP ALUM 100UF 20% 450V RADIAL	C19	Rubycon	Digikey	1189-3221-ND	4.65
C0805 0.10 μF X7R 30ppm/°C 10.00% 50 V	C20	KEMET	Mouser	80-C0805C104K5RACLR	0.147
General Purpose Ceramic Capacitor, 0805, 100pF, 1%, C0G, 30ppm/°C, 100V	C21	Kyocera AVX	Farnell	2332691	0.30779
C0805 0.10 μF X7R 30ppm/°C 10.00% 50 V	C22	KEMET	Mouser	80-C0805C104K5RACLR	0.147
C0805 0.10 μF X7R 30ppm/°C 10.00% 50 V	C23	KEMET	Mouser	80-C0805C104K5RACLR	0.147
C0805 0.10 μF X7R 30ppm/°C 10.00% 50 V	C24	KEMET	Mouser	80-C0805C104K5RACLR	0.147
C0805 0.10 μF X7R 30ppm/°C 10.00% 50 V	C25	KEMET	Mouser	80-C0805C104K5RACLR	0.147

					Supplier Subtotal
Description	Designator	Manufacturer 1	Supplier 1	Supplier Part Number 1	1
C0805 0.10 μF X7R 30ppm/°C 10.00% 50 V	C27	KEMET	Mouser	80-C0805C104K5RACLR	0.147
C0805 0.10 μF X7R 30ppm/°C 10.00% 50 V	C28	KEMET	Mouser	80-C0805C104K5RACLR	0.147
C0805 0.10 μF X7R 30ppm/°C 10.00% 50 V	C29	KEMET	Mouser	80-C0805C104K5RACLR	0.147
Cap Ceramic 22pF 25V C0G 1% Pad SMD 0805 125C Automotive T/R	C30	Multicomp	Farnell	1856222	0.38222
Cap Ceramic 22pF 25V C0G 1% Pad SMD 0805 125C Automotive T/R	C31	Multicomp	Farnell	1856222	0.38222
C0805 0.10 μF X7R 30ppm/°C 10.00% 50 V	C32	KEMET	Mouser	80-C0805C104K5RACLR	0.147
C0805 0.10 μF X7R 30ppm/°C 10.00% 50 V	C33	KEMET	Mouser	80-C0805C104K5RACLR	0.147
CAP ALUM 100UF 20% 450V RADIAL	C34	Rubycon	Digikey	1189-3221-ND	4.65
C0805 0.10 μF X7R 30ppm/°C 10.00% 50 V	C35	KEMET	Mouser	80-C0805C104K5RACLR	0.147
C0805 0.10 μF X7R 30ppm/°C 10.00% 50 V	C36	KEMET	Mouser	80-C0805C104K5RACLR	0.147
Fast Switching Diode, 75 V, 0.3 A, -65 to 150 degC, 2-Pin SOD323, RoHS, Tape and Reel	D1	Diodes	Digikey	1N4148WS-FDIDKR-ND	0.2
Fast Switching Diode, 75 V, 0.3 A, -65 to 150 degC, 2-Pin SOD323, RoHS, Tape and Reel	D2	Diodes	Digikey	1N4148WS-FDIDKR-ND	0.2
250 V, 40 A SWITCHMODE(TM) Schottky Power Rectifier, 2-Pin TO-220, Pb-Free, Tube	D3	ON Semiconductor	Mouser	863-MBR40250G	2.14
DIODE SCHOTTKY 40V 1A SOD123	D5	Diodes	Digikey	1N5819HW-FDIDKR-ND	0.75
DIODE SCHOTTKY 40V 1A SOD123	D7	Diodes	Digikey	1N5819HW-FDIDKR-ND	0.75
DIODE SCHOTTKY 40V 1A SOD123	D8	Diodes	Digikey	1N5819HW-FDIDKR-ND	0.75
	Data Input	Wurth Electronics	Digikey	732-2716-1-ND	1.14
LED Uni-Color White, 78 mW, 20 mA, -40 to 85 degC, 2-Pin SMD, RoHS, Tape and Reel	DS1	Broadcom Avago	Digikey	516-2236-1-ND	0.96
LED Uni-Color White, 78 mW, 20 mA, -40 to 85 degC, 2-Pin SMD, RoHS, Tape and Reel	DS2	Broadcom Avago	Digikey	516-2236-1-ND	0.96
LED Uni-Color White, 78 mW, 20 mA, -40 to 85 degC, 2-Pin SMD, RoHS, Tape and Reel	DS3	Broadcom Avago	Digikey	516-2236-1-ND	0.96
CONN HEADER VERT 2POS 5.08MM	Feedback	TE Connectivity	Mouser	571-3505391	4.4
Isolation Amplifier	IC1	Toshiba	Farnell	2524358	
	INA1	Texas Instruments	Mouser	595-INA240A2PWR	
OPTOISO 3.75KV OPN COLL 8DIP GW	Q1	Broadcom Avago	Newark	98K9935	
				1727-GAN080-650EBEZTR-	
GaNFET GAN080-650EBE	Q2	Nexperia USA Inc.	Farnell	ND	6.75
				1727-GAN080-650EBEZTR-	
GaNFET GAN080-650EBE	Q3	Nexperia USA Inc.	Farnell	ND	6.75
				1727-GAN080-650EBEZTR-	
GaNFET GAN080-650EBE	Q4	Nexperia USA Inc.	Farnell	ND	6.75

					Supplier Subtotal
Description	Designator	Manufacturer 1	Supplier 1	Supplier Part Number 1	1
				1727-GAN080-650EBEZTR-	
GaNFET GAN080-650EBE	Q5	Nexperia USA Inc.	Farnell	ND	6.75
			Chipsmall		
	Q6	DASENIC	LTD	MDD S8050-J3Y	
			Chipsmall		
	Q7	DASENIC	LTD	MDD S8050-J3Y	
330kΩ ±5% 0.4W 0805 Anti-Surge Chip Resistor AEC-Q200	R1	Rohm	Mouser	755-ESR10EZPJ334	0.54
330kΩ ±5% 0.4W 0805 Anti-Surge Chip Resistor AEC-Q200	R2	Rohm	Mouser	755-ESR10EZPJ334	0.54
330kΩ ±5% 0.4W 0805 Anti-Surge Chip Resistor AEC-Q200	R3	Rohm	Mouser	755-ESR10EZPJ334	0.54
	R4	Yageo	Mouser	603-RC0805FR-071KL	0.12
	R5	Yageo	Mouser	603-RC0805FR-071KL	0.12
	R6	Yageo	Mouser	603-RC0805FR-071KL	0.12
	R7	Yageo	Mouser	603-RC0805FR-071KL	0.12
$36k\Omega$ ±1% 0.1W Chip Resistor 0603 Thick Film AEC-Q200 Qualified	R8	KOA Speer			
	R9	Yageo	Mouser	603-RC0805FR-071KL	0.12
	R10	Yageo	Mouser	603-RC0805FR-071KL	0.12
	R11	Yageo	Mouser	603-RC0805FR-071KL	0.12
	R12	Yageo	Mouser	603-RC0805FR-071KL	0.12
	R13	Panasonic	Mouser	667-ERA-6AEB331V	0.42
	R14	Panasonic	Mouser	667-ERA-6AEB331V	0.42
20kΩ ±1% 0.4W 0805 Anti-Surge Chip Resistor AEC-Q200	R15	Rohm	Mouser	755-ESR10EZPF2002	0.19
$36k\Omega$ ±1% 0.1W Chip Resistor 0603 Thick Film AEC-Q200 Qualified	R16	KOA Speer			
330kΩ ±5% 0.4W 0805 Anti-Surge Chip Resistor AEC-Q200	R17	Rohm	Mouser	755-ESR10EZPJ334	0.54
330kΩ ±5% 0.4W 0805 Anti-Surge Chip Resistor AEC-Q200	R18	Rohm	Mouser	755-ESR10EZPJ334	0.54
330kΩ ±5% 0.4W 0805 Anti-Surge Chip Resistor AEC-Q200	R19	Rohm	Mouser	755-ESR10EZPJ334	0.54
330kΩ ±5% 0.4W 0805 Anti-Surge Chip Resistor AEC-Q200	R20	Rohm	Mouser	755-ESR10EZPJ334	0.54
12kΩ ±1% 0.1W Chip Resistor 0603 Thick Film AEC-Q200 Qualified	R21	KOA Speer			
12kΩ ±1% 0.1W Chip Resistor 0603 Thick Film AEC-Q200 Qualified	R22	KOA Speer			
$1 k\Omega \pm 5\%$ 0.4W 0805 Anti-Surge Chip Resistor AEC-Q200	R23	Rohm	Mouser	755-ESR10EZPJ102	0.14
360Ω ±1% 0.4W 0805 Anti-Surge Chip Resistor AEC-Q200	R24	Rohm	Farnell	4009470	1.67
36kΩ ±1% 0.1W Chip Resistor 0603 Thick Film AEC-Q200 Qualified	R25	KOA Speer			

					Supplier Subtotal
Description	Designator	Manufacturer 1	Supplier 1	Supplier Part Number 1	1
RES 0 OHM JUMPER 0603	R26	KOA Speer	Newark	85AH2362	0.035
				2019-	
	R27	KOA Speer	Digikey	RK73H2ATTD3303FCT-ND	0.1
36kΩ ±1% 0.1W Chip Resistor 0603 Thick Film AEC-Q200 Qualified	R28	KOA Speer			
CRGCQ0603 1KΩ 1% ±100ppm/°C 75V	R29	TE Connectivity	Newark	73AC9030	0.002
CRGCQ0603 1KΩ 1% ±100ppm/°C 75V	R30	TE Connectivity	Newark	73AC9030	0.002
	R31	Panasonic	Mouser	667-ERA-6AEB331V	0.42
36kΩ ±1% 0.1W Chip Resistor 0603 Thick Film AEC-Q200 Qualified	R32	KOA Speer			0.1
36kΩ ±1% 0.1W Chip Resistor 0603 Thick Film AEC-Q200 Qualified	R33	KOA Speer			0.1
36kΩ ±1% 0.1W Chip Resistor 0603 Thick Film AEC-Q200 Qualified	R34	KOA Speer			0.1
$36k\Omega$ ±1% 0.1W Chip Resistor 0603 Thick Film AEC-Q200 Qualified	R35	KOA Speer			0.1
36kΩ ±1% 0.1W Chip Resistor 0603 Thick Film AEC-Q200 Qualified	R36	KOA Speer			0.1
EVQ-22705R Switch Tactile N.O. SPST Round Button PC Pins 0.02A 15VDC 2.6N Thru-Hole Radial T/R	SW1	E-Switch	digikey	EG4378CT-ND	1.4
EVQ-22705R Switch Tactile N.O. SPST Round Button PC Pins 0.02A 15VDC 2.6N Thru-Hole Radial T/R	SW2	E-Switch	digikey	EG4378CT-ND	1.4
CONN HEADER VERT 2POS 5.08MM	To Coil	TE Connectivity	Mouser	571-3505391	1.1
MOSFET DRVR 600V 0.36A 2-OUT Hi/Lo Side Non-Inv 8-Pin SOIC	U2	Infineon			1.41
MOSFET DRVR 600V 0.36A 2-OUT Hi/Lo Side Non-Inv 8-Pin SOIC	U3	Infineon			1.41
		Shenzhen Slkormicro Semicon		5399-AMS1117-5.0SOT-	
IC REG LINEAR 3.3V 800MA SOT223	U4	Co., Ltd.	Digikey	89TR-ND	0.24418
20 MHz, Low Noise, RRIO, CMOS Operational Amplifier, 1.8 to 5.5 V, -40 to 125 degC, 8-pin SOIC (D8), Green					
(RoHS & no Sb/Br)	U6	Texas Instruments	Digikey	296-50634-ND	2.08
IC REG LINEAR 3.3V 800MA SOT223	U7				
	U8	Espressif Systems	Mouser	356-SP32S3WM2N32R16V	6.85
	U9	MICROCHIP	Farnell	2450806	51.32
	U10	ON Semiconductor	Farnell	2464587	0.34185
	U11	Nexperia	Newark	Newark 11N8532	0.12488
	USB1	SHOU HAN	LSC	C404968	15.62
Crystal 12MHz ±30ppm (Tol) ±30ppm (Stability) 18pF FUND 500hm 2-Pin HC-49/US SMD T/R	X1	Abracon	Farnell	2101325	0.29013
					10
					61
AC/DC Power Supply, ITE & Medical, 1 Output, 48 W, 12 VDC, 4 A		XP Power	Farnell	2063814	36.9

Appendix 3 Receiver subcircuit Bill of Materials

		Manufacturer Part Number			
Description	Designator	1	Supplier 1	Supplier Part Number 1	Supplier Subtotal 1
CONN HEADER VERT 2POS 5.08MM	+3V3	350539-1	Mouser	571-3505391	5.5
General Purpose Ceramic Capacitor, 0805, 100pF, 1%, C0G, 30ppm/°C, 100V	C1	08051A101FAT2A	Mouser	581-08051A101FAT2A	0.295
General Purpose Ceramic Capacitor, 0805, 100pF, 1%, C0G, 30ppm/°C, 100V	C2	08051A101FAT2A	Mouser	581-08051A101FAT2A	0.295
General Purpose Ceramic Capacitor, 0805, 100pF, 1%, C0G, 30ppm/°C, 100V	C3	08051A101FAT2A	Mouser	581-08051A101FAT2A	0.295
General Purpose Ceramic Capacitor, 0805, 100pF, 1%, C0G, 30ppm/°C, 100V	C4	08051A101FAT2A	Mouser	581-08051A101FAT2A	0.295
General Purpose Ceramic Capacitor, 0805, 100pF, 1%, C0G, 30ppm/°C, 100V	C5	08051A101FAT2A	Mouser	581-08051A101FAT2A	0.295
CAP ALUM 330UF 20% 35V SMD	C6	EEE-FP1V331AP	Farnell	1539515	1.18
CAP ALUM 330UF 20% 35V SMD	C7	EEE-FP1V331AP	Farnell	1539515	1.18
CAP ALUM 330UF 20% 35V SMD	C8	EEE-FP1V331AP	Farnell	1539515	1.18
General Purpose Ceramic Capacitor, 0805, 100pF, 1%, C0G, 30ppm/°C, 100V	C9	08051A101FAT2A	Mouser	581-08051A101FAT2A	0.295
General Purpose Ceramic Capacitor, 0805, 100pF, 1%, C0G, 30ppm/°C, 100V	C10	08051A101FAT2A	Mouser	581-08051A101FAT2A	0.295
C0805 0.10 μF X7R 30ppm/°C 10.00% 50 V	C11	C0805C104K5RAC7411	Mouser	80-C0805C104K5RACLR	0.147
C0805 0.10 μF X7R 30ppm/°C 10.00% 50 V	C12	C0805C104K5RAC7411	Mouser	80-C0805C104K5RACLR	0.147
C0805 0.10 μF X7R 30ppm/°C 10.00% 50 V	C13	C0805C104K5RAC7411	Mouser	80-C0805C104K5RACLR	0.147
C0805 0.10 μF X7R 30ppm/°C 10.00% 50 V	C14	C0805C104K5RAC7411	Mouser	80-C0805C104K5RACLR	0.147
C0805 0.10 μF X7R 30ppm/°C 10.00% 50 V	C15	C0805C104K5RAC7411	Mouser	80-C0805C104K5RACLR	0.147
C0805 0.10 μF X7R 30ppm/°C 10.00% 50 V	C16	C0805C104K5RAC7411	Mouser	80-C0805C104K5RACLR	0.147
			Arrow		
	C17	GRM21BR71H105KA12L	Electronics	GRM21BR71H105KA12L	0.0509
				232-	
CAP ALUM 100UF 20% 450V RADIAL	C18	450BXW100MEFR18X30	Mouser	450BXW100MEFR18X	9.3
C0805 0.10 μF X7R 30ppm/°C 10.00% 50 V	C19	C0805C104K5RAC7411	Mouser	80-C0805C104K5RACLR	0.147
C0805 0.10 μF X7R 30ppm/°C 10.00% 50 V	C20	C0805C104K5RAC7411	Mouser	80-C0805C104K5RACLR	0.147
				232-	
CAP ALUM 100UF 20% 450V RADIAL	C21	450BXW100MEFR18X30	Mouser	450BXW100MEFR18X	9.3
General Purpose Ceramic Capacitor, 0603, 1nF, 10%, X7R, 15%, 50V	C22	06035C102KAT2A	Farnell	499134	0.25229
C0805 0.10 μF X7R 30ppm/°C 10.00% 50 V	C23	C0805C104K5RAC7411	Mouser	80-C0805C104K5RACLR	0.147
C0805 0.10 μF X7R 30ppm/°C 10.00% 50 V	C24	C0805C104K5RAC7411	Mouser	80-C0805C104K5RACLR	0.147
C0805 0.10 μF X7R 30ppm/°C 10.00% 50 V	C25	C0805C104K5RAC7411	Mouser	80-C0805C104K5RACLR	0.147

		Manufacturer Part Number			
Description	Designator	1	Supplier 1	Supplier Part Number 1	Supplier Subtotal 1
C0805 0.10 μF X7R 30ppm/°C 10.00% 50 V	C26	C0805C104K5RAC7411	Mouser	80-C0805C104K5RACLR	0.147
C0805 0.10 μF X7R 30ppm/°C 10.00% 50 V	C27	C0805C104K5RAC7411	Mouser	80-C0805C104K5RACLR	0.147
C0805 0.10 μF X7R 30ppm/°C 10.00% 50 V	C28	C0805C104K5RAC7411	Mouser	80-C0805C104K5RACLR	0.147
C0805 0.10 μF X7R 30ppm/°C 10.00% 50 V	C29	C0805C104K5RAC7411	Mouser	80-C0805C104K5RACLR	0.147
C0805 0.10 μF X7R 30ppm/°C 10.00% 50 V	C30	C0805C104K5RAC7411	Mouser	80-C0805C104K5RACLR	0.147
Cap Ceramic 22pF 25V C0G 1% Pad SMD 0805 125C Automotive T/R	C31	MCMT21N220F250CT	Farnell	1856222	0.147
Cap Ceramic 22pF 25V C0G 1% Pad SMD 0805 125C Automotive T/R	C32	MCMT21N220F250CT	Farnell	1856222	0.147
C0805 0.10 μF X7R 30ppm/°C 10.00% 50 V	C33	C0805C104K5RAC7411	Mouser	80-C0805C104K5RACLR	0.147
C0805 0.10 μF X7R 30ppm/°C 10.00% 50 V	C34	C0805C104K5RAC7411	Mouser	80-C0805C104K5RACLR	0.147
C0805 0.10 μF X7R 30ppm/°C 10.00% 50 V	C35	C0805C104K5RAC7411	Mouser	80-C0805C104K5RACLR	0.147
C0805 0.10 μF X7R 30ppm/°C 10.00% 50 V	C36	C0805C104K5RAC7411	Mouser	80-C0805C104K5RACLR	0.147
C0805 0.10 μF X7R 30ppm/°C 10.00% 50 V	C37	C0805C104K5RAC7411	Mouser	80-C0805C104K5RACLR	0.147
C0805 0.10 μF X7R 30ppm/°C 10.00% 50 V	C38	C0805C104K5RAC7411	Mouser	80-C0805C104K5RACLR	0.147
Fast Switching Diode, 75 V, 0.3 A, -65 to 150 degC, 2-Pin SOD323, RoHS, Tape and Reel	D1	1N4148WS-7-F	Farnell	1843678	0.09965
250 V, 40 A SWITCHMODE(TM) Schottky Power Rectifier, 2-Pin TO-220, Pb-Free, Tube	D2	MBR40250G	Mouser	863-MBR40250G	2.14
250 V, 40 A SWITCHMODE(TM) Schottky Power Rectifier, 2-Pin TO-220, Pb-Free, Tube	D3	MBR40250G	Mouser	863-MBR40250G	2.14
250 V, 40 A SWITCHMODE(TM) Schottky Power Rectifier, 2-Pin TO-220, Pb-Free, Tube	D4	MBR40250G	Mouser	863-MBR40250G	2.14
250 V, 40 A SWITCHMODE(TM) Schottky Power Rectifier, 2-Pin TO-220, Pb-Free, Tube	D5	MBR40250G	Mouser	863-MBR40250G	2.14
250 V, 40 A SWITCHMODE(TM) Schottky Power Rectifier, 2-Pin TO-220, Pb-Free, Tube	D6	MBR40250G	Mouser	863-MBR40250G	2.14
Fast Switching Diode, 75 V, 0.3 A, -65 to 150 degC, 2-Pin SOD323, RoHS, Tape and Reel	D7	1N4148WS-7-F	Farnell	1843678	0.09965
DIODE SCHOTTKY 40V 1A SOD123	D8	1N5819HW-7-F	Farnell	1773475	0.30275
Fast Switching Diode, 75 V, 0.3 A, -65 to 150 degC, 2-Pin SOD323, RoHS, Tape and Reel	D9	1N4148WS-7-F	Farnell	1843678	0.09965
DIODE SCHOTTKY 40V 1A SOD123	D10	1N5819HW-7-F	Farnell	1773475	0.30275
	D11	SS110	Farnell	2675130	0.20436
			LCSC		
	Data Input	MICROQTJ	Electronics	C404968	
LED Uni-Color White, 78 mW, 20 mA, -40 to 85 degC, 2-Pin SMD, RoHS, Tape and Reel	DS1	HSMW-C191	Farnell	1058375	1.1
LED Uni-Color White, 78 mW, 20 mA, -40 to 85 degC, 2-Pin SMD, RoHS, Tape and Reel	DS2	HSMW-C191	Farnell	1058375	1.1
LED Uni-Color White, 78 mW, 20 mA, -40 to 85 degC, 2-Pin SMD, RoHS, Tape and Reel	DS3	HSMW-C191	Farnell	1058375	1.1
LED Uni-Color Red, 52 mW, 20 mA, -40 to 85 degC, 2-Pin SMD, RoHS, Tape and Reel	DS4	HSMS-C190	Farnell	8554765	1.05
LED Uni-Color Yellow, 65 mW, 20 mA, -40 to 85 degC, 2-Pin SMD, RoHS, Tape and Reel	DS5	HSMY-C190	Farnell	2497355	1.19

		Manufacturer Part Number			
Description	Designator	1	Supplier 1	Supplier Part Number 1	Supplier Subtotal 1
Blue LED, 10 mA, 3.9 V, -40 to 100 degC, 2-Pin SMD (0603), RoHS, Tape and Reel	DS6	VLMB1300-GS08	Farnell	2251459	0.251
Fast Acting Fuse, 1 A, 32 V, -55 to 90 degC, 2-Pin SMD, RoHS, Tape and Reel	F1	0467001.NR	Farnell	2148553	1.07
CONN HEADER VERT 2POS 5.08MM	Feedback	350539-1	Mouser	571-3505391	
Isolation Amplifier	IC1	TLP7920(F	digikey	TLP7920(F-ND	12.29
	INA1	INA240A2PWR	Mouser	595-INA240A2PWR	6.24
CONN HEADER VERT 2POS 5.08MM	J1	350539-1	Mouser	571-3505391	1.1
Socket	J2				
Socket	J3	620302124022	Farnell	1841394	9.4
160 μH @ 100 kHz 2 Line Common Mode Choke Through Hole 19A DCR 1.95mOhm	L1	SCR19XV-190-1R5A005JH	Farnell	3807269	5.35
Fixed Ind 220UH 3A 134 Mohm Th	L2	1730240	RS	104-8426	12.54
GaNFET GAN080-650EBE	Q1	GAN080-650EBEZ	Farnell	4198478	#REF!
OPTOISO 3.75KV OPN COLL 8DIP GW	Q2	6N137-300E	Farnell	1085003	2.54
GaNFET GAN080-650EBE	Q3	GAN080-650EBEZ	Farnell	4198478	
	Q4	MMBT8099LT1G	Mouser	863-MMBT8099LT1G	0.84
	Q5	MMBT8099LT1G	Mouser	863-MMBT8099LT1G	
RES 0.005 OHM 1% 1W 0805	R1	WSLP08055L000FEA18	Farnell	2518218	9.7
	R2	RC0805FR-071KL	Mouser	603-RC0805FR-071KL	0.12
330kΩ ±5% 0.4W 0805 Anti-Surge Chip Resistor AEC-Q200	R3	ESR10EZPJ334	Mouser	755-ESR10EZPJ334	0.54
330kΩ ±5% 0.4W 0805 Anti-Surge Chip Resistor AEC-Q200	R4	ESR10EZPJ334	Mouser	755-ESR10EZPJ334	0.54
330kΩ ±5% 0.4W 0805 Anti-Surge Chip Resistor AEC-Q200	R5	ESR10EZPJ334	Mouser	755-ESR10EZPJ334	0.54
RES 0.005 OHM 1% 1W 0805	R6	WSLP08055L000FEA18	Farnell	2518218	9.7
RES 0.005 OHM 1% 1W 0805	R7	WSLP08055L000FEA18	Farnell	2518218	9.7
36kΩ ±1% 0.1W Chip Resistor 0603 Thick Film AEC-Q200 Qualified	R8	RK73G1JTTD3602F			
	R9	RC0805FR-071KL	Mouser	603-RC0805FR-071KL	0.12
	R10	ERA-6AEB331V	Farnell	4137016	0.92086
	R11	ERA-6AEB331V	Farnell	4137016	0.92086
20kΩ ±1% 0.4W 0805 Anti-Surge Chip Resistor AEC-Q200	R12	ESR10EZPF2002	Mouser	755-ESR10EZPF2002	0.19
36kΩ ±1% 0.1W Chip Resistor 0603 Thick Film AEC-Q200 Qualified	R13	RK73G1JTTD3602F			
330kΩ ±5% 0.4W 0805 Anti-Surge Chip Resistor AEC-Q200	R14	ESR10EZPJ334	Mouser	755-ESR10EZPJ334	0.54
330kΩ ±5% 0.4W 0805 Anti-Surge Chip Resistor AEC-Q200	R15	ESR10EZPJ334	Mouser	755-ESR10EZPJ334	0.54
330kΩ ±5% 0.4W 0805 Anti-Surge Chip Resistor AEC-Q200	R16	ESR10EZPJ334	Mouser	755-ESR10EZPJ334	0.54

		Manufacturer Part Number			
Description	Designator	1	Supplier 1	Supplier Part Number 1	Supplier Subtotal 1
330kΩ ±5% 0.4W 0805 Anti-Surge Chip Resistor AEC-Q200	R17	ESR10EZPJ334	Mouser	755-ESR10EZPJ334	0.54
12kΩ ±1% 0.1W Chip Resistor 0603 Thick Film AEC-Q200 Qualified	R18	RK73G1JTTD1202F			
12kΩ ±1% 0.1W Chip Resistor 0603 Thick Film AEC-Q200 Qualified	R19	RK73G1JTTD1202F			
1kΩ ±5% 0.4W 0805 Anti-Surge Chip Resistor AEC-Q200	R20	ESR10EZPJ102	Mouser	755-ESR10EZPJ102	0.14
360Ω ±1% 0.4W 0805 Anti-Surge Chip Resistor AEC-Q200	R21	ESR10EZPF3600	Farnell	4009470	1.67
$36k\Omega$ ±1% 0.1W Chip Resistor 0603 Thick Film AEC-Q200 Qualified	R22	RK73G1JTTD3602F			
RES 0 OHM JUMPER 0603	R23	RK73Z1JTTD	Farnell	4009217	0.06307
	R24	RK73H2ATTD3303F	Mouser	660-RK73H2ATTD3303F	0.1
$36k\Omega$ ±1% 0.1W Chip Resistor 0603 Thick Film AEC-Q200 Qualified	R25	RK73G1JTTD3602F			
CRGCQ0603 1KΩ 1% ±100ppm/°C 75V	R26	CRGCQ0603F1K0	Mouser	279-CRGCQ0603F1K0	0.2
CRGCQ0603 1KΩ 1% ±100ppm/°C 75V	R27	CRGCQ0603F1K0	Mouser	279-CRGCQ0603F1K0	0.2
	R28	ERA-6AEB331V	Farnell	4137016	0.92086
$36k\Omega$ ±1% 0.1W Chip Resistor 0603 Thick Film AEC-Q200 Qualified	R29	RK73G1JTTD3602F			
$36k\Omega$ ±1% 0.1W Chip Resistor 0603 Thick Film AEC-Q200 Qualified	R30	RK73G1JTTD3602F			
$36k\Omega$ ±1% 0.1W Chip Resistor 0603 Thick Film AEC-Q200 Qualified	R31	RK73G1JTTD3602F			
$36k\Omega$ ±1% 0.1W Chip Resistor 0603 Thick Film AEC-Q200 Qualified	R32	RK73G1JTTD3602F			
$36k\Omega$ ±1% 0.1W Chip Resistor 0603 Thick Film AEC-Q200 Qualified	R33	RK73G1JTTD3602F			
	R34	ERA-6AEB331V	Farnell	4137016	0.92086
	R35	ERA-6AEB331V	Farnell	4137016	0.92086
	R36	ERA-6AEB331V	Farnell	4137016	0.92086
EVQ-22705R Switch Tactile N.O. SPST Round Button PC Pins 0.02A 15VDC 2.6N Thru-Hole Radial T/R	SW1	TL59AF100Q	digikey	EG4378CT-ND	1.4
EVQ-22705R Switch Tactile N.O. SPST Round Button PC Pins 0.02A 15VDC 2.6N Thru-Hole Radial T/R	SW2	TL59AF100Q	digikey	EG4378CT-ND	1.4
MOSFET DRVR 600V 0.36A 2-OUT Hi/Lo Side Non-Inv 8-Pin SOIC	U1	IR2101STRPBF	Farnell	2296000	1.41
				926-	
IC REG LINEAR 3.3V 800MA SOT223	U2	Texas Instruments	Mouser	LM1117MPX5.0NOPB	0.797
No Description Available	U3	BM2P129TF-E2	Farnell	3011485RL	1.26
20 MHz, Low Noise, RRIO, CMOS Operational Amplifier, 1.8 to 5.5 V, -40 to 125 degC, 8-pin SOIC (D8), Green (RoHS & no					
Sb/Br)	U4	OPA2322AID	Mouser	595-OPA2322AID	#REF!
				926-	
IC REG LINEAR 3.3V 800MA SOT223	U5	LM1117MPX-3.3/NOPB	Mouser	LM1117MPX3.3NOPB	#REF!
MC74VHC86DR2G	U6	MC74VHC86DR2G	Farnell	2464587	0.34185

		Manufacturer Part Number			
Description	Designator	1	Supplier 1	Supplier Part Number 1	Supplier Subtotal 1
		ESP32-S3-WROOM-2-		356-	
ESP32-WROOM-32 -Micro controller	U7	N32R16V	Mouser	SP32S3WM2N32R16V	6.85
CH340G Seriel	U8	ADM00559	Farnell	2450806	51.32
74HC08D,653	U9	74HC08D,653	Farnell	1201314	0.12488
РСВ					39
Coil					10
Crystal 12MHz ±30ppm (Tol) ±30ppm (Stability) 18pF FUND 500hm 2-Pin HC-49/US SMD T/R	X1	ABLS2-12.000MHZ-D4Y-T	Farnell	2101325	0.6

#REF!

Appendix 4 FCC subcircuit Bill Of Materials

		Manufacturer Part				Supplier Subtotal
Description	Designator	Number 1	Manufacturer Lifecycle 1	Supplier 1	Supplier Part Number 1	1
CONN HEADER VERT 2POS 5.08MM	+1	350539-1	Volume Production	Avnet	350539-1	2.55
YAGEO SMD Multilayer Ceramic Capacitor, 50 V, 0805 [2012 Metric], COG / NPO	C1					
MULTICOMP PRO SMD Multilayer Ceramic Capacitor, 50 V, 1206 [2012 Metric], COG / NPO	C2					
YAGEO SMD Multilayer Ceramic Capacitor, 50 V, 0805 [2012 Metric], COG / NPO	C3					
MULTICOMP PRO SMD Multilayer Ceramic Capacitor, 50 V, 1206 [2012 Metric], COG / NPO	C4					
C0805 0.10 μF X7R 30ppm/°C 10.00% 50 V	C5	C0805C104K5RAC7411	Obsolete	Mouser	80-C0805C104K5RACLR	0.2
C0805 0.10 μF X7R 30ppm/°C 10.00% 50 V	C6	C0805C104K5RAC7411	Obsolete	Mouser	80-C0805C104K5RACLR	0.2
YAGEO SMD Multilayer Ceramic Capacitor, 50 V, 0805 [2012 Metric], COG / NPO	C7					0.1
YAGEO SMD Multilayer Ceramic Capacitor, 50 V, 0805 [2012 Metric], COG / NPO	C8					0.1
YAGEO SMD Multilayer Ceramic Capacitor, 50 V, 0805 [2012 Metric], COG / NPO	C9					0.1
MULTICOMP PRO SMD Multilayer Ceramic Capacitor, 50 V, 1206 [2012 Metric], COG / NPO	C10					0.1
MULTICOMP PRO SMD Multilayer Ceramic Capacitor, 50 V, 1206 [2012 Metric], COG / NPO	C11					0.1
MULTICOMP PRO SMD Multilayer Ceramic Capacitor, 50 V, 1206 [2012 Metric], COG / NPO	C12					0.1
YAGEO SMD Multilayer Ceramic Capacitor, 50 V, 0805 [2012 Metric], COG / NPO	C13					0.1
MULTICOMP PRO SMD Multilayer Ceramic Capacitor, 50 V, 1206 [2012 Metric], COG / NPO	C14					0.1
YAGEO SMD Multilayer Ceramic Capacitor, 50 V, 0805 [2012 Metric], COG / NP0	C15					0.1
MULTICOMP PRO SMD Multilayer Ceramic Capacitor, 50 V, 1206 [2012 Metric], COG / NPO	C16					0.1
MULTICOMP PRO SMD Multilayer Ceramic Capacitor, 50 V, 1206 [2012 Metric], COG / NPO	C17					0.1
MULTICOMP PRO SMD Multilayer Ceramic Capacitor, 50 V, 1206 [2012 Metric], COG / NPO	C18					0.1
MULTICOMP PRO SMD Multilayer Ceramic Capacitor, 50 V, 1206 [2012 Metric], COG / NPO	C19					0.1
MULTICOMP PRO SMD Multilayer Ceramic Capacitor, 50 V, 1206 [2012 Metric], COG / NPO	C20					0.1
MULTICOMP PRO SMD Multilayer Ceramic Capacitor, 50 V, 1206 [2012 Metric], COG / NPO	C21					0.1
MULTICOMP PRO SMD Multilayer Ceramic Capacitor, 50 V, 1206 [2012 Metric], COG / NPO	C22					0.1
MULTICOMP PRO SMD Multilayer Ceramic Capacitor, 50 V, 1206 [2012 Metric], COG / NPO	C23					0.1
YAGEO SMD Multilayer Ceramic Capacitor, 50 V, 0805 [2012 Metric], COG / NP0	C24					0.1
MULTICOMP PRO SMD Multilayer Ceramic Capacitor, 50 V, 1206 [2012 Metric], COG / NPO	C25					0.1
MULTICOMP PRO SMD Multilayer Ceramic Capacitor, 6 pF, 50 V, 0805 [2012 Metric], ±						
0.5pF, COG / NPO	C26					0.1
			Not Recommended for New			
	C27	GRM1555C1H2R0CA01D	Design	Digikey	490-5870-1-ND	0.1

		Manufacturer Part				Supplier Subtotal
Description	Designator	Number 1	Manufacturer Lifecycle 1	Supplier 1	Supplier Part Number 1	1
	Data Input1	679303124022	Volume Production	Digikey	732-2716-1-ND	1.14
CONN HEADER VERT 2POS 5.08MM	FEEDBACK	350539-1	Volume Production	Avnet	350539-1	2.55
	FROM					
CONN HEADER VERT 2POS 5.08MM	INVERTER	350539-1	Volume Production	Avnet	350539-1	2.55
IC XPND 400KHZ I2C SMBUS 24HVQFN (HVQFN24)	IC1	PCA9555BS,118	Volume Production	Farnell	2212100	2.06
					1727-GAN080-	
GaNFET GAN080-650EBE	Q1	NEXPERIA	Manual Solution	Digikey	650EBEZTR-ND	6.4
					1727-GAN080-	
GaNFET GAN080-650EBE	Q2	NEXPERIA	Manual Solution	Digikey	650EBEZTR-ND	6.4
					1727-GAN080-	
GaNFET GAN080-650EBE	Q3	NEXPERIA	Manual Solution	Digikey	650EBEZTR-ND	6.4
					1727-GAN080-	
GaNFET GAN080-650EBE	Q4	NEXPERIA	Manual Solution	Digikey	650EBEZTR-ND	6.4
					1727-GAN080-	
GaNFET GAN080-650EBE	Q5	NEXPERIA	Manual Solution	Digikey	650EBEZTR-ND	6.4
					1727-GAN080-	
GaNFET GAN080-650EBE	Q6	NEXPERIA	Manual Solution	Digikey	650EBEZTR-ND	6.4
					1727-GAN080-	
GaNFET GAN080-650EBE	Q7	NEXPERIA	Manual Solution	Digikey	650EBEZTR-ND	6.4
					1727-GAN080-	
GaNFET GAN080-650EBE	Q8	NEXPERIA	Manual Solution	Digikey	650EBEZTR-ND	6.4
					1727-GAN080-	
GaNFET GAN080-650EBE	Q9	NEXPERIA	Manual Solution	Digikey	650EBEZTR-ND	6.4
					1727-GAN080-	
GaNFET GAN080-650EBE	Q10	NEXPERIA	Manual Solution	Digikey	650EBEZTR-ND	6.4
					1727-GAN080-	
GaNFET GAN080-650EBE	Q11	NEXPERIA	Manual Solution	Digikey	650EBEZTR-ND	6.4
CRGCQ0603 1KΩ 1% ±100ppm/°C 75V	R1	CRGCQ0603F1K0	Volume Production	Farnell	2861461	0.12159
CRGCQ0603 1KΩ 1% ±100ppm/°C 75V	R2	CRGCQ0603F1K0	Volume Production	Farnell	2861461	0.12159
CRGCQ0603 1KΩ 1% ±100ppm/°C 75V	R3	CRGCQ0603F1K0	Volume Production	Farnell	2861461	0.12159
CRGCQ0603 1KΩ 1% ±100ppm/°C 75V	R4	CRGCQ0603F1K0	Volume Production	Farnell	2861461	0.12159
CRGCQ0603 1KΩ 1% ±100ppm/°C 75V	R5	CRGCQ0603F1K0	Volume Production	Farnell	2861461	0.12159

		Manufacturer Part				Supplier Subtotal
Description	Designator	Number 1	Manufacturer Lifecycle 1	Supplier 1	Supplier Part Number 1	1
CRGCQ0603 1KΩ 1% ±100ppm/°C 75V	R6	CRGCQ0603F1K0	Volume Production	Farnell	2861461	0.12159
CRGCQ0603 1KΩ 1% ±100ppm/°C 75V	R7	CRGCQ0603F1K0	Volume Production	Farnell	2861461	0.12159
CRGCQ0603 1KΩ 1% ±100ppm/°C 75V	R8	CRGCQ0603F1K0	Volume Production	Farnell	2861461	0.12159
CRGCQ0603 1KΩ 1% ±100ppm/°C 75V	R9	CRGCQ0603F1K0	Volume Production	Farnell	2861461	0.12159
CRGCQ0603 1KΩ 1% ±100ppm/°C 75V	R10	CRGCQ0603F1K0	Volume Production	Farnell	2861461	0.12159
CRGCQ0603 1KΩ 1% ±100ppm/°C 75V	R11	CRGCQ0603F1K0	Volume Production	Farnell	2861461	0.12159
CRGCQ0603 1KΩ 1% ±100ppm/°C 75V	R12	CRGCQ0603F1K0	Volume Production	Farnell	2861461	0.12159
CRGCQ0603 1KΩ 1% ±100ppm/°C 75V	R13	CRGCQ0603F1K0	Volume Production	Farnell	2861461	0.12159
CRGCQ0603 1KΩ 1% ±100ppm/°C 75V	R14	CRGCQ0603F1K0	Volume Production	Farnell	2861461	0.12159
RES 0.005 OHM 1% 1W 0805	R15	WSLP08055L000FEA18	Volume Production	Digikey	541-2526-1-ND	7.44
Coil						10
CONN HEADER VERT 2POS 5.08MM	TO COIL	350539-1	Volume Production	Avnet	350539-1	2.55
MAX1682EUK+T voltage doubler		MAX1682EUK+T		Digikey	MAX1682EUK+TCT-ND	3.07
Muktiplexer 1 Circuit IC Switch 16:1 1600hm 24-SSOP		296-9226-1-ND				0.46

References

- [1] A. Triviño-Cabrera, J. M. González-González, and J. A. Aguado, *Wireless Power Transfer for Electric Vehicles: Foundations and Design Approach*, Power Systems. Cham: Springer, 2020. doi: 10.1007/978-3-030-26706-3.
- [2] W. M. G. Dyab, M. S. Ibrahim, A. A. Sakr and K. Wu, "Ridge Gap Waveguide Enabled Wireless Power Transfer for Electric Vehicle Applications," *2020 50th European Microwave Conference (EuMC)*, 2021, pp. 852-855, doi: 10.23919/EuMC48046.2021.9338138.
- [3] A. Mahesh, B. Chokkalingam, and L. Mihet-Popa, "Inductive Wireless Power Transfer Charging for Electric Vehicles—A Review," *IEEE Access*, vol. 9, pp. 137667-137713, 2021. doi: 10.1109/ACCESS.2021.3116678.
- [4] Y. Scot, "Homepage of Glasgow City Council," Glasgow.gov.uk, Jun. 2015. [Online]. Available: https://www.glasgow.gov.uk/home.
- [5] M. F. Bagwan, U. S. Jawarkar, T. G. Pal, and A. S. Gugliya, "Wireless Power Transfer Electric Vehicle," *International Advanced Research Journal in Science, Engineering and Technology*, AGNI-PANKH 16, Jawaharlal Darda Institute of Engineering and Technology, Yavatmal, vol. 4, Special Issue 3, Jan. 2017, doi: 10.17148/IARJSET.
- [6] "The History of the Electric Car," Energy.gov. https://www.energy.gov/articles/history-electric-car#
- [7] Mercedes-Benz Group, "Home," [Online]. Available: https://group.mercedes-benz.com. [Accessed: 24-Oct-2024].
- [8] Department for Transport, "Vehicle licensing statistics: April to June 2024," *GOV.UK*, Sep. 24, 2024. https://www.gov.uk/government/statistics/vehicle-licensing-statistics-april-to-june-2024/vehicle-licensing-statisti
- [9] "UK: number of petrol stations 2000-2018 | Statista," *Statista*, 2018. https://www.statista.com/statistics/312331/number-of-petrol-stations-in-the-united-kingdom-uk/
- [10] . Melanie, "How many electric cars are there in the UK 2022," Zap-Map, 2022. https://www.zap-map.com/ev-market-statistics/
- [11] O. N. Nezamuddin, C. L. Nicholas, and E. C. d. Santos, "The Problem of Electric Vehicle Charging: State-of-the-Art and an Innovative Solution," in *IEEE Transactions on Intelligent Transportation Systems*, vol. 23, no. 5, pp. 4663-4673, May 2022, doi: 10.1109/TITS.2020.3048728.
- [12] I. Evtimov, R. Ivanov, G. Kadikyanov, and G. Staneva, "Life cycle assessment of electric and conventional cars energy consumption and CO2 emissions," in *MATEC Web of Conferences*, vol. 234, 2018, Art. no. 00007, doi: 10.1051/matecconf/20182340007.
- [13] "Charging My Electric Vehicle | US EPA," US EPA, Nov. 30, 2022. https://www.epa.gov/greenvehicles/charging-my-electric-vehicle (accessed Oct. 18, 2024).
- [14] Jema Energy, "Opportunity chargers," Accessed: Oct. 23, 2024. [Online]. Available:

https://www.jemaenergy.com/en/producto/opportunity-chargers

- [15] OppCharge, "OppCharge: Opportunity charging for electric vehicles," Accessed: Oct. 18, 2024. [Online]. Available: https://www.oppcharge.org/
- [16] Y. Zhang, S. Chen, X. Li and Y. Tang, "Design of high-power static wireless power transfer via magnetic induction: An overview," in *CPSS Transactions on Power Electronics and Applications*, vol. 6, no. 4, pp. 281-297, Dec. 2021, doi: 10.24295/CPSSTPEA.2021.00027.
- [17] Rail Focus, "Greenford Branch Class 230 Battery Train Trial," YouTube, Jul. 02, 2023. https://www.youtube.com/watch?v=5izy_ZU986g (accessed Oct. 18, 2024).
- [18] I. Mansfield, "Former District line tube train to start GWR battery-train trials in west London," *ianVisits*, Feb. 08, 2024. https://www.ianvisits.co.uk/articles/former-district-line-tube-train-to-start-gwr-battery-train-trials-in-west-london-70069/ (accessed Oct. 18, 2024)
- [19] "Fast-charge battery train put into action," *Railmagazine.com*, Mar. 27, 2024. https://www.railmagazine.com/news/2024/03/27/fast-charge-battery-train-put-into-action (accessed Oct. 18, 2024).
- [20] EonEnergy, "Ultra-fast charging stations," Accessed: Oct. 18, 2024. [Online]. Available: https://www.eonenergy.com/electric-vehicle-charging/ultra-fast-charging-stations.html

- [21] NASA, "Introduction to the Electromagnetic Spectrum NASA Science," *science.nasa.gov*, Aug. 10, 2016. https://science.nasa.gov/ems/01_intro
- [22] Renewables in Africa. "How does a solar panel work?" [Online]. Available: https://www.renewablesinafrica.com/how-does-a-solar-panel-work/ (accessed Oct. 18, 2024).
- [23] Diagram of electrical transformer," Shutterstock. [Online]. Available: https://www.shutterstock.com/image-illustration/diagram-show-how-electrical-transformer-changes-194417840
- [24] Shutterstock. "Induction motor." [Online]. Available: https://www.shutterstock.com/search/induction-motor (accessed Oct. 18, 2024).
- [25] "André-Marie Ampère," Magcraft. https://www.magcraft.com/andre-marie-ampere (accessed Oct. 18, 2024).
- [26] https://www.britannica.com/science/electromagnetism/Faradays-discovery-of-electric-induction
- [27] "Maxwell's Equations," Encyclopaedia Britannica. https://www.britannica.com/science/Maxwells-equations (accessed Oct. 18, 2024).
- [28] A. Brecher, D. Arthur, and U.S. Department of Transportation, Volpe National Transportation Systems Center, "Review and Evaluation of Wireless Power Transfer (WPT) for Electric Transit Applications," 2014. [Online]. Available:
- https://www.transit.dot.gov/sites/fta.dot.gov/files/FTA_Report_No._0060.pdf. Accessed: Oct. 10, 2022.
- [29] N. Shinohara and S. Kawasaki, "Recent Wireless Power Transmission technologies in Japan for space solar power station/satellite," 2009 IEEE Radio and Wireless Symposium, 2009, pp. 13-15, doi: 10.1109/RWS.2009.4957272.
- [30] W. C. Brown, Microwave Power Transmission Systems, 6 Perry Lane, Weston, MA 02193, U.S.A., available online 19 February 1999.
- [31] N. Shinohara, Y. Kubo and H. Tonomura, "Wireless charging for electric vehicle with microwaves," *2013 3rd International Electric Drives Production Conference (EDPC)*, 2013, pp. 1-4, doi: 10.1109/EDPC.2013.6689750.
- [32] Wikipedia. "Magne Charge." [Online]. Available: https://en.wikipedia.org/wiki/Magne Charge (accessed Oct. 18, 2022).
- [33] Conductix-Wampfler. Inductive Power Transfer IPT-Charge. Accessed: Jan. 1, 2021. [Online]. Available: https://www.conductix.us/en/products/ inductive-power-transfer-iptr/inductive-power-transfer-iptr-charge? parent_id=5798.
- [34] A. M. Jawad, R. Nordin, S. K. Gharghan, H. M. Jawad, and M Ismail "Opportunities and Challenges for Near-Field Wireless Power Transfer: A Review
- [35] "Polyphase wireless power transfer system achieves 270-kilowatt charge, sets another world record for electric light-duty passenger vehicles | ORNL," *ORNL*, Jun. 18, 2024. https://www.ornl.gov/news/polyphase-wireless-power-transfer-system-achieves-270-kilowatt-charge-sets-another-world.
- [36] ORNL, Volkswagen Succeed in First 270-kW Wireless Power Transfer," *ASME*. https://www.asme.org/topics-resources/content/ornl,-volkswagen-succeed-in-first-270-kw-wireless-power-transfer (accessed Oct. 18, 2024).
- [37] B. Regensburger, S. Sinha, A. Kumar, S. Maji and K. K. Afridi, "High-Performance Multi-MHz Capacitive Wireless Power Transfer System for EV Charging Utilizing Interleaved-Foil Coupled Inductors," in *IEEE Journal of Emerging and Selected Topics in Power Electronics*, vol. 10, no. 1, pp. 35-51, Feb. 2022, doi: 10.1109/JESTPE.2020.3030757.
- [38] S. Li, Z. Liu, H. Zhao, L. Zhu, C. Shuai and Z. Chen, "Wireless Power Transfer by Electric Field Resonance and Its Application in Dynamic Charging," in *IEEE Transactions on Industrial Electronics*, vol. 63, no. 10, pp. 6602-6612, Oct. 2016, doi: 10.1109/TIE.2016.2577625.
- [39] C. Qiu, K. T. Chau, C. Liu and C. C. Chan, "Overview of wireless power transfer for electric vehicle charging," 2013 World Electric Vehicle Symposium and Exhibition (EVS27), 2013, pp. 1-9, doi: 10.1109/EVS.2013.6914731.
- [40] L. N. Jian, K. T. Chau, D. Zhang, J. Z. Jiang, and Z. Wang, "A magnetic-geared outer-rotor permanent-magnet brushless machine for wind power generation," in *Industrial Applications Conference*, New Orleans, LA, 2007, pp. 573-580.
- [41] S. Suzuki, M. Ishihara, and Y. Kobayashi, "The improvement of the noninvasive power supply system using magnetic coupling for medical implants," *IEEE Transactions on Magnetics*, vol. 47, no. 10, pp. 2811-2814, Oct. 2011.
- [42] "5V-12V ZVS Induction Heating Coil Spare Part," Ram E-Shop. [Online]. Available: https://ram-e-shop.com/product/5v-12v-zvs-induction-heating-coil-spare-part/ (accessed Oct. 18, 2024).
- [43] "Inductor Inductance Formula Equations," Electrical Technology. [Online]. Available: https://www.electricaltechnology.org/2020/10/inductor-inductance-formula-equations.html (accessed Oct. 18, 2024).

- [44] "Solenoid," HowStuffWorks. [Online]. Available: https://science.howstuffworks.com/solenoid.htm (accessed Oct. 18, 2024).
- [45] B. Olukotun, J. S. Partridge and R. W. G. Bucknall, "Loss Performance Evaluation of Ferrite-Cored Wireless Power System with Conductive and Magnetic Shields," *2019 IEEE PES Innovative Smart Grid Technologies Europe (ISGT-Europe)*, 2019, pp. 1-5, doi: 10.1109/ISGTEurope.2019.8905437
- [46] F. Pellitteri, "Wireless Charging Systems for Electric Vehicle Batteries," Dottorato di Ricerca in Ingegneria Elettrica, Elettronica e delle Telecomunicazioni, Matematica e Automatica, Dipartimento di Energia, ingegneria dell'Informazione e modelli Matematici, S.S.D.: ING-IND/32, ING-INF/01, Ciclo: XXVI, Anno Conseguimento Titolo: 2016.
- [47] Y. Nagatsuka, N. Ehara, Y. Kaneko, S. Abe, and T. Yasuda, "Compact contactless power transfer system for electric vehicles," in *2010 International Power Electronics Conference (IPEC)*, 2010, pp. 807–813.
- [48] M. Budhia, G. A. Covic, and J. T. Boys, "Design and optimisation of magnetic structures for lumped Inductive Power Transfer systems," in *Energy Conversion Congress and Exposition, 2009. ECCE 2009. IEEE*, 2009, pp. 2081–2088.
- [49] G. Ombach, D. Kurschner and S. Mathar, "Universal base coil solution for interoperable system for stationary wireless EV charging," *2015 International Conference on Sustainable Mobility Applications, Renewables and Technology (SMART)*, 2015, pp. 1-9, doi: 10.1109/SMART.2015.7399238.
- [50] F. Y. Lin, A. Zaheer, M. Budhia and G. A. Covic, "Reducing leakage flux in IPT systems by modifying pad ferrite structures," 2014 IEEE Energy Conversion Congress and Exposition (ECCE), 2014, pp. 1770-1777, doi: 10.1109/ECCE.2014.6953632.
- [51] G. Wei, X. Jin, C. Wang, J. Feng, C. Zhu and M. I. Matveevich, "An Automatic Coil Design Method With Modified AC Resistance Evaluation for Achieving Maximum Coil—Coil Efficiency in WPT Systems," in *IEEE Transactions on Power Electronics*, vol. 35, no. 6, pp. 6114-6126, June 2020, doi: 10.1109/TPEL.2019.2952120
- [52] O. Simon, T. Krempel, H. Wolf and J. Mahlein, "Flexible secondary pad design for wireless power transfer providing public interoperability," 2017 IEEE International Conference on Environment and Electrical Engineering and 2017 IEEE Industrial and Commercial Power Systems Europe (EEEIC / I&CPS Europe), 2017, pp. 1-7, doi: 10.1109/EEEIC.2017.7977862.
- [53] O. C. Onar, M. Chinthavali, S. L. Campbell, L. E. Seiber and C. P. White, "Vehicular Integration of Wireless Power Transfer Systems and Hardware Interoperability Case Studies," in *IEEE Transactions on Industry Applications*, vol. 55, no. 5, pp. 5223-5234, Sept.-Oct. 2019, doi: 10.1109/TIA.2019.2928482.
- [54] A. Ahmad, M. S. Alam, and A. A. S. Mohamed, "Design and Interoperability Analysis of Quadruple Pad Structure for Electric Vehicle Wireless Charging Application," *IEEE Transactions on Transportation Electrification*, vol. 5, no. 4, pp. 934–945, Dec. 2019, doi: https://doi.org/10.1109/tte.2019.2929443...
- [55] CENEX, "New electric taxi livery for UK's first wireless charging trial," CENEX, 2024. [Online]. Available: https://www.cenex.co.uk/news/new-electric-taxi-livery-for-uks-first-wireless-charging-trial/. [Accessed: 24-Oct-2024].
- [56] Wireless Charging Infrastructure for Electric Transport (WICET), "Home," WICET, 2024. [Online]. Available: https://wicet.co.uk/. [Accessed: 24-Oct-2024].
- [57] O. Simon and D. Shkadarevich, "Application of V2G communication for wireless interoperable power transfer," 2017 *Twelfth International Conference on Ecological Vehicles and Renewable Energies (EVER)*, 2017, pp. 1-5, doi: 10.1109/EVER.2017.7935929.
- [58] Y. Zhao, H. Xu, Y. Shen, H. Han and Z. Yuan, "Research of orderly charging control system for Electrical Vehicles based on Zigbee and GPRS networks," 2014 IEEE Conference and Expo Transportation Electrification Asia-Pacific (ITEC Asia-Pacific), 2014, pp. 1-5, doi: 10.1109/ITEC-AP.2014.6941267.
- [59] S. Ishino, I. Takano, K. Yano, and N. Shinohara, "Frequency-division techniques for microwave power transfer and wireless communication system with closed waveguide," *2016 IEEE Wireless Power Transfer Conference (WPTC)*, 2016, pp. 1-4, doi: 10.1109/WPT.2016.7498769.

- [60] M. Zhixin, F. Aming, Q. Haihong, and P. Pingyan, "Characteristics and Design of Transformer in Loosely Coupled Inductive Power Transfer System," in *2010 International Conference on Electrical and Control Engineering*, WuHan, China, 2010, pp. 3454-3457, doi: 10.1109/iCECE.2010.841.
- [61] N. Kaminski, "State of the art and the future of wide bandgap devices," in Proc. 13th IEEE Eur. Conf. Power Electron. Appl., Sep. 2009, pp. 1–9.
- [62] R. Ramachandran and M. Nymand, "Experimental Demonstration of a 98.8% Efficient Isolated DC–DC GaN Converter," *IEEE Transactions on Industrial Electronics*, vol. 64, no. 11, pp. 9104-9113, Nov. 2017, doi: 10.1109/TIE.2016.2613930.
- [63] Corti, F.; Reatti, A.; Wu, Y.-H.; Czarkowski, D.; Musumeci, S. "Zero Voltage Switching Condition in Class-E Inverter for Capacitive Wireless Power Transfer Applications". *Energies* 2021, 14, 911. https://doi.org/10.3390/en14040911
- [64] A. Polleri, Taufik, and M. Anwari, "Modeling and Simulation of Paralleled Series-Loaded-Resonant Converter," in 2008 Second Asia International Conference on Modelling & Simulation (AMS), Kuala Lumpur, Malaysia, 2008, pp. 974-979, doi: 10.1109/AMS.2008.86.
- [65] N. Mohan, T. M. Undeland, and W. P. Robbins, *Power Electronics: Converters, Applications and Design*, 3rd ed. New York; Chichester: John Wiley, 2003.
- [66] R. L. Steigerwald, "A Comparison of Half-Bridge Resonant Converter Topologies," *IEEE Transactions on Power Electronics*, vol. 3, no. 2, pp. 198-206, Apr. 1988.
- [67] M. Salem, A. Jusoh, N. Rumzi, N. Idris, H. Shekhar Das, I. Alhamrouni, "Resonant power converters with respect to passive storage (LC) elements and control techniques An overview", *Renewable and Sustainable Energy Reviews*, Volume 91,2018, Pages 504-520,ISSN 1364-0321, https://doi.org/10.1016/j.rser.2018.04.020.
- [68] JJ. Yang, Y. Shi, W. Y. Wei, and H. Shen, "A wireless power transfer system based on impedance matching network," *International Journal of RF and Microwave Computer-Aided Engineering*, vol. 27, no. 9, pp. 1-9, 2017, doi: 10.1002/mmce.22437.
- [69] K. Ogawa, N. Oodachi, S. Obayashi, and H. Shoki, "A study of efficiency improvement of wireless power transfer by impedance matching," in 2012 IEEE MTT-S International Microwave Workshop Series on Innovative Wireless Power Transmission: Technologies, Systems, and Applications, 2012, pp. 155-157, doi: 10.1109/IMWS.2012.6215774.
- [70] J. Kim, H. Son, D. Kim, and Y. Park, "Impedance matching considering cross coupling for wireless power transfer to multiple receivers," in 2013 IEEE Wireless Power Transfer (WPT), 2013, pp. 226-229, doi: 10.1109/WPT.2013.6556924.
- [71] M. S. Hosen et al., "A post-mortem study case of a dynamically aged commercial NMC cell under real-life driving conditions," Energies, vol. 16, no. 3, art. 1046, 2023.
- [72] G. Qian, Y. Cheng, G. Chen, S. Chen, P. Zhao, and G. Wang, "Sensitivity Comparison of Impedance Matching Circuits for Inductively Coupled WPT," in 2018 IEEE Wireless Power Transfer Conference (WPTC), 2018, pp. 1-4, doi: 10.1109/WPT.2018.8639374.
- [73] Zhen Zhang; Hongliang Pang, "Control for Single Pickup," in *Wireless Power Transfer: Principles and Applications*, IEEE, 2023, pp.141-177, doi: 10.1002/9781119654117.ch5
- [74] U. Mathure and R. V. S. Ramkrishna, "Simulation of Maximum Efficiency Point Tracking in Wireless Power Transfer Systems using Pulse Density Modulation," 2020 Third International Conference on Multimedia Processing, Communication & Information Technology (MPCIT), Shivamogga, India, 2020, pp. 1-9, doi: 10.1109/MPCIT51588.2020.9350475.
- [75] D. Pehrman, *High Efficiency Inductive Power Transfer Systems for Vehicle Charging*, Ph.D. dissertation, Dept. of Electrical Engineering, Chalmers Univ. of Technology, Gothenburg, Sweden, 2021. ISBN 978-91-7905-513-4.
- [76] S. Y. R. Hui, W. Zhong and C. K. Lee, "A Critical Review of Recent Progress in Mid-Range Wireless Power Transfer," in *IEEE Transactions on Power Electronics*, vol. 29, no. 9, pp. 4500-4511, Sept. 2014, doi: 10.1109/TPEL.2013.2249670.
- [77] W. Zhang and C. C. Mi, "Compensation Topologies of High-Power Wireless Power Transfer Systems," in *IEEE Transactions on Vehicular Technology*, vol. 65, no. 6, pp. 4768-4778, June 2016, doi: 10.1109/TVT.2015.2454292

- [78] E. R. Joy, B. K. Kushwaha, G. Rituraj and P. Kumar, "Analysis and comparison of four compensation topologies of contactless power transfer system," *2015 4th International Conference on Electric Power and Energy Conversion Systems (EPECS)*, Sharjah, United Arab Emirates, 2015, pp. 1-6, doi: 10.1109/EPECS.2015.7368544.
- [79] Y. Yang, M. El Baghdadi, Y. Lan, Y. Benomar, J. Van Mierlo, and O. Hegazy, "Design Methodology, Modeling, and Comparative Study of Wireless Power Transfer Systems for Electric Vehicles," *Energies*, vol. 11, no. 7, p. 1716, Jul. 2018. doi: https://doi.org/10.3390/en11071716.
- [80] M. Singh, S. Samanta, and S. P. Das, "A Generalized Method of Determining Coil and Compensation Circuit Parameters of Basic WPT Topologies," presented at the *2021 National Power Electronics Conference (NPEC)*, Dec. 2021. doi: https://doi.org/10.1109/npec52100.2021.9672507.
- [81] C. -Y. Lu, Y. -R. Chen and H. -C. Chen, "Simultaneous Wireless Power and Data Transfer System Based on SP Compensation Topology," *2024 IEEE Wireless Power Technology Conference and Expo (WPTCE)*, Kyoto, Japan, 2024, pp. 630-635, doi: 10.1109/WPTCE59894.2024.10557269.
- [82] R. Huang, B. Zhang, D. Qiu and Y. Zhang, "Frequency Splitting Phenomena of Magnetic Resonant Coupling Wireless Power Transfer," in *IEEE Transactions on Magnetics*, vol. 50, no. 11, pp. 1-4, Nov. 2014, Art no. 8600204, doi: 10.1109/TMAG.2014.2331143
- [83] R. Narayanamoorthi, A. V. Juliet, and B. Chokkalingam, "Cross interference minimization and simultaneous wireless power transfer to multiple frequency loads using frequency bifurcation approach," *IEEE Trans. Power Electron.*, vol. 34, no. 11, pp. 10898–10909, Nov. 2019, doi: 10.1109/TPEL.2019.2898453.
- [84] G. Blankson, M. Darwish and C. S. Lai, "Wireless Power Transfer System for Electric Vehicle Charging with Frequency Hopping A Concept and Circuit Design," *2023 58th International Universities Power Engineering Conference (UPEC)*, Dublin, Ireland, 2023, pp. 1-6, doi: 10.1109/UPEC57427.2023.10294567.
- [85] H. Lamarr and G. Antheil, "Secret Communication System," U.S. Patent 2,292,387, Aug. 11, 1942.
- [86] "Hedy Lamarr and Patent," Hearing Health Matters. [Online]. Available: https://hearinghealthmatters.org/wp-content/uploads/2014/01/Lamarr-and-Patent.gif. [Accessed: 24-Oct-2024].
- [87] M. K. Simon, J. K. Omura, R. A. Scholtz, and B. K. Levitt, Spread Spectrum Communications Handbook. New York: McGraw-Hill, 1994.
- [88] J. C. Haartsen, "The Bluetooth Radio System," *IEEE Pers. Commun.*, vol. 7, no. 1, pp. 28–36, Feb. 2000.
- [89] E. Dahlman, S. Parkvall, and J. Skold, 5G NR: The Next Generation Wireless Access Technology. Oxford: Academic Press, 2018
- [90] R. L. Pickholtz, D. L. Schilling, and L. I. Milstein, "Theory of Spread-Spectrum Communications—A Tutorial," *IEEE Trans. Commun.*, vol. 30, no. 5, pp. 855–884, May 1982.
- [91] W. Stallings, Wireless Communications & Networks. Boston: Pearson, 2004.
- [92] A. Huang et al., "Optimal matching reactance design and validation in wireless power transfer system for Electric Vehicle based on SAE J2954-RP," 2020 IEEE Wireless Power Transfer Conference (WPTC), 2020, pp. 174-177, doi: 10.1109/WPTC48563.2020.9295576.
- [93] Editor, "ORNL polyphase wireless power transfer system achieves 270kW charge; sets another world record for electric light-duty passenger vehicles," *BatteryIndustry.tech*, Jun. 24, 2024. [Online]. Available: https://batteryindustry.tech/ornl-polyphase-wireless-power-transfer-system-achieves-270kw-charge-sets-another-world-record-for-electric-light-duty-passenger-vehicles/. Accessed: Sep. 13, 2024
- [94] F. Ulaby, E. Michielssen, and U. Ravaioli, *Fundamentals of Applied Electromagnetics*, 6th ed. Upper Saddle River, NJ, USA: Prentice-Hall, 2010.
- [95] R. C. Booton, Computational Methods for Electromagnetics, New York, NY, USA: Wiley-IEEE Press, 1992.
- [96] Nexperia, *GAN190-650EBE: 650V GaN E-mode HEMT Datasheet*. [Online]. Available: https://assets.nexperia.com/documents/data-sheet/GAN190-650EBE.pdf
- [97] B. Razavi, "The Bootstrapped Switch," *IEEE Solid-State Circuits Magazine*, vol. 7, no. 3, pp. 12–15, Summer 2015. [Online]. Available: https://ieeexplore.ieee.org/document/7258484/
- [98] Farnell, "AWG Conversion Calculator." [Online]. Available: https://uk.farnell.com/awg-conversion-calculator

[99] Y. Wang, W. Liu, and Y. Xie, "Design and Optimization for Circular Planar Spiral Coils in Wireless Power Transfer System," in *Proc. 22nd Int. Conf. Electrical Machines and Systems (ICEMS)*, Harbin, China, 2019, pp. 1–4, doi: 10.1109/ICEMS.2019.8922255.

[100] K. Kaizer, "Spiral Coil Calculator," Kaizer Power Electronics. [Online]. Available: https://kaizerpowerelectronics.dk/calculators/spiral-coil-calculator/

[101] Circuits.dk, "Flat Spiral Coil Inductor Calculator." [Online]. Available: https://www.circuits.dk/calculator_flat_spiral_coil_inductor.htm

[102] H. A. Wheeler, "Simple Inductance Formulas for Radio Coils," *Proc. IRE*, vol. 16, no. 10, pp. 1398–1400, Oct. 1928, doi: 10.1109/JRPROC.1928.221309.

[5.12103] Würth Elektronik, 760308101303: WE-WPCC Wireless Power Charging Coil Datasheet. [Online]. Available: https://www.we-online.com/components/products/datasheet/760308101303.pdf

[104] Toshiba, TLP7920 Optocoupler Datasheet, May 2016. [Online]. Available:

https://www.mouser.co.uk/datasheet/2/408/TLP7920 datasheet en 20160523-963935.pdf

[105] Texas Instruments, INA240-Q1: Automotive, High-Precision Current Sense Amplifier Datasheet. [Online]. Available: https://www.ti.com/lit/ds/symlink/ina240-q1.pdf

[106] Multicomp Pro, MP004651 SMD Transformer Datasheet. [Online]. Available: https://www.farnell.com/datasheets/3449666.pdf

[107] Espressif Systems, ESP32 Technical Reference Manual. [Online]. Available:

https://www.espressif.com/sites/default/files/documentation/esp32 technical reference manual en.pdf

[108] Espressif Systems, "ESP32-WROOM-32E & ESP32-WROOM-32UE Datasheet," v1.9x, May 29, 2020 (latest rev per PDF). [Online]. Available: https://www.espressif.com/sites/default/files/documentation/esp32-wroom-32e_esp32-wroom-32ue_datasheet_en.pdf (accessed: Aug. 29, 2025). Espressif Systems

[109] Espressif Systems, "ESP32-WROOM-32 Datasheet," v3.6, 2025. [Online]. Available:

https://www.espressif.com/sites/default/files/documentation/esp32-wroom-32_datasheet_en.pdf (accessed: Aug. 29, 2025). Espressif Systems

[110] Espressif Docs, "Motor Control PWM (MCPWM) — ESP-IDF Programming Guide," 2025. [Online]. Available:

https://docs.espressif.com/projects/esp-idf/en/stable/esp32/api-reference/peripherals/mcpwm.html (accessed: Aug. 29, 2025). Espressif Docs

[111] Espressif Docs, "Analog to Digital Converter (ADC) — ESP-IDF Programming Guide," 2025. [Online]. Available:

https://docs.espressif.com/projects/esp-idf/en/latest/api-reference/peripherals/adc.html (accessed: Aug. 29, 2025). Espressif Docs

[112] STMicroelectronics, "STM32G474xB/xC/xE Datasheet (DS12288 Rev 6)," Nov. 2021. [Online]. Available:

https://www.st.com/resource/en/datasheet/stm32g474cb.pdf (accessed: Aug. 29, 2025). STMicroelectronics

[113] STMicroelectronics, "STM32G4 Series of mixed-signal MCUs with DSP and FPU — Product Page," 2025. [Online]. Available:

https://www.st.com/en/microcontrollers-microprocessors/stm32g4-series.html (accessed: Aug. 29, 2025). STMicroelectronics

[114] Raspberry Pi Ltd., "RP2040 Datasheet," 2025. [Online]. Available: https://datasheets.raspberrypi.com/rp2040/rp2040-datasheet.pdf (accessed: Aug. 29, 2025).

[115] Texas Instruments, "TMS320F280049C — Product Page," 2025. [Online]. Available: https://www.ti.com/product/TMS320F280049C (accessed: Aug. 29, 2025).

[116] Espressif Systems, "ESP32-H2 Series Datasheet," v1.1, Sep. 27, 2024. [Online]. Available:

https://www.espressif.com/sites/default/files/documentation/esp32-h2_datasheet_en.pdf (accessed: Aug. 29, 2025). Espressif Systems

[117] Espressif Systems, "ESP32-H2 — Thread/Zigbee & BLE 5 SoC (Product Page)," 2025. [Online]. Available:

https://www.espressif.com/en/products/socs/esp32-h2 (accessed: Aug. 29, 2025).

[118] Microchip Technology Inc., "dsPIC33EPXXXGP50X, dsPIC33EPXXXMC20X/50X and PIC24EPXXXGP/MC20X Family Data Sheet," DS70000657J, 2020. [Online]. Available:

https://ww1.microchip.com/downloads/aemDocuments/documents/MCU16/ProductDocuments/DataSheets/dsPIC33EPXXXGP50X-dsPIC33EPXXXMC20X-50X-and-PIC24EPXXXGP-MC20X-Family-Data-Sheet-DS70000657J.pdf. Accessed: Aug. 29, 2025.

[119] Microchip Technology Inc., "dsPIC33EPXXXGP50X, dsPIC33EPXXXMC20X/50X and PIC24EPXXXGP/MC20X Family Silicon Errata and Data Sheet Clarification," DS80000533T, 2023. [Online]. Available:

https://ww1.microchip.com/downloads/aemDocuments/documents/MCU16/ProductDocuments/Errata/dsPIC33EPXXXGP50X-dsPIC33EPXXXMC20X-50X-and-PIC24EPXXXGP-MC20X-Family-Silicon-Errata-and-Data-Sheet-Clarification-DS80000533.pdf. Accessed: Aug. 29, 2025.

[120] Nordic Semiconductor, "nRF52840 Product Specification," v1.9, Jun. 28, 2024. [Online]. Available: https://docs.nordicsemi.com/bundle/nRF52840_PS_v1.9/resource/nRF52840_PS_v1.9.pdf (accessed: Aug. 29, 2025).

[121] Nordic Semiconductor, "nRF52840 — Product Page," 2025. [Online]. Available: https://www.nordicsemi.com/Products/nRF52840 (accessed: Aug. 29, 2025).

[122] Texas Instruments, "TMS320F28004x Real-Time Microcontrollers Datasheet," 2025. [Online]. Available: https://www.ti.com/lit/ds/symlink/tms320f280049.pdf (accessed: Aug. 29, 2025).

[123] Texas Instruments, "CC2652R SimpleLink™ Multiprotocol 2.4-GHz Wireless MCU Datasheet," 2025. [Online]. Available: https://www.ti.com/lit/ds/symlink/cc2652r.pdf (accessed: Aug. 29, 2025).

[124] Texas Instruments, "CC2652R — Product Page," 2025. [Online]. Available: https://www.ti.com/product/CC2652R (accessed: Aug. 29, 2025).

[125] Arduino, "ESP-NOW on Nano ESP32," Arduino Documentation. [Online]. Available: https://docs.arduino.cc/tutorials/nano-esp32/esp-now/

[126] E. Andersen, S. Roundy, and B. D. Truong, "Frequency–dependence of power and efficiency for resonant inductive coupling and magnetoelectric wireless power transfer systems," *Smart Materials and Structures*, vol. 31, no. 10, pp. 105026–105041, 2022, doi: 10.1088/1361-665X/ac8bb6.

[127] ON Semiconductor, *MBR40250: 40 A, 250 V Schottky Barrier Rectifier*, MBR40250-D datasheet, Rev. 2, Aug. 2017. [Online]. Available: https://www.onsemi.com/pdf/datasheet/mbr40250-d.pdf

[128] A. Brazil, "A Brief Explanation of Litz Diameters and Tolerances - Rubadue Wire," Rubadue Wire, Dec. 21, 2023. https://rubadue.com/a-brief-explanation-of-litz-diameters-and-tolerances

[129] J. Teel, "Complete cost guide — Developing and manufacturing an electronic product," Predictable Designs, 2024. [Online]. Available: https://predictabledesigns.com/how-much-does-it-cost-to-develop-and-manufacture-new-electronic-product/ (accessed Sep. 1, 2025).

[130] ALLPCB, "Custom PCB Cost Per Unit: A Complete Guide," Nov. 7, 2024. [Online]. Available:

https://www.allpcb.com/blog/pcb-ordering/pcb-cost-per-unit.html (accessed Sep. 1, 2025).

[131] Jaycon, "Injection Moulding Price: A 2025 Guide...," May 9, 2025. [Online]. Available: https://www.jaycon.com/injection-moulding-price-a-2025-guide-for-engineers-procurement/ (accessed Sep. 1, 2025)

[132] EMC Compliance, "Common-mode and differential-mode currents," *EMC Compliance Ltd.*, [Online]. Available: https://emccompliance.co.uk/training/Index.htm?context=130

Accessed: Mar. 27, 2025.

[133] A. Vukicevic, J. Tatar, and A. Radivojevic, "On the evaluation of antenna-mode currents along transmission lines," *IEEE Trans. Electromagn. Compat.*, vol. 49, no. 2, pp. 436–445, May 2007. [Online]. Available:

https://www.researchgate.net/publication/3056916 On the Evaluation of Antenna-Mode Currents Along Transmission Lines Accessed: Mar. 27, 2025.

[134] J. H. Dellinger, "The temperature coefficient of resistance of copper," *Bull. Bureau Standards*, vol. 7, no. 1, pp. 71-100, 1910. Accessed: Mar. 27, 2025.